THE CONSTITUTIVE AND DAMAGE MODELS OF ADDITIVELY MANUFACTURED Ti6Al4V ALLOY

A Thesis Submitted to
the Graduate School of
İzmir Institute of Technology
in Partial Fulfillment of the Requirements for

MASTER OF SCIENCE

in Mechanical Engineering

by
Burak HIZLI

December 2021
İZMİR

ACKNOWLEDGEMENTS

Firstly, I would like to thank my advisor, Prof. Mustafa GÜDEN, for his technical, practical, and incentive guidance throughout my master study. I am indebted to him for accepting me into his research team, and for all the contributions that he made to my personal and professional life. It is a great honor to have him as my advisor and to work with him.

Secondly, I would like to thank Dr. Hakan YAVAŞ and his marvelous team at Additive Manufacturing Technology Center, Turkish Aerospace Industries (TAI) for supplying experimental materials, sharing technical knowledges, and conveying directive feedbacks during my thesis study.

I would like to thank all the members of Dynamic Testing and Modeling Laboratory, IZTECH for the positive work atmosphere and memorable times. I would especially like to thank my colleagues, Çağatay ALBİR and Mesut BAYHAN, for their helpful inputs, technical supports during my experimental studies, and their friendship.

I would like to thank the competent staff of Center For Materials Research, IZTECH for providing technical assistance in the usage of the scanning electron microscope and further microstructural analysis for my thesis study.

Lastly, I would like to express my deepest and greatest gratitude to my mother, Gülfidan ŞAKAR, for being a good friend, patient listener, and encouraging exhorter whenever I felt stuck in the challenging times during my education life. Her existence, unconditional love, and never-ending support empower me to achieve my goals. I would not have succeeded without her. I profoundly appreciate all the sacrifices that she made for me. I will always endeavor throughout my life to make her proud of me.

ABSTRACT

THE CONSTITUTIVE AND DAMAGE MODELS OF ADDITIVELY MANUFACTURED Ti6Al4V ALLOY

Electron Beam Melting (EBM) is one of the metal additive manufacturing methods that enable the fabrication of Ti6Al4V alloy parts with intended shapes in where this alloy is of significant interest such as aerospace and biomedical industries due to its outstanding properties. In this study, the microstructural and mechanical properties of EBM-produced Ti64 were comprehensively investigated. Microstructural analysis was conducted on as-built specimens. Microstructural analysis showed that EBM-produced Ti64 possesses α+β duplex phase with directional microstructural alterations and high porosity fraction in the part volume. Mechanical properties were investigated under tension loadings at quasi-static rates (10^{-3}-10^{-1} s^{-1}) and compression loading at quasi-static and high strain rates (10^{-3}-2154 s^{-1}). Thereafter, Johnson-Cook (JC) strength and damage models were individually calibrated from the experimental results of tension and compression behaviors and experimental fracture strains in order to numerically predict the material flow behavior of EBM-produced Ti64 considering the strain, strain rate, and temperature effects in the case of various loadings combined with temperature changes. EBM-produced Ti64 exhibited proximate mechanical properties in terms of tension and compression behaviors, however extremely low ductile behavior under tension loadings resulting premature failure without necking. Eventual fracture of this material occurred via tearing of the scanned layers for tension loadings and shear crack following the shear band formation propagation on 45° to loading axis for compression loadings. Calibrated JC strength and damage models for EBM-produced Ti64 were able to predict flow behavior and fracture strains within strain rate range between 10^{-3} and 10^{3} s^{-1}. However, the JC strength model could not predict the flow behavior at excessively high strain rates (2154 s^{-1}) due to complex deformation mechanisms including adiabatic heating.

Keywords: Additive Manufacturing, Electron Beam Melting, Ti6Al4V, Mechanical Properties, Johnson-Cook Strength Model, Johnson-Cook Damage Model

ÖZET

EKLEMELİ İMALAT İLE ÜRETİLEN Ti6Al4V ALAŞIMININ YAPISAL VE HASAR MODELLERİ

Elektron Işını ile Ergitme (Electron Beam Melting) (EBM), öne çıkan özelliklerinden dolayı havacılık ve biyomedikal endüstrileri gibi büyük ilgi duyulan yerlerde, Ti6Al4V alaşımı parçaların doğrudan istenilen geometrilerde üretilmesini sağlayan metal eklemeli imalat yöntemlerinden biridir. Bu çalışmada, EBM ile üretilen Ti64'ün mikroyapısal ve mekanik özellikleri kapsamlı bir şekilde araştırılmıştır. Mikroyapısal analizler üretilen numuneler üzerinde yapılmıştır. Mikroyapısal analiz, EBM ile üretilen Ti64'ün yönsel mikroyapısal değişiklikler gösteren α+β ikili fazına ve hacimce yüksek gözenek oranına sahip olduğunu göstermiştir. Mekanik özellikler kuasi-statik hızlarda (10^{-3}-10^{-1} s^{-1}) çekme yükleri ile yarı statik ve yüksek gerinim hızlarında (10^{-3}-2154 s^{-1}) basma yükleri altında incelenmiştir. Daha sonrasında, EBM ile üretilen Ti64'ün sıcaklık değişimleri ile birlikte çeşitli yükleme durumlarında malzeme akma davranışını gerinim, gerinim oranı ve sıcaklık etkilerini dikkate alarak numerik olarak tayin etmek için, Johnson-Cook (JC) mukavemet ve hasar modelleri, çekme ve basma davranışlarının deneysel sonuçlarından ve deneysel kırılma gerinimlerinden ayrı ayrı kalibre edilmiştir. EBM ile üretilen Ti64, çekme ve basma davranışları açısından literatür ile yakın mekanik özellikler göstermiştir, ancak çekme yükleri altında boyun verme olmadan erken kopma ile sonuçlanan son derece düşük sünek davranış göstermiştir. Bu malzemenin nihai kopması çekme yükleri için taranmış tabakaların ayrılması ve basma yükleri için yükleme eksenine 45°' de kesme bandı oluşumunun ardından kesme kırığı ile meydana gelmiştir. EBM ile üretilen Ti64 için kalibre edilmiş JC mukavemet ve hasar modelleri, 10^{-3} ve 10^{3} s^{-1} arasındaki gerinim hızı aralığında akış davranışını ve kırılma gerilmelerini tayin edebilmektedir. Ancak, JC mukavemet modeli adyabatik ısıtmayı da içeren karmaşık deformasyon mekanizmaları nedeniyle aşırı yüksek gerinim hızlarında (2154 s^{-1}) akış davranışını tahmin edememiştir.

Anahtar Kelimeler: Eklemeli İmalat, Elektron Işını ile Ergitme, Ti6Al4V, Mekanik Özellikler, JC Mukavemet Modeli, JC Hasar Modeli

In the memory of my grandmother…

TABLE OF CONTENTS

LIST OF FIGURES

Figure **Page**

Figure **Page**

Figure **Page**

Figure **Page**

Figure **Page**

Figure **Page**

Figure **Page**

LIST OF TABLES

LIST OF ABBREVIATIONS

Ti64	Ti6Al4V
AM	Additive Manufacturing
DED	Directed Energy Deposition
PBF	Powder-Bed Fusion
EBM	Electron Beam Melting
HCP	Hexagonal Close-Packed
BCC	Body-Centered Cubic
FCC	Face-Centered Cubic
FEA	Finite Element Analysis
CAD	Computer-Aided Design
SLM	Selective Laser Melting
SLS	Selective Laser Sintering
DMLS	Direct Metal Laser Sintering
ANN	Artificial Neural Network
ZA	Zerilli-Armstrong
MTS	Mechanical Threshold Stress
ARR	Arrhenius
SHPB	Split Hopkinson Pressure Bar
SRS	Strain Rate Sensitivity
OM	Optical Microscope
SEM	Scanning Electron Microscope
HIP	Hot Isostatic Pressure

CHAPTER 1

INTRODUCTION

1.1. Background

Titanium and its alloys are highly demanded metallic materials in the broad applications of major industries such as aerospace, automotive, marine, and biomedical. More specifically, Ti6Al4V (Ti64) alloy is the most preferred titanium alloy among them due to having excellent and attractive properties as follows: high strength-to-weight ratio, high toughness, durability, superior biocompatibility, long fatigue life, good creep, and corrosion resistance. In recent years, additive manufacturing (AM) techniques such as powder bed fusion (PBF) and direct energy deposition (DED) have gained significant interest in the production of metallic parts using layer-by-layer concept due to advanced capabilities comparing the conventional methods over near-net-shape product manufacturing directly from 3D design almost with no geometrical constraints, minimal material waste, short process time and relatively low cost. As Ti64 has several deterrent issues in manufacturing and post-machining using conventional methods, the manufacturability of Ti64 parts with AM techniques allows easy and efficient fabrication and optimization of the industrial parts with outstanding properties. Electron Beam Melting (EBM) stands as a suitable AM method for Ti64 alloy as being able to manufacture high strength, stress relieved parts within the vacuumed build environment.

EBM systems have started being industrialized in serial production by the companies lately. Generally, produced parts are the functional components that are designed to operate under various loadings and ambient conditions. In order to evaluate the component performance and material behavior for intended conditions, long, time-consuming, and hard-to-accomplish testing procedures need to be completed. Therefore, constitutive and damage models raise as numerical tools that facilitate to predict and demonstrate material behavior by utilizing several material constants under various loading conditions including high-rate loadings, combined with temperature change. In addition to that, the deformation behavior of metals and alloys is a complex phenomenon as the hardening and softening mechanisms which control the deformation under loadings

are affected by several factors such as strain, strain rate, temperature. Also, constitutive and damage models should precisely correlate with the material behavior. At this point, Johnson-Cook (JC) strength and damage models are the most widely used numerical tools accounting for aforementioned factors due to their simplicity, relatively short testing procedure in calibrating the model constants, availability in code libraries of most Finite Element Analysis (FEA) softwares, and their convergence with the exact material behavior.

Although EBM-produced Ti64 alloy has been studied in broad scope, a comprehensive material model consisting of flow and damage characteristics of EBM-produced Ti64 remains an open issue in the literature. This study aims to fulfill the requirement of explicit material models in the intended areas incorporating correctly characterized material properties in order to provide a numerical approach in the prediction of material behavior and facilitate the efficient usage of EBM in the manufacturing of different and complex shaped parts. Therefore, JC strength and damage model constants are individually calibrated for EBM-produced Ti64 based on experimental characterization of this alloy.

1.2. Scope of the Thesis

In this thesis, comprehensive material characterization of EBM-produced Ti64 is conducted in terms of microstructural, mechanical, and fracture properties of vertically built parts. Microstructural properties are investigated based on as-built parts considering surface roughness conditions, phase constitutions, and internal porosities. Experimental testing procedures are conducted for investigating tension at quasi-static rates and compression behavior at both quasi-static and high strain rates. Fracture characteristics of EBM-produced Ti64 are investigated for understanding fracture initiation and progression mechanisms under loadings. Thereafter, in order to develop material models that can be utilized as numerical tools in simulative studies of EBM-produced Ti64 parts, JC strength and damage models and their parameters are calibrated by using experimentally obtained mechanical properties of EBM-produced parts. Also, calibrated parameters and fidelity of the JC strength and damage models are assessed with the experimental data and other proposed models for Ti64 alloy in the literature accordingly.

1.3. Structure of the Thesis

This study is organized into eight chapters. The general structure of the thesis and chapter contents are concisely described as follows:

- Chapter 1: Brief introduction related to thesis background, scope, and general structure of the thesis is stated.
- Chapter 2: Literature survey is compiled based on Ti and Ti alloys, especially Ti64 alloy, and AM methods for metals. The detailed manufacturing process and system schematics of EBM are given.
- Chapter 3: Constitutive models for metals and alloys, their classifications, list of related parameters are given. Also, fundamentals of JC strength and damage models including determination of JC model parameters by using experimental data are described in detail.
- Chapter 4: Experimental methodology used in determining microstructural and mechanical properties of EBM-produced Ti64 is published.
- Chapter 5: Obtained experimental results regarding experimental methodology with other associated findings from primary results, and microscopic images of microstructure and fracture surfaces are presented.
- Chapter 6: Determination of JC strength and damage model parameters for EBM-produced Ti64 by utilizing related experimental data are presented and calibrated parameters are listed.
- Chapter 7: All the experimental findings of this study are discussed and compared with the current literature. Prediction accuracy and conformity of the calibrated JC strength and damage model with experimental material behavior are evaluated and compared with the other proposed JC models for Ti64 in the literature.
- Chapter 8: Conclusions covering the microstructural, mechanical, fracture properties, and JC strength and damage models of studied EBM-produced Ti64 alloy are published. Further suggestions for improving mechanical properties of EBM-produced Ti64 and fidelity of JC strength and damage models are listed.

CHAPTER 2

LITERATURE REVIEW

2.1. Titanium and Its Alloys

Titanium is one of the abundant elements such as iron, aluminum, and magnesium that exist in the earth's crust in high amounts. It was first discovered by an English mineralogist named William Gregor in 1791. However, titanium gained most of the attention in the 1950s, in the period following World War II due to its outstanding properties [1]. Titanium still stands as the fundamental metallic material for the major industries such as aerospace, marine, biomedical, and chemical as it provides three main features compared to other metals listed as the high strength-to-weight ratio, biocompatibility, and corrosion resistance [2, 3] (Table 2.1). It is known that titanium cannot be refined in high purity due to its high affinity to atmospheric gases. Another issue with pure titanium is that pure titanium tends to exhibit low ductility and fracture brittly [1]. Therefore, alloying of titanium with other elements such as Al, V, Sn, Mo, Cr, Zr, and Mo stabilizes the microstructure, enhances its essential mechanical properties, and increases usefulness of titanium alloys in high strength and high temperature applications.

Table 2.1. Comparison of some of the important properties of titanium with other most utilizing metals. (Source: Lütjering and Williams, 2003 [1])

Property / Metal	Ti	Fe	Ni	Al
Melting Temperature (°C)	1668	1538	1455	660
Allotropic Transformation (°C)	882	912	-	-
Crystal Structure	BCC(β)→HCP(α)	FCC(γ)→BCC(α)	FCC	FCC
Room Temperature E (GPa)	115	215	200	72
Yield Stress Level (MPa)	1000	1000	1000	500
Density (g/cm^3)	4.5	7.9	8.9	2.7
Corrosion Resistance	Very High	Low	Medium	High
Reactivity with Oxygen	Very High	Low	Low	High
Price of Metal	Very High	Low	High	Medium

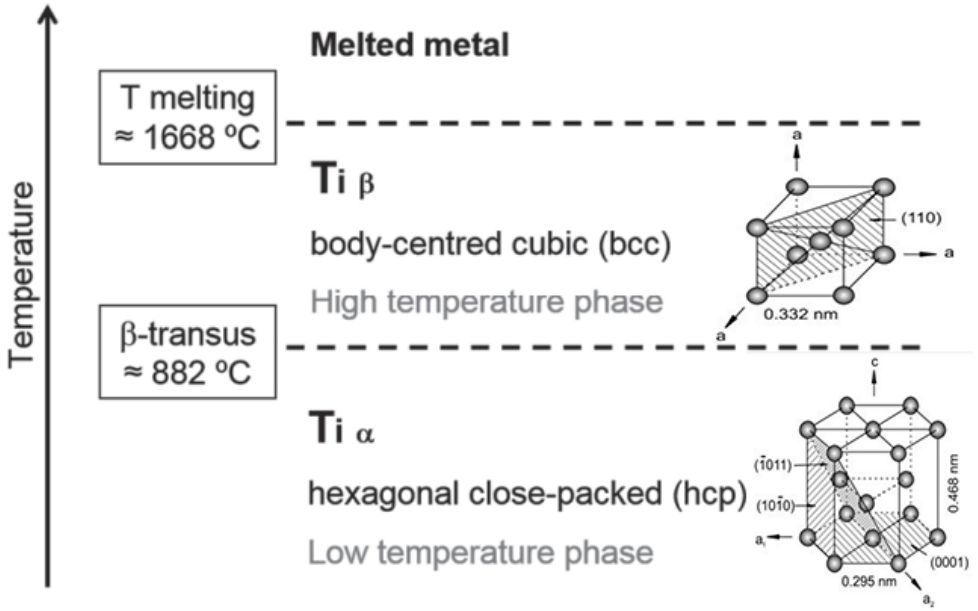

Figure 2.1. Schematic illustration of lattice structures of titanium and transformation temperatures. (Adapted from sources: Murgau, 2016 [4] and Leyens and Peters, 2003 [5])

For pure titanium, the allotropic phase transformation from β to α phase occurs at 882 °C, and the crystal lattice structure changes from hexagonal close-packed (HCP) structure to body-centered cubic (BCC) structure (Figure 2.1). However, exact transformation temperature might be prone to alter depending on the purity of the titanium, type, and quantity of alloying elements [1]. Microstructural formations of titanium are strongly affected by the allotropic transformation. Microstructural formations are dependent on cooling rate from melting temperature down to below β transus temperature. Higher cooling rates result in fine, lamellar structures, even the formation of diffusionless martensite structures. Titanium completely melts and turns into liquid form when the temperature exceeds 1668 °C.

On the other hand, the α phase shows lower deformability as the HCP structure is the most difficult one to deform compared to BCC and FCC structures. Dislocation slip with possible mechanical twinning operates during the plastic deformation of titanium due to having high lattice packing densities for α and β phases as sequentially 91% and 83% and only three usable slip systems in HCP structure [1, 5]. Despite the higher packing density of the α phase, dislocations can move in the β phase more easily than the α phase because of the low energy requirement for dislocation motion as a consequence of the shorter minimal slip path [5].

Titanium alloys are generally classified into four categories based on the crystal structure of the alloy composition at room temperature, can be listed as α alloys, near-α alloys, β alloys, and α+β alloys [6]. α alloys consist of relatively high amounts of α stabilizers such as Al, Sn, O, C and Ga, and small amounts of β stabilizers. The addition of α stabilizers increases the β transus temperature. In contrast to α alloys, near-α alloys contain more concentrations of β stabilizers [5, 7]. Main β stabilizer elements are known as V, Mo, Ta, Nb, and Si, they are further sub-grouped as β-isomorphous and β-eutectoid. Both α and near-α alloys exhibit high resistance to creep, moderate strength, reduced ductility, good weldability, and toughness compared to other titanium alloys but these types of alloys cannot be heat treated due to having a limited amount of β stabilizers. Besides, α and near-α alloys have limited forgeability, generally leading to the occurrence of surface cracks. These alloys are generally implemented in high-temperature applications. [1, 2, 3]. β alloys consist of high amounts of β stabilizers and a trace of α stabilizers [2]. For this case, alloying with β stabilizers reduces the β transus temperature. β alloys have the ability of good hardenability, excellent forgeability and cold workability in the solution-treated conditions, also highly resisting to stress-corrosion cracking. However, β alloys exhibit higher density and lower creep resistance properties [3, 4]. In contrast to other titanium alloys, martensitic phase transformation does not occur for β alloys.

α+β alloys possess a mixture of α and β stabilizers, at least one from each stabilizer group, at room temperature. Microstructural features of these types of alloys show the characteristics of both phases, therefore resultant properties are between α and β alloys. When heated, α+β alloys form a high amount of β phase and reversely, the α phase becomes significant at lower temperatures. Additionally, α+β alloys are often able to be solution-strengthened, so the mechanical properties of these types of alloys are adjustable depending on the treatment process. α+β alloys mainly exhibit the combined properties of high strength, ductility, fatigue, and fracture [1, 5, 6]. Extra Low Interstitials (ELI) version of the α+β alloys offers the properties of high fracture toughness and excellent damage tolerance [1]. α+β alloys are the most widely used titanium alloys in broad scope [5]. The simplest and most known example of α+β alloys is Ti6Al4V, also called Ti64 [3]. Alloying elements for titanium and their stabilizing effects on α and β phases are illustrated in Figure 2.2. In addition to that, some of the commercially available titanium alloys with their categories and individual β transus temperatures are tabulated in Table 2.2.

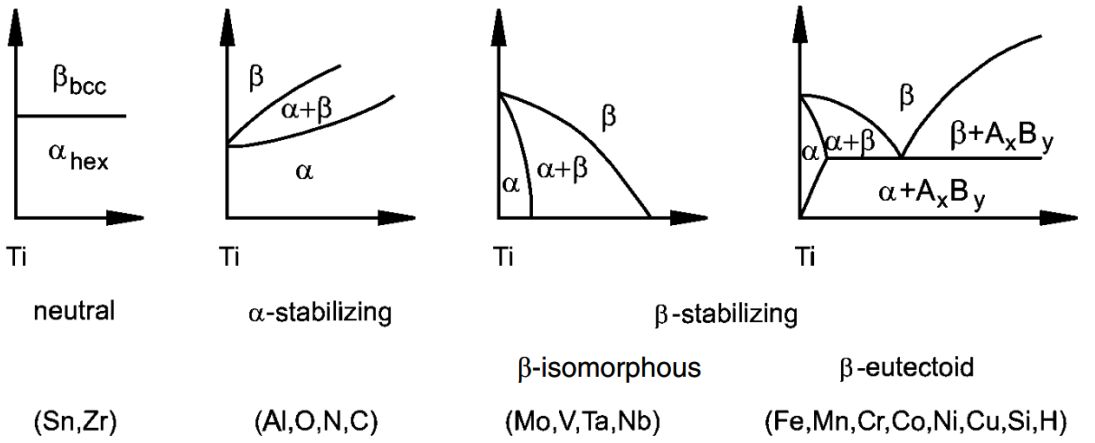

Figure 2.2. Alloying elements for titanium and their stabilizing effects on α and β phases. (Source: Leyens and Peters, 2003 [5])

Table 2.2. Commercially available titanium alloys.
(Adapted from sources: Lütjering and Williams, 2003 [1] and Safdar, 2010 [8])

Alloy Category	**Alloy Composition**	**β Transus Temperature (°C)**
α	Ti-0.2 Pd	915
α	Ti-0.3Mo-0.8Ni	880
α	Ti-5Al-2.5Sn	1040
Near-α	Ti-6Al-2Sn-4Zr-2Mo	995
Near-α	Ti-5Al-5Sn-2Zr-2Mo	980
Near-α	Ti-8Al-1V-1Mo	1040
β	Ti-10V-2Fe-3Al	800
β	Ti-13V-11Cr-3Al	700
β	Ti-3Al-8V-6Cr-4Mo-4Zr	730
α+β	Ti-6Al-4V	995
α+β	Ti-6Al-4V ELI	975
α+β	Ti-6Al-6V-2Sn	945
α+β	Ti-4Al-2Sn-4Mo-0.5Si	975

2.1.1. Ti6Al4V (Ti64) Alloy

Ti6Al4V is one of the α+β alloys which is the most investigated and widely using titanium alloy in commercial industries, 50% annual market share within all titanium products around the world [3, 9]. It mainly contains 5.5-6.75% Al which stabilizes the α phase, 3.5-4.5% V content which stabilizes the β phase, and balanced titanium. Ti64 is firstly developed by Illinois Institute of Technology, USA in 1954, thereafter it became a popular titanium alloy for structural aircraft components with excellent properties and good producibility [1, 8]. Major industries in which Ti64 is extensively utilized are aerospace, biomedical, marine, automobile, energy, and chemical due to its outstanding properties such as high strength, low density, superior biocompatibility, high resistance to creep and corrosion. Important physical properties of Ti64 are listed in Table 2.3. On the contrary of its high usage, manufacturing, and post-machining of Ti64 are difficult tasks since this alloy possesses poor thermal conductivity, high chemical reactivity to oxygen, and inclination to strain hardening. Additionally, its high cost, long time requirements for manufacturing, high material waste due to the subsequent machining for final shape are the other factors that complicate the usage of Ti64 [9].

Table 2.3. Physical properties of Ti64.
(Sources: Lütgering and Williams, 2003 [1] and Donachie, 2003 [3])

Physical Property	Values
β Transus Temperature (°C)	995±20
Melting Temperature (°C)	1604-1660
Density (g/cm^3)	4.429
Elastic Modulus (GPa)	110-140
Yield Strength (MPa)	830
Tensile Strength (MPa)	900
Elongation to Failure (%)	13-16
Poisson's Ratio	0.33
Specific Heat Capacity (J g^{-1} K^{-1})	0.530
Thermal Conductivity (W m^{-1} K^{-1})	7
Linear Thermal Expansion Coefficient (10^{-6} K^{-1})	9.0
Electrical Resistivity (μΩ m)	1.67

Mechanical properties of Ti64 strongly depend on the microstructural formations and distributions of α and β phases as a result of processing history and heat treatment [2]. Ti64 consist of HCP α phase with a small fraction of retained BCC β phase under room conditions when heated above the β transus temperature of 995 °C, α phase completely and reversibly transforms to β phase. Microstructural state of Ti64 is mainly described in three types: fully lamellar, bi-modal, and fully equiaxed microstructures. Ti64 can possess the different morphologies in the final equilibrium state such as globular or primary α, grain boundary allotriomorph α (α_{GB}), α colony, Widmanstätten (basketweave) α platelets, lamellar α+β, prior β phase, martensitic α' and α" phases [1]. Microstructural morphologies form depending on cooling rates from above the β transus temperature. Excessively higher cooling rates (above 410 °C/s) result in diffusionless transformation of HCP α' martensite or orthorhombic α" phase depending on the β phase composition [10]. Thereafter, solution-strengthening and aging treatments in the temperature range between β transus temperature and martensite start temperature (M_s) provide the decomposition of β stabilizer enriched α' martensite into α+β phase. In relatively slow cooling rates, β phase turns into lamellar α+β and α phase forms in the grain boundaries of prior β phases. Additionally, globular α morphology can form from the β phase when the cooling rate is much slower (controlled cooling conditions) [1, 3, 8]. Phase diagram of Ti64 and phase formations corresponding to fast and slow cooling rates are shown in Figure 2.3.

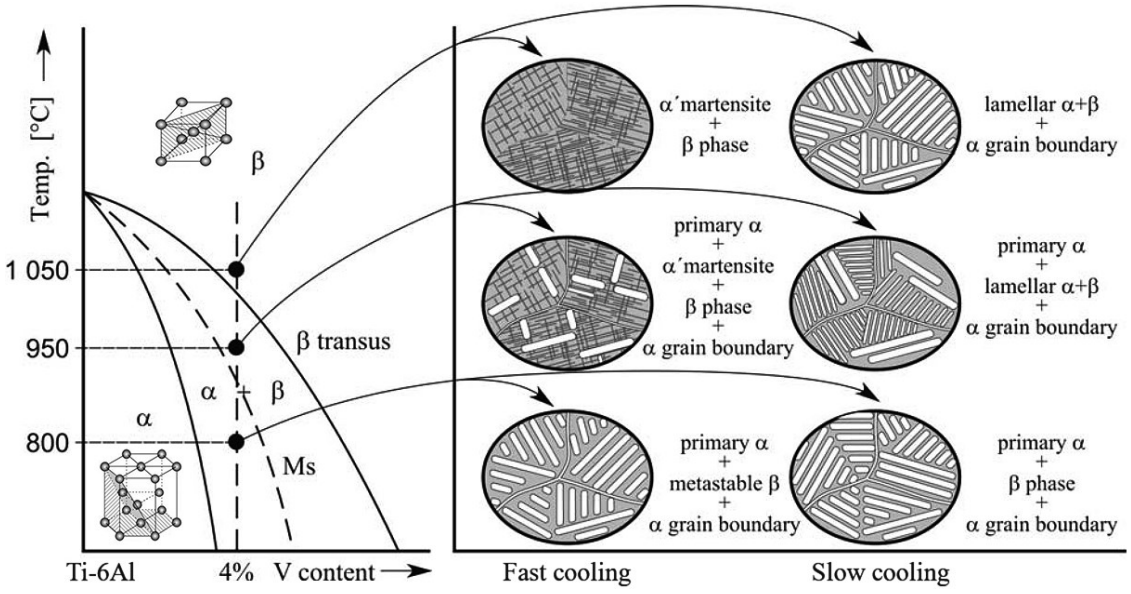

Figure 2.3. Phase diagram of Ti64 and phase morphologies depending on different cooling rates. (Source: Pinke and Réger, 2005 [11]) (Edited)

Other facts about the phase morphologies of Ti64, α phase has a good creep resistance and higher strength compared to the β phase which is the softer phase of Ti64. An increase in the volume fraction of the α phase leads to an increase in strength properties. However, the size of α colony morphology or width of lamellae inversely affect the strength of Ti64 but favor the ductility. Martensitic α' and α'' phases are in metastable conditions due to fast cooling gradient. These martensitic phases result in higher strength and hardness than other morphologies but relatively decrease the ductility and toughness. Moreover, the formation of Widmanstätten morphology helps the strengthening of Ti64 [4].

Al content of Ti64 as an alloying element provides satisfactory strength properties for the alloy without increasing the density since V content enhances the ductility of Ti64 at room temperature [1, 4]. It should also be mentioned that Ti64 contains small amounts of impurity elements in the structure that could potentially affect the resultant mechanical properties of Ti64. Due to the high chemical affinity of Ti64 and uncontrolled manufacturing processes, hydrogen and oxygen can easily diffuse into Ti64. The most hazardous effect is originated from hydrogen content which causes stress-corrosion cracking under high static loadings and corrosion-fatigue under fatigue loadings in humid gaseous environments due to hydrogen embrittlement [1]. Additionally, an increase in oxygen content culminates in more susceptibility to stress-corrosion cracking [6]. Also, higher oxygen content in Ti64 induces higher strength but lowers the other material properties, especially ductility. Oxygen affinity of Ti64 increases with temperature. Consequently, Ti64 is usable in low to moderate temperature ranging up to 350 °C.

Ti64 exhibits strong strain rate sensitivity and temperature dependence in the mechanical responses under tension, compression, and shear loadings in terms of yield stress, ultimate stress, elongation to failure [4, 12]. Increasing strain rates result in higher stress values but lower elongation values. High strain rate sensitivity is particularly observed when Ti64 is deformed at a temperature slightly above the β transus temperature. On the other hand, Ti64 behaves more ductile when exposed to plastic deformation at elevated temperature, but elastic modulus and stress values drastically decrease as a result of softening by temperature [4]. In general, the stress-strain response of Ti64 is similar to other metallic materials. Exemplifier graphs for strain rate sensitivity and temperature effect on the mechanical response of Ti64 are shown in Figure 2.4.

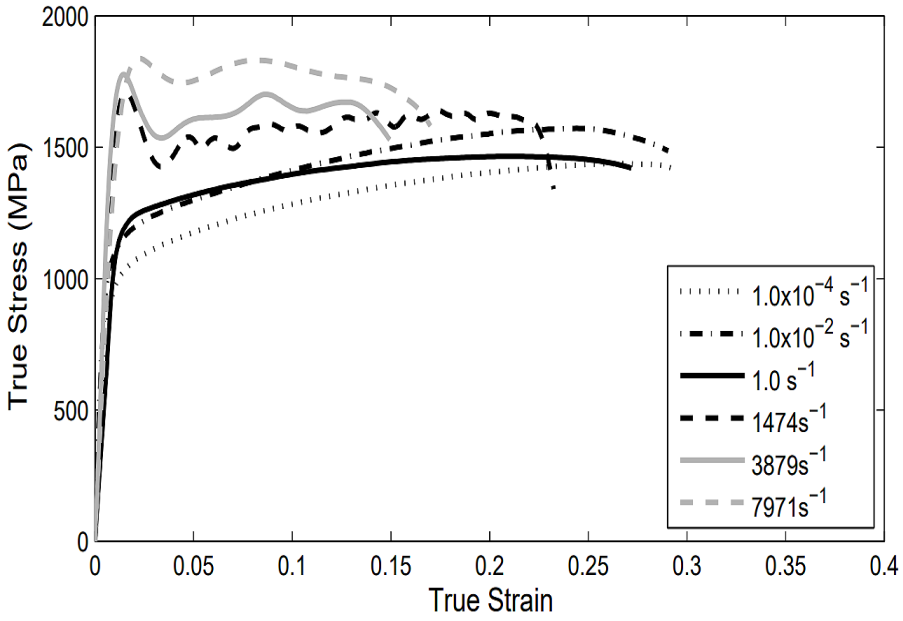

(a)

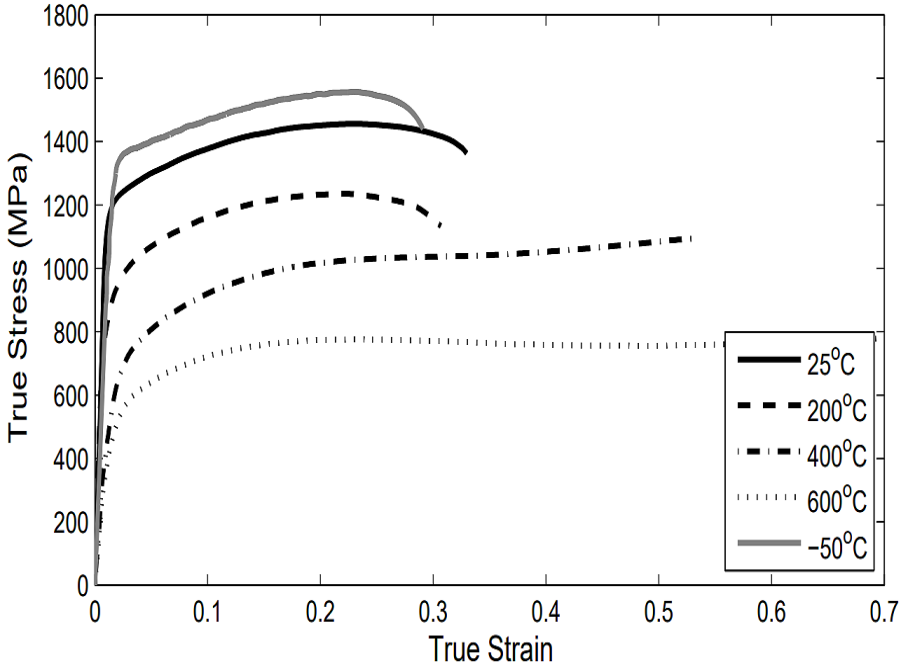

(b)

Figure 2.4. Strain-stress curves of compression behavior of Ti64 at (a) different strain rates, and (b) different temperatures. (Source: Hammer, 2014 [12])

2.2. Additive Manufacturing of Metallic Materials

AM, also called 3D printing or rapid prototyping, is the most recent method that enables the manufacturing of customized 3D parts in a layer-by-layer concept using raw materials, directly from the 3D computer-aided design (CAD) model without any geometrical constraints [9, 13]. In comparison to conventional manufacturing methods, AM offers flexibility in design, the ability to manufacture intricate geometries monolithically, prototyping the parts on-demand use, cost efficiency, minimal material waste, short manufacturing time, and minimum or zero tooling [9, 14]. The unique features of AM have triggered intense attention over the academic and industrial research activities during the time [15]. Developments in AM technology have allowed the emergence and inclusion of the new methods in AM branch. Thus, a broad range of engineering materials from polymers, ceramics, and metals can now be manufactured by AM methods.

AM for metallic materials has important potential in aerospace applications considering the "buy-to-fly" ratio between used raw material mass and final part mass for lightweight components to lower the cost and material waste. Metal AM methods are classified as direct and indirect processes as given in Figure 2.5. Indirect processes are used to manufacture required equipment for the casting of metal parts [16]. Direct processes allow the manufacturing of metallic parts in near-net-shape using metallic raw materials.

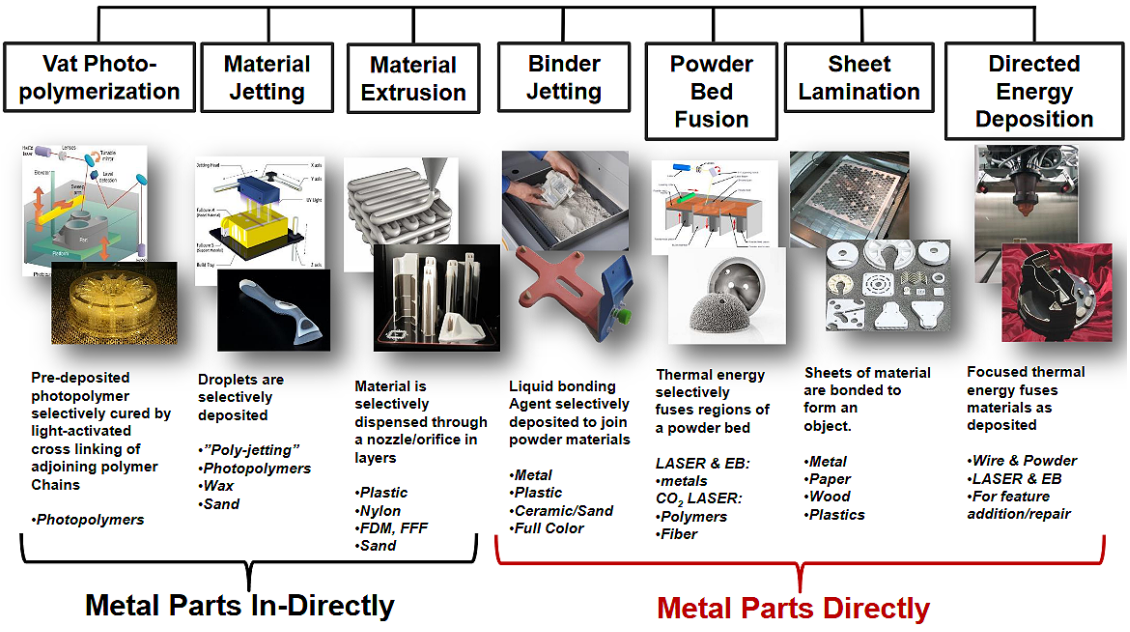

Figure 2.5. In-direct and direct metal AM methods. (Source: Kardys, 2017 [16])

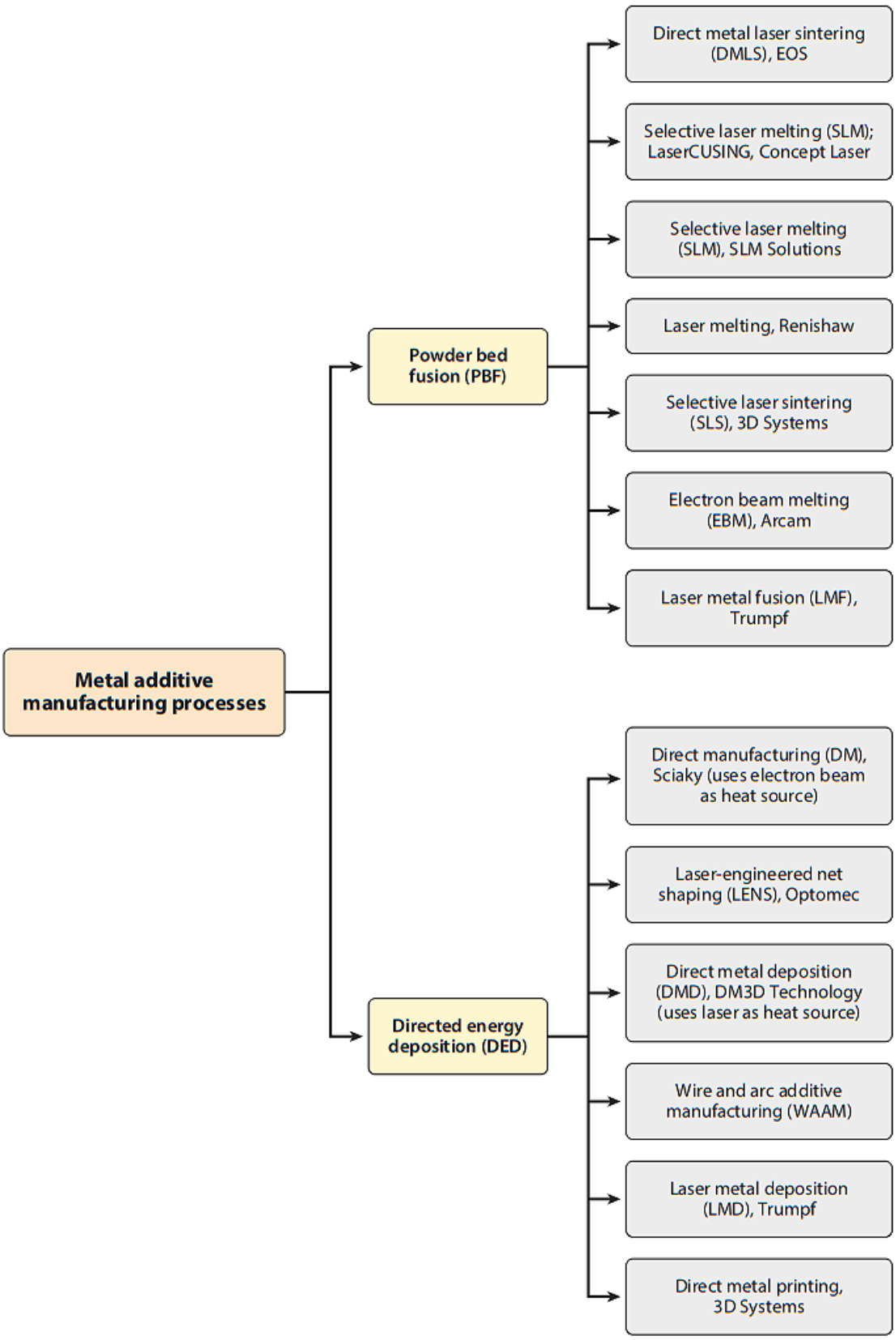

Figure 2.6. AM for metallic materials and their commercial technology providers. (Source: Lewandowski and Seifi, 2016 [17])

Most known metal AM methods and commercial providers are given in Figure 2.6. The methods are generally classified into two groups based on melting or binding mechanism between the layers and feed system: directed energy deposition (DED), and powder-bed fusion (PBF). These two groups are also sub-classified into several methods depending on their unique manufacturing capabilities. These processes have two major inputs such as energy source for heating or melting and feedstock materials to complete the build. Feedstock materials are wire or metal powders depending on the interested AM method. However, the process mechanisms and build conditions of AM methods differ from each other. In PBF methods, manufacturing bases on a base plate of the system as being a bed for powder layers. But, in DED methods, manufacturing progresses with melting the powders that are blown onto or fed wire substrate surface by a coaxial or multi-jet nozzle. In addition to that, different metal powders can be melted simultaneously in DED methods [9]. PBF methods usually use the metal powders as a feedstock material and arc, laser, or electron beam as an energy source during the process. PBF processes are conducted under an inert or vacuumed building atmosphere. For DED-based methods, wire or metal powders can be the feedstock material, and mostly laser energy is utilized in the process. Usage of PBF based methods is often witnessed in the applications compared to DED methods. A comparative information table related to these AM methods and other processing features is published in Table 2.4.

Current producible materials by using metal AM methods are mainly titanium alloys, Co-Cr alloys, nickel-based superalloys, tool steels, copper, aluminum alloys, and high-entropy alloys. Journal distribution chart for studied AM materials in 10 years is given in Figure 2.7. Metal AM methods are capable of manufacturing fully dense parts similar to as-manufactured conventionally [9, 18]. However, as already mentioned, the main considerations in metal AM are headed over to reduction of cost and material usage mainly in aerospace. Thus, topology-based optimization activities are able to be conducted in order to reach improved structural performance with optimum part mass and geometry for intended components without sacrificing the mechanical properties. Moreover, in the biomedical industry, AM applications could lead to the manufacturing of biomedical implants that can individually be customized for the patient's needs in terms of implant geometry and required properties [19]. However, it should be mentioned that there are many issues existing with regards to certification, standardization, and sustainability in AM for metals, further progression is needed to be achieved in the upcoming period for increasing the adaption and efficiency of metal AM methods [20].

Table 2.4. Metal AM methods and their process features. (Source: Kim, 2020 [21])

Defect or Feature	Laser Melting	EBM	DED - Powder fed	DED - Wire fed	Binder Jetting	Sheet Lamination
Feedstock	Powder	Powder	Powder	Wire	Powder	Sheets
Heat Source	Laser	Electron beam	Laser	Laser / E-beam	N/A: kiln	N/A: ultrasound
Atmosphere	Inert	Vacuum	Inert	Inert/Vacuum	Open air	Open air
Part Repair	No	No	Yes	Yes	No	No
New Parts	Yes	Yes	Yes	Yes	Yes	Yes
Multi-material	No	No	Possible	Possible	Infiltration	Yes
Porosity	Low	Low	Low	Low	High	At sheet
Residual Stress	Yes	Low	Yes	Yes	Unknown	Unknown
Cracking	Yes	Not Typical	Yes	Yes	Fragile Green	No
Delamination	Yes	Yes	Yes	Yes	No	Yes
Rapid Solidification	Yes	Yes	Yes	Yes	No	No
***In situ* Aging**	No	Yes	No	No	No	No
Mesh Structures	Yes	Yes	No	No	Limited	Limited
Surface Finish	Medium-rough	Rough	Medium-poor	Poor but smooth	Medium-rough	Machined
Substrate Adherence	Yes	Material dependent	Yes	Yes	N/A	Yes

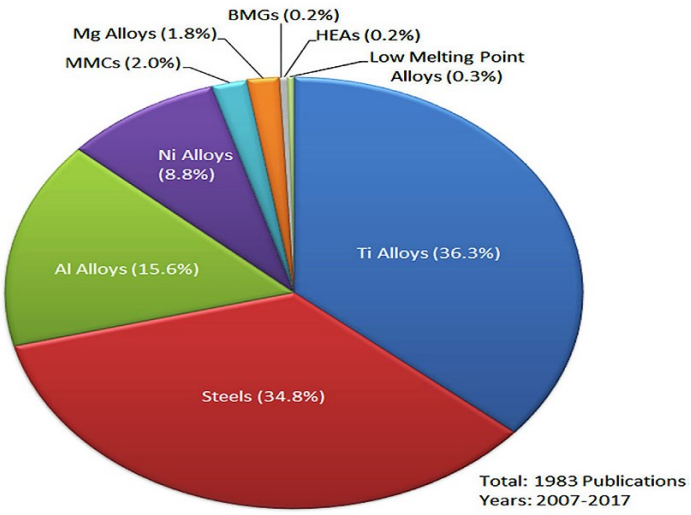

Figure 2.7. Journal distribution of studied AM metal materials between the years of 2007-2017. (Source: Dev Singh et al., 2021 [22])

2.2.1. Directed Energy Deposition (DED)

DED technique is known as core to the AM because laser-assisted manufacturing has been in use since the late 1990s [23]. DED methods can be further classified as laser-based, electron beam-based, plasma-based, and electric arc-based DED. However, laser-based DED methods are highly implemented in the applications, as well as in studies within the literature [24]. The principle behind the DED is to manufacture the metal parts by melting the continuously feeding metal powder or wire onto the substrate surface utilizing high-energy heat sources such as laser or electron beam. The inert gas flow carries the raw powders to the melt zone during the melting process when the powder feedstock is used. Also, inert gas flow provides the chemically inactive and controlled build environment in order to avoid contamination of reactive gases. The processing route starts with designing the 3D part model, thereafter, slicing the main part geometry into many 2D layers with several micron thicknesses. The final metal part is created after successfully melting and solidifying all sliced layers sequentially. Commercially available DED methods and their providers are previously given in Figure 2.6. An exemplifier schematic of the laser-based DED process is illustrated in Figure 2.8.

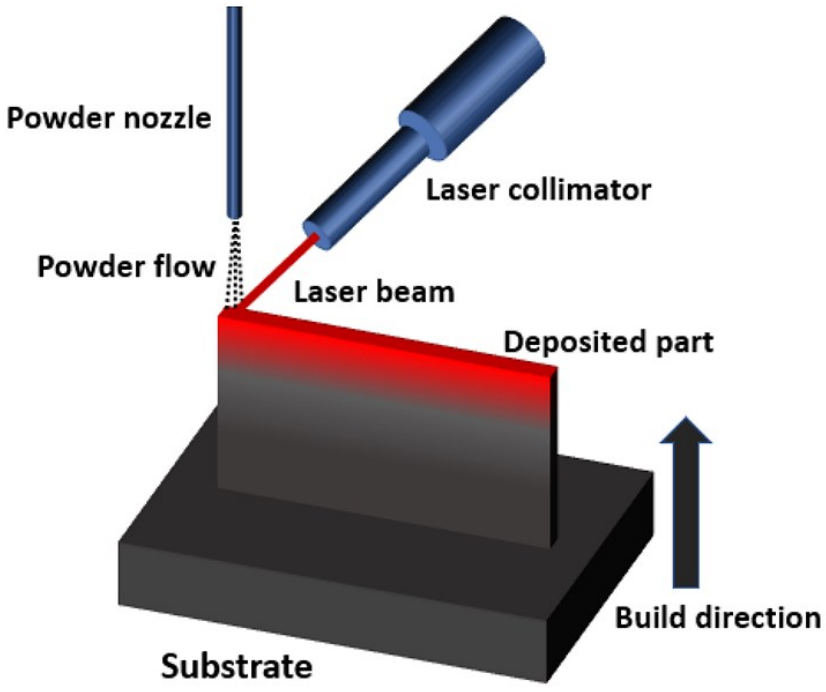

Figure 2.8. Schematic of DED process. (Source: Chen et al., 2020 [25])

DED process offers some unique features as follows: high-rate material deposition, relatively coarse powder or wire feedstock, ability to manufacture big-sized components up to dimensions of several meters, and, most specifically, simultaneous multi-material manufacturing [23]. This feature of DED allows a higher degree of freedom in composition design and manufacturing compositionally graded materials [9]. Moreover, DED methods exhibit suitability to repairment of high-value metal components. The process principle of DED can accomplish the patching of worn or damaged regions of metal components even thin-walled structures like turbine blades with excellent metallurgical bonding and minimal material waste (Figure 2.9). After the repairment, damaged components can possess equivalent or better mechanical properties [9, 26, 27].

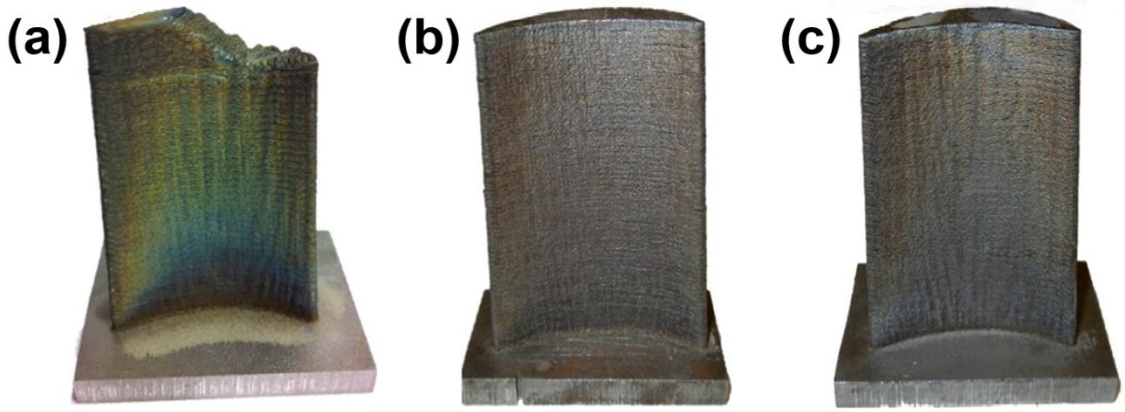

Figure 2.9. Repairing a turbine blade by DED process: (a) damaged blade, (b) original undamaged blade, and (c) repaired blade. (Source: Wilson et al., 2014 [26])

In contrast to mentioned features of DED methods, there are several deterrent issues that limit the use of DED methods. These issues are generally addressed to stock material issues, process and machine tool issues, defects, productivity issues, safety issues, repair-specific issues, compositional issues, and part quality issues. In order to increase the effectiveness of DED methods, relations between process-structure-property-performance should be completely understood in priority [28].

2.2.2. Powder-Bed Fusion (PBF)

PBF methods stand for the advanced manufacturing technology to be used for the parts with more complexities [22]. PBF methods essentially rely on the sense that layer-by-layer manufacturing of the final product by selectively melting or sintering the dispensed metal powder layers most widely using a high thermal energy laser or electron beam within the enclosed build chamber [9, 19, 20]. The schematic of the PBF method is illustrated in Figure 2.10. The working principle of PBF allows the manufacturing directly from the 3D CAD model to the near-net-shaped final product. Process cycle of PBF methods can sequentially be ordered as follows: (1) creation of 3D CAD design of the part and conversion of the file format to stereolithography (STL), (2) slicing the 3D model into thin layers, (3) preheating base plate, (4) dispensing the powder layer on a base plate (substrate) by rake system, (5) locally melting the powder layer with increasing the temperature above the melting temperature of metal using laser or electron beam, (6) solidification of the layers and (7) completion of the process. When one layer is entirely melted, the base plate moves downward. then the system continues in the repeating melting manner described in numbers 4, 5, and 6 until the entire part built is completed.

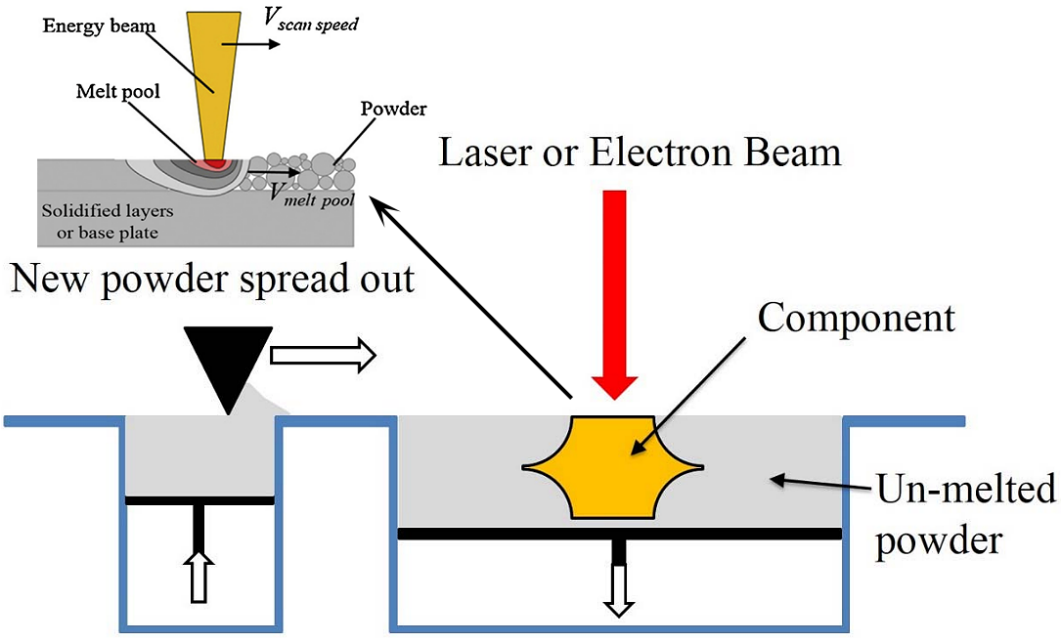

Figure 2.10. Schematic of PBF method during its process.
(Adapted from sources: Gong et al., 2014 [29] and Kahlin, 2017 [30])

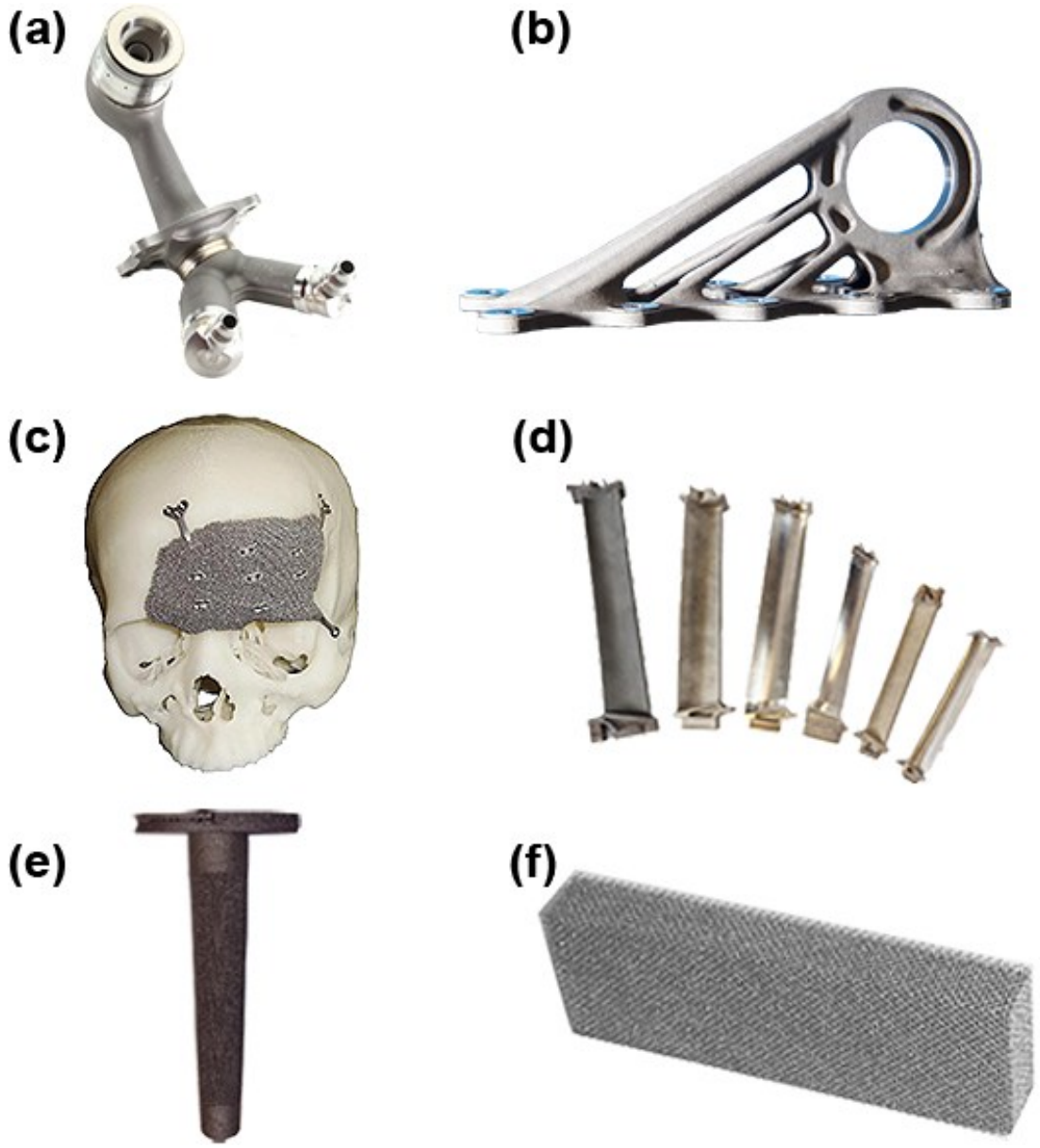

Figure 2.11. Some of the PBF-produced components and implants: (a) CFM LEAP engine fuel nozzle (Source: GE Additive Brochure [31]), (b) a structural bracket for Airbus A350 XWB (Source: Airbus [32]), (c) skull implant (Source: Parthasarathy et al., 2011 [33]), (d) GE-9X engine turbine blades (Source: GE Additive Website [34]), (e) knee implant (Source: Gaytan et al., 2009 [35]) and (f) lattice structure. (Source: GE Additive Website [34])

Some of the PBF-produced components are given in Figure 2.11. An important fact about PBF is that final product quality can potentially be controlled with the bottom-up approach by controlling microstructure, directly linked with microstructure, properties of final product utilizing appropriately varying process parameter [22]. Additionally, the

PBF process is conducted under inert or vacuumed build conditions in order to protect the product from the entrapment of atmospheric gases into metal during layer melting. The vacuum system allows the manufacturing of reactive materials such as γ-TiAl intermetallic alloy [14]. Also, relatively small-sized components can be manufactured due to having a small build volume inside the build chamber. In contrast to DED methods, fine grade metal powders are used as feedstock material. PBF methods are capable of producing near-isotropic materials as laser or electron beam penetrates through several previously melted layers and re-melts them. This situation provides enhanced interlayer fusion [20]. Moreover, PBF methods can be more economically beneficial when the unfused powders are recycled after the process and reused in the next manufacturing process [20]. However, heat dissipation from the melted region to adjacent powders could negatively affect the powder chemistry and size distribution. This likely causes to increase in internal porosity fraction due to the extra oxygen content of reused powder and irregular-shaped powders [20]. Internal porosities directly alter the mechanical characteristics of the built part. PBF methods are not applicable for part repairments, unlike the DED method.

PBF methods, more specifically, SLM and EBM are the most preferred metal AM methods among the others given in Figure 2.6. Also, SLM and EBM have similar working principles, the only heat source for melting the layers changes. In contrast to SLM, attention on EBM has been increasing due to higher resulting part density, faster building rate, and stress-relieved products resulting from the hot processing nature of EBM [9, 19, 28]. Relatively high manufacturing cost is the main disadvantage of EBM.

2.2.2.1. Electron Beam Melting (EBM)

EBM was first patented in 1993 with the principle of melting the electrically conductive materials and proposed for the commercial industry by Arcam AB, a Swedish company now subsidiary of GE Aviation, in 2002. Arcam remains a big EBM technology provider around the world and offers several models of EBM machines to the commercial industries such as Q10plus, Q20plus, A2X, Spectra H, and Spectra L for specific use. Among them, EBM Q20plus has been developed and released for manufacturing Ti64 components for aerospace applications using production level (P-material) Grade 5 and Grade 23 powders [36, 37]. In this study, EBM Q20plus system was employed to produce

the experimental Ti64 parts. Therefore, only EBM Q20plus features will be described in this section. Technical specifications of the EBM machine are tabulated in Table 2.5. Also, a detailed schematic of the EBM machine and exploded views of functional assembly sections are illustrated in Figure 2.12.

EBM process is a preset automatic system that is fully controlled by a system computer without any human interactions during the process. In contrast to other laser-based PBF methods such as SLM and SLS, EBM utilizes high heating energy generated by electron gun up to 6 kW during the melting process with the newer models of EBM machines. EBM can be called as "clean process" as the build chamber is pressurized at 5 x 10^{-4} mbar in a vacuum in order to avoid the reaction of atmospheric gases with the powders or melted zones, triggered by high temperature in the chamber, and reflection of electrons due to collision with gas atoms in the build atmosphere [20]. This allows the more safely material processing for chemically attractive metals such as Ti64. After the emergence of "multi-beam" technology for EBM, the electron beam can simultaneously melt multiple locations with 1-70 spots in a short period of time [19, 38].

Table 2.5. Technical specifications of Arcam EBM Q20plus machine.
(Source: Arcam EBM Systems [36])

Specification	**Value**
Max. build size	350 x 380 mm(Ø/H)
Max. beam power	3000 W
Cathode type	Single crystalline
Min. beam diameter	140 µm
Max. EB translation speed	8000 m/s
Active cooling	Water-cooled heat sink
Vacuum base pressure	5 x10^{-4} mbar (chamber pressure before the start of the process)
Build atmosphere	4 x 10^{-3} mbar (partial pressure of He)
He consumption, build process	4 l/h
He consumption, build cool down	100-150 l/build
Power supply	3 x 400 V, 32 A, 7 kW
Size approx.	2400 x 1300 x 2945 mm (W x D x H)
Weight	2900 kg
CAD interface	Standard: STL

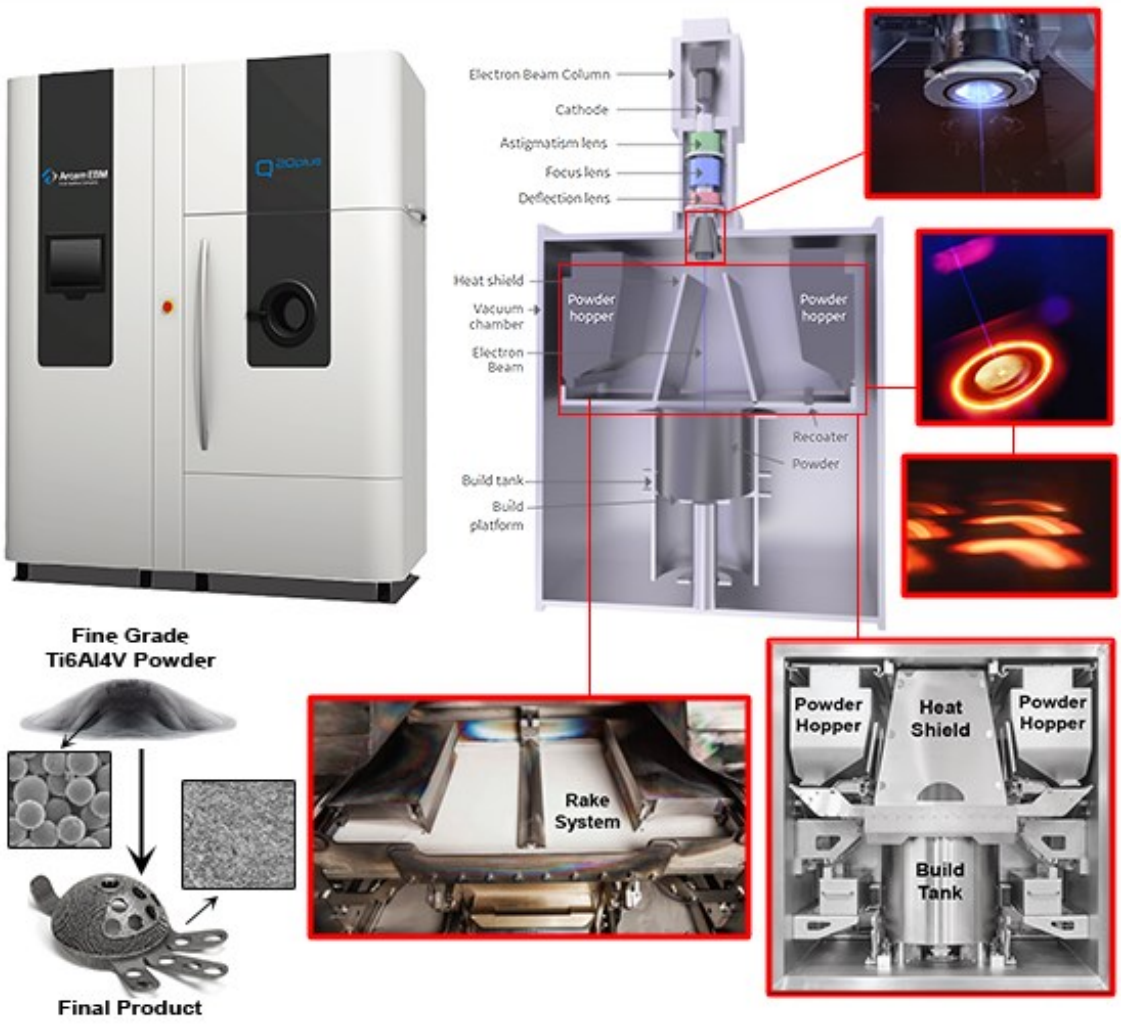

Figure 2.12. Detailed schematic of Arcam EBM Q20plus machine.
(Adapted from sources: Arcam EBM brochures [37, 38])

EBM machine assembly mainly consists of electron beam column, magnetic lenses, build chamber, and build tank. The electron beam column of the EBM machine has a similar working principle with an electron microscope. It possesses a cathode and anode assembly that produce a potential difference of around 60 kV. The heated tungsten or lanthanum hexaboride (LaB_6) cathodic filament emits the electrons at a high speed, so it generates the electron beam when the electric current passes through the filament. For the EBM Q20plus machine, LaB_6 filament is employed in the electron beam column to be used in the processing of Ti64 alloy [39]. The beam current generally varies between 1-50 mA that enabling reaching maximum beam power of 3 kW for the EBM Q20plus machine during the process. The electron beam can travel onto the build platform at high speeds, as previously mentioned, up to 8000 m/s depending on beam power. The electron

beam is controlled by magnetic lenses (coils) in terms of shape, size, and deflection using an electro-magnetic field. The astigmatism lenses and focus lenses placed below the electron gun adjust the beam shape and control the size of the beam for constant focalization, respectively. Deflection lenses are responsible for controlling the beam position according to melt zone locations on the build platform (base plate). Scanning parameters of electron beam such as focus and scan speed are sequentially adjusted by focus offset and speed function [13]. Additionally, during the process, the electron gun is vacuumed between 10^{-7} and 10^{-6} mbar.

The build chamber is assembled by build tank, powder hoppers, and rake system. The melting process occurs on the build platform which is located inside the build tank. Build platform is capable of moving parallel to the vertical axis to create an available space for a new powder layer depending on layer thickness once a layer melt is completed. The powder layer thickness for the EBM process is usually between 50 – 200 μm [13]. The function of the powder hoppers is to store metal powder as a feedstock material that is used to manufacture the metal part. The rake system undertakes powder dispensing with a certain layer thickness onto the build platform or already deposited layers for the melting process of the next layer. Prior to the melting process, the build chamber is pressurized with low-level helium around 10^{-3} mbar in order to prevent electrostatic charging, also known as smoke effect [39]. In addition to that, helium provides less interference with electron beam due to having a smaller atom size.

The manufacturing process of EBM follows the similar steps described in Section 2.2.2. Layer processing steps during the EBM manufacturing are shown in Figure 2.13. Building initiates after 3D CAD model introduced to EBM system in appropriate file format. Thereafter, metal powder is dispensed on the base plate with pre-determined layer thickness via stainless steel rake system. Following that, preheating of the powder layer is conducted with the low current electron beam and relatively high scan speed, electron beam scans the build area several times to heat up the base plate. Preheating is an essential process for two reasons: minimizing the thermal gradient between the melted layers and sintering the powders to increase electrical conductivity and process stability for avoiding smoke effect. The smoke effect can be described as the situation that causes uncontrolled dispersion of charged fine grade powders due to repulsive electrostatic forces [39, 40]. After completion of preheating, the layer melting process starts to melt and fuse the sliced layer of the 3D part. This process relies on melting the powders by using the heat energy generated from kinetic collisions of high-speed electrons and dispensed powders.

Electrons can transfer their energy to dispensed powders at around 70% of the speed of the light during the kinetic collisions. This results in raising the negative charge of the powders [20]. Firstly, the electron beam scans the inner and outer boundaries of the part geometry which is known as “contour”. Secondly, the electron beam continues in-filling to melt the powder area within the contours. During this operation, the electron beam follows the specific line patterns which are known as “hatch”. The distance between the adjacent hatches is called as “line offset”. Line offset is also referred as “overlap”. A respective image for the scanning pattern during the EBM process is shown in Figure 2.14. Contour, hatch, and line offset parameters are directly effective on the part quality and its resultant properties. Therefore, these parameters should be determined properly in order to prevent internal defects [41]. When the electron beam completed the melting process of the entire layer, the base plate is lowered by the powder layer thickness to make room for the next layer. Then, the powder dispensing, preheating, and melting process is conducted repetitively until all sliced layers are completely fused and designed part geometry is created.

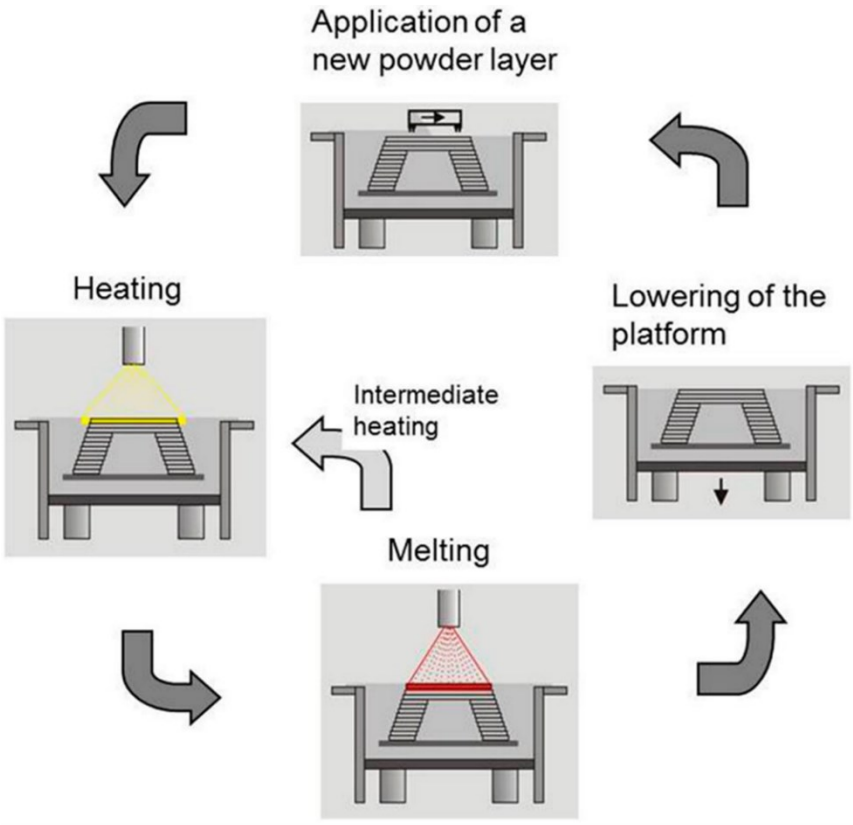

Figure 2.13. Layer processing schematic of EBM machine.

(Source: Körner, 2016 [39])

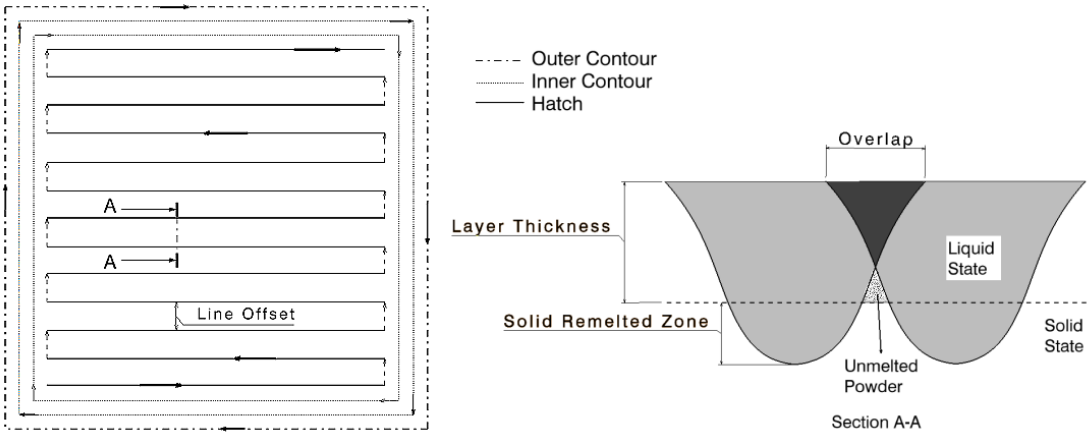

Figure 2.14. Scanning pattern of electron beam during layer manufacturing.
(Source: Yiğitbaşı, 2018 [41])

After completion of the melting process, the build platform is left for cooling down to room temperature. The cooling rate can be expedited by pumping helium into the build chamber. Thereafter, the build tank is disassembled from the machine to be taken into Powder Recovery System (PRS), sandblasting for removing sintered powders surrounding the part as the manufactured part is found embedded inside the sintered powder bed. The recovered powders after sandblasting can be recycled and reused in the next manufacturing attempts.

The main processes in which the electron beam actively operates are preheating and melting. However, wafer and net processes are individually employed if the support geometry processing is needed and porous structured geometries such as lattices are intended to manufacture, respectively. Additionally, process settings of preheating, melting, wafer, and net are determined by the build theme which controls the beam function accounting beam current, speed function, focus offset, and line offset parameters.

EBM is an advantageous AM method in several aspects. Usage of electron beam benefits more energy-efficient process because electrons can penetrate far into powders and homogenously melt the dispensed powders comparing laser-based PBF methods. Representative illustrations of energy transfer and penetrability of EBM and laser are given in Figure 2.15. The high absorption efficiency of EBM ensures low power consumption and helps to reduce production costs. Another cost-reducing feature is that EBM processes powder with bigger particles which can be procured up to 50% lower

price [39]. Powder bed heating results in less energy requirement and a shorter time for reaching melting temperature compared to SLM. Also, this condition increases productivity. As being a hot process, EBM allows the manufacturing of brittle and crack-prone alloys such as TiAl [39]. Most importantly, EBM has the ability of manufacturing almost no post-process and tooling required residual stress-relieved parts with correct microstructure, and proximate mechanical properties to wrought counterparts. However, there are several negative features existing for EBM. Its higher expense compared to conventional methods, the surface quality of the final product, internal porosity are the crucial issues to likely be encountered in the usage of EBM technology.

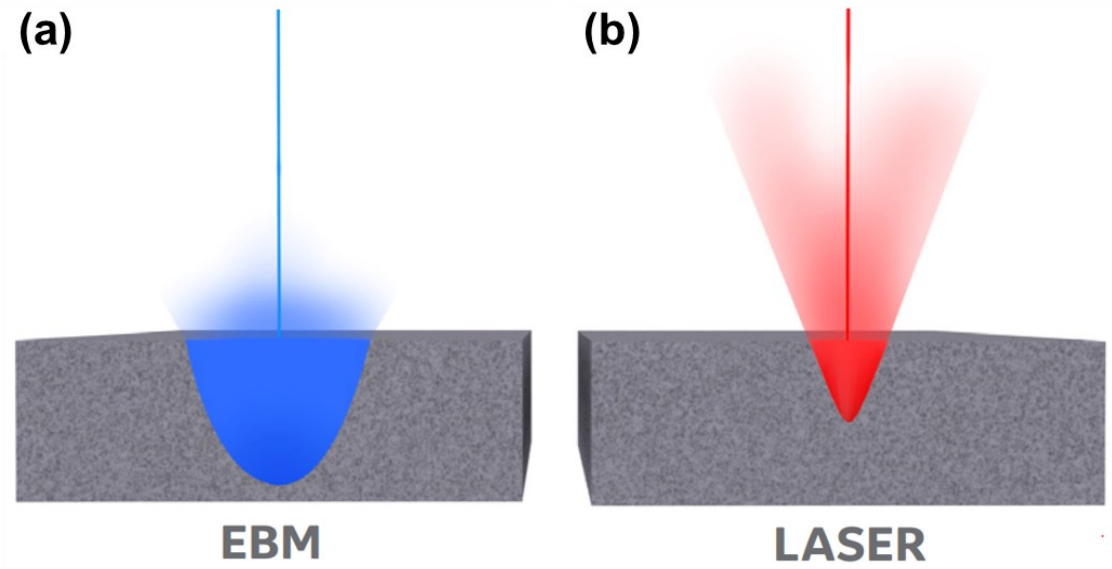

Figure 2.15. Energy transfer and penetrability of (a) EBM technology, and (b) laser technology. (Source: Arcam EBM Brochure [38])

CHAPTER 3

CONSTITUTIVE MODELS FOR METAL AND ALLOYS

3.1. Constitutive Models and Their Applications

Under the various loading types and different temperatures, the deformation behavior of metals and alloys exhibits alterations depending on the effects of strain, strain rate, and temperature on the mechanical response of the materials. Hence, constitutive equations for constitutive models have been developed or modified to predict the crucial material properties in the case of subjecting to static and dynamic loadings. Constitutive equations are the mathematical formulations that define stress (σ) as a function of strain (ε), strain rate ($\dot{\varepsilon}$), and temperature (T). The generalized form may be written as

$$\sigma = f(\varepsilon, \dot{\varepsilon}, T) \tag{3.1}$$

The deformation of metallic metals is known to be complex since both hardening and softening processes involve at the microstructural level at the same time. Due to this complexity, the use of constitutive equations together with computer codes provides a suitable computation method for deformation processes [42]. Finite Element (FE) technique is the most frequently used method of computation with a help of a constitutive equation [43, 44]. Therefore, the determination of an appropriate constitutive equation in FE simulations is considered very important for constructing a comprehensive and precise material model [42, 45, 46]. A determined constitutive equation should be capable of simulating the deformation at wide ranges of strain rates and temperatures using relatively fewer constants in order to shorten the calibration of equation [47, 48, 49]. Some widely used constitutive equations developed for modeling metallic materials are tabulated in Table 3.1. The constants or material model parameters of each equation are also shown in the same table.

Table 3.1. Constitutive equations developed for metallic materials and the constants.

Name	Equation	Parameters
Holloman [50]	$\sigma_f = K\varepsilon^n$	K, n: Material parameters
Ludwik [51]	$\sigma_f = \sigma_0 + K\varepsilon^n$	σ_0, K, n: Material parameters
Johnson-Cook (JC) Strength Model [52]	$\sigma_f = \left(A + B\varepsilon_{pl}^n\right)\left[1 + C\mathrm{In}\left(\frac{\dot{\varepsilon}}{\dot{\varepsilon}_0}\right)\right]\left[1 - \left(\frac{T - T_r}{T_m - T_r}\right)^m\right]$	A, B, C, n, m: Material parameters, $\dot{\varepsilon}$: Strain rate, $\dot{\varepsilon}_0$: Reference strain rate, T: Absolute temperature, T_r : Reference temperature, T_m: Melting temperature
Johnson-Cook (JC) Damage Model [53]	$\varepsilon_f = [D_1 + D_2 exp(D_3\sigma^*)]\left[1 + D_4 In\left(\frac{\dot{\varepsilon}}{\dot{\varepsilon}_0}\right)\right]\left[1 + D_5\left(\frac{T - T_r}{T_m - T_r}\right)\right]$	D_1, D_2, D_3, D_4, D_5 : material damage constants σ^*: Stress triaxiality, $\dot{\varepsilon}$: Strain rate, $\dot{\varepsilon}_0$: Reference strain rate, T: Absolute temperature, T_r : Reference temperature, T_m: Melting temperature
Modified Johnson Cook (MJC) [54]	$\sigma_f = (A_1 + B_1\varepsilon + B_2\varepsilon^2)\left[1 + C_1\mathrm{In}\left(\frac{\dot{\varepsilon}}{\dot{\varepsilon}_0}\right)\right] exp\left[\left(\lambda_1 + \lambda_2\mathrm{In}\left(\frac{\dot{\varepsilon}}{\dot{\varepsilon}_0}\right)\right)(T - T_r)\right]$	A, B, C, λ_1, λ_2, m: Material parameters, $\dot{\varepsilon}$: Strain rate, $\dot{\varepsilon}_0$: Reference strain rate, T: Absolute temperature, T_r : Reference temperature
Zerilli-Armstrong (ZA) [55]	$\sigma = C_0 + C_1\exp\left(-C_3T + C_4TIn\left(\frac{\dot{\varepsilon}}{\dot{\varepsilon}_0}\right)\right) + C_5\varepsilon^n \quad (for\ BCC)$ $\sigma = C_0 + C_2\varepsilon^{\frac{1}{2}}\exp\left(-C_3T + C_4TIn\left(\frac{\dot{\varepsilon}}{\dot{\varepsilon}_0}\right)\right) \quad (for\ FCC)$	$C_0, C_1, C_2, C_3, C_4, C_5, n$: material constants $\dot{\varepsilon}$: Strain rate, $\dot{\varepsilon}_0$: Reference strain rate, T: Absolute temperature
Modified Zerilli-Armstrong (MZA) [56]	$\sigma = (C_1 + C_2\varepsilon^n)\exp\left[(-(C_3 + C_4\varepsilon)(T - T_r) + (C_5 + C_6(T - T_r)\mathrm{In}\left(\frac{\dot{\varepsilon}}{\dot{\varepsilon}_0}\right)\right]$	$C_1, C_2, C_3, C_4, C_5, C_6, n$: material constants $\dot{\varepsilon}$: Strain rate, $\dot{\varepsilon}_0$: Reference strain rate, T: Absolute temperature, T_r: Reference temperature
Combined Johnson-Cook and Zerilli-Armstrong (JC-ZA) [57]	$\sigma = \left(A + B\varepsilon_p^n\right)exp\left[-C_3T + C_4TIn\left(\frac{\dot{\varepsilon}}{\dot{\varepsilon}_0}\right)\right]$	A, B, n, n_0, C_3, C_4: Material constants, $\dot{\varepsilon}$: Strain rate, $\dot{\varepsilon}_0$: Reference strain rate, T: Absolute temperature,
Khan-Huang-Liang (KHL) [58]	$\sigma = \left[A + B\left(1 - \frac{In\dot{\varepsilon}}{InD_0}\right)^{n_1}\varepsilon^{n_0}\right]\left(\frac{\dot{\varepsilon}}{\dot{\varepsilon}_0}\right)^C\left(\frac{T_m - T}{T_m - T_r}\right)^m$	A, B, n_1, n_0, C, m : Material constants D_0= non-dimensionalize strain term (10^6 s^{-1}) $\dot{\varepsilon}$: Strain rate, $\dot{\varepsilon}_0$: Reference strain rate, T: Absolute temperature, T_r : Reference temperature, T_m: Melting temperature
Modified Khan-Huang-Liang (KHLM) [59]	$\sigma = \left[A + B\left(1 - \frac{In\dot{\varepsilon}}{InD_0}\right)^{n_1}\left(\frac{T_0 - \frac{T}{2}}{T_0}\right)^{n_2}\varepsilon^{n_0}\right]\left(\frac{\dot{\varepsilon}}{\dot{\varepsilon}_0}\right)^C\left(\frac{T_m - T}{T_m - T_r}\right)^m$	A, B, n_1, n_2, n_0, C, m : Material constants D_0 = non-dimensionalize strain term (10^6 s^{-1}) $450 < T_0 < 700\ °C$ $\dot{\varepsilon}$: Strain rate, T_m: Melting temperature, $\dot{\varepsilon}_0$: Reference strain rate T_r: Reference temperature T: Ambient temperature

(cont. on next page)

Table 3.1. (cont.)

Name	Equation	Parameters
Khan-Liang-Farrokh (KLF) [60]	$\sigma = \left[\left(a + \frac{k}{d^{n^*}}\right) + B\left(\frac{d}{d_0}\right)^{n_2}\left(\left(1 - \frac{In(\dot{\varepsilon}^p)}{In(D_0^p)}\right)\left(\frac{T_m}{T}\right)\right)^{n_1}(\varepsilon^p)^{n_0}\right] \times \left(\frac{\dot{\varepsilon}^p}{\dot{\varepsilon}^{p*}}\right)^c \left(\frac{T_m - T}{T_m - T_r}\right)^m$	$a,\ k,\ B,\ n_2,\ n_1,\ n_0,\ c,\ m$: Material parameters $\dot{\varepsilon}^p$: Strain rate, $\dot{\varepsilon}^{p*}$: reference strain rate, T: Absolute temperature, T_r : Reference temperature, T_m: Melting temperature, d, d_0: Average grain sizes, D_0^p: upper bound strain rate (1 s^{-1}) n^*: Hall-Petch relationship (0.5)
Arrhenius Model (ARR) [61]	$\dot{\varepsilon} = AF(\sigma)exp\left(-\frac{Q}{RT}\right) \qquad Z = \dot{\varepsilon}exp\left(\frac{Q}{RT}\right)$ $F(\sigma) = \begin{cases} \sigma^n & \alpha\sigma < 0.8 \\ exp(\beta\sigma) & \alpha\sigma > 1.2 \\ [\sinh(\alpha\sigma)]^n & for\ all\ \sigma \end{cases}$	A, α, n: material constants $\alpha = \frac{\beta}{n}$ $\dot{\varepsilon}$: strain rate, R: universal gas constant (8.31 $Jmol^{-1}K^{-1}$) Q: activation energy ($kJmol^{-1}$)
Fields-Backhofen (FB) [62]	$\sigma = K\varepsilon^n\dot{\varepsilon}^m$	K, n, m : material constants
Molinari-Ravichadran (MR) [63]	$\sigma = \hat{\sigma}(d)\left(\frac{\delta}{\delta_0}\right)\left(\frac{\dot{\varepsilon}}{\dot{\varepsilon}_0}\right)^{\frac{1}{m}}$	m: material constant d: grain size, $\dot{\varepsilon}$: strain rate, $\dot{\varepsilon}_0$: reference strain rate, δ: internal characteristic length
Voce [64]	$\sigma = \sigma_s + \left[(\sigma_0 - \sigma_s)exp\left(-\frac{\varepsilon}{\varepsilon_r}\right)\right]$	σ_s: saturation stress, σ_0: yield stress, ε_r: relaxation strain
Voce-Kocks (VK) [65]	$\sigma = \sigma_{s0}\left(\frac{\dot{\varepsilon}}{\dot{\varepsilon}_{s0}}\right)^{\left(\frac{kT}{\mu b^3}\right)} + \left[\left(\sigma_{k0}\left(\frac{\dot{\varepsilon}}{\dot{\varepsilon}_{k0}}\right)^{\left(\frac{kT}{\mu b^3 A^T}\right)} - \sigma_{s0}\left(\frac{\dot{\varepsilon}}{\dot{\varepsilon}_{s0}}\right)^{\left(\frac{kT}{\mu b^3}\right)}\right)\exp\left(-\frac{\varepsilon}{C_1 \times \left(\frac{\dot{\varepsilon}_0}{\dot{\varepsilon}}\right)^{C_2}}\right)\right]$	$\sigma_{s0}, \sigma_{k0},\ C_1, C_2, A$: material constants $\dot{\varepsilon}$: strain rate, μ: temp. dependent shear modulus b: The Burgers vector k: Boltzman constant
Mechanical Threshold Stress (MTS) [66]	$\sigma_f = \sigma_a + (S_i\sigma_i + S_e\sigma_e)\left\{1 - \left[\left(\frac{T}{T_m}\right) \times exp\left[\theta^*\left(1 - \frac{T}{T_m}\right)\right]\right]\right\}$ $S_i = \left[1 - \left(\frac{kT}{E(T)b^3 g_{0i}}\right) In\left(\frac{\dot{\varepsilon}_{0i}}{\epsilon}\right)^{\frac{1}{qi}}\right]^{\frac{1}{pi}}$ $S_e = \left[1 - \left(\frac{k_b T}{E(T)b^3 g_{0e}}\right) In\left(\frac{\dot{\varepsilon}_{0e}}{\epsilon}\right)^{\frac{1}{qe}}\right]^{\frac{1}{pe}}$	$p_i,\ q_i,\ p_e,\ p_e$: material parameters θ^*: homologous temperature, E: elastic modulus, E_0: elastic modulus at 0 K, σ_a: athermal component of stress, σ_i: intrinsic component of the flow stress, σ_e: strain hardening component of the flow stress, S_i: temperature-dependent scaling factor, S_e: strain rate dependent scaling factor, T: Absolute temperature, T_m: Melting temperature, $\dot{\varepsilon}_{0i}, \dot{\varepsilon}_{0i}$: reference strain rates $g_{0i},\ g_{0e}$: normalized activation energies, k_b: Boltzmann constant, b: The Burgers vector

Constitutive equations are broadly classified into three groups; phenomenological, physical-based, and artificial neural network (ANN) [67]. Phenomenological equations are derived from the calculation of flow stress using merely empirical relations and depending on that, the material constants are determined corresponding to the individual stages that the material undergoes during plastic deformation [68]. Curve-fitting techniques are applied to the experimental tension or compression stress-strain curves in order to determine the constants of the constitutive equation. Phenomenological equations are preferred in FE simulations since they require fewer constants to be determined and are simple, and available in most FE code libraries.

Physical-based equations are established using the specific physical relations of microstructural aspects [68]. Plastic deformation is affected by the physical state of materials such as work hardening, dislocation density, dynamic recovery, dynamic recrystallization, grain size, and phase transformation. The introduction of these individual parameters in the formulation increases the consistency of the formulation with experimental results. On the other side, physical-based equations require a relatively intense testing procedure. For that reason, these equations are not seen as an applicable tool in the prediction of flow behavior.

Artificial neural network (ANN) models differ from the constitutive equations discussed above in that they do not integrate the deformation mechanism into prediction. The sense behind them is to compute the flow stress using artificial intelligence, statistics, machine learning, and parallel processing. A representative model for ANN is shown in Figure 3.1. The general construction of ANN consists of neurons under three processing layers named as input layer, hidden layer, and output layer, respectively. Neurons have the ability of adaptive learning and demonstrate complex and nonlinear relations after introducing adequate experimental data. Computations start with the entry of primary data into input layer neurons, then progress through the hidden layer to the output layer using outputs from each neuron. Finally, the data are generated by the output layer. In recent years, the ANN model has gained an increasing interest on the account of its suitability to any complex conditions which cannot be computed by phenomenological and physical-based equations [69, 70, 71, 72].

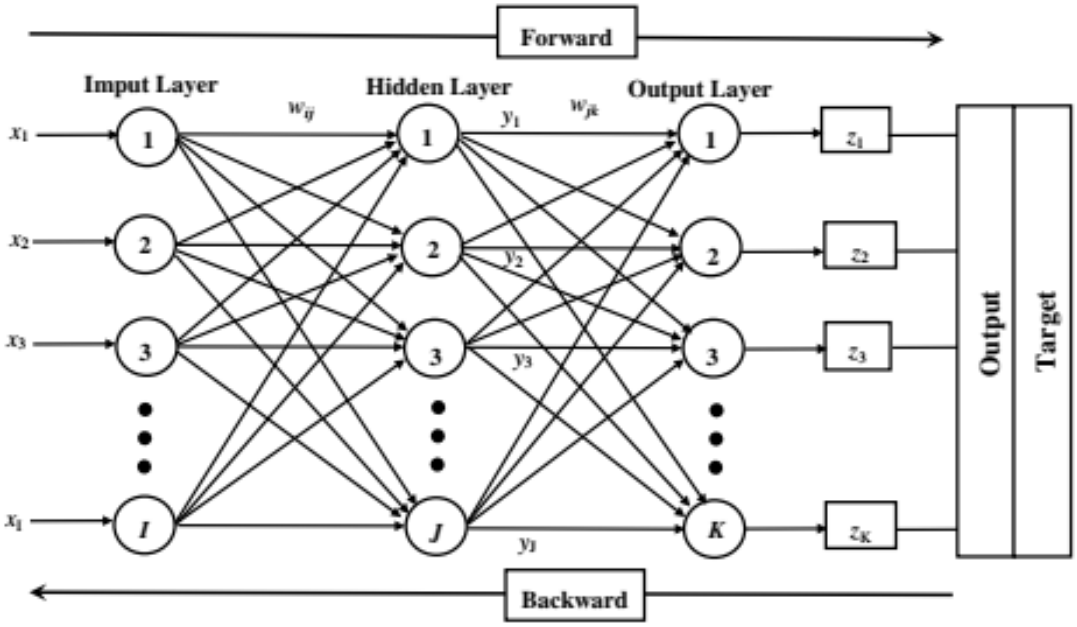

Figure 3.1. Illustration of the structure of ANN model.
(Source: Lin et al., 2008 [71])

Johnson-Cook (JC) and Zerilli-Armstrong (ZA) models are the most widely used constitutive equations owing to their availability in most commercial FEA software. Particularly, the incorporation of the state of stress on plasticity and failure in the deformation process of the ductile materials makes the JC models (strength and failure model) very suitable for FE simulations [46, 73]. However, the coefficients of the JC models show sensitivity to any changes in the microstructure [46]. Furthermore, the thermal softening and small strain rate dependence of material at high strain rates lead to incompatibility between the JC strength model and experimentally characterized material behavior [74]. In order to increase the fidelity of the JC strength model, some researchers proposed modified versions by introducing new variables and/or developed relations in the already-defined relations [75, 76, 77]. These modifications are the inclusions of the coupling effects of strain-hardening, strain rate-hardening, and thermal softening to provide more precise predictions under a wide range of temperature and strain rates [67]. The modified versions of the JC models were reported to show well agreement with the experiments and being able to reproduce the material behavior for a variety of deformations such as hot working, forming, machining, ballistic impact, and like [43, 78, 79, 80, 81].

ZA model is the most preferred constitutive equation among the physical-based equations. The construction of the ZA model relies on the combination of strain hardening, strain rate, and temperature effects with the dislocation mechanics [67]. However, the ZA model cannot be applied to high-temperature deformation of metals, since an approximation in its formulation and the strain rate effect on thermal activation area that affects the dislocation motion in FCC metals has not been considered [49]. Therefore, as similar to JC models, several studies proposed alternative versions of the ZA equation by introducing more variables to enhance the applicability of the model and enabling the inclusion of the absolute effect of strain rate and the coupled effect of strain with temperature. Moreover, there are several well-matched results with absolute deformation behavior reported in the literature for the use of original and modified ZA models, but those studies were generally driven by investigational purposes [49, 82, 83] .

Besides JC and ZA models, Mechanical Threshold Stress (MTS) model and Arrhenius (ARR) equation (incorporated with the sine hyperbolic law) have gained popularity in many engineering applications [47, 84]. MTS model is a physical-based constitutive model which involves both the thermal and athermal stress components in relation to the dislocation density, grain size, distribution of the solute atoms, and other long-range barriers that hinder the dislocation motion [66, 85]. The main disadvantage of the MTS model is its complex form which causes deficiency in defining the effect of strain [49]. Specifically, in the prediction of high-temperature flow behavior, the ARR equation exhibits a better correlation with the material behavior including the strain, strain rate, and temperature relations [42, 86]. In this thesis, the JC strength and failure models of the EBM-produced Ti64 alloy were determined.

3.2. Johnson-Cook Constitutive Models

The JC models consist of two empirical equations that are constructed to numerically predict the equivalent flow stress and the fracture strain, respectively. In the following subsections, these equations and the determination of the respective material constants will be explained in detail.

3.2.1. Johnson-Cook Strength Model

The Johnson-Cook strength model was first proposed in 1983 to establish an analytical approach for predicting the von Mises equivalent flow stress (σ_{eq}) as a function of plastic strain, strain rate, and temperature [52]. The von Mises equivalent stress (σ_{eq}) and equivalent plastic strain (ε_{pl}) sequentially are

$$\sigma_{eq} = \sqrt{\frac{3}{2}\sigma_{ij}\sigma_{ij}} \tag{3.2}$$

$$\varepsilon_{pl} = \varepsilon_t - \frac{\sigma_y}{E} \tag{3.3}$$

where, σ_{ij} is the deviatoric stress tensor, ε_t is the total strain, σ_y is the yield stress, and E is the elastic modulus. The flow rule counts for the normality rule suitable for the von Mises stress function [87]. The JC strength model is given as

$$\sigma_f = \left(A + B\varepsilon_{pl}^{n}\right)\left[1 + CIn\left(\frac{\dot{\varepsilon}}{\dot{\varepsilon}_0}\right)\right]\left[1 - \left(\frac{T - T_r}{T_m - T_r}\right)^{m}\right] \tag{3.4}$$

where, A, B, n, C, and m are the yield stress, hardening modulus, strain hardening coefficient, strain rate constant, and thermal softening constant, respectively. In Equation 3.4, $\dot{\varepsilon}$ is the strain rate, $\dot{\varepsilon}_0$ is the reference strain rate, T is the temperature, T_m is the melting temperature of the material, and T_r is the reference or room temperature. The first bracket of the equation stands for isothermal stress in the plastic region as a function of strain including the hardening rule. The second and third brackets of the equation enable the inclusion of the strain rate and temperature effects on the material flow stress, respectively. High strain rate deformation results in an adiabatic temperature rise in metallic materials due to the conversion of deformation energy into heat. Nearly 90% of plastic work is converted into heat in metallic materials [48, 88]. The following relation given in Equation 3.5 is used to calculate the temperature rise due to adiabatic heating.

$$\Delta T = \frac{\beta}{\rho C_p} \int_0^{\varepsilon_{pl}} \sigma_{eq} d\varepsilon_{pl} \tag{3.5}$$

where ΔT is the temperature rise due to adiabatic heating, β is the Taylor-Quinney coefficient representing the proportion of plastic work transformed into heat, ρ is the material density, and C_p is the specific heat.

3.2.1.1. Determination of A, B, and n Parameters

The first three parameters of the JC strength equation, A, B, and n, are determined from the true stress-true plastic strain curves obtained from the uniaxial tension or compression tests conducted at the reference strain rate ($\dot{\varepsilon}_0$) and reference temperature (T_r). At the reference strain rate and temperature, Equation 3.4. is

$$\sigma_f = \left(A + B\varepsilon_{pl}^n\right) \tag{3.6}$$

Rearranging Equation 3.6 gives the following relation

$$\left(\sigma_f - A\right) = B\varepsilon_{pl}^n \tag{3.7}$$

Taking the logarithm of both sides of Equation 3.6 results in

$$\ln\left(\sigma_f - A\right) = \ln B + n \ln \varepsilon_{pl} \tag{3.8}$$

Hence, the slope of a linear fit to $\ln\left(\sigma_f - A\right)$-$\ln \varepsilon_{pl}$ curve, as seen in Figure 3.2(a), gives the value of n, while the intercept of the fit gives the value of B. Since A represents the yield stress, it is directly determined from the true stress-true strain curve. The determination of A, B, and n can also be handled by applying a direct curve-fitting of

Equation 3.6 with the true stress-true plastic strain curve, as seen in Figure 3.2(b). Note that determining A parameter before the fitting process increases the accuracy of the fitting.

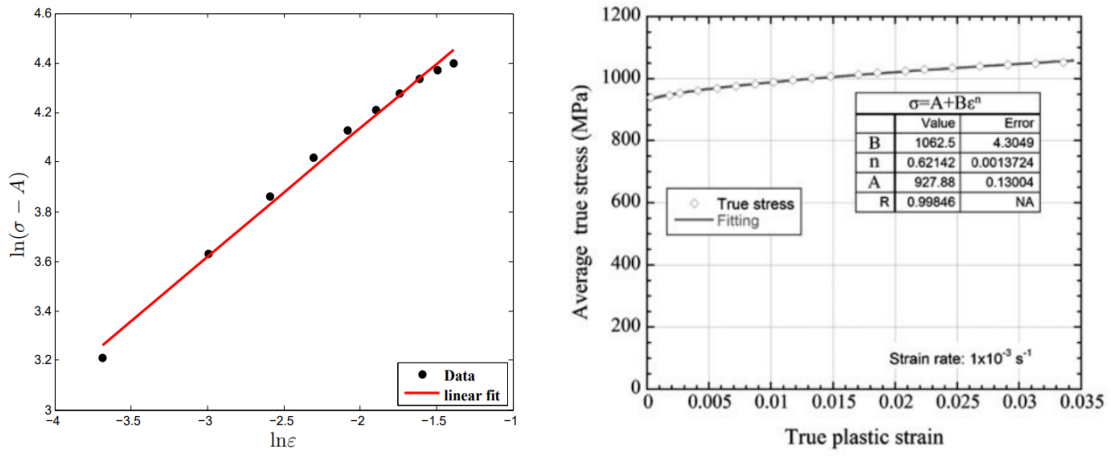

(a) **(b)**

Figure 3.2. Examples of curve-fitting to calculate the first bracket parameters (a) linear regression analysis, (b) direct curve-fitting. (Sources: Murugesan et al., 2019 [89] and Çakırcalı et al., 2013 [90])

3.2.1.2. Determination of *C* Parameter

In order to determine the strain rate hardening parameter, C, the uniaxial tension or compression tests are required at the quasi-static and high strain rates and the reference temperature (T_r). Then, Equation 3.4 reduces to the following form

$$\sigma_f = \left(A + B\varepsilon_{pl}^n\right)\left[1 + CIn\left(\frac{\dot{\varepsilon}}{\dot{\varepsilon}_0}\right)\right] \tag{3.9}$$

After rearranging, Equation 3.9 becomes

$$\left[\frac{\sigma_f}{\left(A + B\varepsilon_{pl}^n\right)}\right] - 1 = CIn\left(\frac{\dot{\varepsilon}}{\dot{\varepsilon}_0}\right) \tag{3.10}$$

Hence, the slope of $\left[\frac{\sigma_f}{\left(A+B\varepsilon_{pl}^{n}\right)}\right]$ vs. $In\left(\frac{\dot{\varepsilon}}{\dot{\varepsilon}_0}\right)$ curve at a specific ε_{pl} gives the value of C, as seen in Figure 3.3. In order to obtain a valid value of C, the specific plastic strain should be carefully selected. At low strains, the oscillations in the stress values in dynamic tests hinder the determination of flow stress accurately, while the adiabatic heating at high strains causes significant reductions in flow stresses. The selected strain should be large enough to skip stress oscillations and small enough to avoid excessive heating of the test sample.

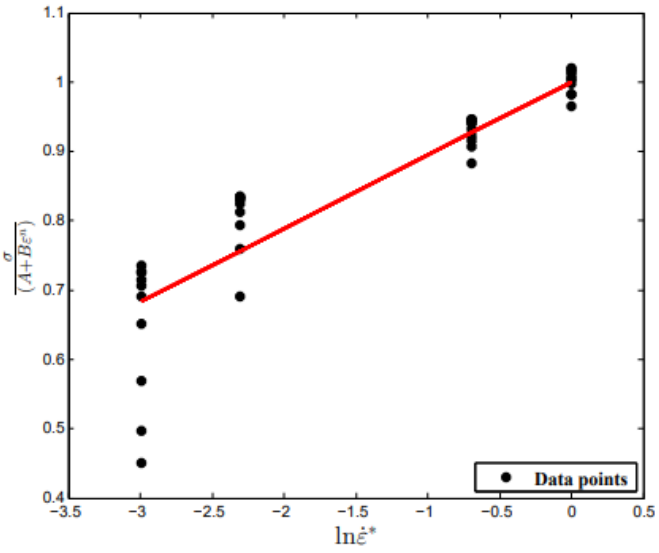

Figure 3.3. An example to the determination of C parameter.
(Source: Murugesan et al., 2019 [89])

3.2.1.3. Determination of m Parameter

The last parameter of the JC strength model, known as temperature softening constant, m, is calculated from the true stress-true strain curves obtained from uniaxial tension or compression tests performed at elevated temperatures and the reference strain rate. In this case, Equation 3.4 becomes

$$\sigma_f = \left(A + B\varepsilon_{pl}^{n}\right)\left[1 - \left(\frac{T - T_r}{T_m - T_r}\right)^{m}\right] \tag{3.11}$$

The temperature term in Equation 3.11 can also be written in a short form as $(1 - T^{*m})$. Equation 3.11 is then rearranged as

$$1 - \frac{\sigma_f}{\left(A + B\varepsilon_{pl}^{n}\right)} = T^{*m} \tag{3.12}$$

And taking the natural logarithm of both sides of Equation 3.12 gives the following relation

$$\ln\left[1 - \frac{\sigma_f}{\left(A + B\varepsilon_{pl}^{n}\right)}\right] = m \ln T^{*} \tag{3.13}$$

Hence, the slope of $\ln\left[1 - \frac{\sigma_f}{\left(A+B\varepsilon_{pl}^{n}\right)}\right]$ vs. $\ln T^{*}$ curve at a specific ε_{pl} gives the value of m, as seen in Figure 3.4.

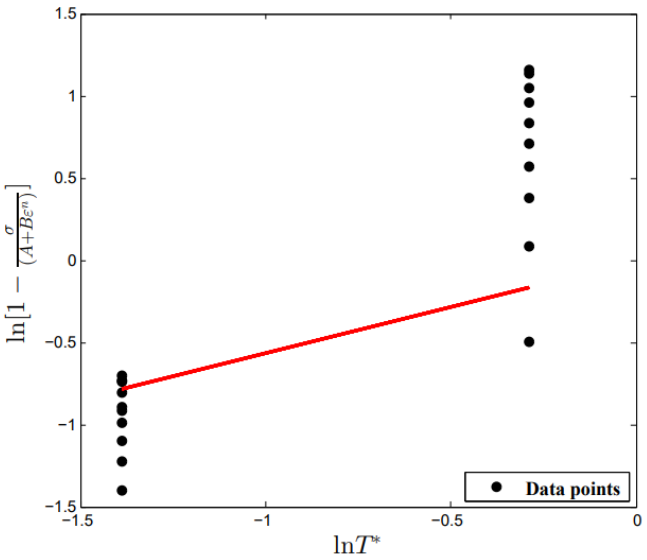

Figure 3.4. An example to the determination of m parameter.

(Source: Murugesan et al., 2019 [89])

3.2.2. Johnson-Cook Failure Model

The second constitutive equation proposed by Johnson and Cook is the determination of fracture strain as a function of the triaxial stress state, strain rate, and temperature. Figure 3.5 presents the evolution of damage with strain in a mechanical test. The failure of a material initiates after a certain number of dislocations generated and microcracks propagation at point B (Figure 3.5). Once the damage is initiated, flow stress starts decreasing.

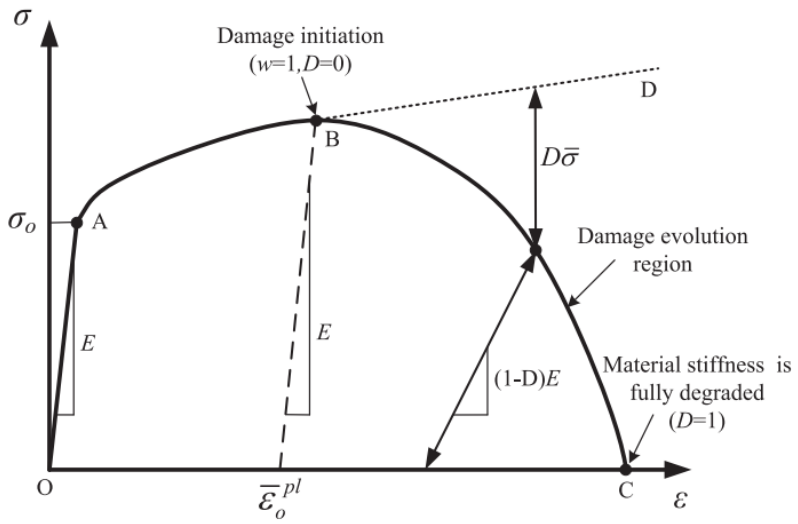

Figure 3.5. Strain to failure history curve of most metallic materials.
(Source: Wang et al., 2015 [91]).

The failure criterion or damage parameter (D) is defined as

$$D = \sum \frac{\Delta\varepsilon_{pl}}{\varepsilon_f} \tag{3.14}$$

where, $\Delta\varepsilon_{pl}$ is the incremental change in the equivalent plastic strain during the deformation and ε_f is the corresponding strain at failure. The value of the damage parameter varies between 0 and 1, and the material fails when $D \geq 1$. However, a

threshold plastic strain might exist in the damage evolution [87]. In this case, the equivalent stress and failure evolution can be proposed through Equations 3.15 and 3.16 as

$$D = \begin{cases} 0, & when\ \varepsilon_{pl} < \varepsilon_d \\ \dfrac{D_c}{\varepsilon_f - \varepsilon_d}\varepsilon_{pl}, & when\ \varepsilon_{pl} \geq \varepsilon_d \end{cases} \tag{3.15}$$

$$\sigma_d = (1 - D)\sigma_{eq} \tag{3.16}$$

where, D_c is the critical damage parameter, ε_d is the damage threshold strain, and σ_d is the failure stress. The JC failure equation is given as

$$\varepsilon_f = [D_1 + D_2 exp(D_3\sigma^*)]\left[1 + D_4 In\left(\frac{\dot{\varepsilon}}{\dot{\varepsilon}_0}\right)\right]\left[1 + D_5\left(\frac{T - T_r}{T_m - T_r}\right)\right] \tag{3.17}$$

where, D_1, D_2 and D_3 are the triaxial stress state parameters, D_4 is the strain rate parameter, D_5 is the temperature parameter, and σ^* is the stress triaxiality

$$\sigma^* = \frac{\sigma_h}{\sigma_{eq}} \tag{3.18}$$

The von Mises equivalent stress is

$$\sigma_{eq} = \sqrt{\frac{1}{2}(\sigma_1 - \sigma_2)^2 + (\sigma_2 - \sigma_3)^2 + (\sigma_1 - \sigma_3)^2} \tag{3.19}$$

And σ_h is the hydrostatic stress and given as

$$\sigma_h = \frac{\sigma_1 + \sigma_2 + \sigma_3}{3} \tag{3.20}$$

where, σ_1, σ_2 and σ_3 are the principal stresses. Equation 3.5 remains valid until $\sigma^* \leq 1.5$. For $\sigma^* > 1.5$, different relationships are needed [53].

After the initiation of failure during the uniaxial tension test, the cross-sectional area of the specimen starts to decrease with the triaxial straining due to the transformation of the stress state from uniaxial to triaxial (Figure 3.6). In this case, the stress in the neck region differs from the equivalent uniaxial stress. The triaxial state of stress affects the failure strain [92]. Generally, tension test specimens with different radii notches are tested in order to determine the effect of stress triaxiality on the failure strain.

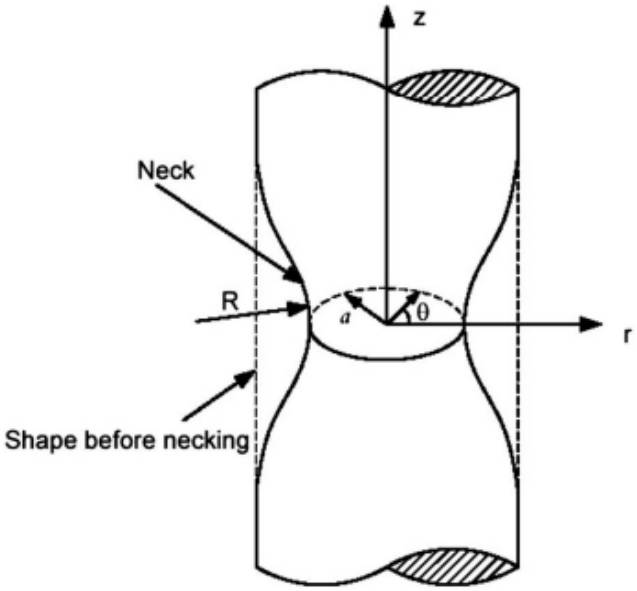

Figure 3.6. View of the necking region in a round tension specimen.
(Source: Bai et al., 2009 [92])

The stress triaxiality at the center of a neck region in a tension specimen can simply be estimated by Bridgman's relation [93]

$$\sigma^* = \frac{1}{3} + \ln\left(1 + \frac{a}{2R}\right) \tag{3.21}$$

where, a is the radius of the cross-sectional area of the neck, and R is the local radius of the neck in a round bar specimen as seen in Figure 3.7. The uniform equivalent strain at fracture in the cross-sectional area of the neck is calculated by using the following relations

$$\varepsilon_f = 2\ln\left(\frac{A_0}{A_f}\right) = \ln\left(\frac{d_0}{d_f}\right) \tag{3.22}$$

where, A_0 is the initial cross-sectional area of the notched specimen, A_f is the final area at the fracture, d_0 is the initial diameter of the notched specimen and d_f is the final diameter at the fracture (Figure 3.7). Equations 3.21 and 3.22 are frequently employed in the calibration of the JC damage equation.

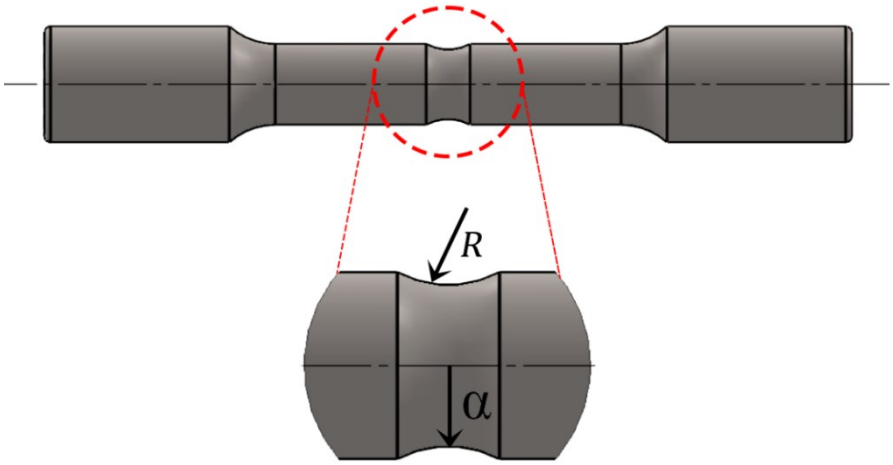

Figure 3.7. A notched tension specimen and the exploded view of the notch region.

3.2.2.1. Determination of D_1, D_2 and D_3 Parameters

The first bracket of the JC failure model in Equation 3.17 involves the triaxial stress state parameters, D_1, D_2 and D_3, which are sequentially the initial failure strain, exponential factor, and triaxiality factor. These parameters can be determined by testing unnotched and notched tension specimens at the reference strain rate and temperature. By doing these, Equation 3.17 is reduced to

$$\varepsilon_f = [D_1 + D_2 exp(D_3 \sigma^*)] \tag{3.23}$$

Fitting Equation 3.23 with the experimental failure strain vs. stress triaxiality curve gives the values of D_1, D_2 and D_3. For the precise fitting, at least 3 consistent test data should be used for each stress triaxiality selected. An example of curve fitting to determine D_1, D_2 and D_3 is shown in Figure 3.8.

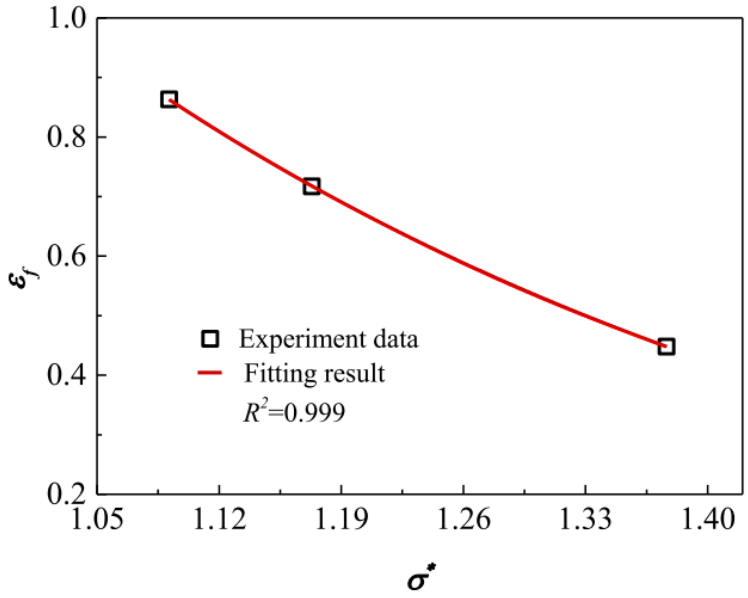

Figure 3.8. An example of curve fitting to determine D_1, D_2 and D_3.
(Source: Cao et al., 2020 [94])

3.2.2.2. Determination of D_4 Parameter

The strain rate parameter of the JC failure model, D_4, is determined from the failure strains of unnotched specimens tested at different strain rates and the reference temperature. At the reference temperature, Equation 3.17 is

$$\varepsilon_f = [D_1 + D_2 exp(D_3\sigma^*)]\left[1 + D_4 In\left(\frac{\dot{\varepsilon}}{\dot{\varepsilon}_0}\right)\right] \tag{3.24}$$

After rearranging, Equation 3.25 gives

$$\frac{\varepsilon_f}{[D_1 + D_2 exp(D_3 \sigma^*)]} - 1 = D_4 In\left(\frac{\dot{\varepsilon}}{\dot{\varepsilon}_0}\right) \tag{3.25}$$

Hence, D_4 parameter can be obtained by plotting the failure strain-logarithmic strain rate curve (normal strain rate axis can be drawn in case of all the considered strain rates within the quasi-static range) and by applying a linear curve fitting, as seen in Figure 3.9.

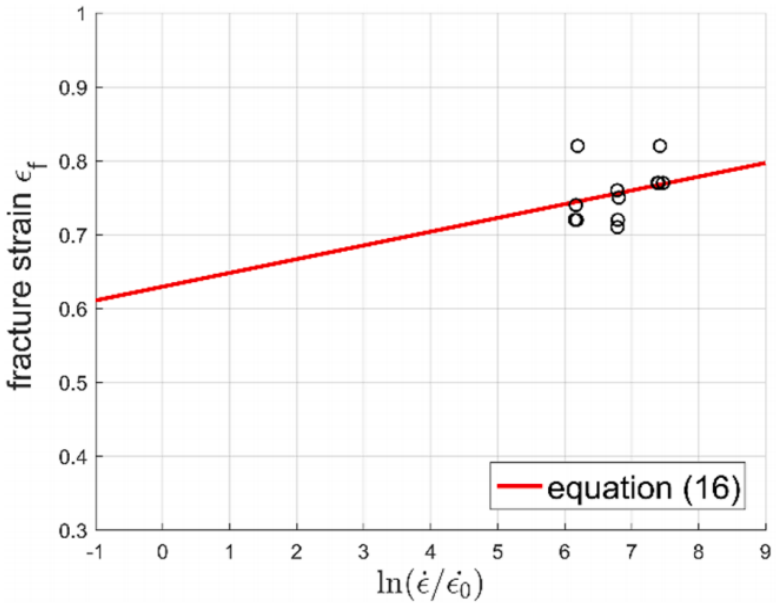

Figure 3.9. An example of linear curve-fitting to determine D_4.
(Source: Gerstgrasser et al., 2021 [95])

3.2.2.3. Determination of D_5 Parameter

The last parameter of the JC failure model, D_5, is found from the failure strains obtained from the tests on the unnotched specimens at different temperatures and the reference strain rate. At the reference strain rate, Equation 3.17 is

$$\varepsilon_f = [D_1 + D_2 exp(D_3 \sigma^*)]\left[1 + D_5\left(\frac{T - T_r}{T_m - T_r}\right)\right] \tag{3.26}$$

Rearranging Equation 3.26 gives the following form

$$\frac{\varepsilon_f}{[D_1 + D_2 exp(D_3 \sigma^*)]} - 1 = D_5 \left(\frac{T - T_r}{T_m - T_r}\right) \tag{3.27}$$

Hence, fitting the above equation with the experimental failure strain-temperature curve gives the value of D_5, as seen in Figure 3.10.

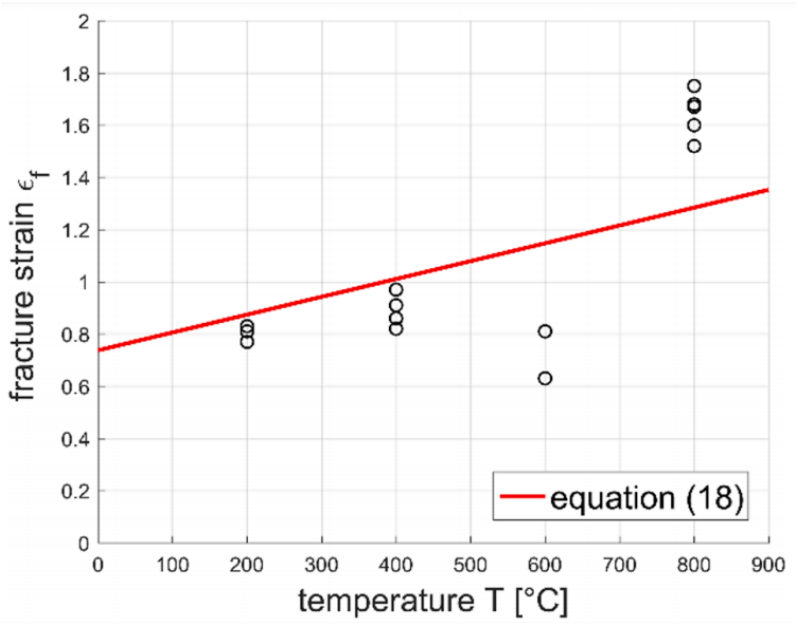

Figure 3.10. A representative curve of the linear curve-fitting process used in determining D_5 parameter. (Source: Gerstgrasser et al., 2021 [95])

CHAPTER 4

EXPERIMENTAL DETAILS

4.1. Materials

The test specimens were built in an Arcam Q20plus EBM system installed at TAI (Turkish Aerospace Industries). System was programmed by using EBM 5.2.24 built theme prior to the manufacturing process. A Ti64 ELI Grade 5 spherical powder, produced by Arcam AB, with a particle size range of 30-110 µm (Figure 4.1(a) and (b)), was used to fabricate Ti64 specimens. The chemical composition of the used powder published by supplier [96] is tabulated in Table 4.1.

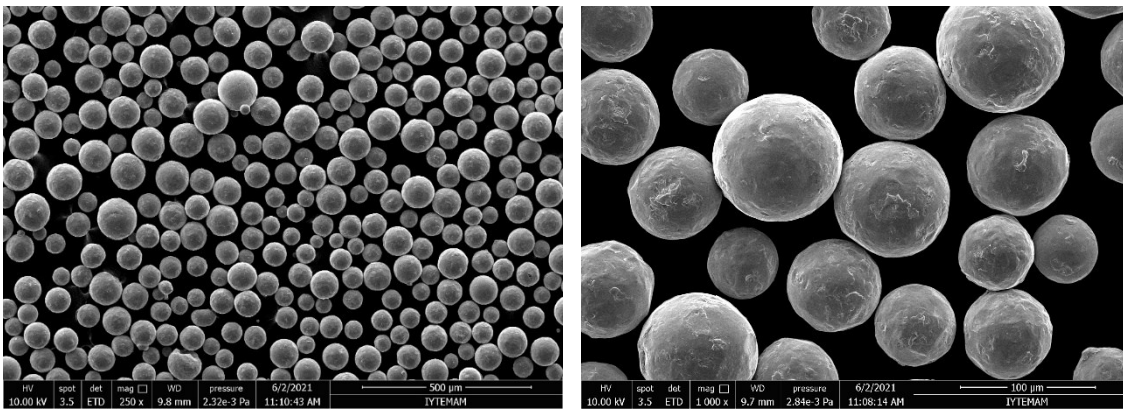

(a) **(b)**

Figure 4.1. Magnified view of Ti64 ELI powder (a) at 250x magnification and (b) at 1000x magnification.

Table 4.1. The chemical composition of Ti64 ELI Grade 5 powder.
(Source: Arcam Ti64 ELI Brochure [96])

Element	**Al**	**V**	**C**	**Fe**	**O**	**N**	**H**	**Ti**
Fraction	6%	4%	0.03%	0.10%	0.10%	0.01%	0.003%	Balance

All specimens were built in a vertical orientation without using any support and by applying the same process parameters. Three types of cylindrical specimens, sequentially having the dimensions of Ø12 mm x 75 mm, Ø10mm x 29.5 mm, and Ø15 mm x 5 mm, were fabricated in different batches. The pictures of the as-built specimens after EBM are shown in Figure 4.2(a-e) and the fabrication settings during preheating, melting, and net processing are tabulated in Table 4.2.

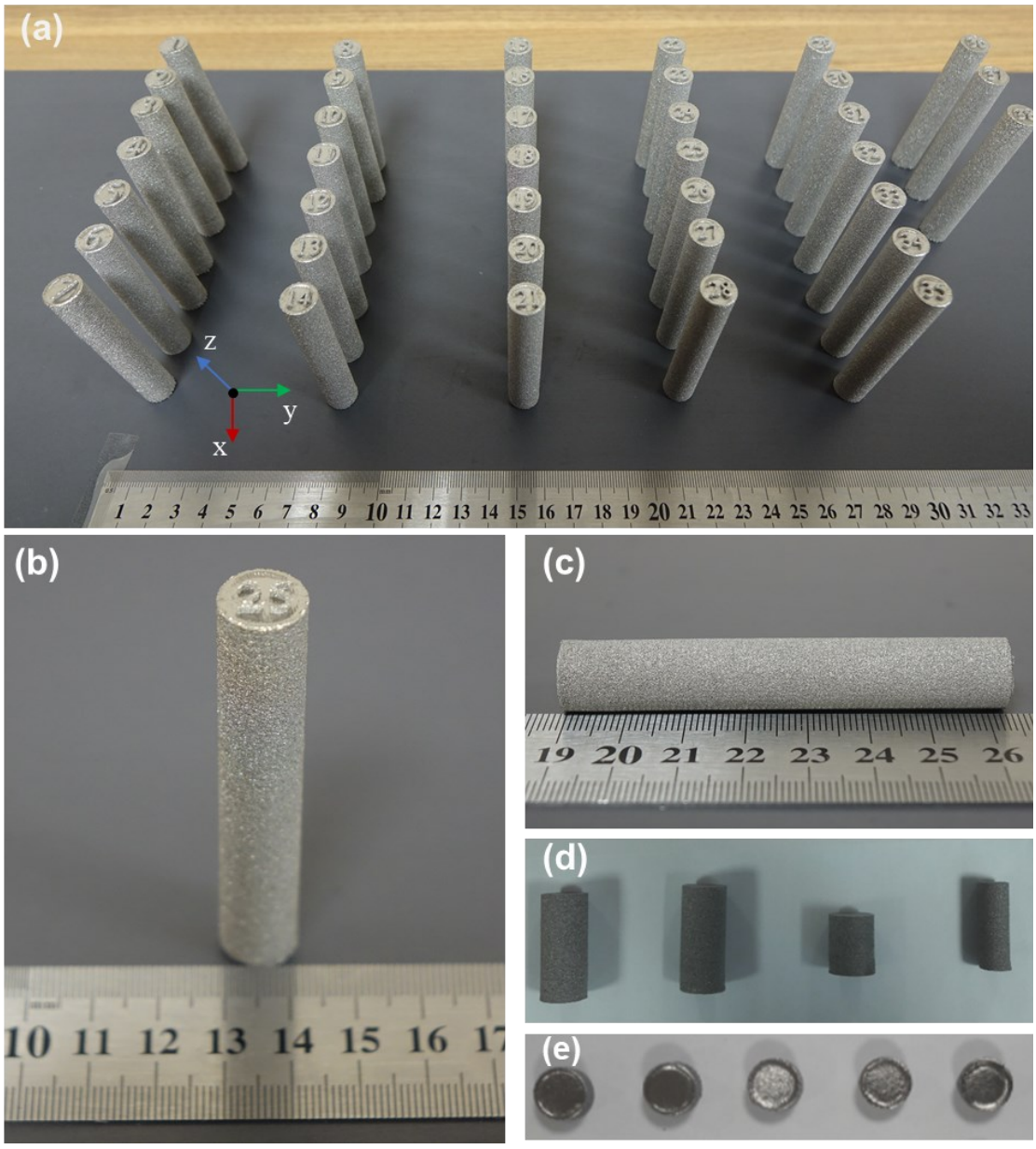

Figure 4.2. As-built EBM Ti64 specimens (a) a batch of fabrication (b) vertical view, (c) horizontal view, (d) the specimens for microstructural analysis, and (e) flat specimens.

Table 4.2. Process settings used in the fabrication of as-built specimens by EBM.

Process	Parameter			Value
Preheating	Focus Offset			44 mA
	Heating Focus Offset			100 mA
	Maximum Heating Time			60 s
	Maximum Beam Current			36 mA (I) – 45 mA (II)
	Minimum Beam Current			36 mA (I) – 45 mA (II)
	Number of Repetitions			3
	Beam Speed			40500 mm/s
	Line Offset			0.4 mm
	Hatch Depth			0.09 mm
Melting	Surface Temperature			925 °C
	Scanning Layer Thickness			90 µm
	Contour Numbers			3
	Contours	Outer Contours	Beam Speed	450 mm/s
			Beam Current	9 mA
			Beam Offset	0.27 mm
			Focus Offset	6 mA
		Inner Contours	Beam Speed	450 mm/s
			Beam Current	9 mA
			Beam Offset	0.18 mm
			Focus Offset	6 mA
	Hatch	Max. Beam Current		28 mA
		Min. Current		3.5 mA
		Line Offset		0.22 mm
		Hatch Depth		0.09 mm
Net Process	Surface Temperature			750 °C
	Scanning Layer Thickness			90 µm
	Contour Numbers			4
	Contours	Outer Contours	Beam Speed	400 mm/s
			Beam Current	3.2 mA
			Beam Offset	0.2 mm
			Focus Offset	0 mA
		Inner Contours	Beam Speed	400 mm/s
			Beam Current	3.2 mA
			Beam Offset	0.08 mm
			Focus Offset	0 mA
	Hatch	Max. Beam Current		3 mA
		Min. Current		0 mA
		Line Offset		0.2 mm
		Hatch Depth		0.07 mm

4.2. Sample Preparations

As-built specimens having the dimensions of Ø10mm x 29.5 mm and Ø15mm x 5.70 mm were prepared for the microhardness tests and metallographic analysis. For the hardness test, specimens were firstly cut into several pieces by using a precision cutting machine, afterward grinded and polished via classical methods. Hardness tests were conducted on the surfaces in the building and perpendicular to the building direction (Figure 4.3).

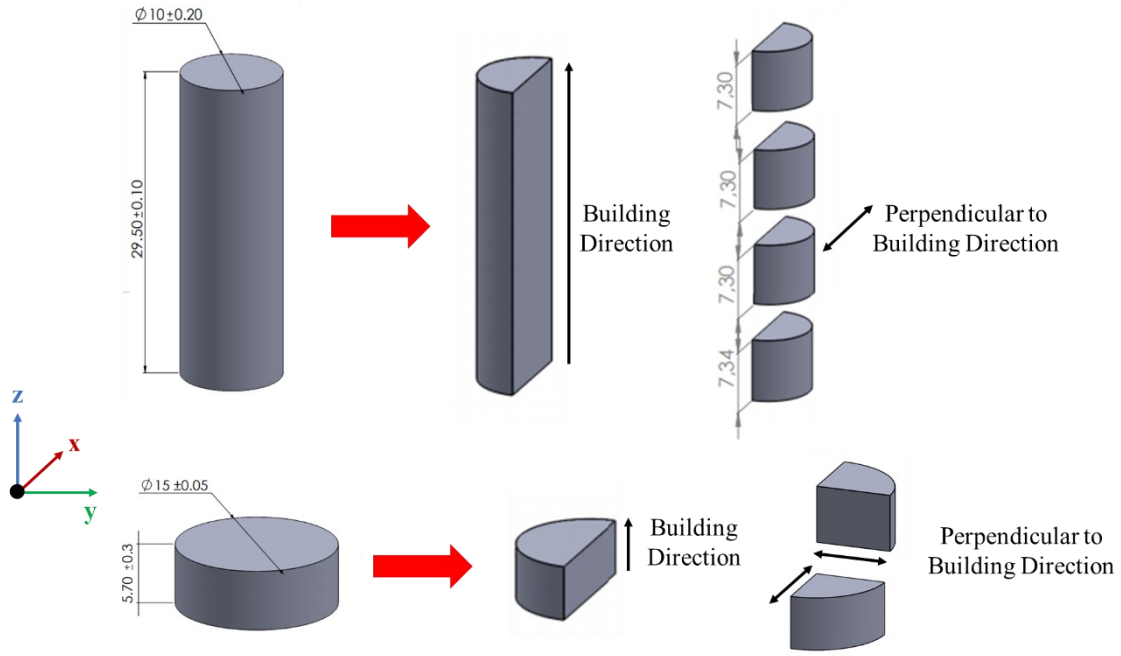

Figure 4.3. Hardness and metallography specimens and their related surfaces.

Standard tension test specimens were machined in a CNC machine from Ø12mm x 75 mm as-built bars in accord with the ASTM E8/E8M-16a standard. These specimens had a diameter of 6 mm, a gauge length of 24 mm, and a reduced parallel section length of 30 mm [97] (Figure 4.4). Non-standard tension specimens had a notch of different radii at the center of the gauge length. The diameters of the reduced section in the notch zone of non-standard specimens were machined with the same gauge diameter, 6 mm, as the standard ones. Additionally, the length of the reduced parallel section was also kept at 30 mm for non-standard specimens (Figure 4.4). Standard and non-standard tension specimens were employed in quasi-static tests (10^{-3}-10^{-1} s^{-1}).

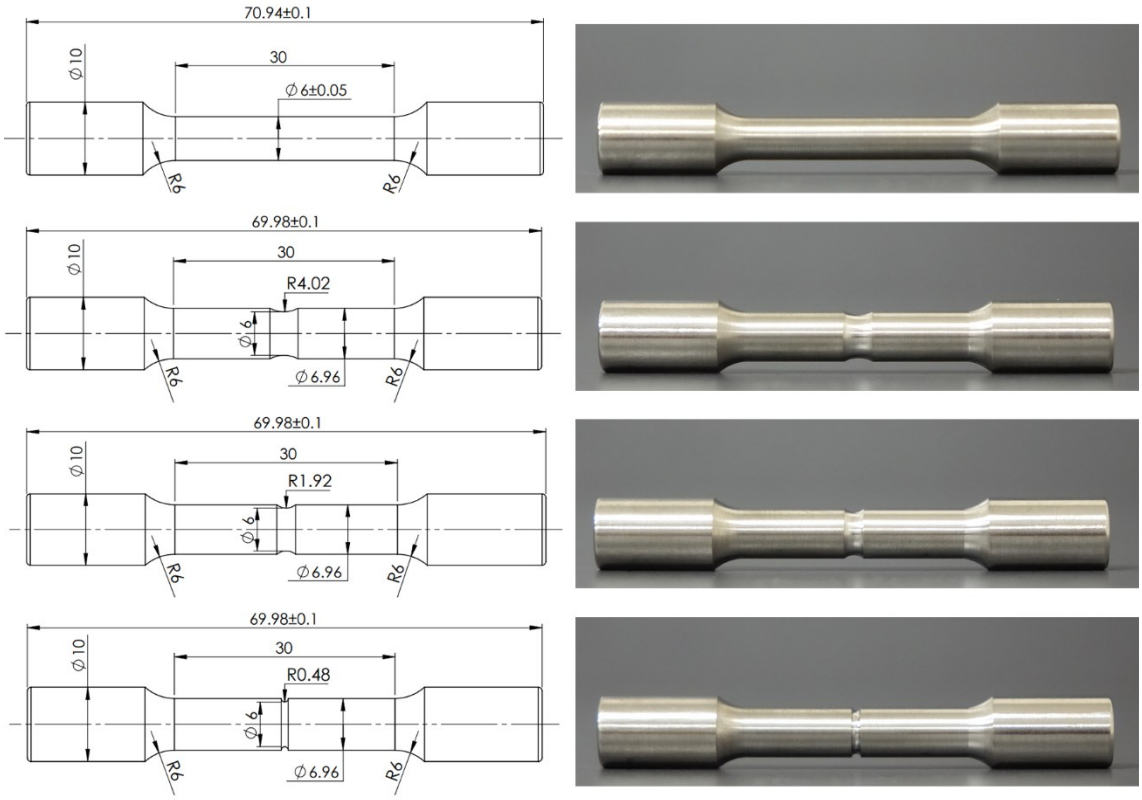

Figure 4.4. Tension test specimens used for quasi-static and dynamic tests and technical drawings of the specimens.

The compression test specimens had a diameter of 6mm diameter and varying lengths depending on the length to diameter (L/D) ratio as depicted in Figure 4.5. These specimens were machined in a CNC from Ø10 mm x 29.5 mm as-built specimens. The L/D ratios were selected 0.8, 1, 2, and 3 as described in ASTM E9-19, corresponding to the length of 4.8 mm, 6 mm, 12 mm, and 18 mm, respectively [98]. All compression test specimens were tested at the quasi-static strain rate range (10^{-3}-10^{-1} s^{-1}), while the specimens with the L/D ratios of 0.8 and 1 were additionally tested at high strain rates in a compression type Split Hopkinson Pressure Bar (SHPB).

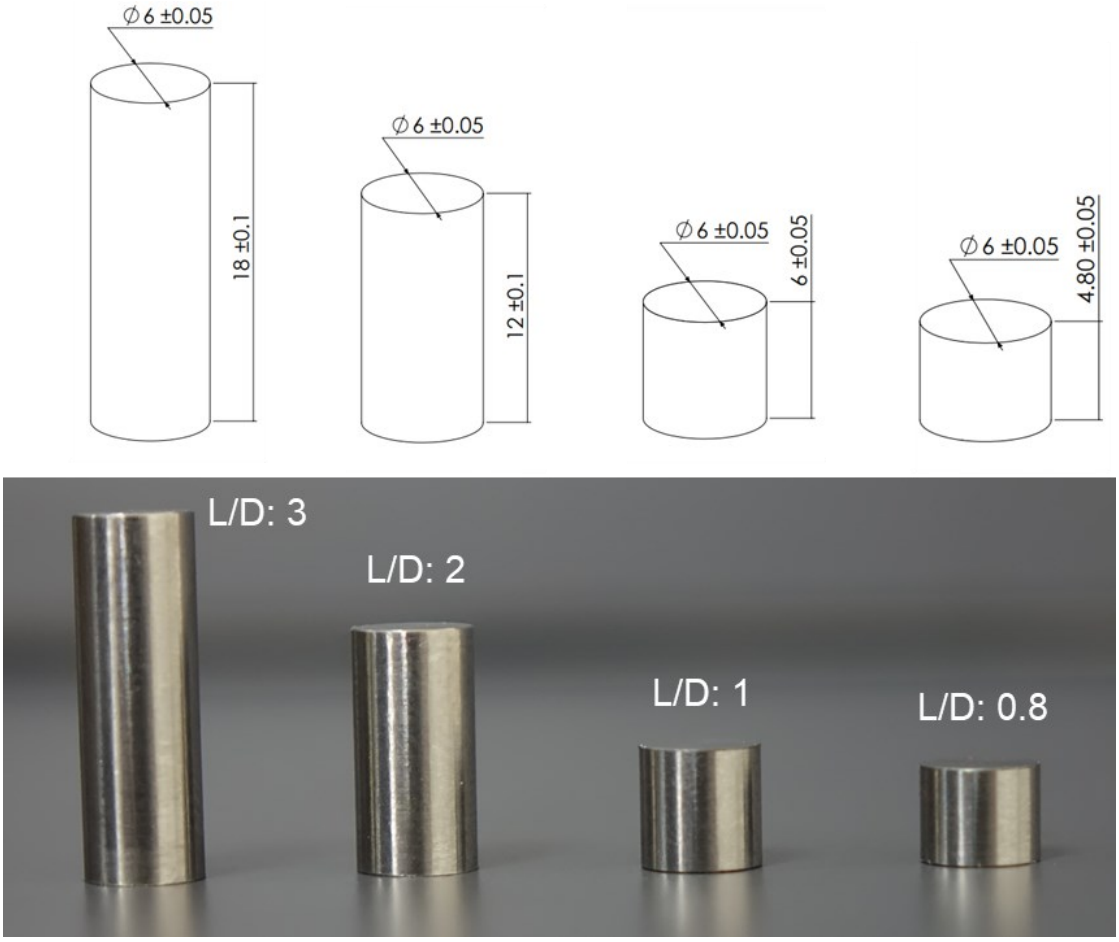

Figure 4.5. Compression test specimens used in quasi-static and dynamic tests and technical drawings of the specimens.

4.3. Metallographic Analysis

In the scope of the thesis, as-built EBM Ti64 specimens for microscopy were prepared through standard metallography composed of cutting, mounting, grinding, polishing, and etching as seen in Figure 4.6(a). For the surface roughness inspections, as-built specimens were analyzed via FEI Quanta 250 FEG scanning electron microscope. The microstructural analysis of the polished-etched and tested and fractured samples was performed in a Meiji Techno IM7200 optical microscope and FEI Quanta 250 FEG scanning electron microscope (Figure 4.6(b)). The polished samples were etched using a Kroll solution (3 ml HF + 6 ml HNO_3 + 100 ml H_2O).

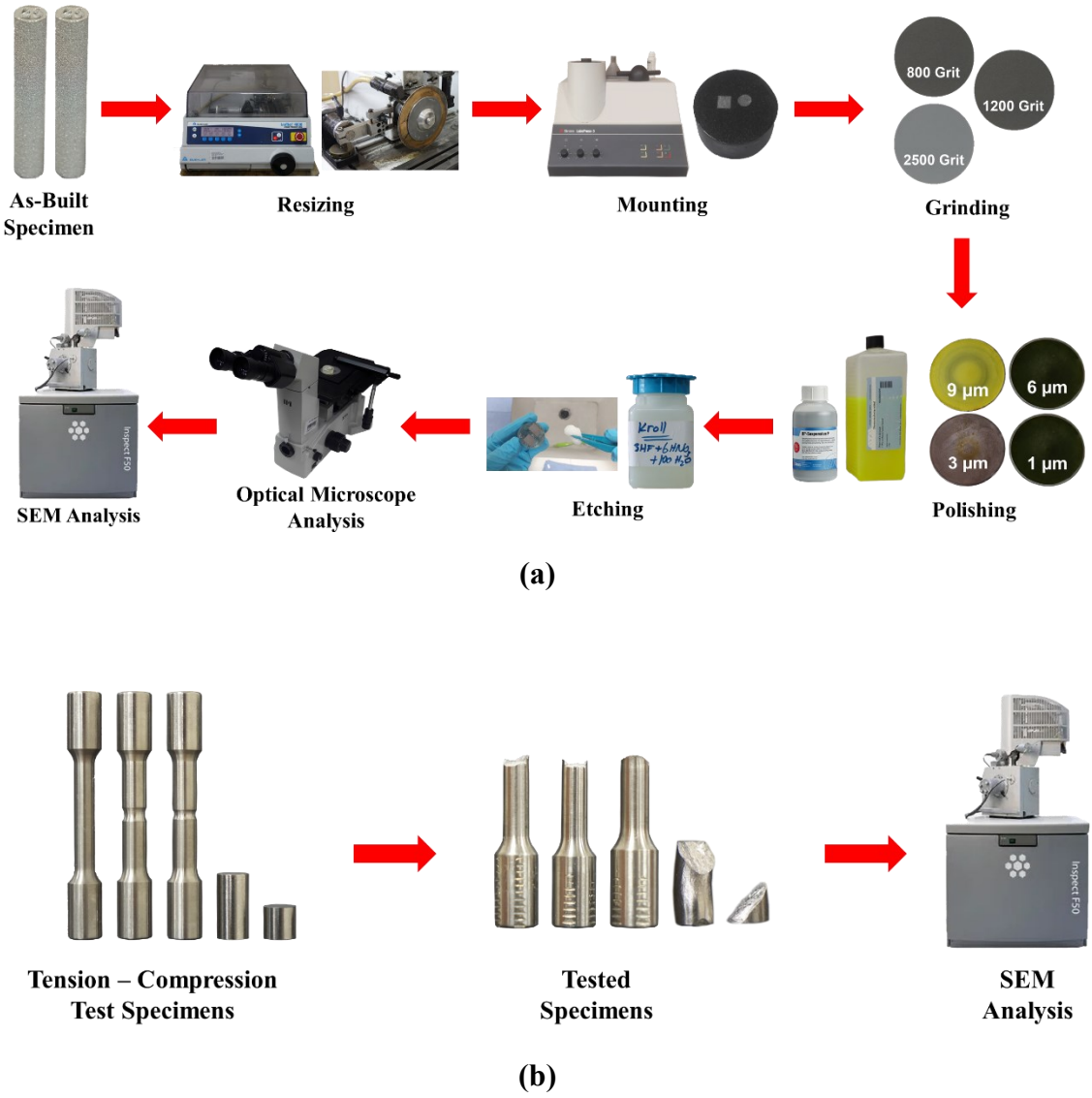

Figure 4.6. Procedures in metallographic analysis (a) as-built examination, (b) fracture analysis for tested specimens.

4.4. Density and Porosity Measurement

The simple and fast method of the density, relative density, and porosity measurements is known as Archimedes' method [99]. Archimedes' principle relies on the determination of the amount of the displaced liquid after submerging a part in a liquid. In another way, the difference between measured part mass in the air and measured mass in a liquid with a known density gives the volume and the density of the part. Density (ρ),

relative density (RD), and percentage of porosity (%P) can be calculated by utilizing the following relations

$$\rho = \frac{m_{air}\ x\ \rho_{liquid}}{m_{air} - m_{liquid}} \tag{4.1}$$

$$RD = 1 - \frac{\rho}{\rho_{ref}} \tag{4.2}$$

$$\%P = \frac{V_0 - V}{V_0}\ x\ 100 \tag{4.3}$$

where m_{air} is the part mass in air, m_{liquid} is the part mass in the liquid, V_0 is the volume of the full dense part, V is the calculated volume of the part, ρ_{liquid} is the density of the liquid, and ρ_{ref} is the reference density for the part.

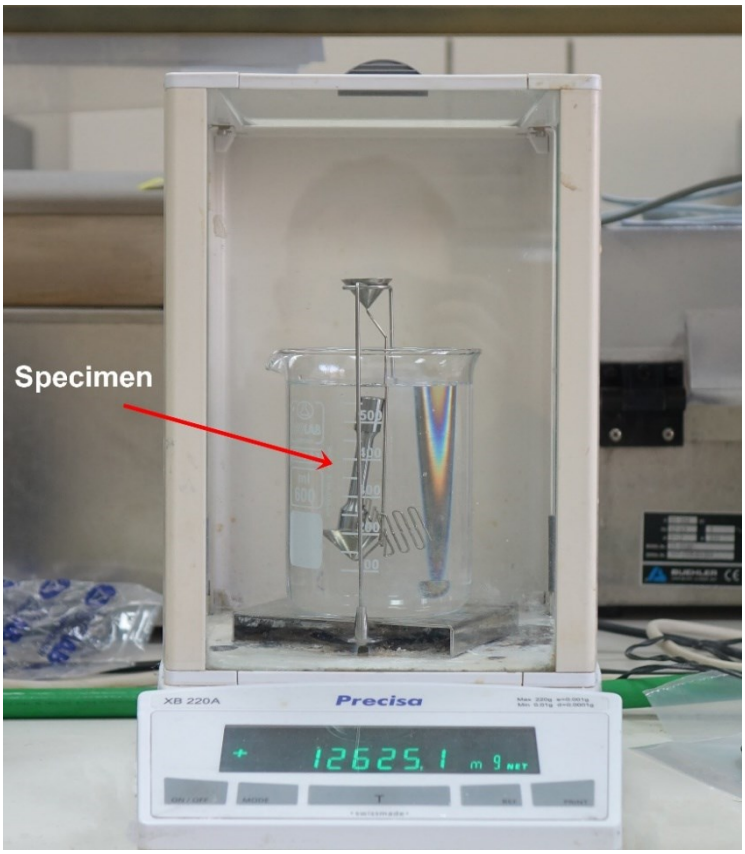

Figure 4.7. Precision balance with Archimedes apparatus.

The density and porosity calculations of all the EBM Ti64 tension and compression test specimens were made by measuring the mass of each specimen in the air and after immersing in water. The mass measurements were performed in a Precisa XB220A precision balance with an Archimedes apparatus as seen in Figure 4.7. In the determination of porosity level, the reference density value of Ti64 was taken as 4.429 g/cm^3.

4.5. Vickers Microhardness Test

Microhardness test is a type of mechanical testing method that enables the determination of the material response to local plastic deformation caused by a force created by a micro-indenter. In the Vickers microhardness test, a pyramidal diamond indenter is used to deform a small area on the material surface by a load ranging 1-1000 g in a certain dwell time. After the indentation, the distances between diagonals of the indented area are measured by using a calibrated microscope. Thereafter, the following relation is used to convert distance measurements into hardness numbers (HV).

$$HV = 1854.4\, x\, \frac{P}{d^2} \tag{4.4}$$

where P is the applied force and d is the mean diagonal length of indentation in μm.

The microhardness tests of EBM Ti64 specimens were conducted on the polished surfaces of the thermoset resin-mounted specimens using a Shimadzu HMV-2 Microhardness Tester as seen in Figure 4.8. The tests complied with the ASTM E384-16 standard [100]. The applied load by the indenter was selected 4.903 N corresponding to HV 0.5 load with a dwell time of 10 s.

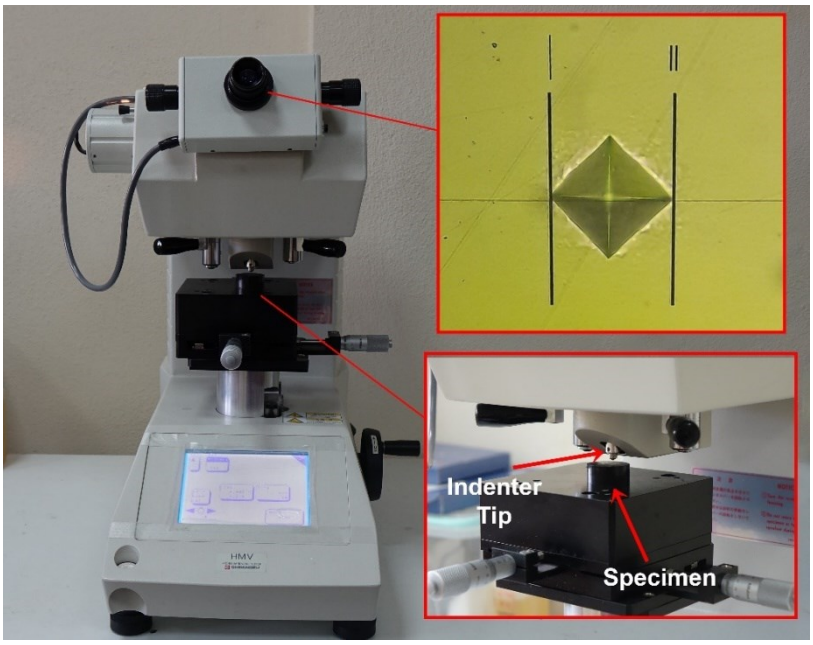

Figure 4.8. Shimadzu HMV-2 Microhardness Tester.

4.6. Quasi-Static Tests

4.6.1. Quasi-Static Tension Tests

Quasi-static tension tests of EBM-produced Ti64 specimens were conducted in a Shimadzu AG-X 300 kN universal testing machine. Test setup and devices employed in the system are illustrated in Figure 4.9. The tests were performed until fracture at the strain rates of 10^{-3}, 10^{-2}, and 10^{-1} s^{-1} at room temperature, complying with the instructions of ASTM E8/E8M-16 standard [97]. A non-contact video extensometer was used to record the displacement during the tests. During the tests, an external digital camera was used to record the deformation. In order to measure the change in the gauge length, two gauge markers were adhered onto the upper and lower boundaries of the gauge zone to make that zone recognizable by the extensometer. At least three tests were performed at each strain rate and the tested and fractured specimens were preserved in a desiccator until the microscopic analysis.

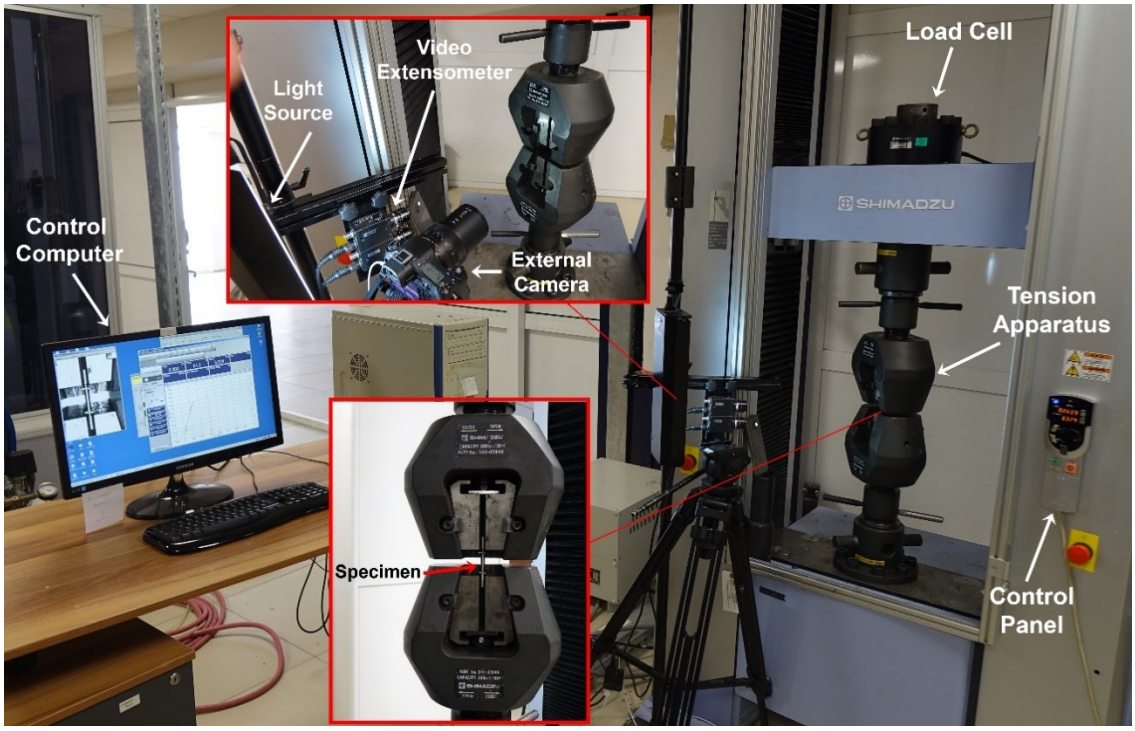

Figure 4.9. Quasi-static tension test setup.

The engineering stress (σ_{eng}) was calculated using

$$\sigma_{eng} = \frac{P}{A_0} \tag{4.5}$$

where P is the applied load and A_0 is the initial cross-sectional area of the specimen. The engineering strain (ε_{eng}) was calculated as

$$\varepsilon_{eng} = \frac{l_f - l_0}{l_0} = \frac{\Delta l}{l_0} \tag{4.6}$$

where, l_0 is the initial gauge length and l_f is the final gauge length of the specimen. The true stress (σ_{true}) and true strain (ε_{true}) were sequentially determined as

$$\sigma_{true} = \frac{P}{A_i} \tag{4.7}$$

$$\varepsilon_{true} = \ln\frac{l_i}{l_0} \tag{4.8}$$

where, A_i and l_i are the instantaneous cross-sectional area and length of the specimen. The engineering stress-strain data were converted into true stress-strain data by considering no volume change in plastic deformation as

$$A_0 l_0 = A_i l_i \tag{4.9}$$

Then Equation 4.7 is written as

$$\sigma_{true} = \sigma_{eng}\left(1 + \varepsilon_{eng}\right) \tag{4.10}$$

And Equation 4.8 is written as

$$\varepsilon_{true} = \ln\left(1 + \varepsilon_{eng}\right) \tag{4.11}$$

The true strain rate ($\dot{\varepsilon}_{true}$) was calculated using the following relation

$$\dot{\varepsilon}_{true} = \frac{d\varepsilon_{true}}{dt} \tag{4.12}$$

where *t* is the time.

4.6.2. Quasi-Static Compression Test

Quasi-static compression tests were performed also using the same Shimadzu AG-X 300 kN universal testing machine by using the compression rigid platens as seen in Figure 4.10. As with the tension tests, the compression tests were also conducted at strain

rates of 10^{-3}, 10^{-2}, and 10^{-1} s^{-1} at room temperature. These tests were performed by following the testing instructions given in the ASTM E9-19 standard, except for slight alterations in the dimensions and configurations of test specimens in order to reach more correlative results [98]. At least two repeating tests were performed for each strain rate and D/L ratio. The displacements were recorded by a non-contact video extensometer. Gauge markers were stuck on both platens to identify the gauge length been tracked by the extensometer. Because of the small length of the compression test specimens, gauge length was taken as the exact length of the specimen by sticking the gauge marker on the testing platens instead of sticking the gauge markers on the specimen. During the tests, an external digital camera was used to record the deformation. All tested specimens were preserved in a desiccator until the microscopic analysis. The true stress and strain in the compression tests were calculated using the following relations

$$\sigma_{true} = \sigma_{eng}\left(1 - \varepsilon_{eng}\right) \tag{4.13}$$

$$\varepsilon_{true} = -\ln\left(1 - \varepsilon_{eng}\right) \tag{4.14}$$

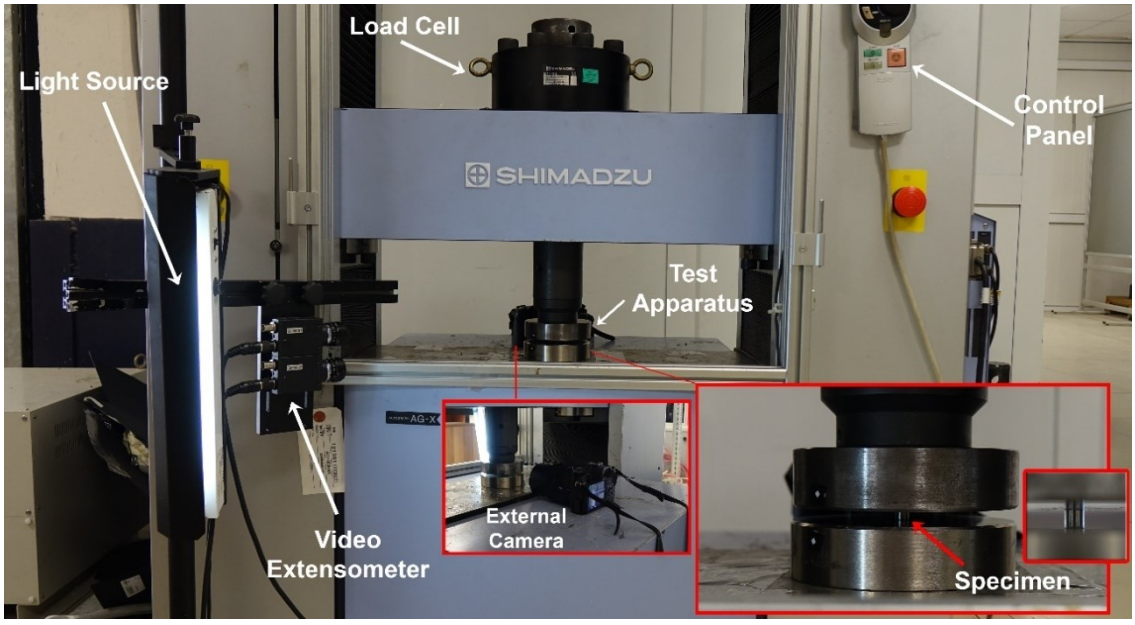

Figure 4.10. Quasi-static compression test setup.

4.7. High Strain Rate Test

4.7.1. Split Hopkinson Pressure Bar (SHPB) Tests

SHPB test is a commonly used experimental procedure for testing at high strain rates, within a range 10^1-10^4 s^{-1} [101]. The SHPB tests mainly rely on loading the specimen with a one-dimensional elastic stress wave which is created by the collision of the bars. A schematic of the SHPB test set-up is shown in Figure 4.11. Typical SPHB assembly consists of three main components which are bars, compressed gas gun, and data acquisition. There are three horizontally positioned cylindrical bars in the assembly namely striker bar, incident bar, and transmitter bar. The testing specimen is placed between the incident and transmitter bars. At the beginning of the test, the gas gun in the system is filled with nitrogen gas until about an adequate pressure level, then the striker bar is accelerated by the release of the compressed nitrogen gas stored in the gas gun. Accelerated striker bar travels in the barrel, and hits on the incident bar which results in the creation of an elastic compressive stress wave on the incident bar. This compressive wave propagates through the incident bar and reaches the specimen-incident bar interface. The magnitude of the wave is measured as voltage data by the strain gauges on the incident bar.

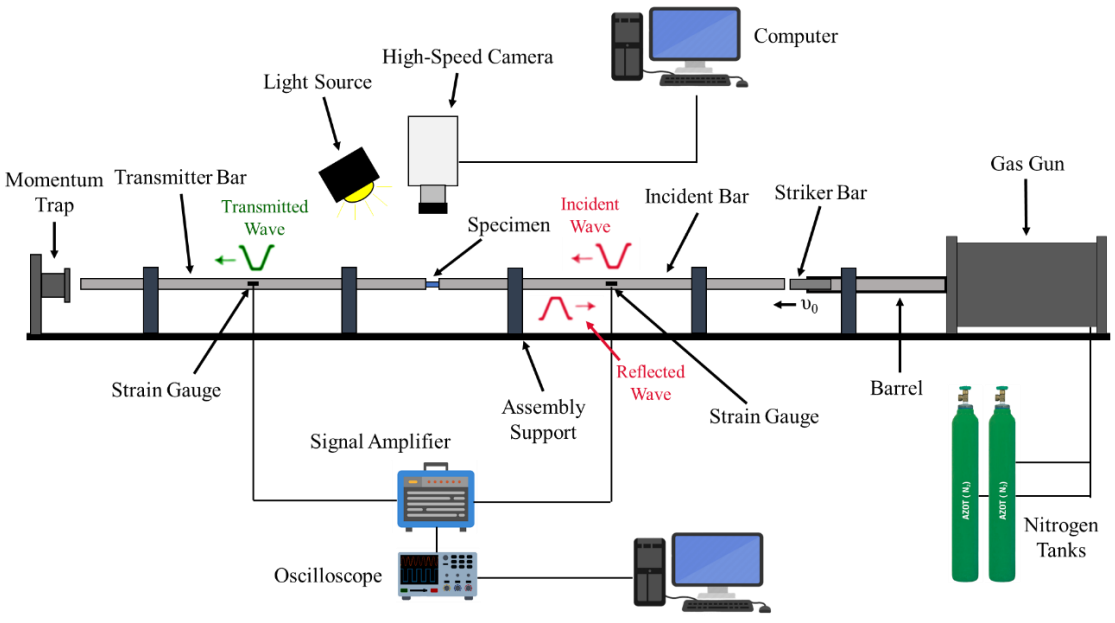

Figure 4.11. Schematic of SHPB test setup.

At the specimen-incident bar interface, part of the compressive wave is transmitted to the transmitter bar as a compressive wave and a part of it is reflected back to the incident bar as a tensile wave as shown in Figure 4.12. The magnitude of the transmitted stress is measured by the strain gauges on the transmitter bar. All the strain gauge measurements are performed by a signal conditioner and the conditioned wave data are recorded as a voltage-time history by the oscilloscope integrated into the test setup. A momentum trap located at the end of the transmitter bar is usually used to dump the energy of the stress wave and to hamper the fly-off of the transmitter bar.

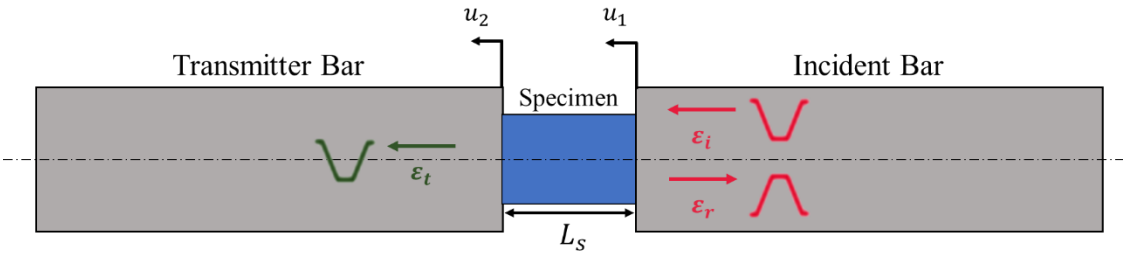

Figure 4.12. Specimen and bar interfaces.

After the impact of the striker bar onto the incident bar with a velocity of v_0, a rectangular-shaped elastic stress wave is created on the incident bar, which is given as

$$\sigma_b = \frac{E_b v_0}{2C_b} \tag{4.15}$$

And the strain on the bar is

$$\varepsilon_b = \frac{\sigma_b}{E_b} = \frac{v_0}{2C_b} \tag{4.16}$$

where, σ_b and ε_b are the maximum stress and strain on the bar, E_b is the elastic modulus of the bar, C_b is the wave velocity of the bar and v_0 is the impact velocity of the striker bar. The elastic incident wave produced after the impact of the striker bar travels in a certain period of time which is known as the time window (T_w), which is

$$T_w = \frac{2L_{SB}}{C_b} \tag{4.17}$$

where, L_{SB} is the length of the striker bar. The time window of the wave depends on the length of the striker bar and the wave velocity of the bar.

The displacements of the incident bar, u_1, and transmitter bar, u_2, sequentially are given as

$$u_1 = C_b \int_0^t (-\varepsilon_t + \varepsilon_r) dt \tag{4.18}$$

$$u_2 = -C_b \int_0^t \varepsilon_t dt \tag{4.19}$$

And the strain of the specimen is

$$\varepsilon_s = \frac{u_1 - u_2}{L_s} = \frac{C_b}{L_s} \int_0^t (-\varepsilon_t + \varepsilon_i - \varepsilon_r) dt \tag{4.20}$$

where, ε_i, ε_t, and ε_r are the incident, transmitted, and reflected waves, respectively. L_s is the length of the specimen. The derivation of the strain with respect to time gives the strain rate ($\dot{\varepsilon}_s$) of the specimen as

$$\dot{\varepsilon}_s = \frac{d\varepsilon_s}{dt} = \frac{C_b}{L_s} (-\varepsilon_t + \varepsilon_i - \varepsilon_r) \tag{4.21}$$

Forces produced in the incident bar, F_1, and transmitter bar, F_2, can be written sequentially as

$$F_1 = A_b E_b (\varepsilon_i + \varepsilon_r) \tag{4.22}$$

$$F_2 = A_b E_b \varepsilon_t \tag{4.23}$$

where, A_b is the cross-sectional area of the bar. For the SPHB test, it is assumed forces produced in the incident and transmitter bar are equal ($F_1 = F_2$). Using that, the following equation can be established

$$\varepsilon_t = \varepsilon_i + \varepsilon_r \tag{4.24}$$

Substituting Equation 4.20 into Equations 4.22 and 4.23 gives the strain and strain rate of the specimen as

$$\varepsilon_s = -\frac{2C_b}{L_s}\int_0^t \varepsilon_r \, dt \tag{4.25}$$

$$\dot{\varepsilon}_s = -\frac{2C_b\varepsilon_r}{L_s} \tag{4.26}$$

The stress in the test specimen ($\sigma_s(t)$) is

$$\sigma_s(t) = \frac{A_b E_b \varepsilon_t}{A_s} = \frac{A_b E_b(\varepsilon_i + \varepsilon_r)}{A_s} \tag{4.27}$$

where, A_s is the cross-sectional area of the specimen. Also, the stress in the specimen can be calculated based on the average summation of all three waves which can be expressed as the division of the average of the total force to the cross-sectional area of the specimen.

$$\sigma_s(t) = \frac{A_b E_b(\varepsilon_i + \varepsilon_r + \varepsilon_t)}{2A_s} = \frac{F_1 + F_2}{2A_s} \tag{4.28}$$

Since the main output from the SHPB test is the voltage-time history, the strain and stress of the specimen can be converted by using the following equations

$$\varepsilon_s = \frac{2\varepsilon_t(V)}{V_{exc}GK_{gain}(1+v)} \tag{4.29}$$

$$\sigma_s = \frac{A_b E_b}{A_s}\left[\frac{2\varepsilon_t(V)}{V_{exc}GK_{gain}(1+v)}\right] \tag{4.30}$$

In Equations 4.29 and 4.30, V_{exc} is the excitation voltage, G is the strain gauge factor, K_{gain} is the signal conditioner gain and v represents Poisson's ratio of the bar.

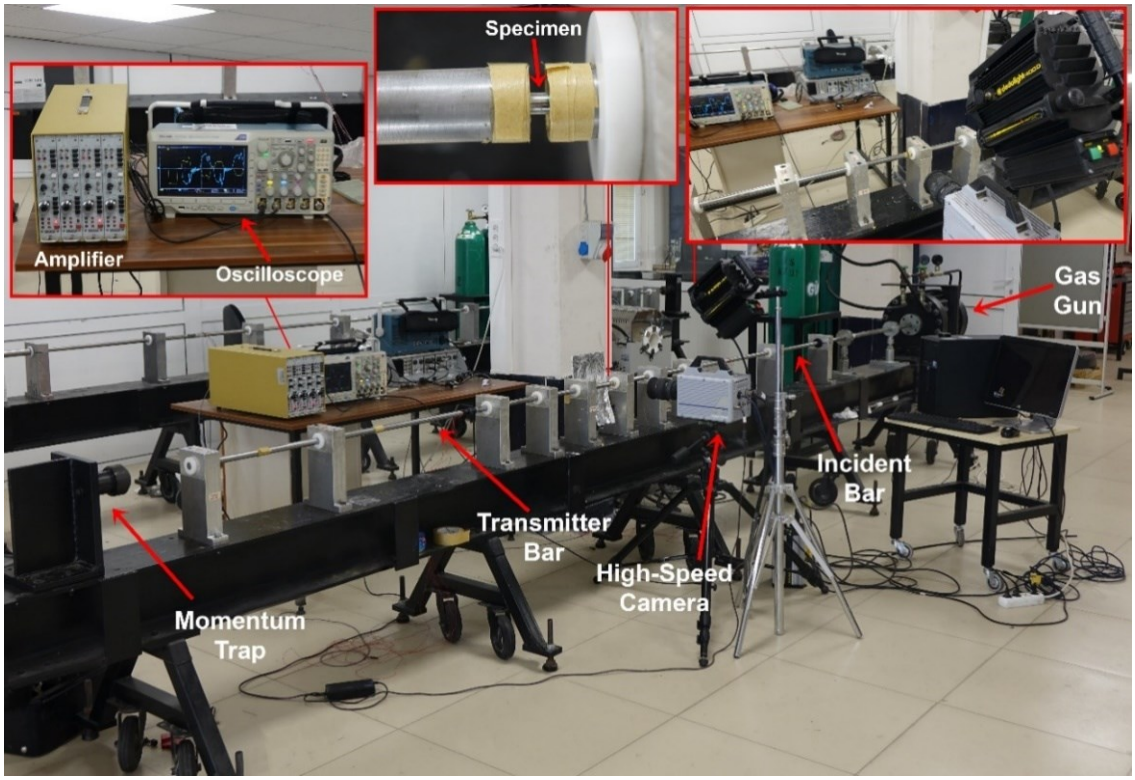

Figure 4.13. SHPB test apparatus set-up used in this study.

A picture of the used SHPB test setup in this study is shown in Figure 4.13. The bars of the used SPHB test apparatus were made of high-strength steel, possessing a common diameter of 20 mm and 25 cm, 200 cm, and 200 cm lengths for the striker, incident, and transmitter bar, respectively. The essential physical properties of the bar material are tabulated in Table 4.3. The average strain rates in the compression SHPB test using 2, 6, and 8 bar gas gun pressures were 605 s^{-1}, 1130 s^{-1}, and 2150 s^{-1}, respectively. Cylindrical specimens having L/D ratio of 1 were tested at 605 s^{-1} and 1130 s^{-1} while the specimens with L/D ratio of 0.8 were tested at 2150 s^{-1}. Strain measurements were carried by Wheatstone full bridge strain gauges bonded on the incident and transmitter bars and the strain gauges were symmetrically positioned at 75 cm away from the specimen. A digital oscilloscope was integrated into the SHPB setup to record wave signals as voltage-time data. The values for excitation voltage, strain gauge gain factor, the signal conditioner gain, and the bar's Poisson's ratio were 10V, 2.13, 200, and 0.31,

respectively. The deformation of the specimens was recorded by a Fastcam Photron high-speed camera at 20000 frames per second with a help of Dedolight Daylight 400D lighting equipment.

Table 4.3. Physical properties of bar components of SHPB.

Physical Properties	**Values**
Density	7.85 g/cm^3
Elastic Modulus	210 GPa
Poisson's Ratio	0.30
Elastic Wave Velocity	5188 m/s
Hardness	≈ 60 HRC

CHAPTER 5

EXPERIMENTAL RESULTS

5.1. Microstructural Analysis of As-built Parts

SEM images showing the surface of an EBM-produced as-built Ti64 sample at various magnifications are shown in Figure 5.1. As is seen in the same micrographs, the surface of as-built Ti64 contains partially melted surface-adhered powder particles. These adhered particles resulted from the high thermal radiation of the scanned layers to the adjacent raked powders during the melting process. The adhered powders deteriorate the surface quality of EBM-produced Ti64. Therefore, a post-removal process is generally required to reduce the surface roughness and to obtain a better surface morphology.

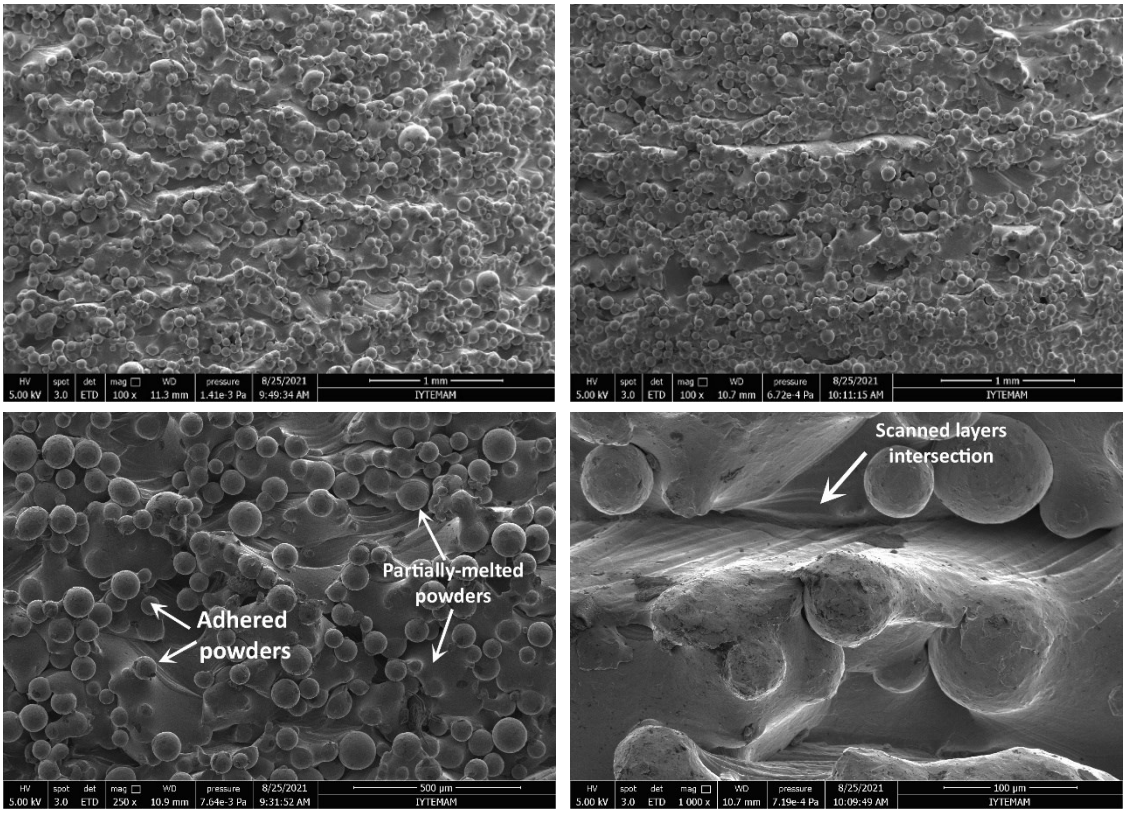

Figure 5.1. SEM images of the surface of an as-built Ti64 at 100, 250, and 500x magnifications.

Figure 5.2(a-h) and Figure 5.3(a-h) show the OM and SEM micrographs of the microstructure of as-built Ti64, respectively. In these micrographs, Z-direction is the EBM build direction (Z (BD)). The microstructure of EBM Ti64 consists of α (HCP), martensitic α′ (HCP), and β (BCC) phases. As is seen in Figure 5.2(a) and (b), the columnar prior β grains solidified first from melt pool are oriented through build direction in irregular shapes, in 110-150 μm size, and composed of α+β and, in some grains, α′ martensite (Figure 5.2(c)). The columnar grains are seen at higher magnifications in Figure 5.3(a) and (b). As a characteristic of EBM-produced Ti64, columnar grains are potentially formed due to an epitaxial growth occurred by a steep temperature gradient that provides nucleation and propagation of grains parallel to heat flux after re-melting of previous layers. Columnar grains are also detected in the ZY plane stretching out along the build direction. Microstructural observations also show that EBM-produced Ti64 possesses different microstructural morphologies which are illustrated in Figure 5.2(b), (c), and (d). The finer α and β phases form Widmanstätten-like structure, also called basket-weave, in which α platelets align in different directions and β phase exhibit both dot-like and rod-like morphologies (Figure 5.3(c) and (h)). The α layer(α_{GB}) is identified in the continuous form located at the grain boundaries of prior β grains as shown in Figures 5.3(f) and (g). It is also seen in Figure 5.3(c), α platelets are arranged in order and form colony morphology which can be easily distinguished from basket-weave structure (marked by white dotted outline in Figure 5.3(c)). The microstructures of Ti64 alloy are known thermal gradient dependent. Under excessive cooling rate in solidification, β phase transforms into martensitic α′ microstructure within the prior β grains. In Figure 5.2(b) and Figures 5.3(c), (e), (f), and (g), α′ martensite phases are marked by arrows. Existence of α′ martensite is attributed to high alterations in local thermal gradient in EBM process.

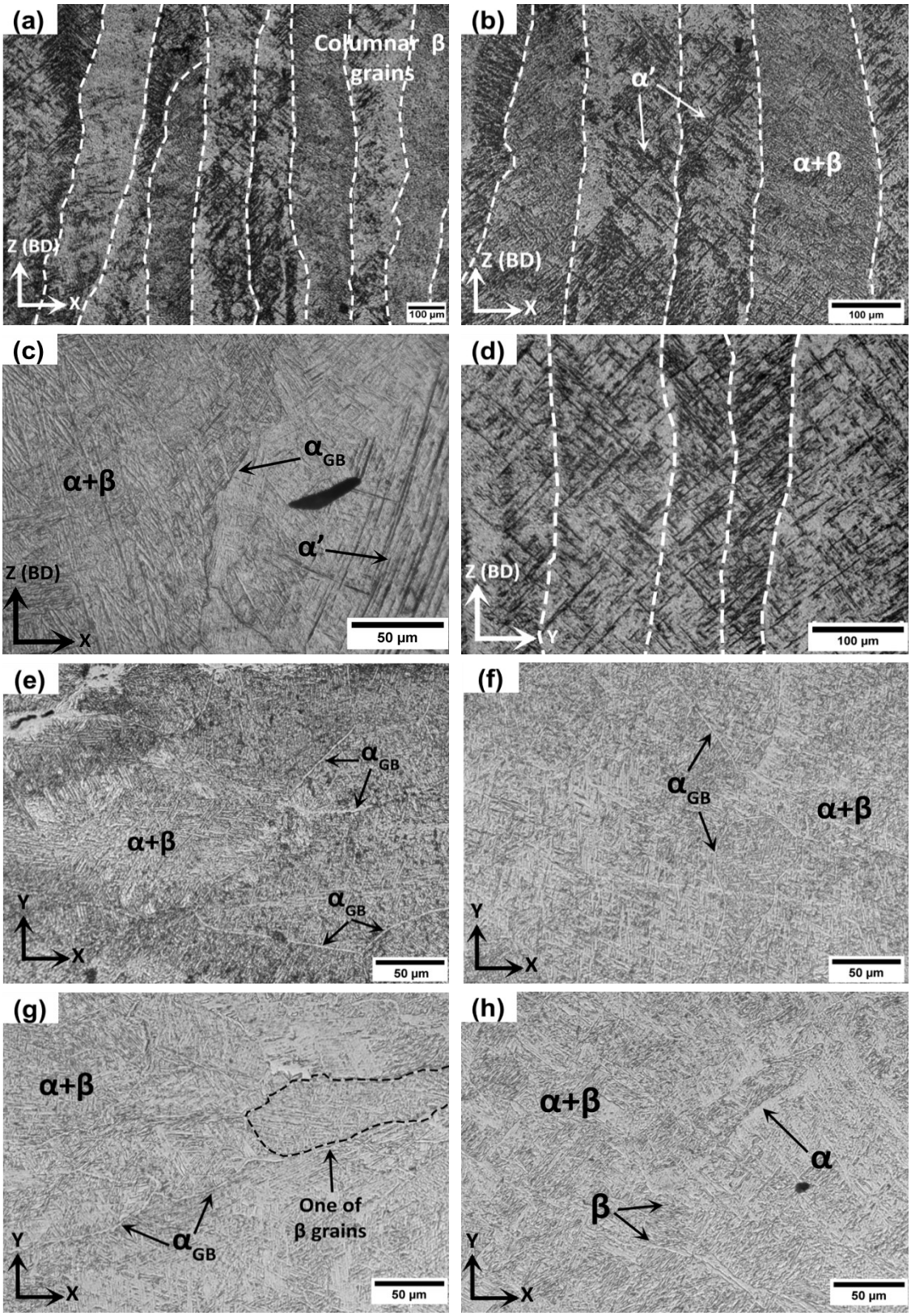

Figure 5.2. OM micrographs of as-built EBM Ti64 (a) and (b) columnar grains through BD and phases at 5x magnification, (c) BD at 20x magnification, (d) columnar grains in XY plane and (e), (f), (g), and (h) views from normal to BD at 20x magnification and phases.

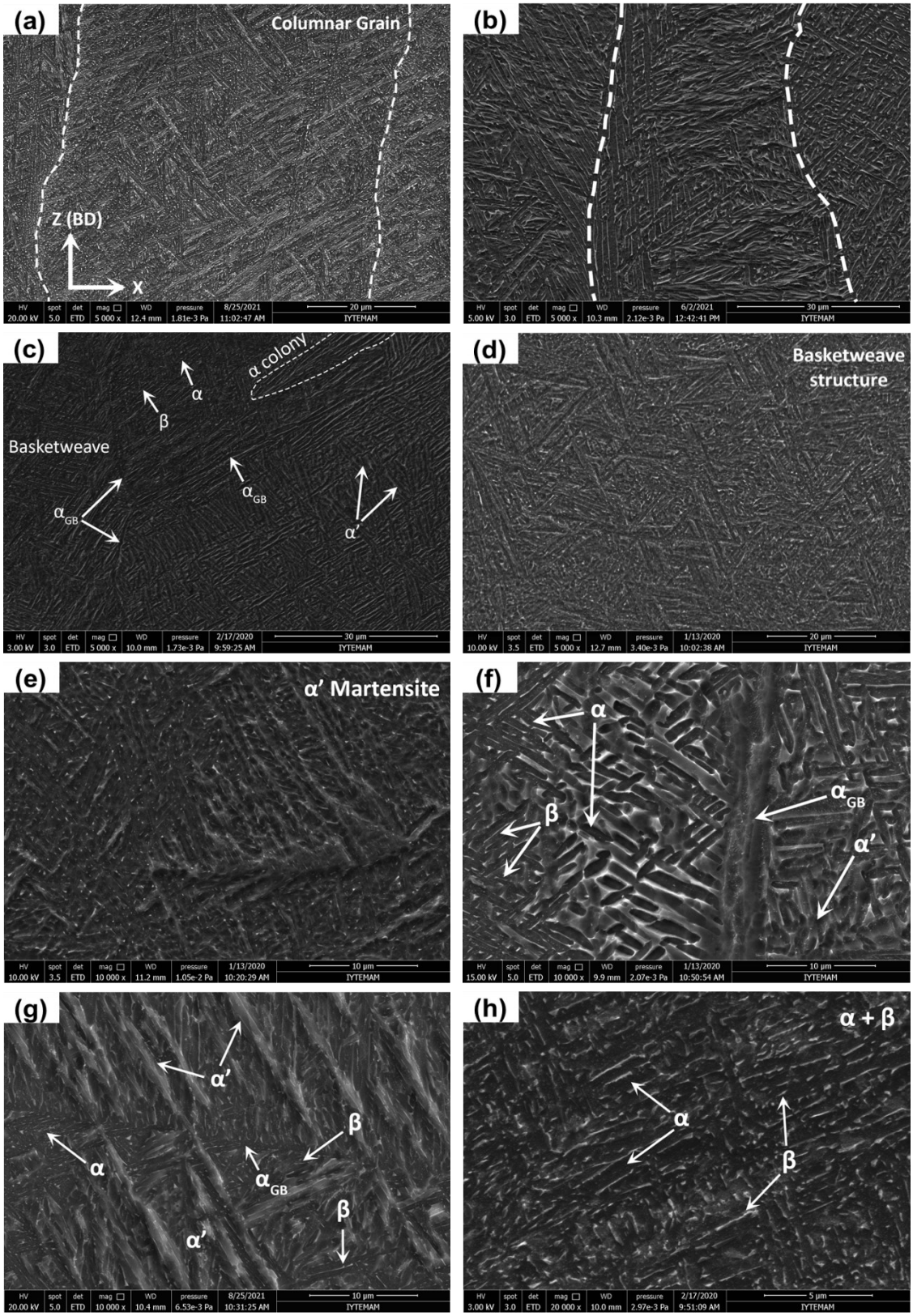

Figure 5.3. SEM micrographs of as-built EBM Ti64 (a) and (b) columnar grains through BD and phases at 5000x magnification, (c) phases at 5000x magnification, (d) basket-weave structure, (e) α′ martensite structure, (f), (g), and (h) existing phases at 10000x and 20000x magnifications.

A three-dimensional view of an EBM-produced Ti64 bulk part is shown in Figure 5.4. The columnar grains through the build direction are clearly seen and continuous throughout the part height in both ZX and ZY planes. The darkest regions in Figure 5.4 correspond probably to the martensite locations at where the excessive cooling gradient occurred. In the XY plane (perpendicular to the build direction), the grains are nearly equal-axed and formed mostly by α+β dual-phase.

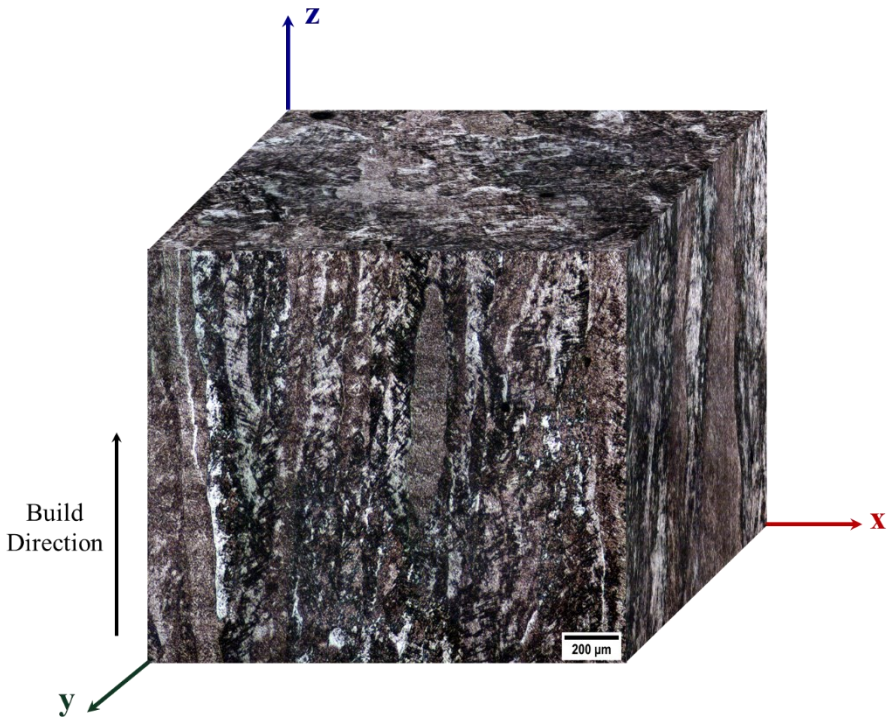

Figure 5.4. Combination of microstructural views with regards to all three axes relative to build direction.

As-built specimens have various shapes of porosities that are essentially caused by gas entrapment due to the vacuum environment in the building chamber of EBM, and lack of fusion as a consequence of insufficient melting energy (Figure 5.5). Gas and lack-of-fusion voids were identified at all locations. Partially melted or non-melted powders are observed to be embedded inside the lack-of-fusion defects (Figure 5.5). The lack of fusion voids are observed to be bigger than the gas voids and are mostly located near the outer wall of the specimen. The areal dimensions of the lack of fusion voids are up to 0.0744 mm^2 which is 50 times that of gas voids (Figure 5.5). A relatively high rate of the

presence of porosities also confirms a high porosity level in the as-received EBM samples, around 2.065 % calculated in Section 5.2. Sharp edges of lack of fusion voids become high stress-concentration sites, causing a quick crack progression and hence a low ductility under tensile loading.

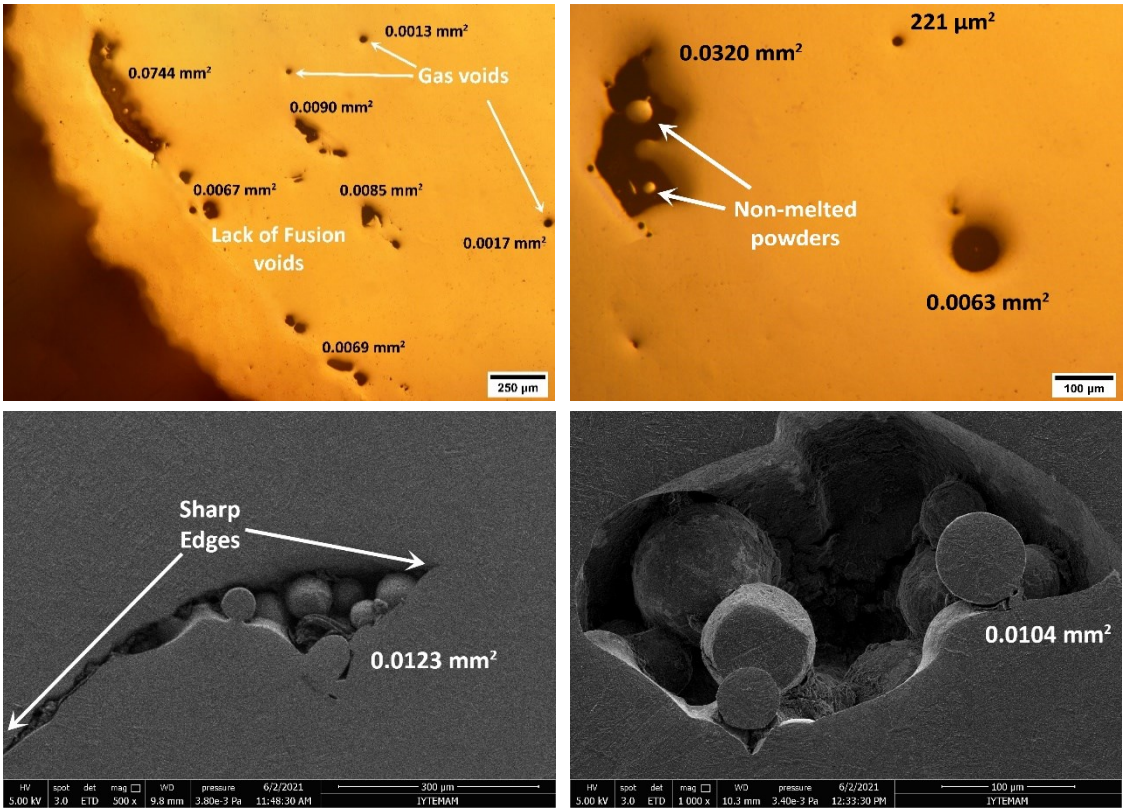

Figure 5.5. Some of the inspected porosities within the microstructure of the as-built parts and their measured dimensions.

5.2. Porosity and Volume Fraction Calculations

The weight measurements, volume, actual density, and percent porosity calculations of EBM-produced Ti64 parts are tabulated in Table 5.1 through Table 5.5. The weight measurements under water were completed using 25 cm^3 distilled water with an approximate density of 0.99 g/cm^3 for the Archimedes method. The nominal density of bulk Ti64 as a reference was taken as 4.429 g/cm^3. According to the calculations,

averaged values of density, relative density and percent porosity of EBM-produced Ti64 bulk parts are sequentially 4.337 ± 0.005 g/cm^3, 0.979 ± 0.001, and 2.065 ± 0.099%.

Table 5.1. Density and percent porosity of standard (unnotched) tensile test specimens.

Specimen Number	Weight in Air (g)	Weight in Water (g)	Volume (cm^3)	Actual Density (g/cm^3)	Porosity (%)
1	16.382	12.624	3.803	4.308	2.741
3	16.356	12.620	3.781	4.326	2.323
4	16.402	12.669	3.778	4.342	1.970
5	16.409	12.667	3.787	4.333	2.164
6	16.413	12.675	3.783	4.339	2.035
7	16.405	12.655	3.795	4.323	2.396
8	16.401	12.666	3.780	4.339	2.028
9	16.394	12.658	3.781	4.336	2.096
10	16.395	12.666	3.774	4.345	1.906
11	16.398	12.665	3.778	4.341	1.994
Average	**16.396**	**12.657**	**3.784**	**4.333**	**2.165**
St. Dev.	**0.016**	**0.019**	**0.009**	**0.011**	**0.255**

Table 5.2. Density and percent porosity of tensile test specimens with 0.65 stress triaxiality (R= 4.02 mm).

Specimen Number	Weight in Air (g)	Weight in Water (g)	Volume (cm^3)	Actual Density (g/cm^3)	Porosity (%)
12	17.757	13.709	4.097	4.335	2.130
13	17.758	13.700	4.107	4.324	2.365
14	17.790	13.742	4.097	4.343	1.948
15	17.801	13.741	4.109	4.333	2.177
16	17.780	13.733	4.095	4.341	1.979
17	17.808	13.752	4.105	4.339	2.042
18	17.805	13.747	4.107	4.336	2.107
19	17.795	13.733	4.111	4.329	2.258
20	17.811	13.747	4.113	4.331	2.219
Average	**17.789**	**13.734**	**4.104**	**4.334**	**2.136**
St. Dev.	**0.020**	**0.018**	**0.007**	**0.006**	**0.135**

Table 5.3. Density and percent porosity of tensile test specimens with 0.91 stress triaxiality (R= 1.92 mm).

Specimen Number	Weight in Air (g)	Weight in Water (g)	Volume (cm^3)	Actual Density (g/cm^3)	Porosity (%)
21	17.819	13.742	4.126	4.319	2.487
22	17.770	13.717	4.102	4.332	2.179
23	17.748	13.720	4.076	4.354	1.694
24	17.767	13.726	4.089	4.345	1.905
25	17.745	13.703	4.090	4.338	2.051
26	17.754	13.709	4.093	4.337	2.074
27	17.761	13.712	4.098	4.335	2.132
28	17.747	13.727	4.068	4.362	1.504
29	17.729	13.690	4.087	4.337	2.066
30	17.736	13.732	4.052	4.377	1.171
Average	**17.758**	**13.718**	**4.088**	**4.344**	**1.926**
St. Dev.	**0.025**	**0.015**	**0.020**	**0.017**	**0.377**

Table 5.4. Density and percent porosity of tensile test specimens with 1.75 stress triaxiality (R= 0.48 mm).

Specimen Number	Weight in Air (g)	Weight in Water (g)	Volume (cm^3)	Actual Density (g/cm^3)	Porosity (%)
31	17.793	13.746	4.095	4.345	1.907
32	17.764	13.710	4.103	4.330	2.236
33	17.799	13.750	4.098	4.344	1.922
34	17.800	13.747	4.102	4.340	2.014
35	17.785	13.734	4.100	4.338	2.048
36	17.780	13.735	4.093	4.344	1.930
37	17.784	13.741	4.091	4.347	1.860
38	17.781	13.728	4.102	4.335	2.118
Average	**17.786**	**13.736**	**4.098**	**4.340**	**2.004**
St. Dev.	**0.012**	**0.013**	**0.004**	**0.006**	**0.126**

Table 5.5. Density and percent porosity of compression tests specimens with L/D=1.

Specimen Number	Weight in Air (g)	Weight in Water (g)	Volume (cm^3)	Actual Density (g/cm^3)	Porosity (%)
1	0.771	0.594	0.179	4.304	2.814
5	0.748	0.577	0.173	4.317	2.537
6	0.737	0.569	0.170	4.335	2.123
7	0.746	0.576	0.172	4.336	2.094
8	0.744	0.575	0.171	4.350	1.778
9	0.742	0.573	0.171	4.339	2.042
10	0.745	0.575	0.172	4.330	2.225
11	0.741	0.573	0.170	4.358	1.592
12	0.739	0.571	0.170	4.339	2.038
15	0.707	0.546	0.163	4.343	1.931
16	0.742	0.573	0.171	4.351	1.752
19	0.739	0.570	0.171	4.321	2.438
20	0.741	0.572	0.171	4.346	1.884
Average	**0.742**	**0.573**	**0.171**	**4.336**	**2.096**
St. Dev.	**0.014**	**0.010**	**0.003**	**0.015**	**0.341**

5.3. Microhardness Results

The hardness tests were performed based on the long axis being the building direction. The sample was cut into two through the cross-section and then one cut-piece was split into 7.30 mm-long four pieces as previously given in Figure 4.3. The hardness tests were performed through the build direction (in the Z-axis) and the diameter (XY plane). The hardness through the build direction of the specimen was taken at three locations: left, center, and right then these hardness numbers were then averaged. The hardness through diameter was taken in line pattern from the contact surface with the base plate, 7.34 mm apart, 14.64 apart, and 21.94 mm apart from the base plate. The variations of hardness along the building direction and the diameter are shown in Figure 5.6(a). The hardness across (through Z-axis) varies between 366 and 380 HV until about a distance of 17 mm from the base plate of the used EBM system (shown by an arrow in the same figure). After about 17 mm, the hardness values decrease to an average of 355 HV. The hardness measurements through diameter also confirm high hardness near the base plate.

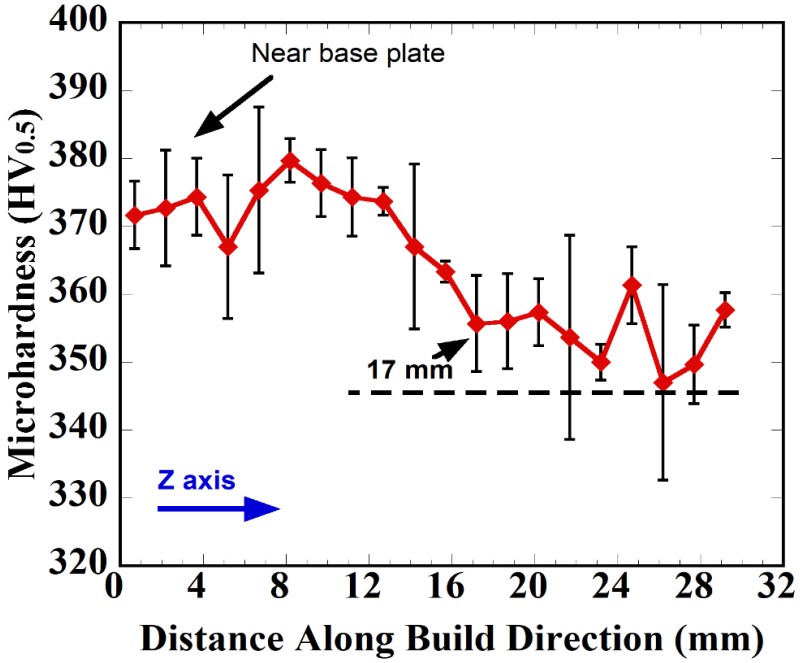

(a)

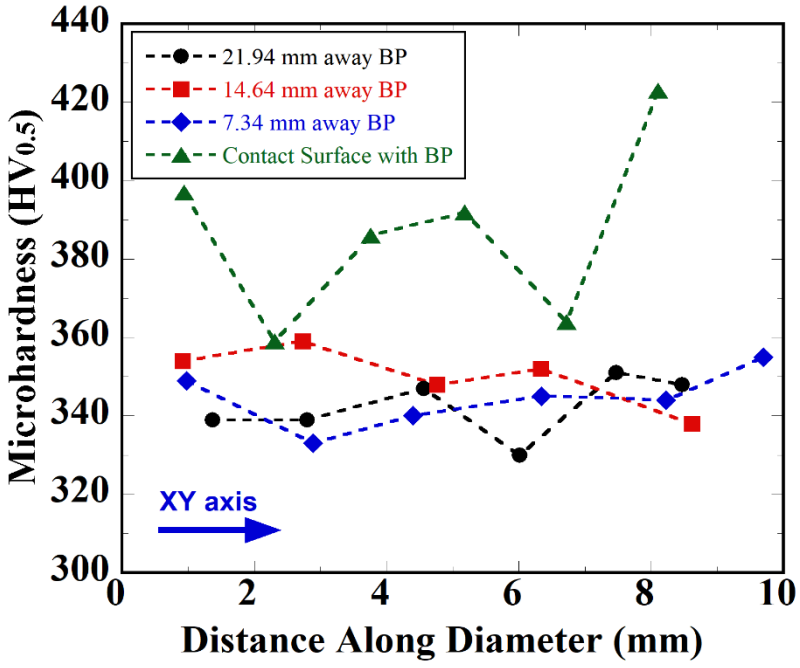

(b)

Figure 5.6. Microhardness results of EBM produced Ti64 bulk part (a) measurements through build direction and (b) measurements on the perpendicular planes to build directions starting from contact surface with base plate, 7.30 mm away, 14.64 mm away, 21.94 mm away from the base plate.

As seen in Figure 5.6(b), the contact surface with- base plate shows hardness values comparably higher than those of the surfaces located away from the base plate. As the height of the specimen increases, the diameter hardness values seen in Figure 5.6(b) decrease and reach an average value of 345 HV, which is slightly lower than the average hardness in the Z-axis when the height is higher than 17 mm. These hardness numbers correspond to the flow stresses of 1196-1242 MPa (VH/3) near the base plate in the Z direction and XY plane and 1161-1128 MPa when 17 mm away from the base plate through Z and XY direction, respectively. The hardness values show an anisotropy between the XY plane and Z direction. The anisotropy was found as much as 79 MPa between Z and XY directions.

A MATLAB code was compiled to produce a 2D contour map of microhardness distributions within the specimen borderlines based on the measurements and their corresponding coordinates. Related 2D contour maps in the Z direction and perpendicular directions in the XY plane are shown in Figure 5.7. It can be verified that the decrease in the microhardness values through the build direction and uniformation of the obtained microhardness results as the color range degrades through the build direction. This decrease is also seen in the colorized views for the relative distances in the perpendicular direction. Additionally, as being noticeable, the highest microhardness variation happens only near the base plate by lowering approximately 8.3%.

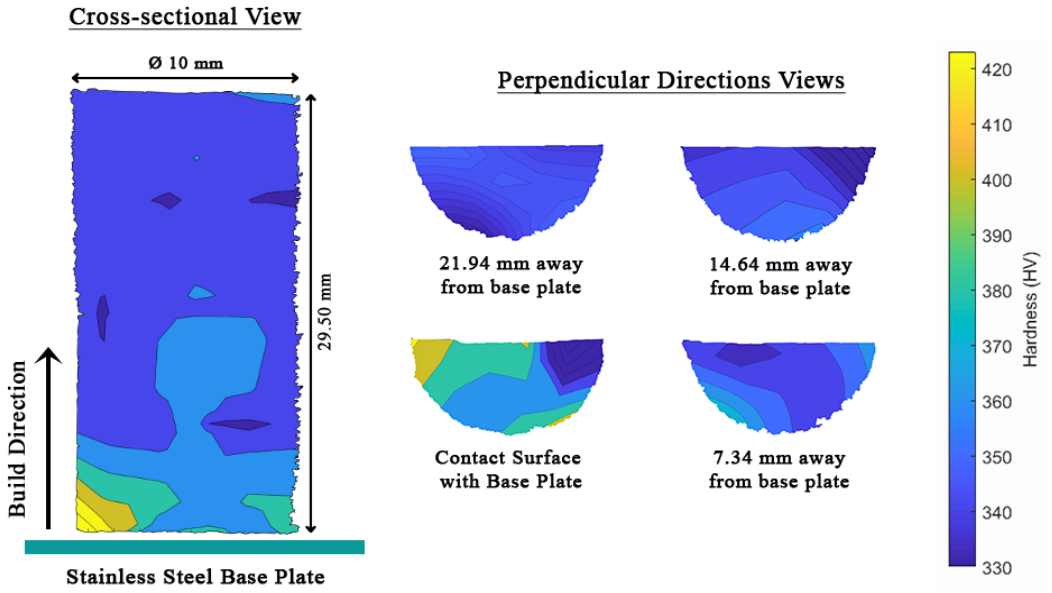

Figure 5.7. Contour maps of hardness through build direction and perpendicular to build directions.

5.4. Quasi-Static Tests

5.4.1. Tension Tests

True stress-true strain curves of quasi-static tensile specimens at the strain rates of $1x10^{-3}$, $1x10^{-2}$, and $1x10^{-1}$ s^{-1} are sequentially shown in Figure 5.8(a-c). As is seen in the same figure, three tests performed at each strain rate exhibit very similar stress-strain curves. Note that the true stress and true strain calculations were made by using the standard formulations since the EBM Ti64 specimens fractured without undergoing necking.

EBM Ti64 specimens initially deform elastically until yield point, thereafter, plastic deformation starts and the specimens fractured without necking (Figure 5.8(a-c)). However, the specimens exhibit extremely low ductility under tension. Test specimens fracture at the average strains of 3.13% ± 0.71, 3.15% ± 0.15 and 4.50% ± 2.59 at 10^{-3}, 10^{-2} and 10^{-1} s^{-1}, respectively. The average yield strengths are 887 MPa ± 20.7 MPa, 938 MPa ± 12 MPa and 1043 MPa ± 18.3 MPa, and ultimate tensile strengths are 1090 MPa ± 5.3 MPa, 1128 MPa ± 14.8 MPa and 1157 MPa ± 33.9 MPa at 10^{-3}, 10^{-2} and 10^{-1} s^{-1}, respectively. The elastic moduli of EBM Ti64 alloy at 10^{-3}, $10^{-2,}$ and 10^{-1} s^{-1} are sequentially determined 113.6 GPa ± 9.4 GPa, 118.9 GPa ± 2 GPa, and 124.1 GPa ± 5.8 GPa. Two true stress-true strain curves of the specimens tested at 10^{-3}, $10^{-2,}$ and 10^{-1} s^{-1} are shown all together in Figure 5.9. As it is seen in the same figure, EBM Ti64 alloy exhibit a strain rate sensitive yield and tensile strength behavior. As the strain rate increases from 10^{-3} s^{-1} to 10^{-1} s^{-1}, the yield strength increases by 156 MPa and tensile strength by 67 MPa. The increased fracture strains of the specimens tested at 10^{-1} s^{-1} seen in Figure 5.9 are due to the adiabatic heating.

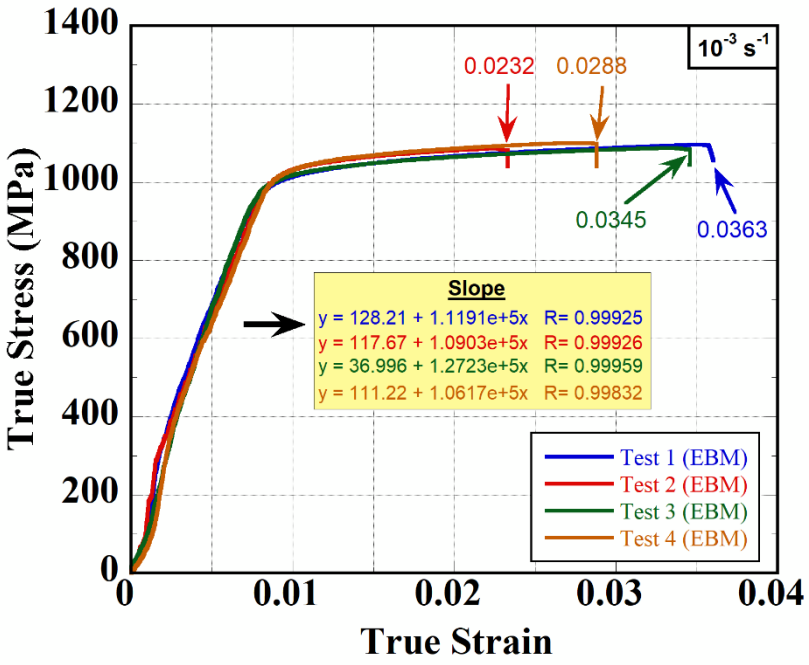

(a)

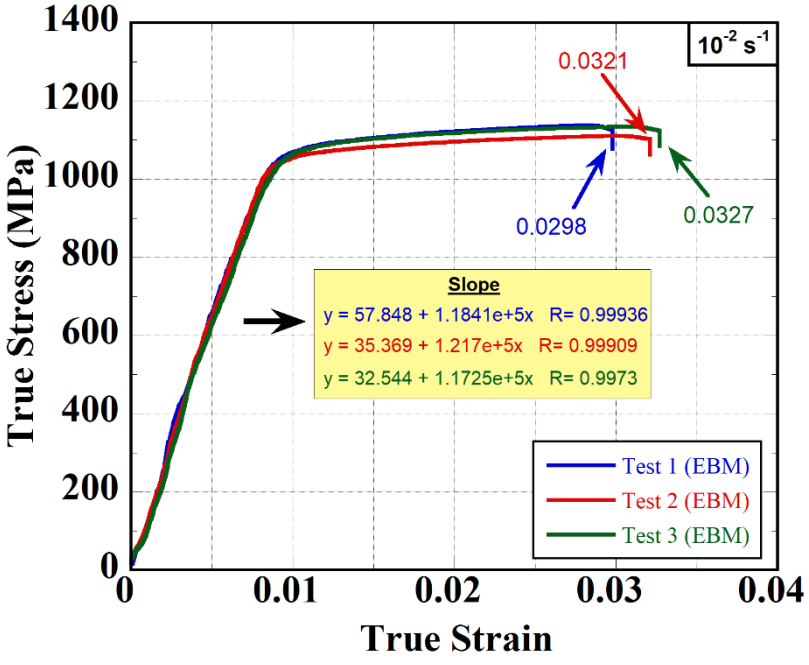

(b)

Figure 5.8. True stress-true strain curves of EBM Ti64 at (a) $1x10^{-3}$, (b) $1x10^{-2}$, and (c) $1x10^{-1}$ s^{-1}.

(cont. on next page)

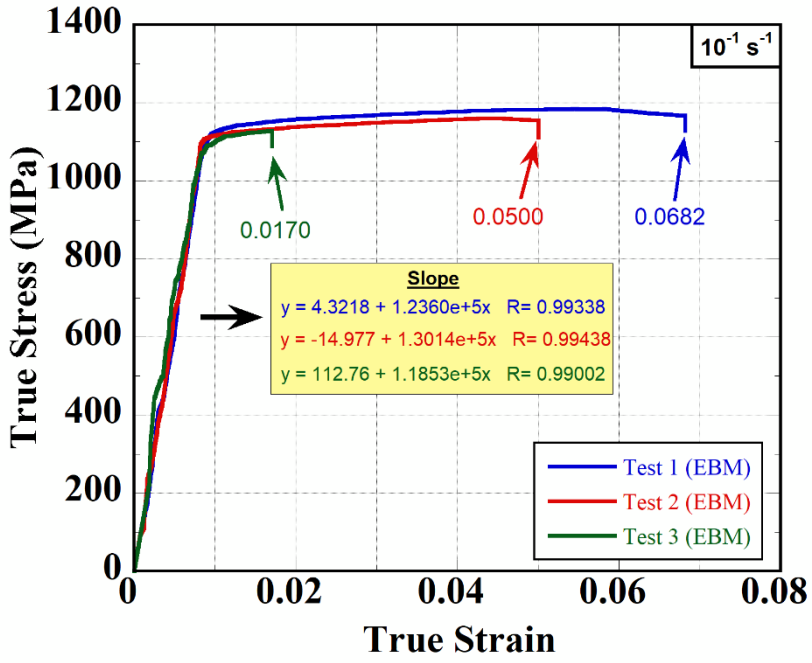

(c)

Figure 5.8. (cont.)

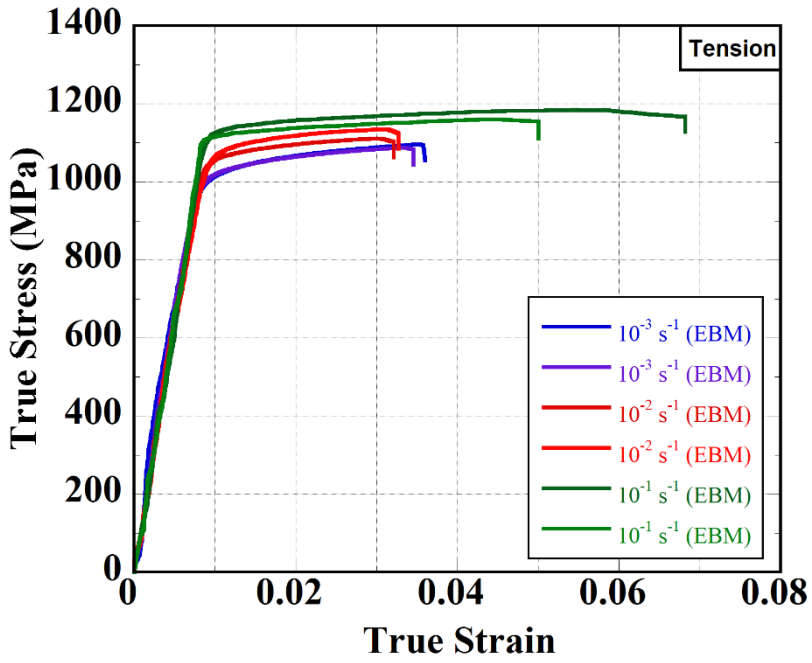

Figure 5.9. Comparative true stress-true strain curves EBM Ti64 at quasi-static strain rates.

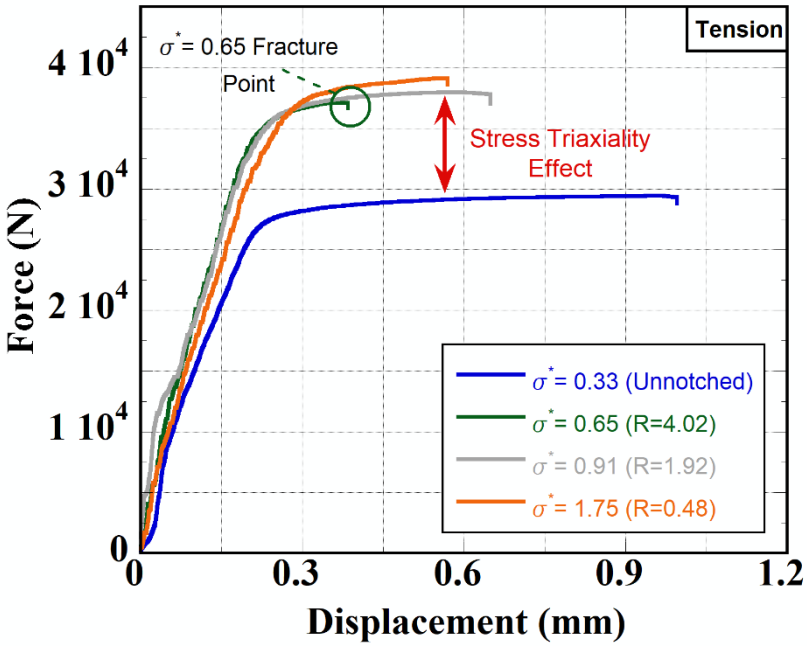

Figure 5.10. Load-displacement curves of notched and unnotched specimens.

The load-displacement curves of the notched specimens of different stress triaxiality (0.65, 0.91, and 1.75) at 10^{-3} s^{-1} are shown in Figure 5.10, together with that of an unnotched specimen at the same strain rate. As is seen in Figure 5.10, the load values of notched specimens are higher (around 8.7 kN), while the fracture strains are lower than those of unnotched specimens. The specimens with the stress-triaxiality of 0.65 have the lowest displacement. Notched specimens fractured in a similar brittle manner with unnotched specimens.

The pictures of test specimens at different strains until about the fracture are shown in Figure 5.11(a-d), sequential for the unnotched specimen and the specimens with 0.65, 0.91, and 1.75 stress triaxiality. The fracture of unnotched specimens occurs at different locations within the gage length, while all notched specimens fracture at the notch region. It is also clearly seen in Figure 5.11(a-d) that no necking forms in the specimens before the fracture.

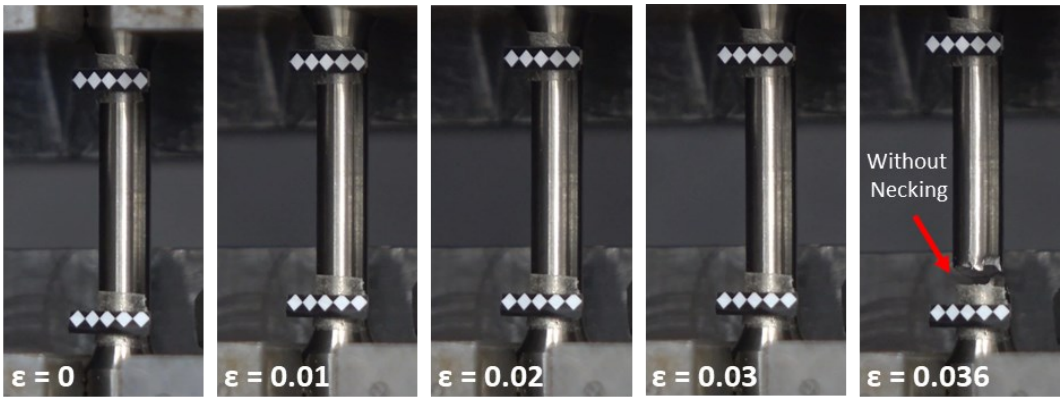

(a)

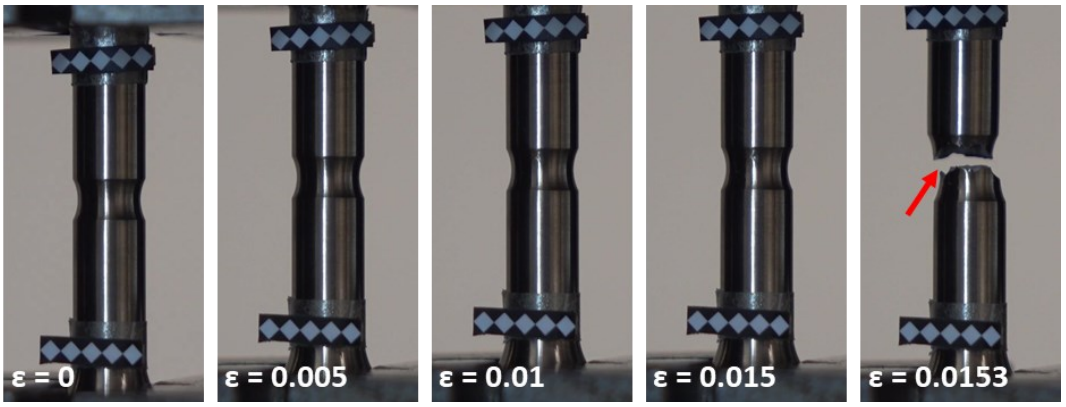

(b)

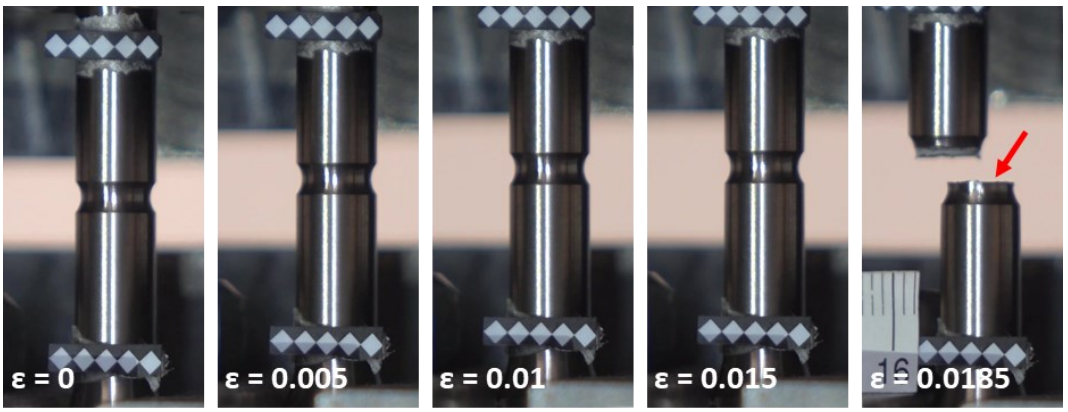

(c)

Figure 5.11. The pictures of the test specimens at different strains until about the fracture (a) unnotched and stress triaxiality of (b) 0.65, (c) 0.91, and (d) 1.75 range.

(cont. on next page)

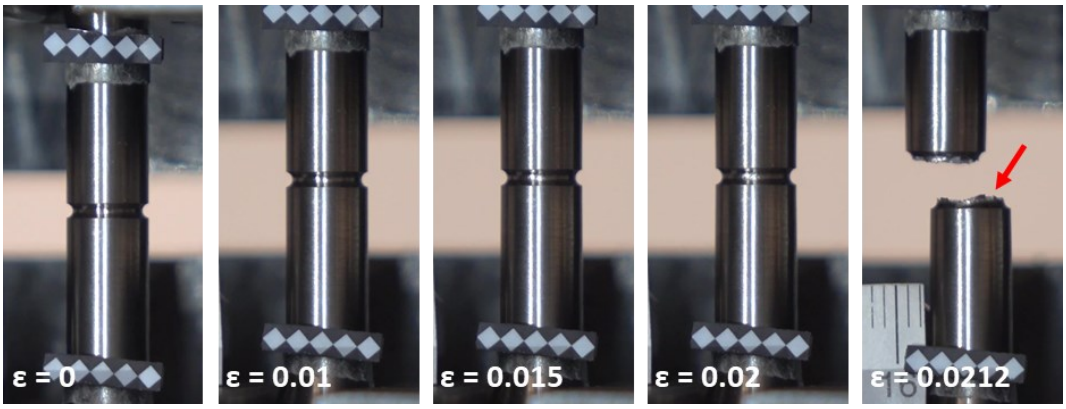

(d)

Figure 5.11. (cont.)

Table 5.6. Total strain, fracture strain, and reduction in the area at fracture values of EBM Ti64 tensile tests.

Stress Triaxiality	Strain Rate (s^{-1})	Total Strain (%)	Fracture Strain (%)	Reduction in Area (%)
0.33	10^{-3}	3.13 ± 0.71	5.90 ± 0.46	5.73 ± 0.45
0.33	10^{-2}	3.15 ± 0.15	6.01 ± 0.34	5.82 ± 0.37
0.33	10^{-1}	4.50 ± 2.59	7.40 ± 0.20	7.13 ± 0.18
0.65	10^{-3}	1.35 ± 0.15	4.47 ± 0.21	4.36 ± 0.20
0.91	10^{-3}	1.75 ± 0.26	4.63 ± 0.21	4.51 ± 0.19
1.75	10^{-3}	1.72 ± 0.37	3.60 ± 0.20	3.52 ± 0.19

The experimental strains of tensile tests are tabulated in Table 5.6 at different strain rates and stress triaxiality. The total strain in Table 5.6 was calculated by using the chance of the specimen length and the fracture strain was calculated by the change of area at the fracture site. As noted in the same table, length-based strain calculations result in extremely low values in comparison with the areal-based strain calculations. As the strain rate increases from 10^{-3} to 10^{-1} s^{-1}, the total strain, fracture strain, and reduction in cross-sectional area of unnotched specimen increase by 16.6%, 25.4%, and 24.4%, respectively. As expected, for the other triaxiality ranges, raise in stress triaxiality from 0.33 to 1.75 results in lower values by the reduction of 42.5% in total strain, 39% in fracture strain, and 38.5% in the cross-sectional area of the tested specimens. It should be noted that 0.65

range results exhibit perceptible discrepancies over the considered parameters in addition to load-displacement response previously stated using Figure 5.10.

The strain hardening of the plastic deformation of EBM-produced Ti64 is shown in Figure 5.12 at $1x10^{-3}$, $1x10^{-2}$, and $1x10^{-1}$ s^{-1}. The strain hardening (Θ) was calculated using the following relation [102]

$$\Theta = \frac{d\sigma_f}{d\varepsilon_{pl}} \tag{5.1}$$

An initial drop in the strain hardening is identified at all strain rates following a drop below 5 GPa (Figure 5.12). In the respective curves of the strain rates of 10^{-3} s^{-1} and 10^{-2} s^{-1}, a similar trend in the strain hardening is seen: the strain hardening and thermal softening continuously occur in a balanced manner at these strain rates. The thermal softening becomes effective after a plastic strain of 0.022 and the specimens tested at 10^{-2} and 10^{-3} s^{-1} fail at about 0.03 strain without exhibiting thermal softening. While adiabatic heating is detected at the 10^{-1} s^{-1} tests. At this strain rate, the specimen fracture after an ultimate strength as seen in Figure 5.9. When the true plastic strain increases to 0.045, thermal softening becomes more effective. The slip-driven plasticity culminates in a negative strain hardening rate, as opposed to that, the twinning-driven plasticity that causes a positive strain hardening rate. It can be stated that EBM-produced Ti64 exhibits mostly slip-driven deformation mechanism at the quasi-static strain rates, except the specimens tested at 10^{-1} s^{1}. As shown by a circle in Figure 5.12, after 0.22 strain, the slope of the strain hardening curve at 10^{-1} s^{1}starts to increase. This may signal the onset of twinning.

The strain rate sensitivity (SRS) parameter (m) is given as [103]

$$m = \frac{d\log\sigma}{d\log\dot{\varepsilon}} \tag{5.2}$$

Figure 5.13 shows the logarithm of yield stress and the flow stress at 0.01, 0.015, and 0.02 as a function of the logarithm of strains rate. The slopes of linear fits to the stresses

in the same figure give the value of *m*. Comparatively a higher value of *m*, 0.0352, is found for the yield strength. In the plastic region, the SRS parameter decreases with increasing strain and reaches the lowest value of 0.0153 at around 0.02 strain.

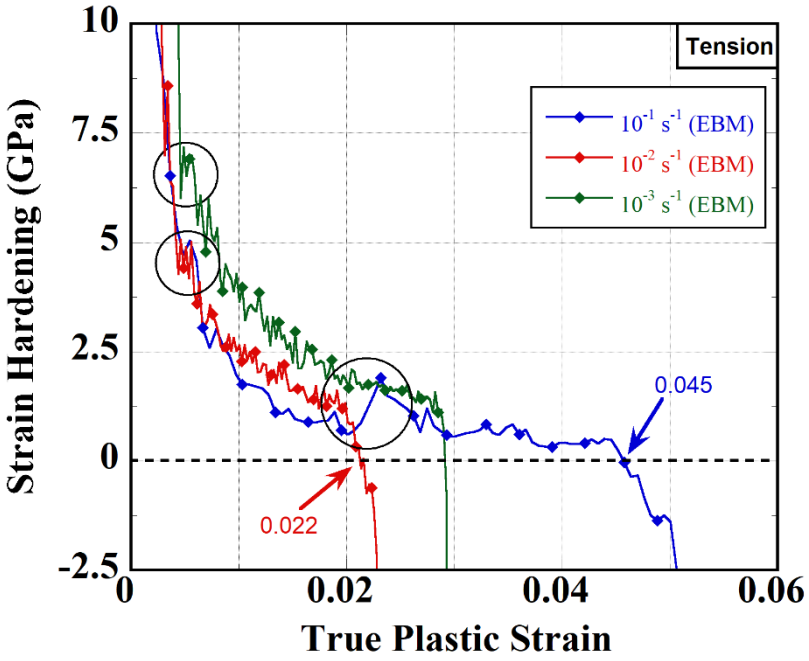

Figure 5.12. Representative strain hardening curves at $1x10^{-3}$, $1x10^{-2}$, and $1x10^{-1}$ s^{-1}.

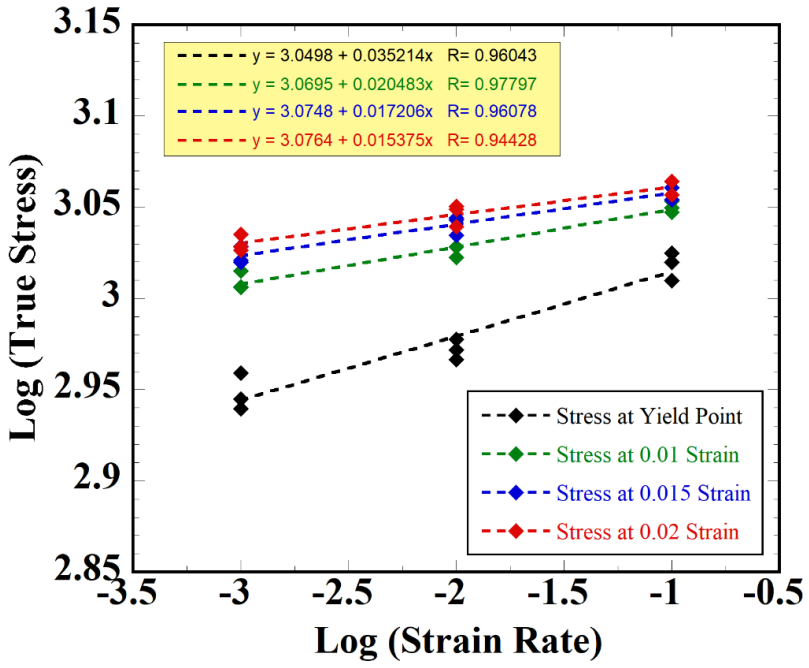

Figure 5.13. Strain rate sensitivity of EBM Ti64 at quasi-static strain rates.

5.4.2. Compression Tests

Compression true stress-true strain curves of EBM Ti64 at $1x10^{-3}$, $1x10^{-2}$, and $1x10^{-1}$ s^{-1} are shown in Figures 5.14(a-c), respectively. Three compression stress-strain curves at $1x10^{-3}$ s^{-1} and two compression stress-strain curves at $1x10^{-2}$ and $1x10^{-1}$ s^{-1} are very similar to each other as seen in Figures 5.14(a-c). EBM-produced Ti64 specimens deform under compression firstly elastically and then plastically and finally the compression specimen fracture by forming deformation shear bands diagonal to the loading axis. The representative true stress-true strain curves at $1x10^{-3}$, $1x10^{-2}$, and $1x10^{-1}$ s^{-1} are shown in Figure 5.15 altogether. As with the tension test, the compression tests yield, and ultimate strengths are seen strain rate sensitive. As the strain rate increases from 10^{-3} s^{-1} to 10^{-1} s^{-1}, the yield strength and ultimate strength increase by 17.9 and 2.1%, respectively. The average yield strengths were sequentially 889 MPa ± 10.8 MPa, 980 MPa ± 9.9 MPa, and 1048 MPa ± 37.5 MPa at $1x10^{-3}$, $1x10^{-2,}$ and $1x10^{-1}$ s^{-1}. The average ultimate strengths were 1448 MPa ± 13.5 MPa, 1480 MPa ± 25.2 MPa, and 1462 MPa ± 1 MPa at $1x10^{-3}$, $1x10^{-2}$, and $1x10^{-1}$ s^{-1}, respectively. The fracture strain also increases with increasing strain rate. The average failure strains were 33.6% ± 2.86, 35.60% ± 1.56 and 50.75% ± 3.75 at $1x10^{-3}$, $1x10^{-2}$, and $1x10^{-1}$ s^{-1}, respectively. The highest failure strain increase at 10^{-1} s^{-1} confirms the effect of adiabatic heating at this strain rate (Figure 5.15). The compression true stress-strain curves of the samples with different L/D ratios are shown in Figure 5.16.

The pictures of deforming compression test specimens at different strains with the L/D ratios of 0.8, 1, 2, and 3 are further shown in Figure 5.17(a-d), respectively. Test specimens with L/D ratios 0.8 and 1 deform homogenously until shear fracture (Figure 5.17(a-b)), while the specimens with the L/D=2 and 3 show bending deformation (Figure 5.17(c-d)), leading to lower failure strains (Figure 5.16). As the L/D ratio increases from 0.8 to 3, both the compressive strength and failure strain decrease as seen in Figure 5.16. However, the yield strength is not significantly affected by the L/D ratio.

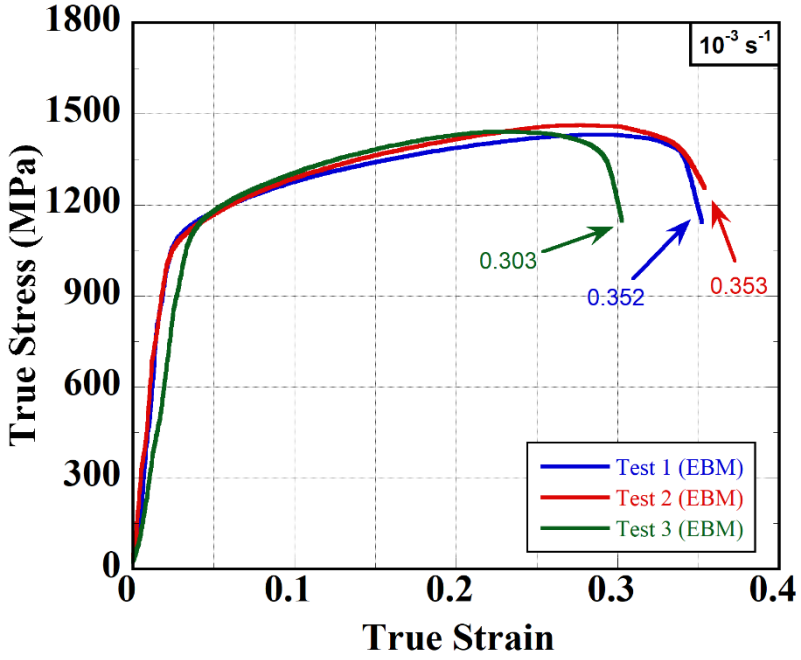

(a)

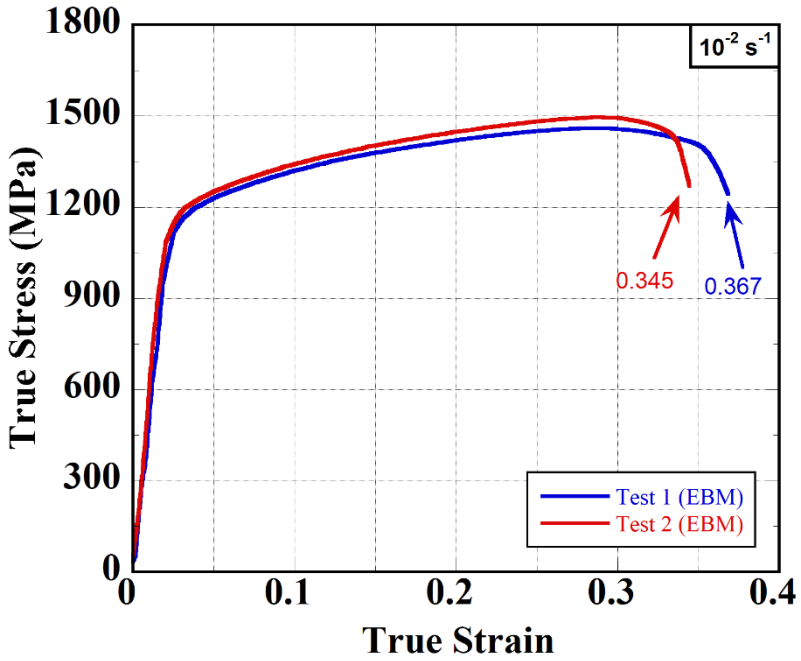

(b)

Figure 5.14. Compression true stress-true strain curves of EBM Ti64 at (a) $1x10^{-3}$, (b) $1x10^{-2}$, and (c) $1x10^{-1}$ s^{-1}.

(cont. on next page)

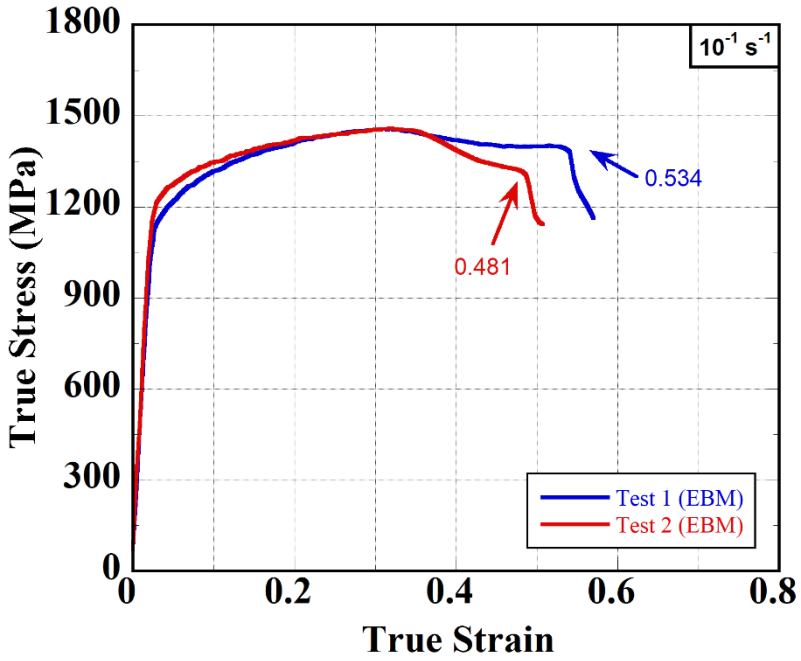

(c)

Figure 5.14. (cont.)

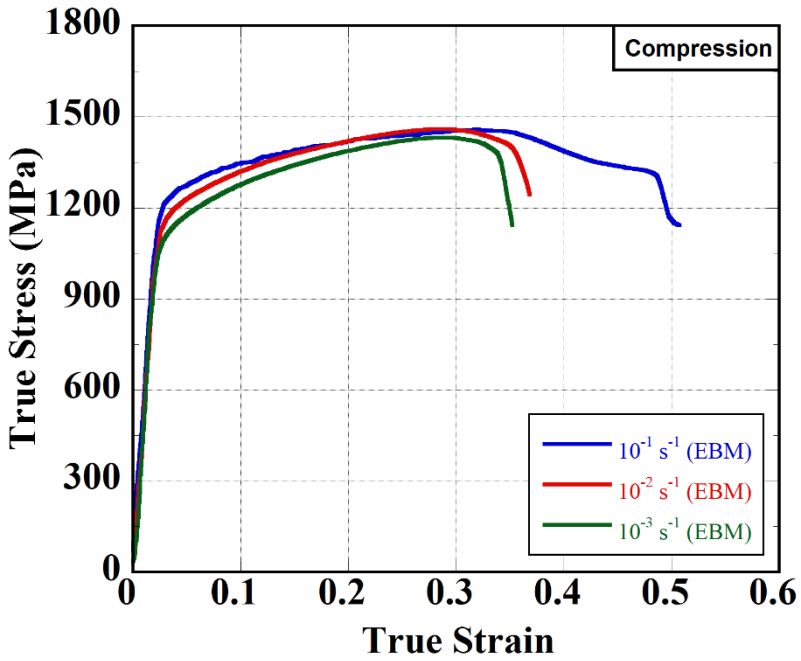

Figure 5.15. Representative true stress-true strain graph for compression tests of EBM Ti64 at the quasi-static rates.

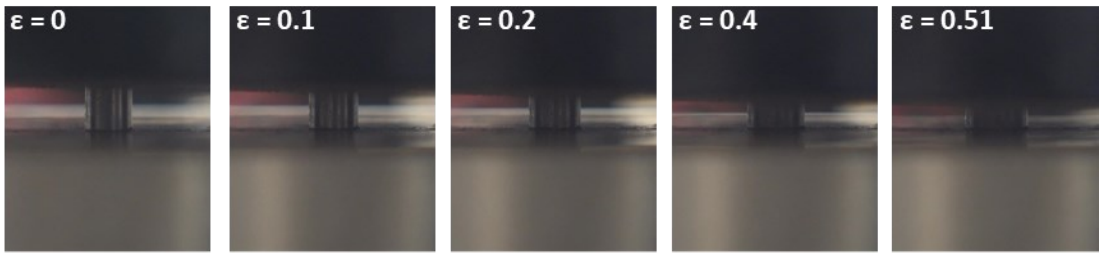

(a)

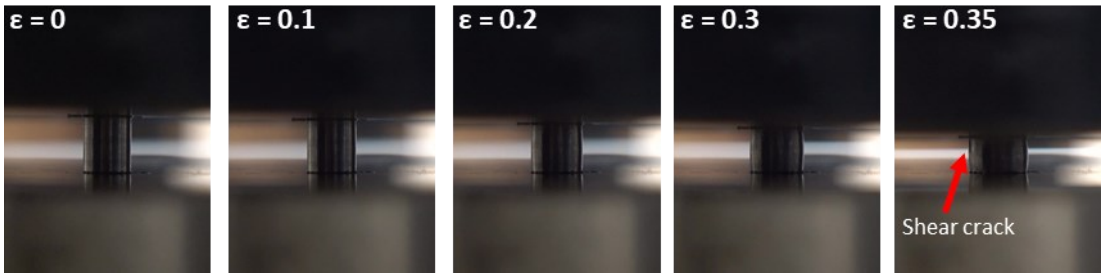

(b)

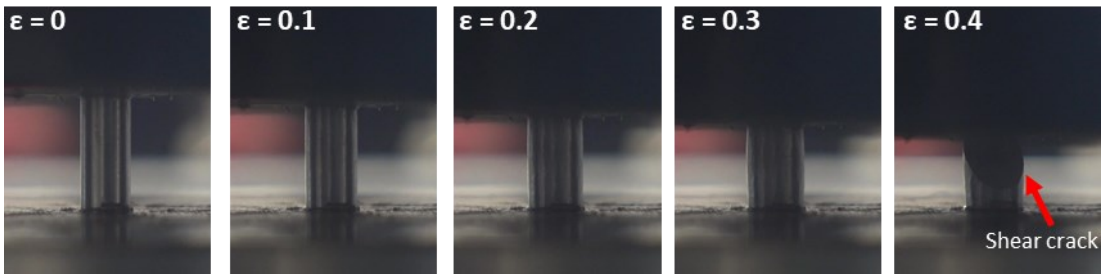

(c)

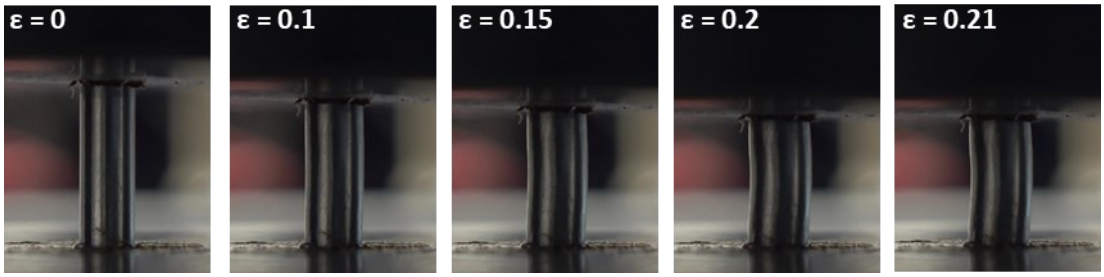

(d)

Figure 5.16. The pictures of deforming compression test specimens at different strains with the L/D ratios of (a) 0.8, (b) 1, (c) 2, and (d) 3.

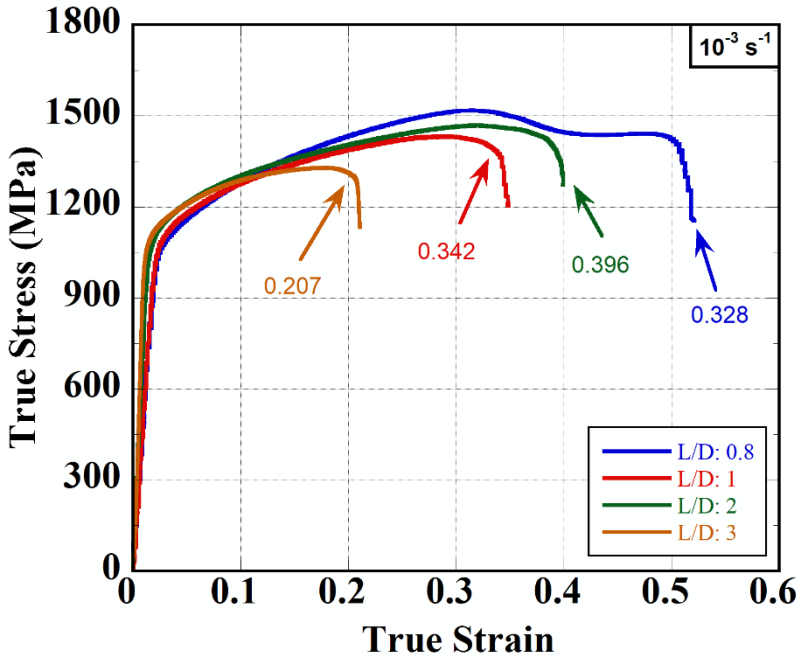

Figure 5.17. True stress-true strain curves of compression tests at 10^{-3} s^{-1} and different L/D ratios.

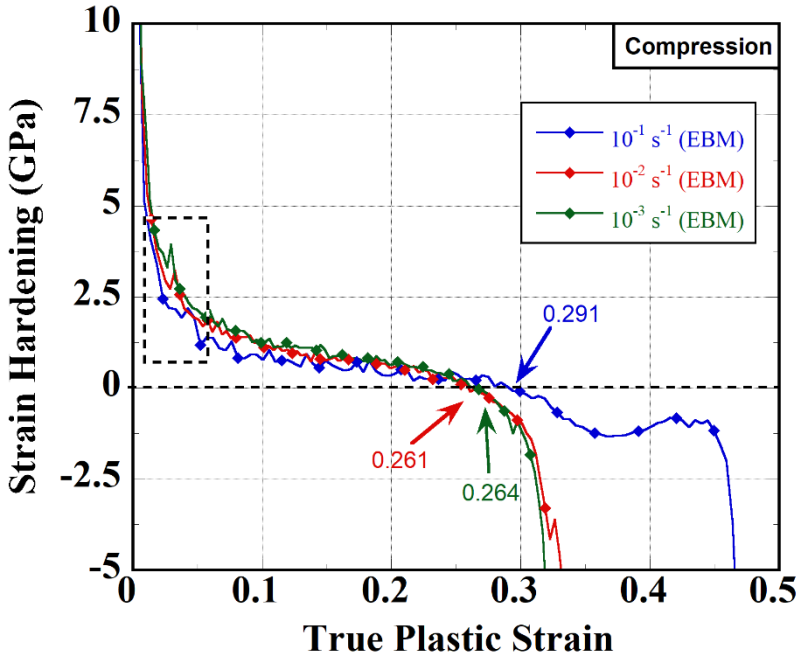

Figure 5.18. Representative figure for strain hardening behaviors under quasi-static compression tests at strain rates of $1x10^{-3}$ s^{-1},$1x10^{-2}$ s^{-1}, and $1x10^{-1}$ s^{-1}.

The strain hardening curve of EBM-produced Ti64 under quasi-static compressive loadings is shown in Figure 5.18 at three quasi-static strain rates. The hardening rate starts to descend under 5 GPa and shows a plateau region between 2.5 GPa and 0 GPa. The failure and/or thermal softening process is activated when the plastic strains meet the threshold level at 0.261, 0.264, and 0.291 for the strain rates of 10^{-3} s^{-1}, 10^{-2} s^{-1}, and 10^{-1} s^{-1}, respectively. The adiabatic heating is seen at 10^{-1} s^{-1} as the increased failure strain. EBM-produced Ti64 plastically deforms via mostly slip-driven mechanisms.

Figure 5.19 shows the logarithm of yield stress and the flow stress at 0.1, 0.15, and 0.2 as a function of the logarithm of strains rate. Comparatively a higher value of *m*, 0.036, is found for the yield strength as with the tension test. This value is very much like the one determined for the tension test (0.0352). As the strain increases, the value of *m* decreases significantly. It reduces to 0.014 at a strain of 0.05, which is comparable with the one (0.015) determined in tension at a strain of 0.02.

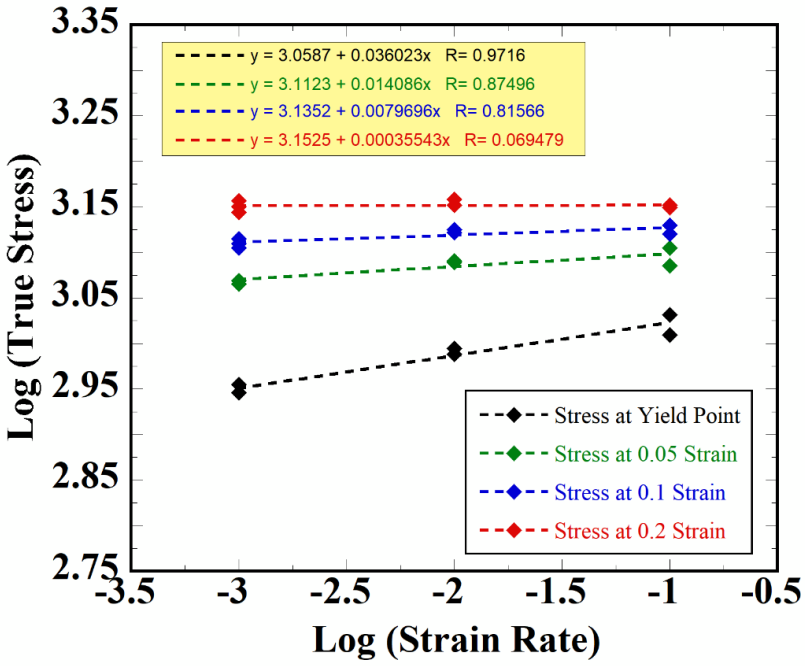

Figure 5.19. Strain rate sensitivity on the compression response of EBM Ti64.

5.5. High Strain Rate Tests

Typical voltage-time graphs of SHPB tests at different gas gun pressures are shown in Figure 5.20. As the gas gun pressure increases from 2 to 6, and 8, the magnitude of the incident and reflected waves increases, showing higher strain rates on the tested sample as the pressure increases.

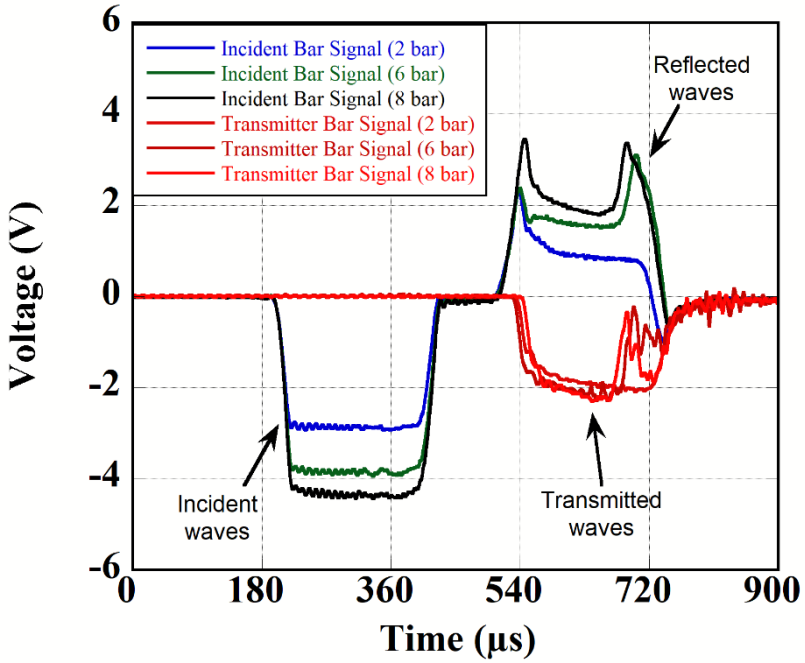

Figure 5.20. Voltage-time histories of SPHB tests of EBM Ti64 at the pressures of 2, 6, and 8 bars.

The true stress-true strain curves obtained from the SHPB tests at the gas gun pressures of 2,6, and 8 bar are shown in Figure 5.21(a-c), respectively. The variations of the true-strain rate with true-strain are also shown in the same figures. As marked in Figure 5.21(a-c), the average strain rate was determined as 605 s^{-1} for 2 bar tests, 1331 s^{-1} for 6 bar tests, and 2154 s^{-1} for 8 bar tests. The average yield strength of EBM-produced Ti64 specimens was determined 1222 MPa ± 35 MPa, 1227 MPa ± 69.5 MPa, and 1404 MPa ± 38 MPa at 605, 1131, and 2154 s^{-1}, respectively. The ultimate compression strengths were sequentially 1518 MPa ± 38 MPa, 1605 MPa ± 65.2 MPa, and 1480 MPa ± 46 MPa at 605, 1131, and 2154 s^{-1}. The specimens tested at 605 s^{-1} did not fracture during the tests (Figure 5.22(a)), while shear crack formations are visible in the specimens

tested at 1131 s^{-1}, and 2154 s^{-1}, starting at 4.4% and 5.1% strains, respectively (Figure 5.22(c-d)). Eventually, total strains are 17.7% ± 1.3%, and 29.1% ± 3.4% at 1131 s^{-1} and 2154 s^{-1}, respectively. The highest strain at 605 s^{-1} is about 12% ±1%.

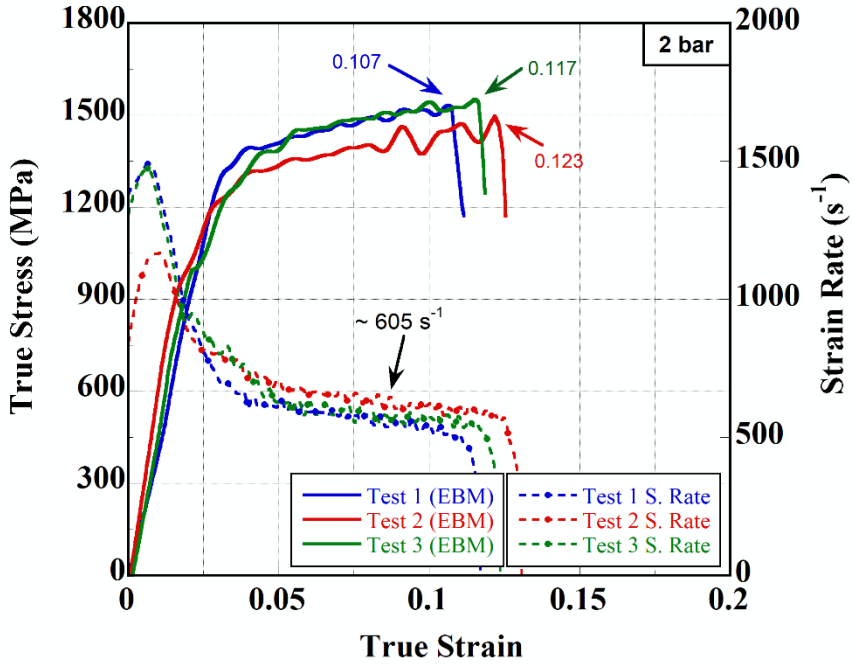

(a)

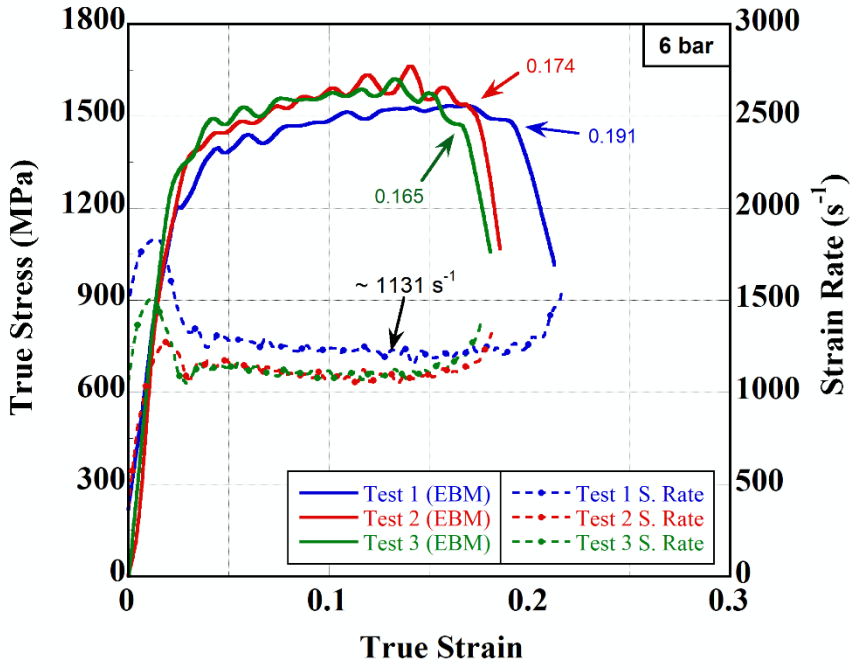

(b)

Figure 5.21. The true stress-true strain and true strain rate-true stress curves of the specimens tested with the gas gun pressure (a) 2, (b) 6, and (c) 8 bar.

(cont. on next page)

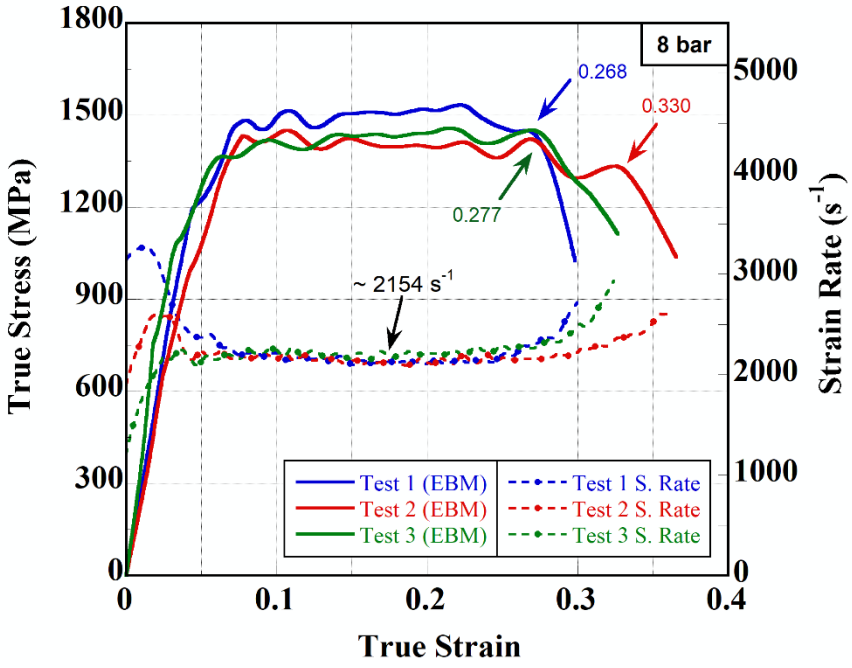

(c)

Figure 5.21. (cont.)

The representative true stress-true strain and true strain rate-true stress and strain hardening-true strain curves at different strain rates are shown in Figure 5.23(a-b). The yield and ultimate strength increase with increasing strain rate by 14.8% and 5.8%, respectively. However, ultimate strength starts to decrease as the strain rate exceeds 1131 s^{-1}. The reduced ultimate strength above 1131 s^{-1} is due to the thermal softening induced by adiabatic heating. Additionally, relatively high ductile behavior under the 2154 s^{-1} rate might be attributed to the consequence of the thermal softening rooted in adiabatic heating. An initial drop in strain hardening within elastoplastic transition is also identified in the high strain rate response of EBM-produced Ti64 (Figure 5.23(b)). In contrast to quasi-static range tests, twinning deformation is found to be more prone to occur at high-rate tests. Nevertheless, the flow behavior of EBM-produced Ti64 consists of both slip-driven and twinning deformation until the initiation of thermal softening. As indicated by arrows in Figure 5.23(b), the thermal softening process becomes dominant when the plastic strain values reach 0.080, 0.134, and 0.141 for the strain rates of 605 s^{-1}, 1131 s^{-1}, and 2154 s^{-1}, respectively. Also noted in the same figure, strain hardening, and thermal softening proceed in a balanced manner in the excessive strain rates.

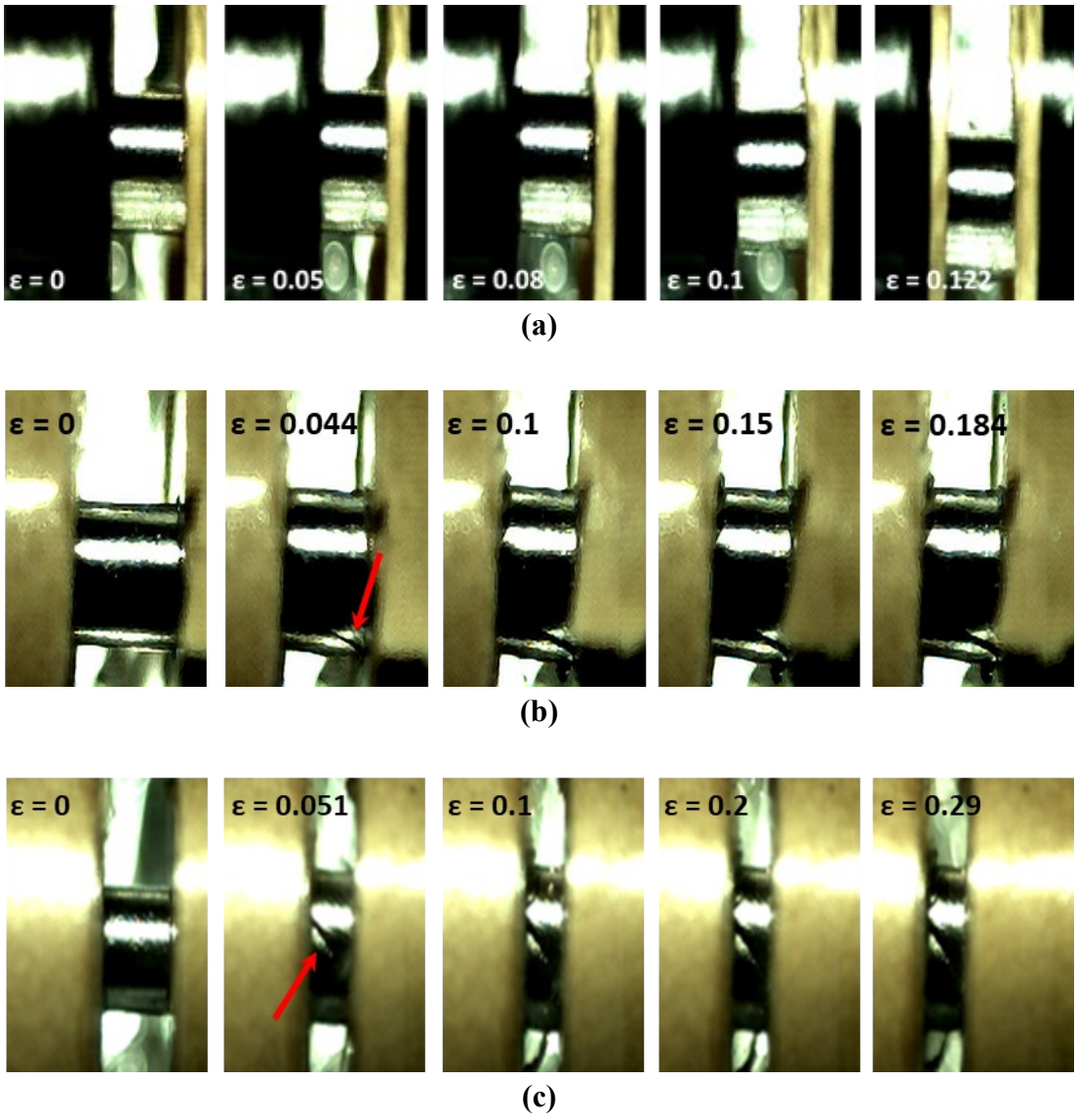

Figure 5.22. The deformation pictures of the specimens (at different strains) tested at (a) 605, (b) 1131, and (c) 2154 s^{-1}.

EBM-produced Ti64 shows strain rate sensitive flow stress behavior also under high strain rate loadings. Figure 5.24 shows the logarithm of yield stress and the flow stress at 0.1, 0.15, and 0.2 as a function of the logarithm of both quasi-static and high strain rates. The SRS parameters based on yield strength are again highest as compared with those based on flow stress at 0.05, 0.1, and 0.2 strains combined with the quasi-static strain rates. It can generally be interpreted that, increase in strain rate becomes less effective on the strain rate sensitivity of EBM-produced Ti64 at increasing strains. More precisely, in the marked region indicated by dotted lines, excessive strain rate regimes

extremely lessen the strain rate sensitivity as the considered points in the figure are taken place in almost the same stress levels.

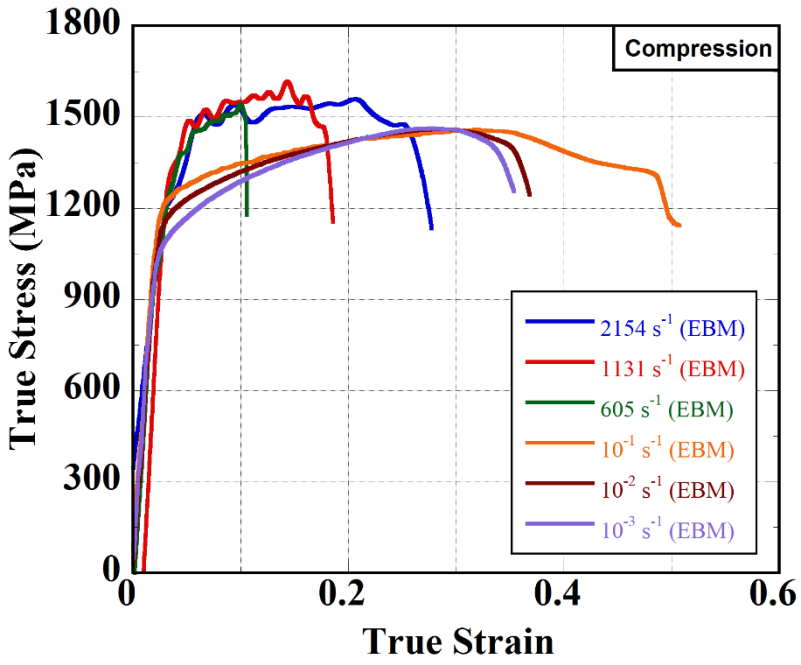

(a)

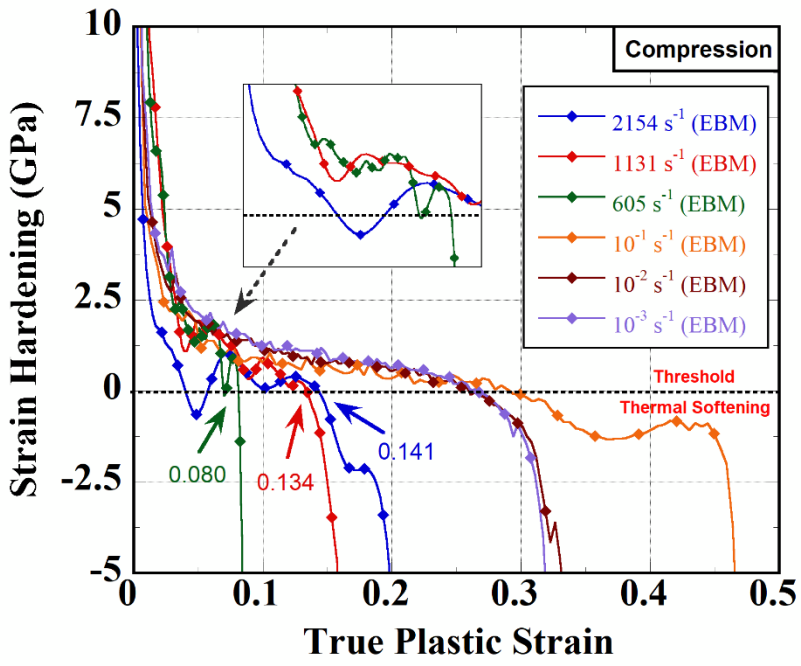

(b)

Figure 5.23. The representative (a) true stress-true strain and true strain rate-true stress and (b) strain hardening-true strain curves at different strain rates.

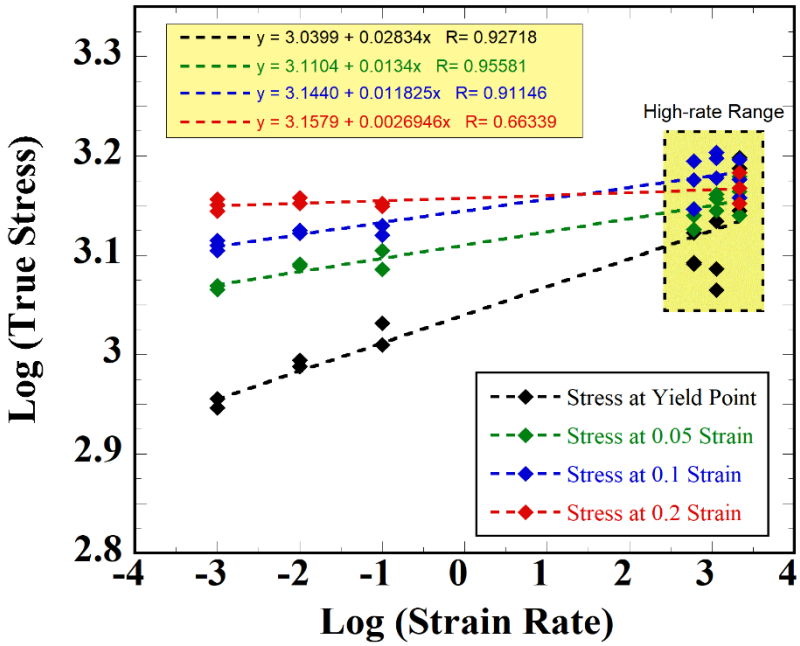

Figure 5.24. Strain rate sensitivity of the compression response of EBM Ti64 considering both quasi-static and high strain rates.

5.6. Fracture Surface Analysis

SEM micrographs of the fracture surfaces of the tensile tested EBM-Ti64 specimens at different magnifications are shown in Figures 5.25 through 5.28. The fracture surfaces of tested EBM-Ti64 tensile specimens are composed of brittle and ductile regions as marked by A and B in Figure 5.25(b). The flat fracture surface of brittle regions resembles a cleavage-like crack progression. The brittle fracture is most likely resulted from the defects in the as-built specimens, mostly from the lack of fusion regions as explicitly seen in Figure 5.26. As revealed in the same figure, non-melted and partially melted powders are highly seen inside the lack of fusion defects and the amount of these powders is considerably high in some regions.

On the other hand, the lack of fusion defects are generally identified near the outer wall of the tensile specimens. They are found to be initiators of the crack progression process and ultimate fracture of the tensile specimens due to their irregular and imperfect shapes. It should be noted that the dimensions of these defects are substantially wide as seen in Figure 5.27.

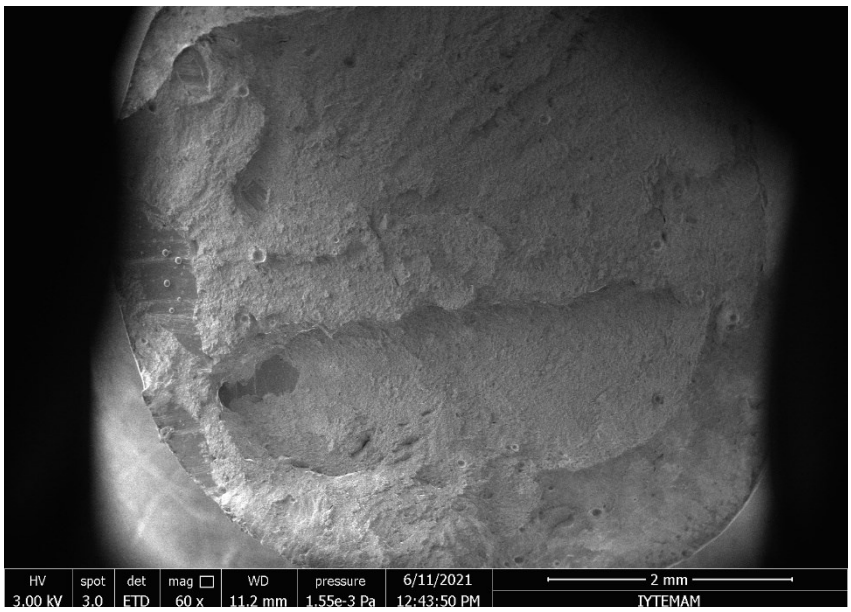

(a)

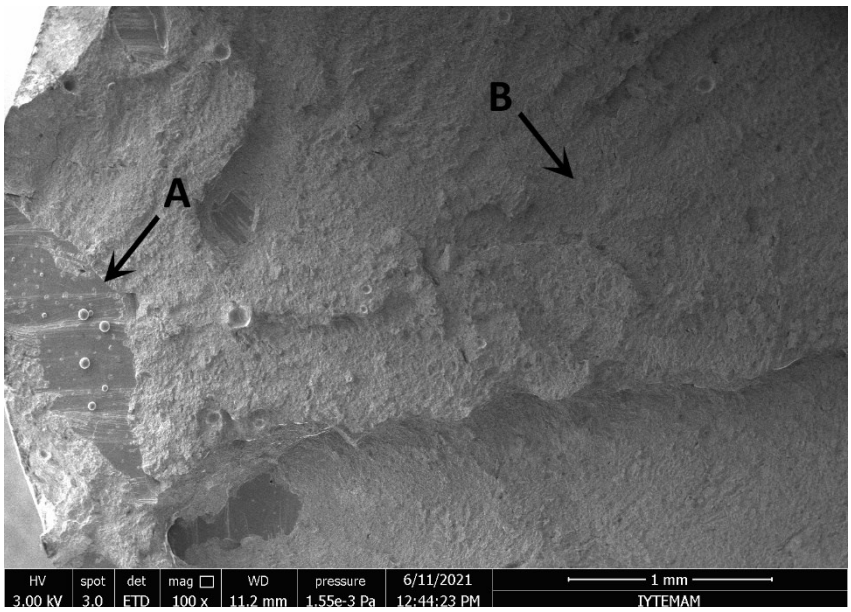

(b)

Figure 5.25. SEM images of fracture surfaces of EBM Ti64 tensile specimens (a) exact surface view at 60x magnification (black edges due to ETD detector limits), and (b) at 100x magnification.

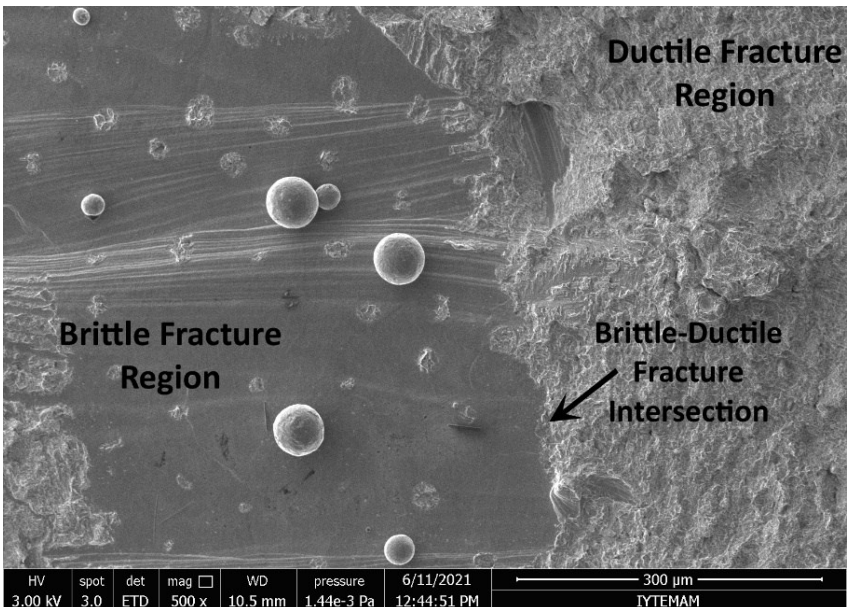

(a)

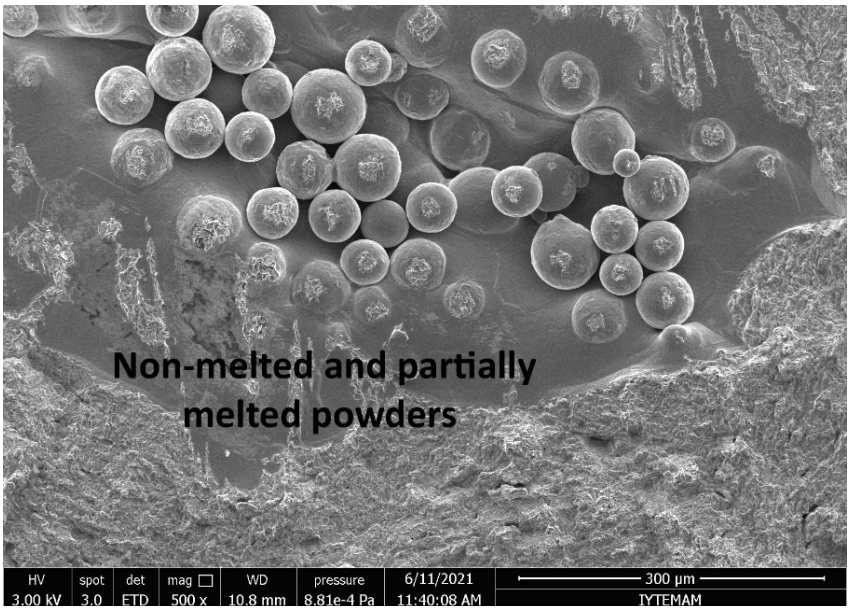

(b)

Figure 5.26. Magnified SEM images of (a) ductile and brittle fracture zones, and (b) non-melted and partially melted powders existing in the vicinity of brittle fracture regions of EBM Ti64 tensile specimens.

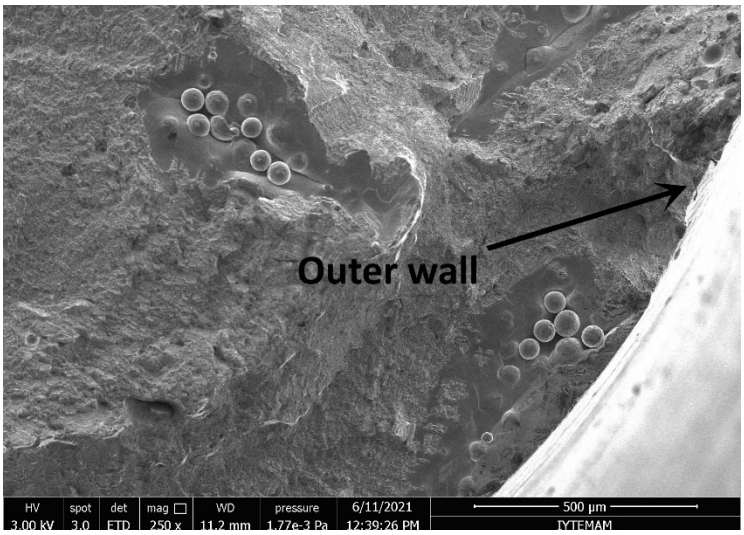

Figure 5.27. Location of lack of fusion defects on the fracture surface of EBM-Ti64 tensile specimens.

The ductile fracture region of EBM-produced Ti64 is composed of dimples as seen in Figure 5.28 and small particles are seen inside these dimples (Figure 5.28(b)). The material around the rigid particles is highly elongated, debonded, and finally separated under tensile loads, leaving small ridged particles inside the dimples. The reduced dimple size in the fracture surface of EBM-produced Ti64 seen in Figure 5.28(b) and (c) confirms a finer microstructure development in EBM-produced Ti64, resulting from relatively high cooling rates in the EBM process.

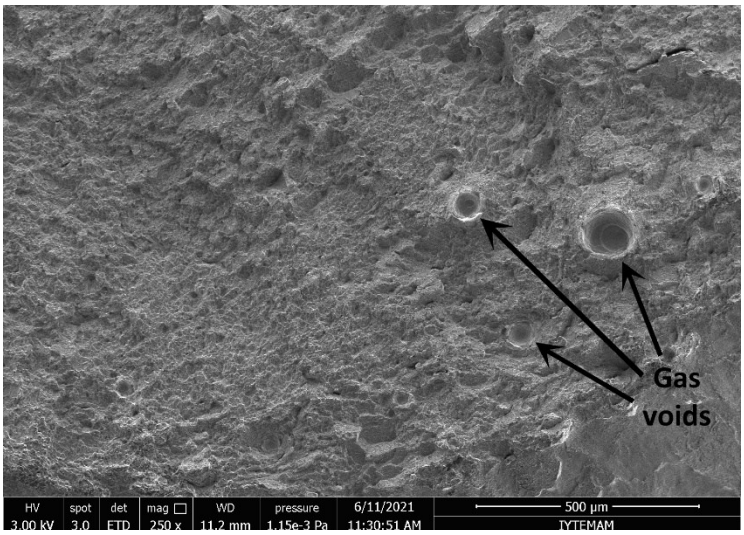

(a)

(cont. on next page)

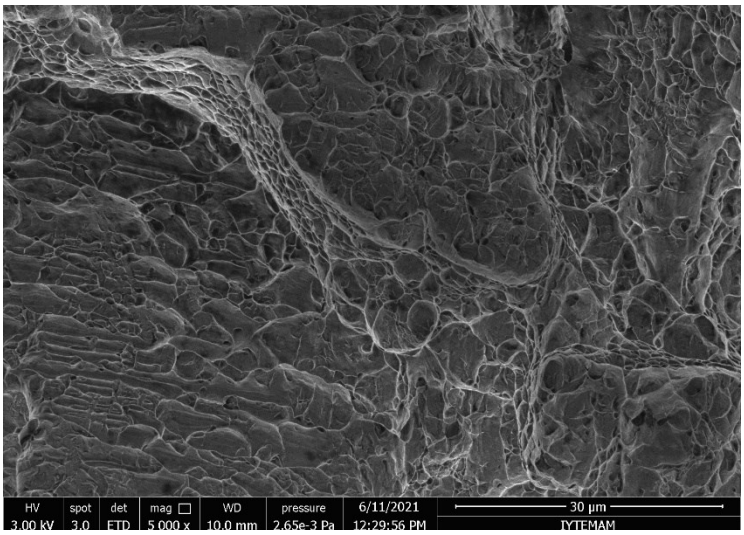

(b)

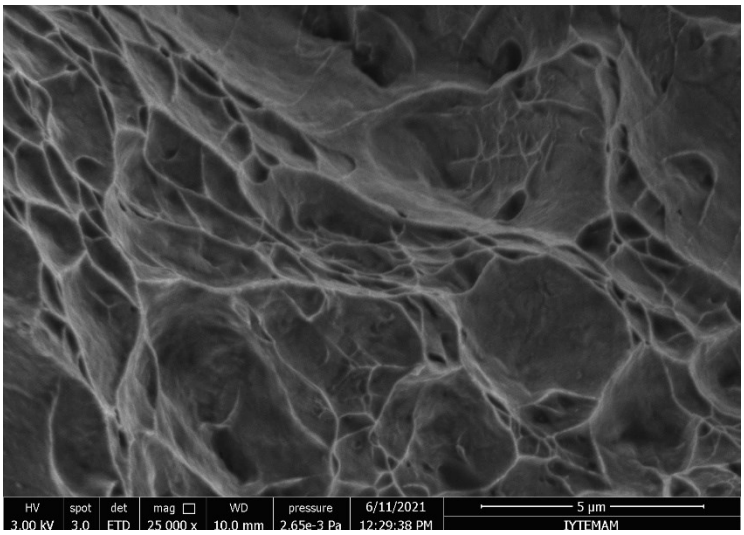

(c)

Figure 5.28. SEM images of ductile fracture regions of tested EBM-produced Ti64 tensile specimens (a) dimples and gas voids in the vicinity at 250x, (b) dimples at 5000x, and (c) dimples at 25000x.

SEM micrographs of the fracture surfaces of the tested EBM-Ti64 compression specimen at different magnifications are shown in Figure 5.29 and Figure 5.30. EBM-Ti64 undergoes failure by forming shear bands that propagate diagonal to the loading direction. A large ductility reduction is seen in the tensile stress-strain curve of EBM-produced Ti64 as the tensile loads tend to open these defects, while compressive loads tend to close these defects, leading to a relatively small reduction in the compression ductility. As the large strains are achieved for EBM-produced Ti64 under compressive

loadings, shear band formation is likely to occur where the intensive shear stress localization reached Figure 5.29 illustrates the presence of shear dimples and smeared surfaces throughout the shear plane at low and high magnifications. Smeared surfaces are formed by abrasion under frictional force due to sliding of the separated parts of the tested specimen on each other during the compression test. As seen in Figure 5.30, shear dimples have small sizes similar to tensile dimples. It might be attributed to none or low-level thermal softening occurrence in the quasi-static region as the high thermal softening increases the viscous flow of the material under excessive loading conditions.

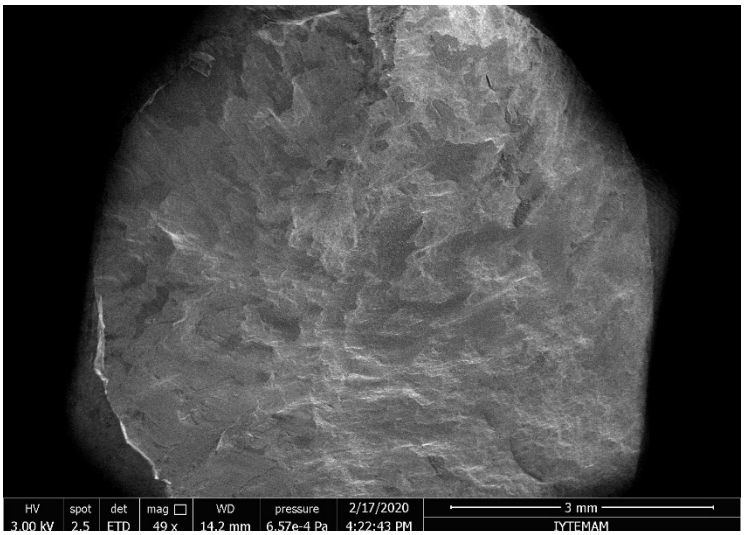

(a)

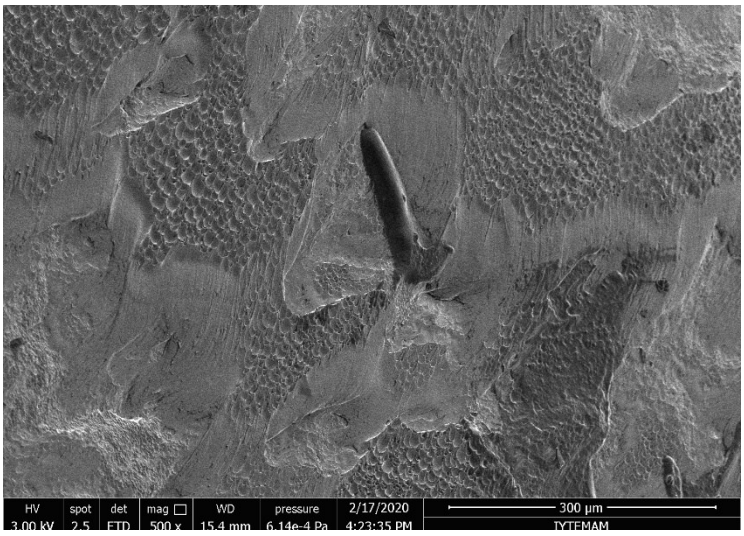

(b)

Figure 5.29. SEM images of the fracture surface of EBM-produced Ti64 compression test specimen (a) exact surface view (black edges due to EDT detector limits), and (b) shear dimples and smeared regions.

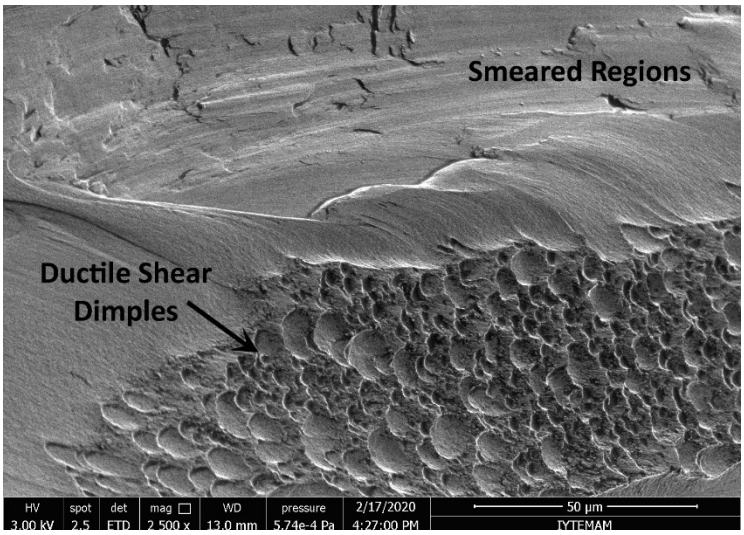

Figure 5.30. A detailed view of ductile shear dimples and smeared regions of EBM-produced Ti64 compression specimen.

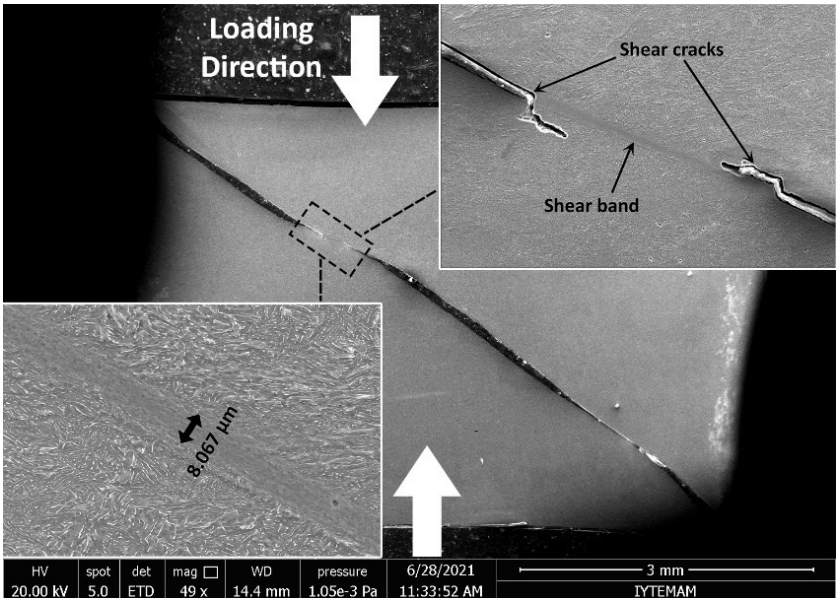

Figure 5.31. View of shear band in EBM-produced Ti64 formed during the quasi-static compression test.

Shear band formation in both quasi-static and high rate conditions is sequentially illustrated in Figure 5.31 and Figure 5.32. Although the quasi-static specimen is almost completely fractured by the shear band, the high rate specimen exhibits microcracks in other regions in addition to the shear band. It is seen that the shear band width for the quasi-static test is considerably smaller than the one for the high-rate test. Wider shear

band formation is likely due to the thermal softening as a consequence of adiabatic heating around 150 °C under the high-rate loadings. Thermal softening also facilitates the initiation and propagation of microcracks and voids in the stress-induced regions.

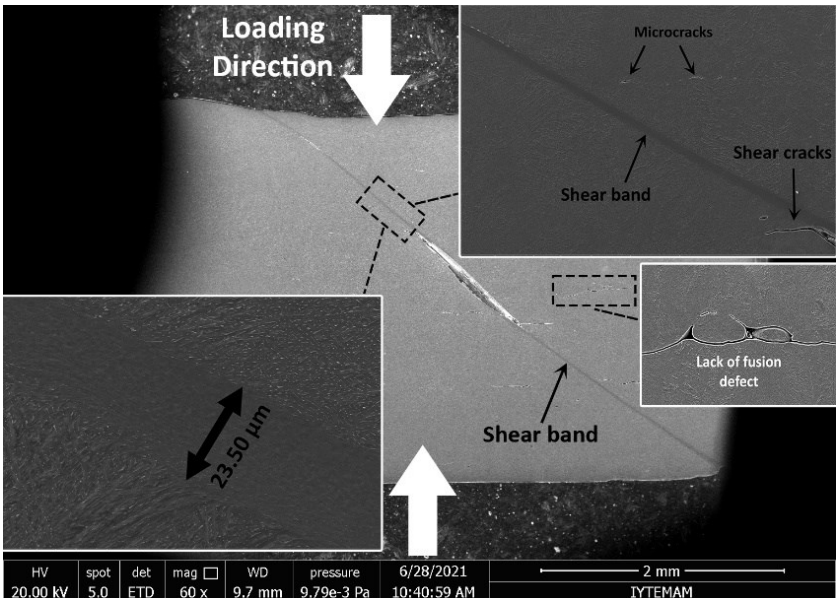

Figure 5.32. View of shear band in EBM-produced Ti64 formed during the high-rate compression test.

CHAPTER 6

DETERMINATION OF PARAMETERS OF JOHNSON-COOK MATERIAL MODELS FOR EBM Ti6Al4V

6.1. Determination of JC Strength Model Parameters

In this section, the determination of JC strength model parameters previously given as formulation in Equation 3.4 will be carried out in detail. Thereafter, calibrated parameters will be tabulated with other related material parameters in Section 6.3.

6.1.1. Determination of A, B, and n parameters

Determination of first bracket parameters of JC strength model for EBM-produced Ti64 using direct curve fitting and linear regression techniques on tension data are shown in Figures 6.1 and 6.2, respectively. Since A parameter stands for yield stress, it was taken from the initial point at where the slope of the curve shows excessive decrease at the end of the elastic region, just before the elastoplastic transition starts. In order to increase the accuracy of the direct curve-fitting technique, 0.2% offset yield stress was not considered due to causing inconsistency in the logarithmic fitting process. A parameter was accepted as the lowest yield stress among the tension tests data for both tension and compression response of the EBM-produced Ti64. To find out B, and n parameters, plastic flow data between the endpoint of the elastoplastic region and ultimate strength points were selected to apply curve-fitting techniques. Additionally, for the linear regression technique, the natural logarithm of both true flow stress and true plastic strain data were taken then the linear fitting process was applied. It should be mentioned that three test data from both tension and compression were processed individually, thereafter average values of B, and n parameters were calculated. After completing these procedures, A, B, and n parameters for tension were sequentially found as 868 MPa, 460.02 MPa, and 0.1899 from direct-curve fitting and 868 MPa, 469.39 MPa, and 0.1945 from linear regression technique.

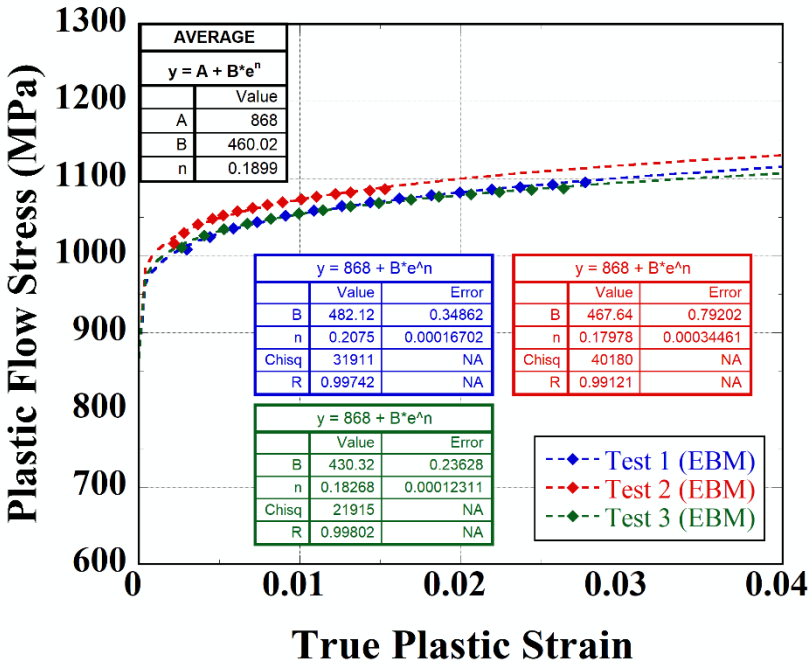

Figure 6.1. Determination of A, B, and n parameters using direct-fitting on true flow stress-true plastic strain data of EBM-produced Ti64 from tension tests.

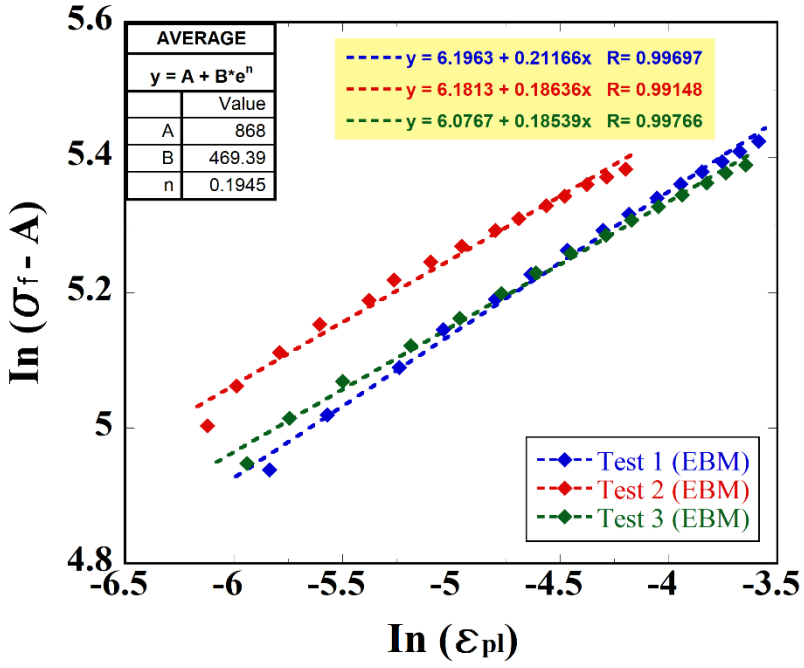

Figure 6.2. Linear regression technique on the determination of A, B, and n parameters from tension tests of EBM-produced Ti64.

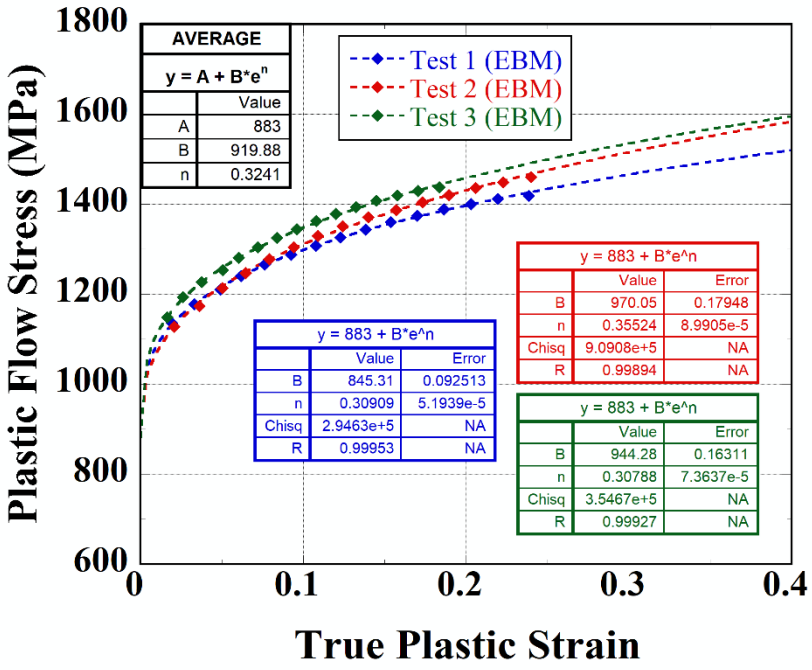

Figure 6.3. Determination of A, B, and n parameters using direct-fitting on true flow stress-true plastic strain data of EBM-produced Ti64 from compression tests.

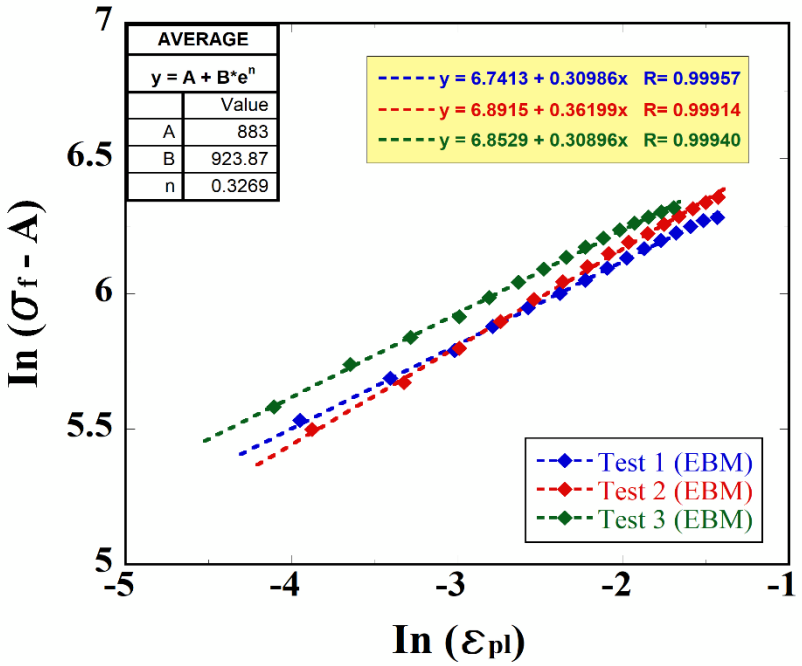

Figure 6.4. Linear regression technique on the determination of A, B, and n parameters from compression tests of EBM-produced Ti64.

Determination of A, B, and n parameters from compression response of EBM-produced Ti64 using direct curve fitting and linear regression techniques are shown in Figure 6.3 and Figure 6.4, respectively. Same determination procedures that were applied on tension response were carried out for the compression response as well. Thereafter, A, B, and n parameters from compression data were sequentially found as 883 MPa, 919.88 MPa, and 0.3241 using direct-curve fitting and 883 MPa, 923.87 MPa, and 0.3264 using linear regression technique. It is seen that calibrated parameters from both tension and compression are consistent with each other for these fitting techniques.

6.1.2. Determination of C parameter

Determination of C parameter of JC strength equation based on tension and compression behavior at different strain rates are illustrated in Figure 6.5 and Figure 6.6, respectively. For the tension behavior, test data of solely quasi-static strain rates from 10^{-3} s^{-1} to 10^{-1} s^{-1} were processed to calibrate C parameter while both quasi-static and high-rate tests ranging from 10^{-3} s^{-1} up to 2154 s^{-1} were considered for compression behavior.

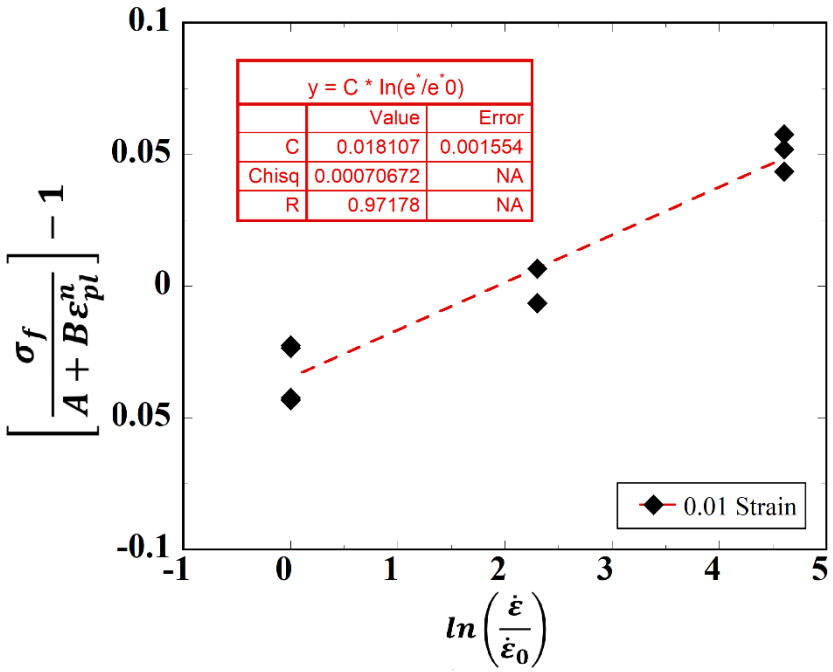

Figure 6.5. Determination of C parameter for tension response of the EBM-produced Ti64.

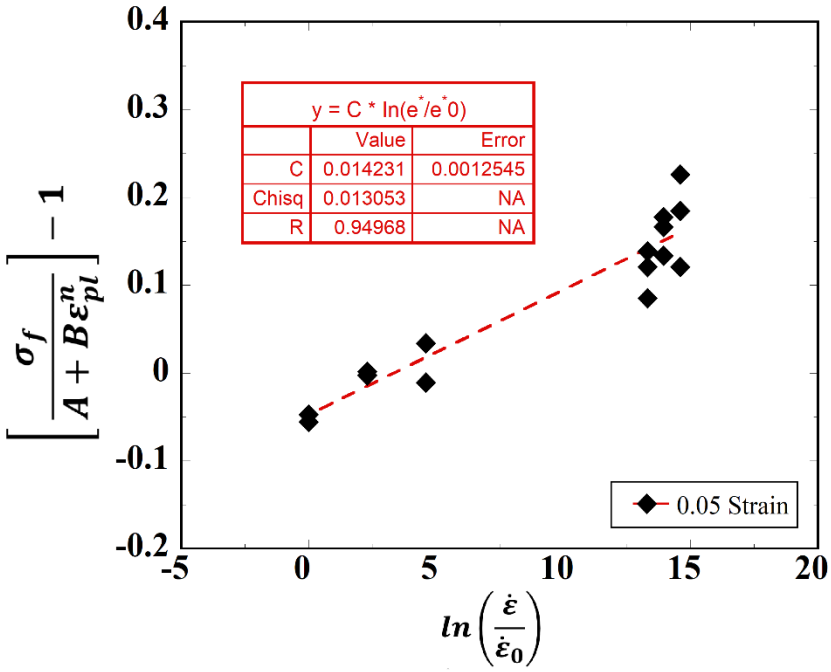

Figure 6.6. Determination of C parameter for compression response of the EBM-produced Ti64.

In order to accurately calibrate the strain rate parameter, appropriate strain values in the tension and compression flow behaviors were selected considering the avoidance of the stress oscillations during the elastoplastic transition and thermal softening due to adiabatic heating. Therefore, strain values for the calibration process were taken as 0.01 and 0.05 for tension and compression behaviors, respectively. After applying linear curve-fitting, C parameters were found as 0.0181 and 0.0142 for tension and compression behaviors of EBM-produced Ti64, respectively.

6.1.3. Determination of m parameter

Due to the unavailability in testing the EBM-produced Ti64 specimens at the elevated temperatures between 900–1300 °C, required data for determination of temperature parameter (m) of the JC strength model were taken from the study of Sangid et. al. considering 0.2% offset yield stress change by temperature increase [104]. In addition to that, yield stress values at reference temperature were taken from performed tension

tests within this study. As seen in Figure 6.7, m parameter was found as 0.862 for both tension and compression behaviors.

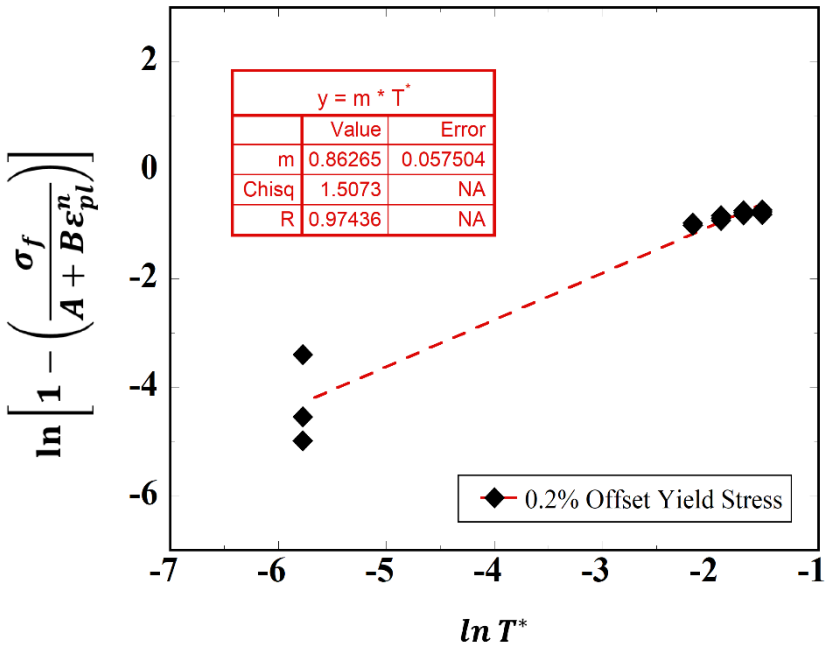

Figure 6.7. Determination of m parameter for the EBM-produced Ti64.

6.2. Determination of JC Failure Model Parameters

In this section, JC failure model parameters of EBM-produced Ti64 with calibration processes will be given in detail according to their appearance sequence in Equation 3.17. Determined JC damage parameters for EBM-produced Ti64 will then be published in Table 6.2.

6.2.1. Determination of D_1, D_2 and D_3 parameters

Determination of triaxial stress state parameters of JC damage model, D_1, D_2 and D_3, is shown in Figure 6.8. The calibration process was conducted based on the fracture strain data taken from 0.33, 0.91, and 1.75 triaxiality range tests. 0.65 range was not

included in the calibration process due to fracturing at insufficient strain values. After applying exponential fitting, D_1, D_2 and D_3 parameters were found as 0.0256, 0.0438, and -0.823, respectively.

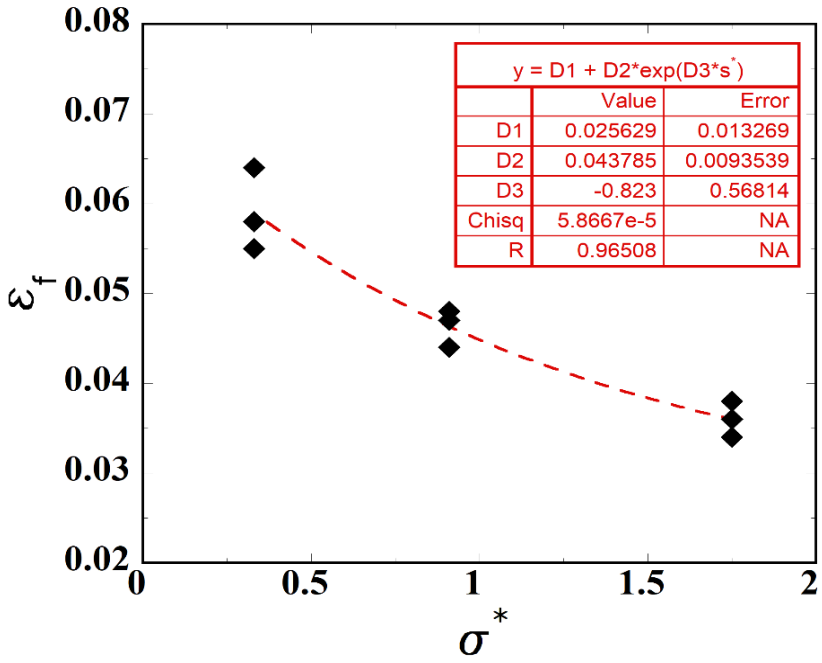

Figure 6.8. Determination of D_1, D_2 and D_3 parameters for EBM-produced Ti64.

6.2.2. Determination of D_4 parameter

Determination of strain rate parameter (D_4) of the JC failure model is shown in Figure 6.9. Fracture strains obtained from unnotched (0.33 triaxiality range) specimen tests under different strain rates were taken into account in the calibration process of D_4 parameter. After completing the linear curve fitting process, D_4 parameter was found as 0.0552 for the strain rate effect on the failure strain of the EBM-produced Ti64.

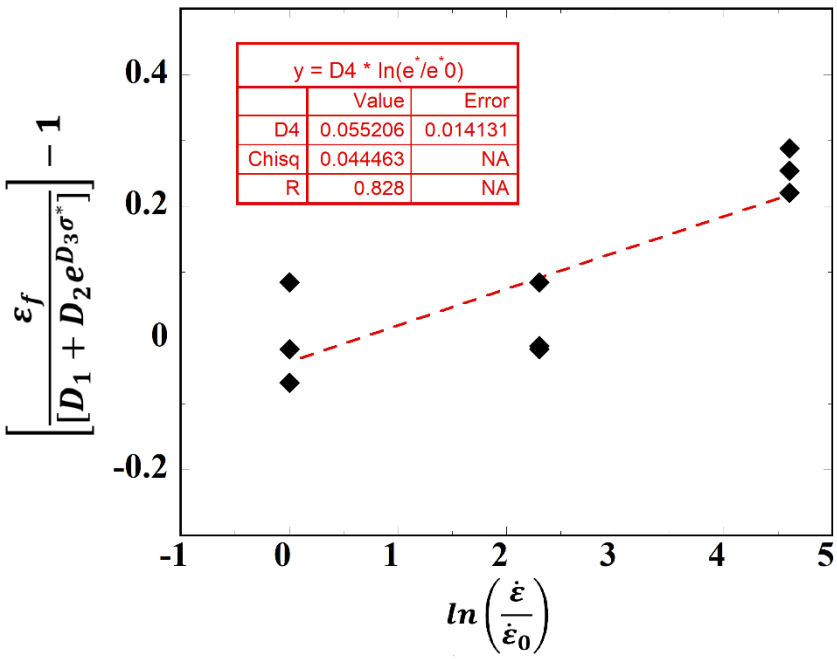

Figure 6.9. Determination of D_4 parameter for EBM-produced Ti64.

6.2.3. Determination of D_5 parameter

As the elevated temperature tests were unable to be completed, determination of D_4 parameter of the JC failure model was needed to be taken from another study. Therefore, D_4 parameter was chosen as 3.87 from the study conducted at Lawrence Livermore National Laboratory, considering the convergence of the other parameters [105].

6.3. Calibrated Model Parameters For EBM-Produced Ti64

JC strength and failure model parameters calibrated in the above sections are sequentially tabulated in Table 6.1 and Table 6.2.

Table 6.1. JC strength model parameters for EBM-produced Ti64.

Testing Type	A **(MPa)**	B **(MPa)**	n	C	m	$\dot{\varepsilon}_0$ **(s^{-1})**
Tension Direct fitting	868	460.02	0.1899	0.0181	0.862	10^{-3}
Tension L. Regression	868	469.39	0.1945	0.0181	0.862	10^{-3}
Compression Direct fitting	883	919.88	0.3241	0.0142	0.862	10^{-3}
Compression L. Regression	883	923.87	0.3269	0.0142	0.862	10^{-3}

Table 6.2. JC failure model parameters for EBM-produced Ti64.

D_1	D_2	D_3	D_4	D_5
0.0256	0.0438	-0.823	0.0552	3.87

CHAPTER 7

DISCUSSIONS

7.1. Surface Roughness, Microstructural Analysis, and Porosity

EBM-produced Ti64 is a rough-surfaced material in the as-built condition (Figure 5.1). The poor surface quality and morphology can be distinguished even with bare eyes. This problem is reported as a typical situation for the EBM process in the literature [106, 107]. Exemplifier comparative images are also shown in Figure 7.1(a) and (b). Additionally, EBM-produced parts show higher surface roughness compared to other AM methods. The root cause of higher surface roughness is the thermal radiation as the electron beam generates higher melting energy than other methods [9]. There are three reasons for high surface roughness: (1) the staircase effect related to the multi-layered manufacturing by EBM, (2) the adherence of partially melted particles to the outer surface of the manufactured parts, and (3) the existence of porosities and non-melted regions [108]. It is stated that the process parameters have a major effect on the surface roughness of EBM-produced Ti64 parts [8, 109]. Increasing part thickness causes an increase in surface roughness. The energy density of the electron beam controlled by the beam current, the offset focus, and the scan speed is another factor on the surface roughness of EBM-produced parts [8].

Build orientation changes the surface roughness, for instance, a 30% increase in the surface roughness was noted when the specimens were manufactured vertically. [109]. On the other hand, rough surface characteristics directly and detrimentally affect the mechanical properties of EBM-produced Ti64, especially the fatigue resistance [106, 110, 111]. In order to eliminate issues caused by the surface roughness, several techniques were proposed to deplete roughness level and enhance the surface quality such as polishing, machining for simple geometries, chemical etching, and vibrahoning for intricate geometries [9].

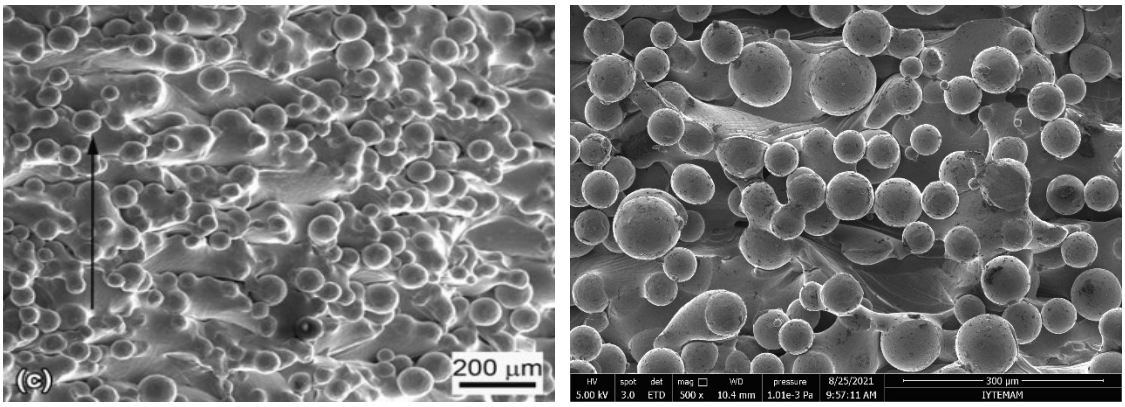

(a) **(b)**

Figure 7.1. Similar surface roughness images from (a) a study in literature (Source: Rafi et al., 2013 [106]), and (b) this study.

In this study, microstructural findings indicate the existence of α+β duplex phase colony and basketweave morphologies in an almost fully lamellar structure. Also, EBM-produced Ti64 possesses a very fine microstructure compared to wrought Ti64 [112]. These microstructural morphologies are similar to the findings of several studies published in the literature [106, 110, 112, 113, 114]. Microstructure images of Ti64 related to manufacturing processes including this study are illustrated in Figure 7.2(a-d). The microstructural formations in Ti64 are thermal history-dependent so that various transition products such as lathlike α, colony α, acicular α, and HCP martensitic α′ occur following the decomposition of β phase [115, 116]. Phase transformation within the microstructure of EBM-produced Ti64 consists of three stages [112]. Following the melting of raked powders at ~1900 °C by electron beam, the solidification stage starts with the formation of BCC structure (prior β phase ($L \rightarrow \beta_p$)); thereafter, rapid cooling from β transus temperature (around 995 ± 20 °C) to lower temperatures, sequential phase transformation occurs as (1) the HCP structured α phase at the grain boundaries of prior β phase ($\beta_p \rightarrow \alpha_{GB}$), (2) basketweave (Widmanstätten) plates nucleate inside the prior β phase ($\beta_p \rightarrow \alpha+\beta$), and (3) formation of α colonies at where the cooling rate slightly higher [112]. The aforementioned transformations are diffusion-controlled, in which V diffuses to β phase and Al diffuses to α phase during the transformation [112]. When the cooling rate is extremely high, HCP structured martensitic α′ phase and orthorhombic martensitic α″ phases form directly from prior β phase ($\beta_p \rightarrow \alpha' - \alpha''$) as a result of diffusionless transformation [9, 112]. Connected with that excessive rapid cooling, in some regions as seen in Figure 5.2 and Figure 5.3, low

amount of α′ martensite phase is inspected in the microstructure of the studied EBM-produced Ti64 bulk parts because local thermal gradient reaches around the critical rate of 410 °C/s that enables the formation of incompletely transformed (metastable) α′ martensite phase [10] (Figure 7.3). As it is known that the base plate is heated and maintained at around 700 °C during the EBM process, it allows the decomposition of α′ martensite formed after rapid cooling from melting temperature to martensite start temperature (M_s) into α+β phase (α′→ α+β) due to shorter transformation time (about 30 min.) than holding time on the base plate of EBM until the manufacturing process ends [112]. However, the existence of α′ martensite phase in acicular or lenticular (plate-like) structures proves that α′→α+β transformation is not completed thoroughly for the studied EBM-produced Ti64 parts. In the last stage, there is no phase transformation occurred after the formation of α+β duplex phase, including α′ in this case, as the thermal gradient decreases slowly [9, 10].

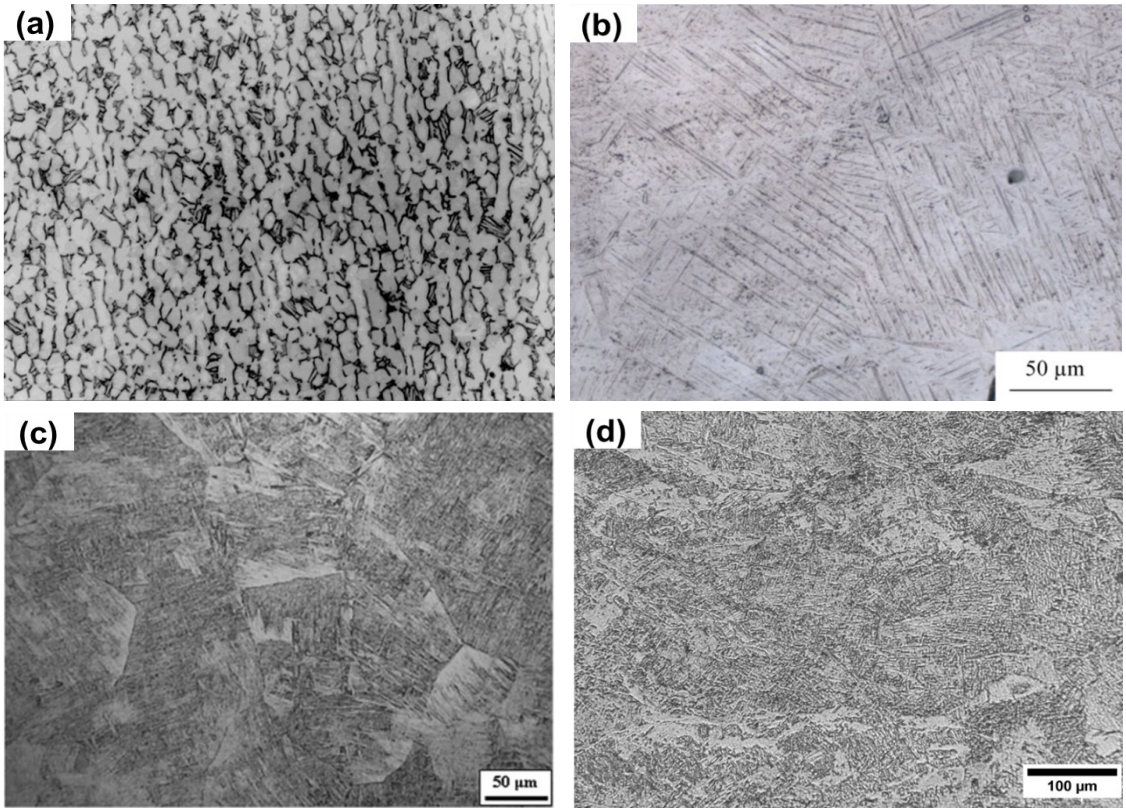

Figure 7.2. Microstructures of Ti64 from the literature with regards to the manufacturing process (a) wrought Ti64 (Source: Murr et al., 2009 [117]), (b) SLM-produced Ti64 (Source: Hao et al., 2016 [118]), (c) EBM-produced Ti64 (Source: Gong et al., 2014 [114]), and (d) from this study.

There are 12 crystallographic α orientations satisfying the Burger's relationship in prior β grains during $\beta_p \rightarrow \alpha+\beta$ transformation, which ensue the weaker α texture intensity than β texture according to the results from the study of de Formanoir et al [110]. In addition to these, the mechanical properties of EBM-produced Ti64 are strongly influenced by the microstructural phases and their distributions [119]. The existence of the α′ martensite phase in the microstructure prompts low ductility and contributes to fragmentation at low strains than required strain limits, as seen in SLM-produced Ti64 studies [9, 116, 120]. Phase formation and distribution have close relation with the process parameters employed in the EBM system.

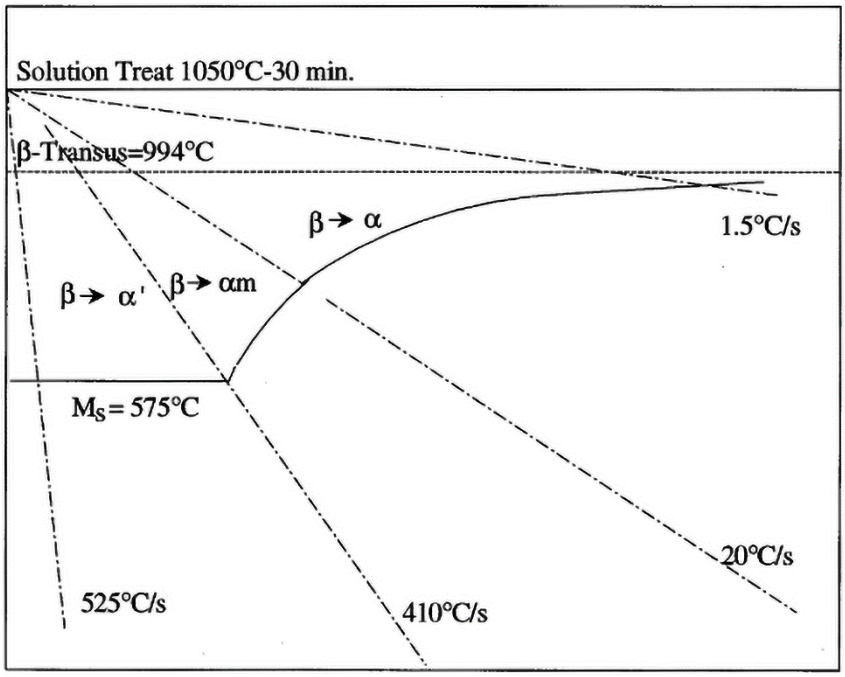

Figure 7.3. Transformations from β phase to α and α′ phases as a function of cooling rates. (Source: Ahmed and Rack, 1998 [10])

Another feature of manufacturing Ti64 alloy by EBM process is the microstructural dependence to the build orientation with respect to the build direction [121]. It is seen in this study that the massive columnar prior β grains are stretching through the build direction (Z-axis) while the near equiaxed grain formations are found in the perpendicular direction to the build direction (XY plane). Similar grain morphologies were encountered and reported previously in the literature [113, 114, 122, 123]. The schematic

of the columnar grains with phase morphologies is shown in Figure 7.4. The formation of columnar grains is due to the epitaxial growth by the thermal gradient parallel to the build direction in that prior β grains form and align through the heat flux after re-melting of previous layers with the electron beam energy [122]. Another factor for the formation of columnar grains is that the irreversible plastic deformation within the weaker phase (β phase for Ti64) appears during the phase transformation, which is able to cause permanent shape change [124]. The thermal gradient through the build direction may lead to plastic deformation and help the growth of prior β grains. It is known that the columnar structure possesses strong fiber texture <001>$_\beta$ which proceeds perpendicular to deposited layers [115, 122]. Also, columnar structure causes high microstructural anisotropy which is propounded as the main reason for alterations in the micromechanical properties since the EBM-produced Ti64 differently responds under the loadings depending on build orientation.

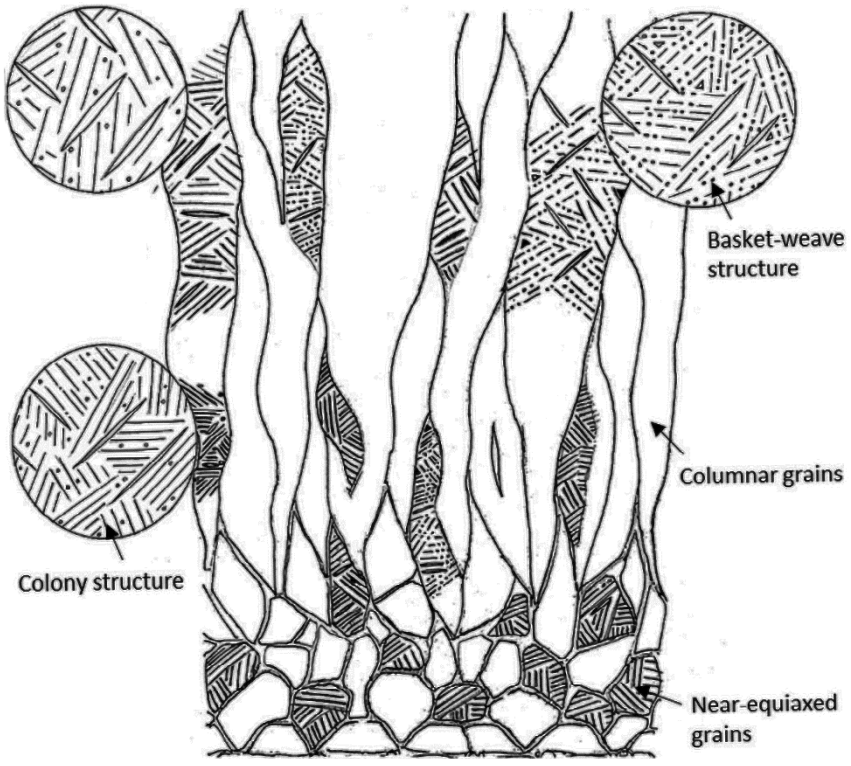

Figure 7.4. Schematic of columnar grains of EBM-produced Ti64.
(Source: Tan et al., 2015 [123])

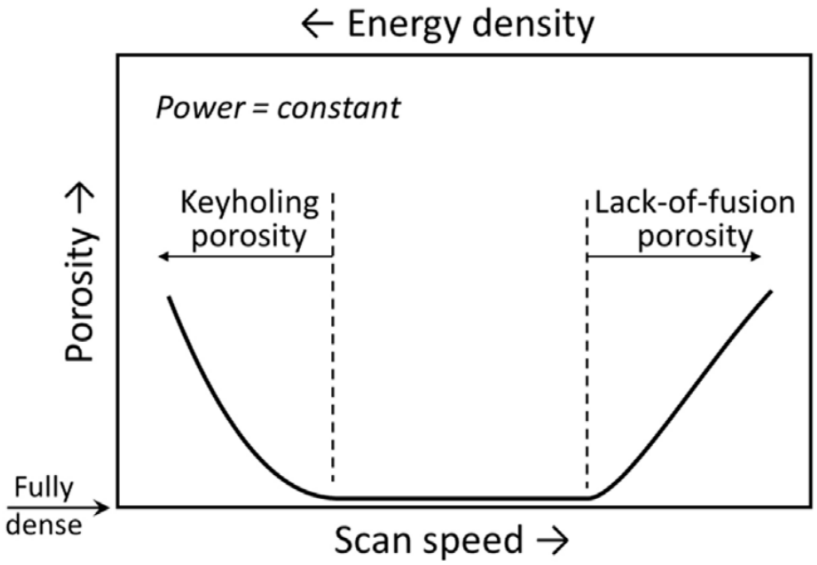

Figure 7.5. Formation of lack of fusion and keyhole voids as a function of scan speed and energy density. (Source: Tang et al., 2017 [125])

Porosities with varying shapes and dimensions are commonly pronounced for the AM applications of Ti64 alloy [9, 126, 127, 128]. Porosities in EBM-produced Ti64 parts are generally classified in two categories regarding their main nuisance to produce as (1) gas voids which are in spherical shapes and generated due to gas entrapment into the molten metal emerged from the oxygen content of the used powder or vacuum of the environment, and (2) lack of fusion voids with irregular shape and sizes which are revealed at the boundaries of scanned layers due to insufficient melting energy [9]. Additionally, the lack of fusion voids become keyhole voids when the melting energy increases as a result of lower scanning speed and high electron beam energy [125, 129] (Figure 7.5). Lack of fusion voids can be suggested as more hazardous defects than gas voids as they have sharp tips on the edges and stand between the adjacent layers (Figure 7.6(a)). For this study, both gas and lack of fusion voids including keyhole voids were identified from OM and SEM images in the microstructural analysis irrespective of build orientation and as-built part dimensions (Figure 5.5). Non-melted and partially melted powders highly appeared inside the lack of fusion voids. Similar findings were reported in the publications that focused on the porosity-mechanical property relations [127, 128]. It is already known that internal defects such as porosities have an absolute effect on the macro-mechanical properties of EBM-produced Ti64 [128]. It is seen from Figure 5.5(a), specifically, size variations of lack of fusion voids are enormously big. Therefore, premature fracture characteristics of tensile specimens would likely be attributed to

scanned layer separation following crack propagation originated from the sharp edges of the lack of fusion defects. The volume fraction of the porosities for the studied EBM-produced Ti64 was excessively higher than those of reported works [126, 130]. Porosity fraction is highly affected by the process settings and generally found to be less than 1% [128, 129, 131, 132]. A higher porous structure causes a decrease in the actual density and relative density of the as-built parts. Actual density and relative density of EBM-produced Ti64 parts were previously measured and sequentially found 4.388 g/cm^3, and 99.03%, respectively. These are higher than the measured values in the studied EBM-produced Ti64 parts, 4.337 g/cm^{3,} and 97.9%, respectively [132]. As the tensile specimens are relatively big-sized parts, the probability of the presence of the lack of fusion voids increases. The excessive porosity fraction of this study might be attributed to the size of the EBM-produced parts. Hence, EBM-produced Ti64 would likely exhibit deteriorated mechanical properties similar to tensile properties of studied EBM-produced parts. It should be noted that the porosity measurement can be conducted using more precise methods than Archimedes method such as X-ray tomography and 2D microscopy to reveal the specified relation.

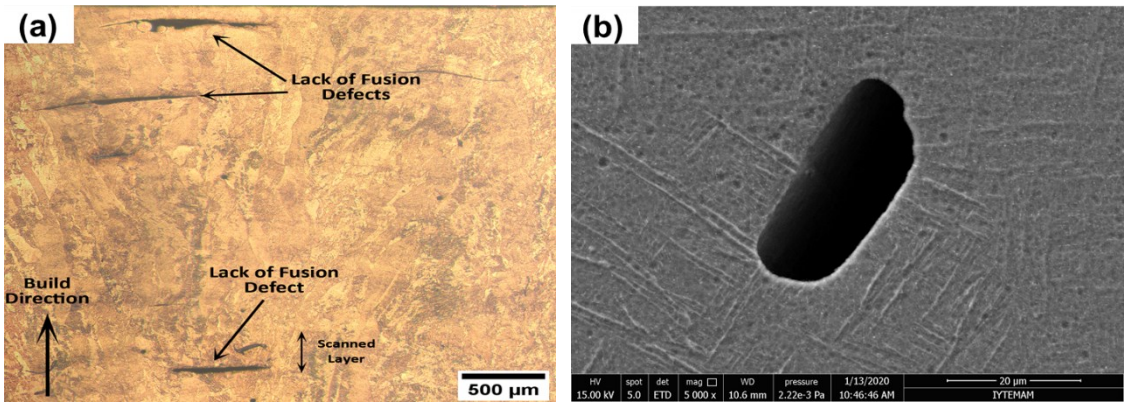

Figure 7.6. Views of irregular-shaped porosities in the microstructure of studied EBM-produced Ti64 (a) lack of fusion voids under OM, and (b) keyhole pore under SEM.

Internal porosities stand as the most critical factor that determines the mechanical response and endurance of the EBM-produced Ti64 rather than microstructural variations and anisotropy [128]. Optimization of the process parameters used in AM leads to achieving less porous structured parts. It is reported that lower scan speed and higher melting energy

provide the reduction of the gas voids existing in structure [9]. Additionally, high melting input energy alleviates the occurrence of lack of fusion voids [133]. According to the microstructural analysis of the studied EBM-produced Ti64 parts, internal porosities are found to have remarkable volume inside the bulk parts. In order to reduce the internal porosities and develop efficient manufacturing settings, some efforts might be headed to optimization studies of EBM process parameters which were used to produce the specimens for this study. On the other hand, several researchers have focused on the heat treatments as secondary processes to eliminate the encountered microlevel problems of AM methods and their deleterious effects [134, 135, 136, 137]. For that purpose, thermal post-processes such as Hot Isostatic Pressure (HIP) and heat treatments can be implemented to reduce the inherent anisotropy by modifying the microstructure of the as-built parts. However, heat treatment applications are unable to annihilate the internal porosities [9]. Only HIP was reported as the effective method in reducing or shrinking the internal porosities [127, 135]. Hereby, HIP method could be applied to as-built EBM-produced Ti64 parts to improve the mechanical properties, especially the ductility of this material.

7.2. Microhardness Properties of EBM-Produced Ti64

A bar chart of the average microhardness values published in the literature and obtained in this study is shown in Figure 7.7. Measured microhardness data from EBM-produced Ti64 bulk part present comparable hardness values with the literature [119, 120, 138, 139, 140, 141, 142]. Additionally, directional anisotropy is detected as the microhardness varies with the measurement directions relative to the build direction: 364.18 ± 10.28 HV in the build direction (Z-axis), and 356.17 ± 22.74 HV in the perpendicular to the build direction (XY plane), respectively. Directional anisotropy is a common finding for EBM-produced Ti64 which was also noted in previous studies [141, 143]. Directional anisotropy results from the alterations of the microstructure regarding the build orientation. It should be noted that higher microhardness values are measured from the areas which are near the base plate of the EBM system and microhardness values exhibit a slight decrease through the built height (Figure 5.6). Higher microhardness near the base plate is likely due to the higher cooling rate in these areas as a consequence of high heat dissipation from the interface between the as-built part and stainless-steel base plate [117, 123]. Microhardness

decrease along build height was also found previously [117, 144]. However, a little discrepancy over the build height-microhardness relation was reported based on the investigation of microstructural properties of an impeller manufactured by using EBM [119]. It was reported that microhardness values exhibited an increasing trend along the build direction in contrast to the present study. This situation might be attributed to manufactured geometry-microstructural feature relation. Furthermore, microhardness variations generally represent the phase and morphology alterations in the microstructure.

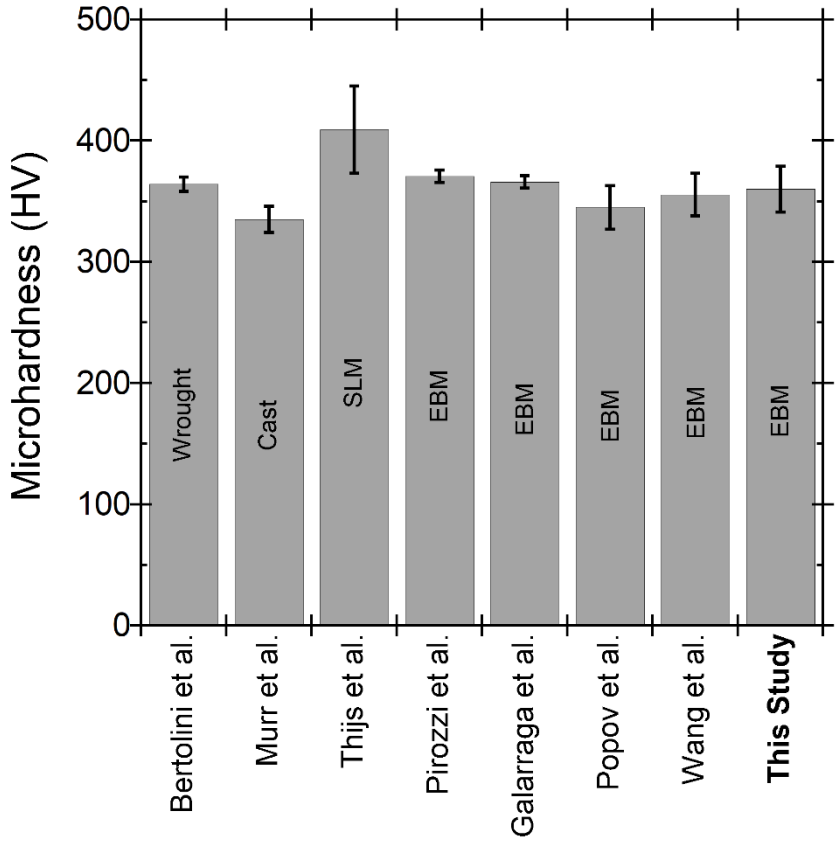

Figure 7.7. Microhardness results of Ti64 alloy taken from literature based on manufacturing methods.

Hardness test enables the assessments based on the impact of processing on the mechanical properties easily and non-destructively [123]. Several researchers proposed simple relations in order to predict the macro-mechanical properties such as yield and ultimate strength using microhardness data. For Ti64 alloy and its electron beam welded joints, linear relations between the microhardness (H_v) and yield (σ_y) and ultimate strength (σ_u) were proposed as [145]

$$\sigma_y = 3.013H_v - 127.012 \quad (7.1)$$

$$\sigma_u = 3.586H_v - 237.900 \quad (7.2)$$

Other reported relations for metals and alloys are as follows [146]

$$\sigma_y = \frac{H_v}{3}(0.1)^n \quad (7.3)$$

$$\sigma_u = \left(\frac{H_v}{2.9}\right)\left(\frac{n}{0.217}\right)^n \quad (7.4)$$

where n represents the strain hardening exponent. The yield and ultimate strengths are estimated sequentially 958.2 MPa and 1053.7 MPa using Equations 7.1 and 7.2, and 760.6 MPa and 1187.9 MPa using Equations 7.3 and 7.4. It is noticed that Equations 7.1 and 7.2 better predict the strengths of the studied EBM-produced Ti64 alloy than Equations 7.3 and 7.4. A similar finding was also reported previously [123].

7.3. Mechanical Properties of EBM-Produced Ti64

The reported and standard mechanical properties of Ti64 are tabulated in Table 7.1, together with the properties obtained in the present study. The mechanical properties of AM methods tabulated in Table 7.1 belong to as-built machined conditions. As noted in Table 7.1, the EBM-produced Ti64 studied exhibits similar mechanical properties with the laser-based PBF and conventionally produced Ti64 under both tension and compression. Additionally, the mechanical properties of investigated alloy comply with the related standards and Arcam EBM company specifications. However, the ductility of EBM-produced Ti64 is much lower than that of the standards and reported studies in the literature, similar to SLM-produced Ti64 alloy.

As the as-built specimens possess relatively high surface roughness which causes the stress concentration and crack initiation, test specimens were machined into exact dimensions in order to avoid surface roughness effect [147, 148]. The removal of rough surfaces leads to higher ductility [147]. Nevertheless, the ductility of EBM-produced Ti64 under tensile tests did not show noticeable improvement after machining in this study, and the specimens fractured at ~3% strain. On the other hand, necking occurrence is not verifiable from the test stress-strain curves. Previously, quasi-static tension tests on EBM-produced Ti64 using cylindrical and flat specimens were performed [41, 121]. Visual evidence that depicted the limited necking occurrence before fracture for both as-built and as-built machined specimens was reported. Fracture under tension loadings without necking is thought to be a consequence of a quite high level of discontinuous and sharp-shaped porosities in the bulk form, which initiates brittle fracture. A cup-and-cone type fracture with the fine dimpled central region and the prominent shear lips are seen in Figure 7.8 in a tested and fractured EBM-Ti64 specimen, which is common to the tensile tested specimens, examples can be found in previous studies [41, 121, 149].

In order to improve the mechanical properties of additively manufactured Ti64 by PBF methods, thermomechanical treatments such as HIP and annealing are implemented as a post-treatment for as-built parts to modify the microstructure and eliminate the internal defects and voids [21, 149, 150]. The effectiveness of these post-treatments was indicated by several studies in terms of essential mechanical, fatigue, and creep properties [132, 148, 151]. HIP is also reported as a beneficial process to improve corrosion resistance and mechanochemical performance of EBM-produced Ti64 [149]. Additionally, the effects of the HIP on mechanical properties based on macro and microstructural assessments were also studied [7, 132]. It was found that the HIP process remarkably enhanced the ductility of EBM-produced Ti64. However, strength values slightly decreased after HIP process but remained above the standard limits. On the other hand, the effects of heat treatments on the mechanical and microstructural properties of EBM-produced Ti64 at different holding temperatures and cooling conditions were also studied [120, 150]. The heat treatment showed an improved ductility however, the mechanical properties slightly decreased similar to HIP process. Since the tested Ti64 specimens in this study suffer from extremely low ductility under tension loadings, HIP and heat treatments can be employed using optimum heating and cooling parameters in order to enhance the ductility of EBM-produced Ti64 to around the standardized level of 10%.

Table 7.1. Mechanical properties of Ti64 alloy reported in several studies and standards.

Process	Build Orientation	Testing Method	0.2% σ_y (MPa)	σ_U (MPa)	Elongation (%)	Reference
Wrought	Vertical	Tension	942 ± 8	942 ± 8	12.5 ± 1.2	Wysocki et al. [143]
Wrought	Horizontal	Tension	832 ± 10	933 ± 7	13 ± 1.5	
Wrought	All	Tension	>795	>860	>10	ASTM F136 [152]
Cast	-	Tension	865	980	13.5	Vilaro et al. [153]
Cast	All	Tension	758	860	>10	ASTM F1108 [154]
Forged (Mill-annealed)	-	Tension	970	1030	16	Zhai et al. [155]
SLM	Vertical	Tension	1050 ± 40	1180 ± 30	8.5 ± 1.5	Qiu et al. [156]
SLM	Horizontal	Tension	1070 ± 50	1250 ± 50	5.5 ± 1	
SLM-HIP	All	Tension	925-1000	1000-1100	12-18	
SLM	Vertical	Compr.	≈ 1150	1780	20-35	Qiao et al. [157]
SLM	Horizontal	Compr.	≈ 1150	2024	15-20	
SLM	Vertical	Compr.	1167 ± 115	1681 ± 74	35 ± 10	Losertová and Kubeš [158]
EBM	Vertical	Tension	812 ± 12	851 ± 19	3.6 ± 0.9	Edwards et al. [159]
EBM	Horizontal	Tension	783 ± 15	833 ± 22	2.7 ± 0.4	
EBM	Vertical	Tension	957 ± 8.9	1104 ± 17.5	11 ± 1.30	Rodriguez et al. [102]
EBM	Vertical	Compr.	1114 ± 34.5	1414 ± 56.2	-	
EBM	Vertical	Tension	879 ± 8	953 ± 8.8	13.8 ± 0.8	Ackelid and Svenson [131]
EBM	Horizontal	Tension	870 ± 12	971 ± 3.1	12.1 ± 0.8	
EBM	Vertical	Tension	928 ± 13.3	1011 ± 14.8	13.6 ± 1.4	Lu et al. [132]
EBM-HIP	Vertical	Tension	813 ± 14.3	908 ± 3.2	17.7 ± 0.9	
EBM	Vertical	Tension	940 ± 23	1023 ± 21	10 ± 2	Yiğitbaşı [41]
EBM	Horizontal	Tension	895 ± 14	988 ± 13	15 ± 4	
EBM	Vertical	Tension	1001 ± 42	1073 ± 45	11 ± 1	Galarraga et al. [120]
EBM Annealed	Vertical	Tension	847 ± 90	998 ± 52	13 ± 7	

(cont. on next page)

Table 7.1. (cont.)

Process	Build Orientation	Testing Method	0.2% σ_y (MPa)	σ_U (MPa)	Elongation (%)	Reference
EBM	Vertical	Tension	973	1066	10.72	Mohammadhosseini [7]
EBM	Horizontal	Tension	981	1055	8.12	
EBM-HIP	Vertical	Tension	882	935	14.9	
EBM-HIP	Horizontal	Tension	868	988	11.2	
EBM	Vertical	Compr.	1060 ± 32	1310 ± 35	32.4 ± 0.2	
EBM-HIP	Vertical	Compr.	968	1508	≈ 23	Austin et al. [160]
EBM	All	Tension	930	970	16	Arcam EBM [96]
EBM-SLM	All	Tension	>760	>825	>10	ASTM F3001 [161]
EBM	Vertical	Tension	1028 ± 15.1	1090 ± 5.3	3.13 ± 0.71	**This Study**
EBM	Vertical	Compr.	1042 ± 28.5	1448 ± 13.5	33.6 ± 2.86	

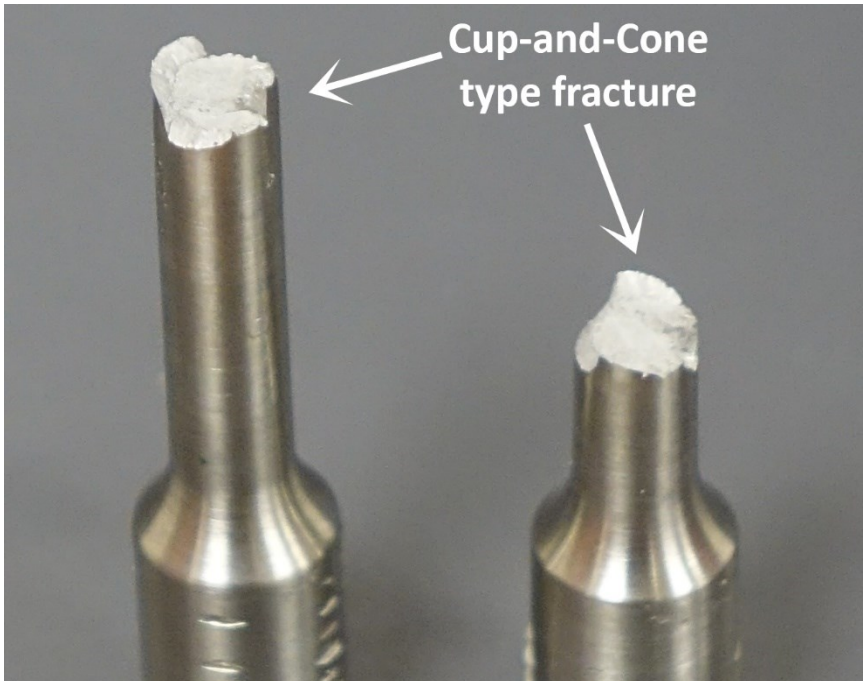

Figure 7.8. View of cup-and-cone type fracture topography after quasi-static tension.

The compression tested EBM-produced Ti64 in the present study exhibited ductile fracture mode at both quasi-static and high strain rates. The main fracture mode was shear cracks, 45° to the loading direction as illustrated in Figure 7.9(a) and (b). After the stress

reaches ultimate compressive strength during a test, thermal softening turns into a significant factor that facilitates the shear fracture of the specimen with the help of dislocation annihilation [73]. The formation of adiabatic shear bands is not desirable as it decreases the energy dissipation capability of the material [7]. However, Ti and Ti alloys tend to fail by shear cracks following the formation of adiabatic shear bands when they are exposed to high rate loadings or quasi-static loadings combined with high temperatures [162]. Deformation characteristic of EBM-produced Ti64 under compression shows strong strain rate sensitivity. Specimens can resist higher stresses but experience lower ductility under high-rate loadings as the total strain decreases around 30% to around 4-5%, corrected from the test frames of 1131 s^{-1} and 2154 s^{-1} (Figure 5.17). This situation is proven for conventionally produced Ti64 as well [73].

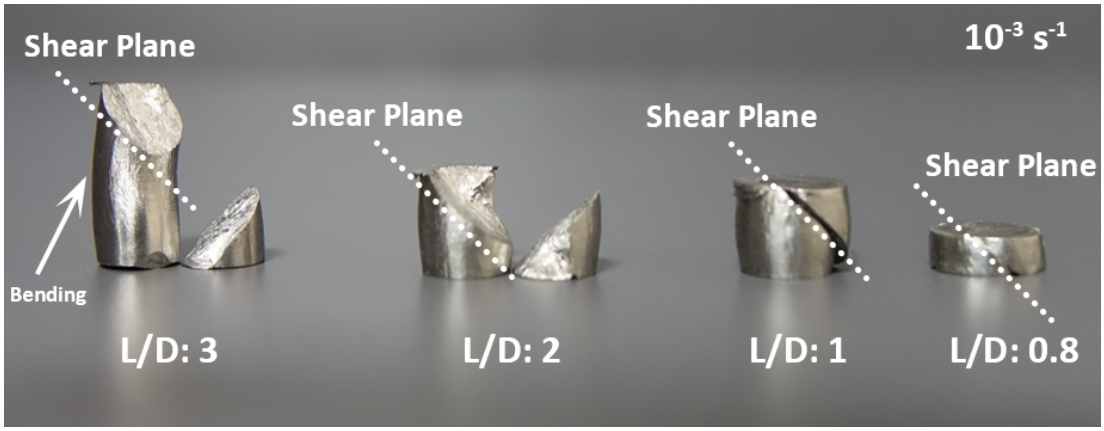

(a)

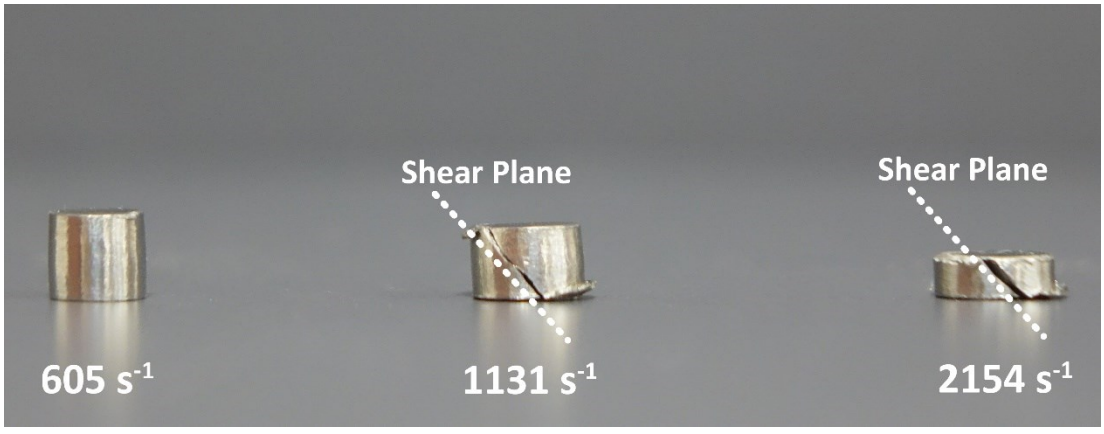

(b)

Figure 7.9. Views of deformed specimens under compression loadings at (a) quasi-static strain rates, and (b) high strain rates.

As it is seen from the test graphs under Section 5.4.1, EBM-produced Ti64 behaves like a perfectly plastic material under tension during the plastic flow. This condition is also confirmed by a low tensile strain hardening exponent, ~0.19 using the Ludwig equation. Low strain hardening capability is more pronounced under tension, while the strain hardening exponent increases to 0.32 under compression. As often reported for Ti64, the strain hardening comprises of multiple stages which correspond to the deformation mechanism changes [102, 163]. These stages can be characterized by excessive alterations in the slope of the strain hardening curve. The deformation starts with dislocation slip then, as the strain increases, twinning appears. Dislocation slip is generally reactivated prior to the onset of thermal softening. Abrupt hardening rate rise on the onset of twinning is ascribed to dynamic Hall-Petch hardening effect [164]. It is seen from Figure 5.23(b) that the twinning generation rate is higher in the high strain rate curves than in the quasi-static curves and the twinning generation rate suppresses the dislocation slip at high strain rates. Twinning becomes a more active deformation mechanism in the case of high-rate deformation [163]. Respective strain hardening-true plastic strain curves of EBM-produced Ti64 within this study indicate similar trends with those of pure Ti and Ti64. [102, 165]. In addition to these, strain rate conversely influences the strain hardening rate as verified from Figures 5.12, 5.18, and 5.23. Approximate strain hardening rate exhibits a noticeable decrease from ~2.38 GPa to ~1.02 GPa when the strain rate increase from 10^{-3} to 10^{-1} s^{-1} for the tension test. Likewise, for the compression tests, the approximate strain hardening rate decreases from ~900 MPa to ~350 MPa when the strain rate increase from 10^{-3} to 2154 s^{-1}. It should be mentioned here that the overall strain hardening rate of compression is much lower than that of tension. This difference might be attributed to the thermal softening effect as EBM-produced Ti64 deforms until about larger strains under compression.

It is commonly known that increasing strain rate increases the strength of Ti64 [166]. A comparison between the quasi-static and dynamic compression of the investigated Ti64 shows that the flow stress increases as the strain rate increases to higher values excluding the tests at 2154 s^{-1}. It was previously stated that strength values did not increase when the strain rate exceeded 10^3 s^{-1} limit [167, 168]. The material response at 2154 s^{-1} can be linked to excessive heating of the specimen, leading to softening. Moreover, the flow behavior of EBM-produced Ti64 alters with the variation of strain rate.

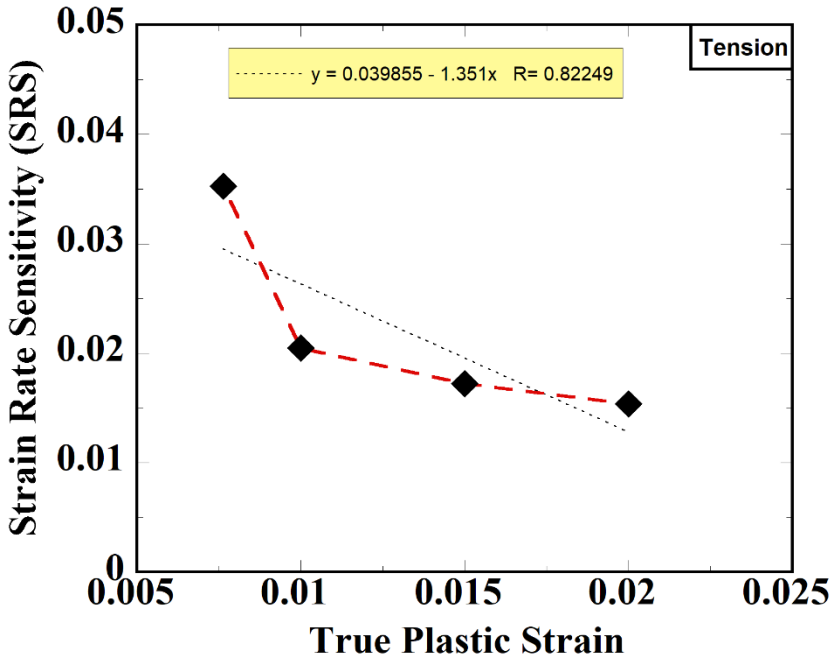

(a)

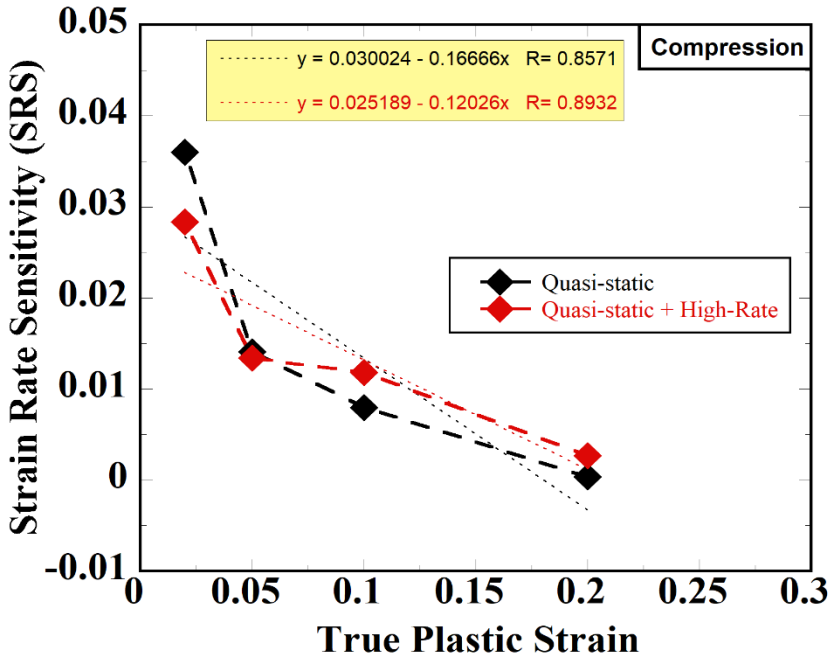

(b)

Figure 7.10. SRS variation with plastic strain increase for (a) quasi-static tension, and (b) the combination of quasi-static and high-rate compression behavior.

It is known that twinning has a significant role in the plastic deformation of Ti64 under high-rate loadings since slip-driven deformation is the main mechanism under quasi-static loadings [102, 163]. Interactions with twins hinder the dislocation slip and cause flow localization. Therefore, stress-strain instability in high-rate compression tests appears as a consequence of flow localization and then cracking occurrence, leading to abrupt losses in load-bearing capacity (Figure 5.21) [73].

As it is already stated, Ti64 alloy shows a strain rate sensitivity mechanical property. More specifically, required stress to maintain the plastic deformation is dependent on the strain rate rather than strain [169]. Therefore, the SRS parameters were calculated for the quasi-static tension, quasi-static compression, and quasi-static and high-rate compression. The calculated SRS values of tension and compression are shown in Figure 7.10(a) and (b) at increasing strains. The determined SRS parameters are further found to be consistent with the literature [170]. These values also show that EBM-produced Ti64 exhibits a positive SRS likewise the conventionally produced Ti64 [171, 172]. Additionally, similar SRS trends are identified for the quasi-static tension and compression as the strain increases the SRS decreases as seen in the same figures. Similar results were reported previously [172]. As seen from Figure 7.10(b), high-rate compression response is moderately affected by SRS with strain increase compared to quasi-static compression response. The variation of strain rate sensitivity within the plastic strain regime is accepted as an indication of microstructural changes connected with the dominant deformation mechanism [121].

7.4. Fracture Surface Analysis

The fracture surface analysis of the studied EBM-produced Ti64 showed common observations with previous studies [106, 121, 173]. Some findings are presented in Figure 7.11 (a-d). The fracture surface images of tested specimens under tension loadings reveal the characteristic of trans-granular fracture composing of equiaxed dimples with a constant size distribution following the coalescence of micro-voids, similar to previous studies. [106, 173] (Figure 5.26). However, EBM-produced Ti64 also shows brittle fracture features in some regions. Fracture initiation generally originated from the lack of fusion defects

which causes material discontinuity in the bulk parts. Since the lack of fusion defects consist of partially melted powders, these type of defect zones are often distinguished in the fractographs of the tested EBM-produced Ti64 specimens (Figure 5.25 and Figure 5.26).

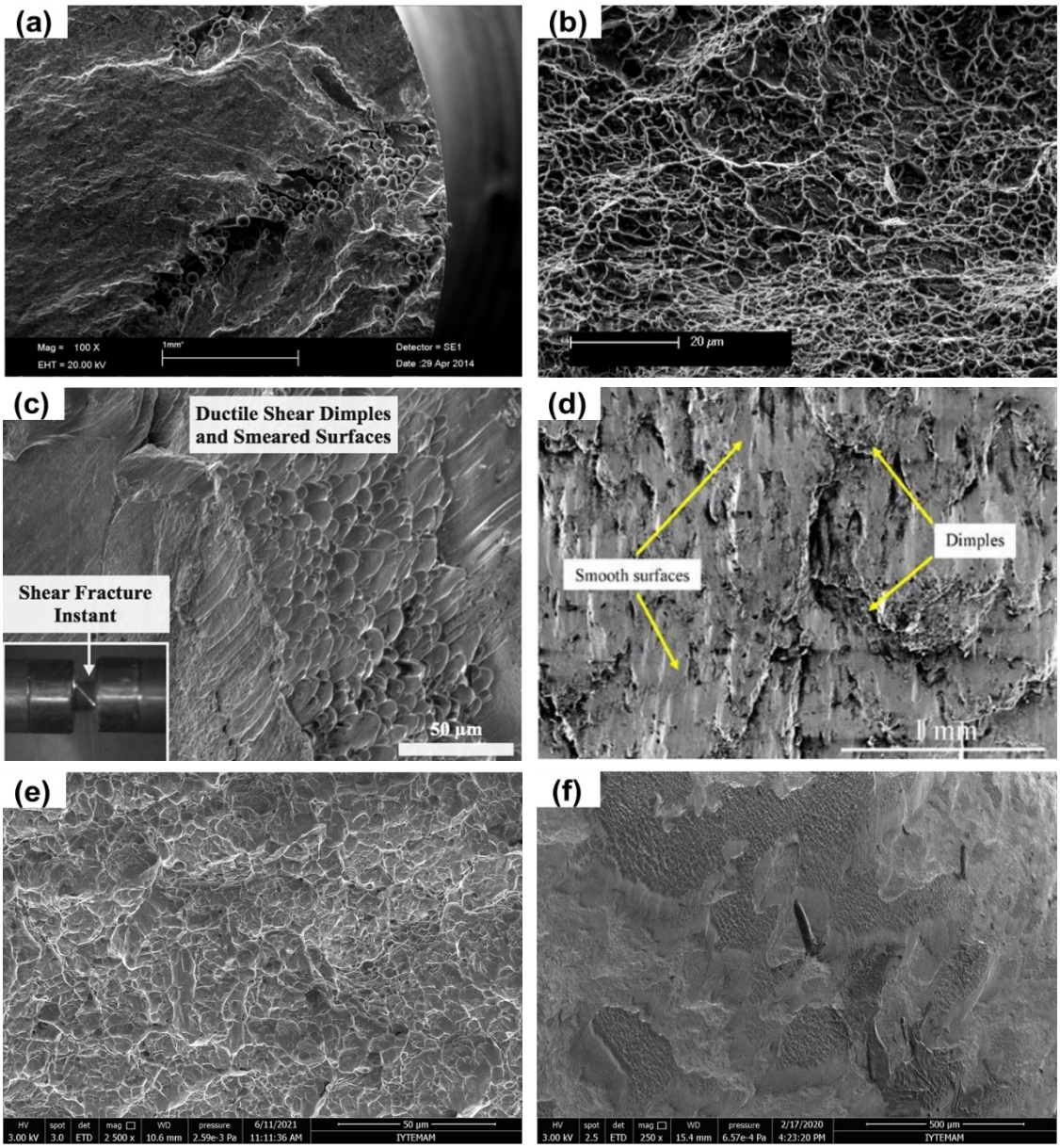

Figure 7.11. Fracture surfaces of specimens under (a) and (b) tension loadings (Source: Mohammadhosseini et al.,2015 [7]), (c), and (d) compression loadings (Sources: Rodriguez et al.,2018 [102] and Alaghmandfard et al., 2020 [174]) and (e) and (f) tension and compression from this study.

Fracture propagation occurs via tearing of the scanned layers in which crack strides within the columnar prior β grains. Another fact about the lack of fusion defects in this study is that they are inspected mostly in the locations near the outer wall of the as-built parts. Hence, premature fracture under tension loadings occurs in more facilitated conditions.

On the other hand, the studied EBM-produced Ti64 under compression loading exhibits shear crack following the shear band propagation on a 45° plane as seen in Figure 5.31 and Figure 5.32. Shear crack formation under compression is a common fracture type for Ti64 regardless of the manufacturing method used [7, 102, 175, 176, 177]. In the respective fractographs of shear crack zones, shear dimples at where the ductile deformation occurs and smeared regions at where heavy shear deformation occurs or the frictional forces between the cracked parts wear the fracture surface are highly visible. Similar observations on the compression fracture mode were also found in the literature [102, 105, 178] (Figure 7.11). The shear band width increases as the strain rate increases from lower to higher rates. The adiabatic heating reaches about 150 °C during the high-rate deformation. Excessive adiabatic heating would help the softening of the regions nearby the flow-induced locations.

7.5. Evaluations of JC Strength and Failure Model Parameters

JC strength model parameters of previous studies are listed in Table 7.2 together with those of the present study. Comparative graph of experimental results and predicted results with JC strength model using calibrated parameters of studied EBM-produced Ti64 for tension loading response and predicted flow stress vs. experimental flow stress curves are shown in Figure 7.12(a) and (b). Predicted stress data within the strain rates of 10^{-3}, and 10^{-2}, and 10^{-1} exhibit well agreement with the experimental results. However, loss of prediction accuracy and increase of error are detected with the strain rate increase. This situation is probably due to the complex deformation history of the EBM-produced Ti64.

Table 7.2. JC strength model parameters for Ti64 reported in the literature.

Process / Testing Type	A (MPa)	B (MPa)	n	C	m	Reference
Commercial / Compression	782.7	498.4	0.28	0.028	1.0	Lee et al. [177]
Commercial / Compression	724.7	683.1	0.47	0.035	1.0	Lee at al. [179]
Commercial / Compression	997.9	653.1	0.45	0.0198	0.7	Seo et al. [180]
Commercial / Compression	870	990	1.01	0.008	1.4	Dumitrescu et al. [181]
Commercial / Compression	1098	1092	0.93	0.014	1.1	Lesuer [105]
Commercial / Compression	968	380	0.421	0.0197	0.577	Calamaz et al. [182]
Commercial / Compression	862	331.2	0.34	0.0120	0.8	Meyer and Kleponis [82]
Commercial / Compression	896	656	0.50	0.0128	0.8	
Commercial / Compression	1104	1036	0.6349	0.01390	0.7794	Khan et al. [183]
Commercial / Tension	984	520.3	0.5102	0.015	0.8242	Macdougal and Harding [184]
Commercial / Compression	1119	838.6	0.4734	0.01921	0.6437	Nemat-Nasser et al. [175]
Commercial / Compression	831.3	857.9	0.302	0.015	0.724	Chen et al. [185]
Commercial / Both	1055	426	0.5033	0.023	0.8	Yatnalkar [186]
Commercial / Compression	1062	431	0.50	0.016	0.69	Hammer [12]
Commercial / Both	1019.5	674.1	0.92	0.03	0.457	Wang et al. [187]
Commercial / Compression	1000	780	0.47	0.033	1.02	Wu and Zhang [188]
Commercial / Punch	1050	955	0.63	0.011	1	Dabboussi and Nemes [189]
Commercial / Tension	969.36	528.636	0.5747	0.0937	0.4938	Raut et al. [190]

(cont. on next page)

Table 7.2. (cont.)

Process / Testing Type	A (MPa)	B (MPa)	n	C	m	Reference
Commercial / Tension	927.88	1062.5	0.6214	0.0167	0.753	Kıranlı [48]
Commercial / Compression	927	1150	0.8674	0.008674	0.753	
Commercial / Tension	0	1207.48	0.010	0.041	0.621	Perez et al. [191]
Commercial / Tension	869.4	649.5	0.3867	0.0093	0.7579	Kotkunde et al. [192]
Commercial / Tension	797.46	305.7	0.2857	0.0196	-	Hu et al. [193]
Commercial / Shear	771.78	269.3	0.2242	0.012	-	
Commercial / Compression	941.33	470.55	0.4655	0.0242	-	
Commercial / Compression	920	380	0.578	0.042	0.633	Hou et al. [194]
SLM / Compression	1032	1301	0.466	0.009	-	Liu et al. [176]
SLM / Tension	997	746	0.325	-	-	Wang and Li [195]
LMD / Compression	871	1026	0.54	0.06	-	Austin et al. [160]
EBM / Compression	950	1046	0.52	0.068	-	
EBM / Tension	790	1230	0.075	-	-	Mirone et al. [173]
EBM / Tension	868	460.02	0.1899	0.0181	0.862	**This Study**
EBM / Compression	883	919.88	0.3241	0.0142	0.862	

In order to evaluate the prediction accuracy of the calibrated JC strength model parameters for tension behavior of EBM-produced Ti64 within this study, the plastic flow stresses are calculated by using different sets of JC parameters listed in Table 7.2. Only the JC strength model parameters offered by Macdougal and Harding, Chen et al., and Yatnalkar show agreement with the experimental results of this study in comparison to other listed sets of JC strength parameters.

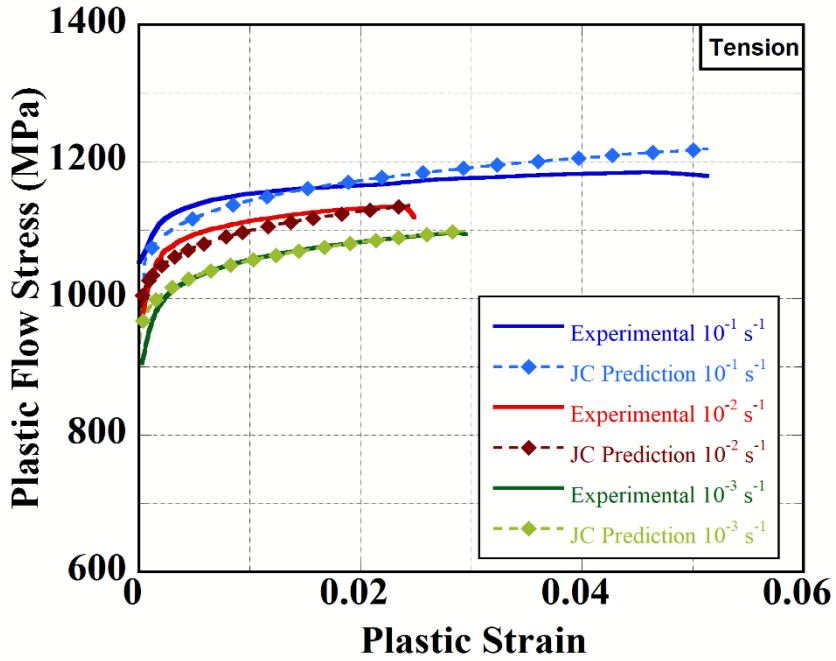

(a)

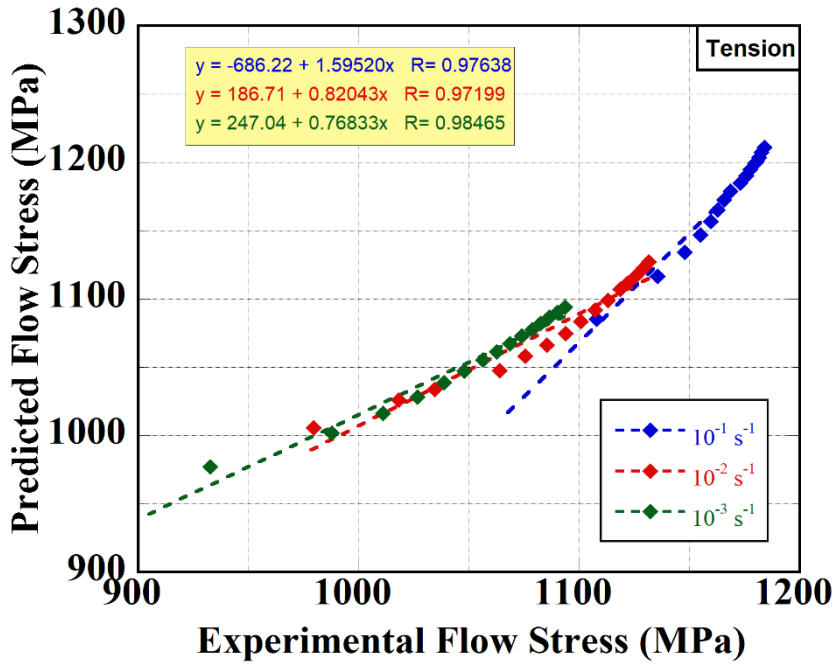

(b)

Figure 7.12. Comparative graphs of (a) experimental results and JC predictions for tension behavior of studied EBM-produced Ti64, and (b) predicted flow stress by JC vs. experimental flow stress.

A comparative graph for predicted flow stress data using parameters of the mentioned researchers including calibrated JC parameters within this study and experimental results is shown in Figure 7.13 at the reference strain rate of 10^{-3} s^{-1}. The JC parameters of Macdougal and Harding underestimate, while the JC parameters of Yatnalkar overestimates the flow behavior of EBM-produced Ti64. In contrast to these, calibrated JC strength model parameters within this study show well agreement with the experimental flow behavior of EBM-produced Ti64. After reaching the ultimate stress, the predicted flow behavior for this study slightly differs from the experimental flow behavior.

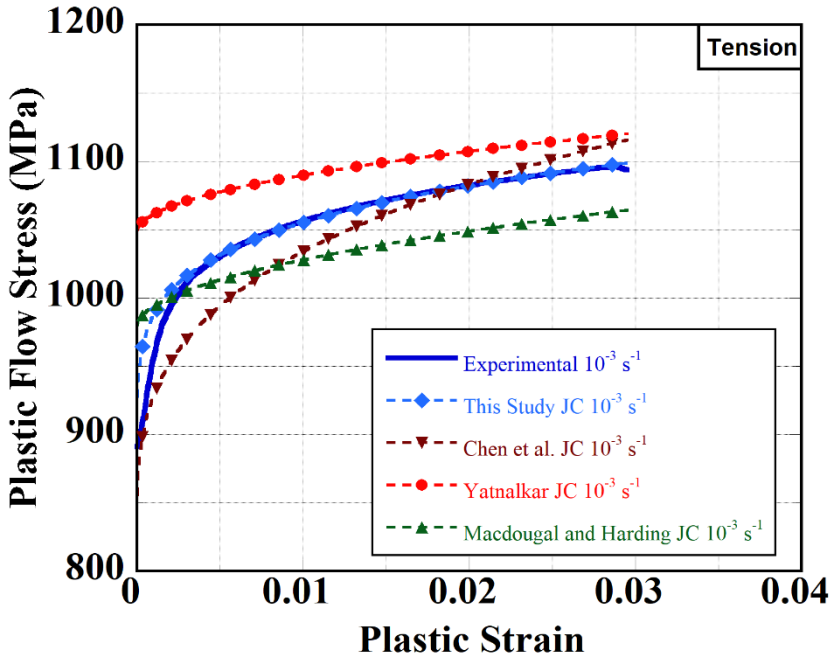

Figure 7.13. Comparison of prediction accuracy of tension JC strength parameters found in this study with the given parameters in the literature.

The predicted and experimental flow stress-strain curves at quasi-static and high strain rates are shown in Figure 7.14 and Figure 7.15, respectively. The calibrated JC strength model parameters agree well with the experimental behavior at the quasi-static strain rates (Figure 7.14). While the JC strength model slightly overestimates the experimental flow stresses at high strain rates (Figure 7.15), the JC strength model does not match the experimental stress at 2154 s^{-1}. The complex deformation characteristic of

EBM-produced Ti64 under excessive high-rate loadings could not be predicted accurately by using the JC strength model. As previously discussed, high-rate loadings lead to changes in the deformation type which directly affects the strain hardening and thermal softening of Ti64 alloy. Additionally, the JC strength model implies that the flow stress increases in an almost linear manner as the plastic strain is accumulated by the material. For these reasons, the JC strength model loses its accuracy in predicting the exact material behavior, but it is able to calculate convergent stress values. A related graph for comparing predicted and experimental flow stresses at all strain rates is given in Figure 7.16.

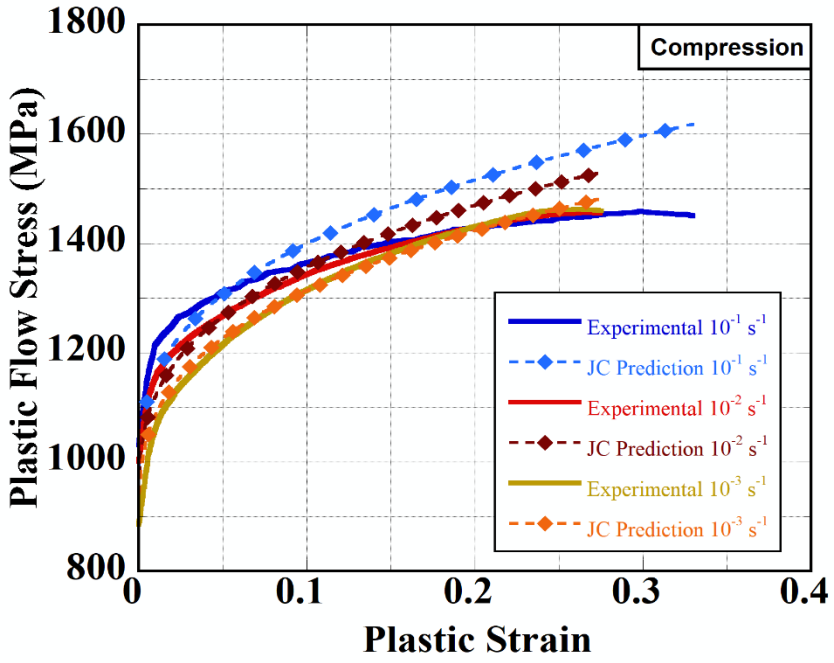

Figure 7.14. Comparative graphs of experimental results and JC predictions for the compression behavior of studied EBM-produced Ti64 for quasi-static test regime.

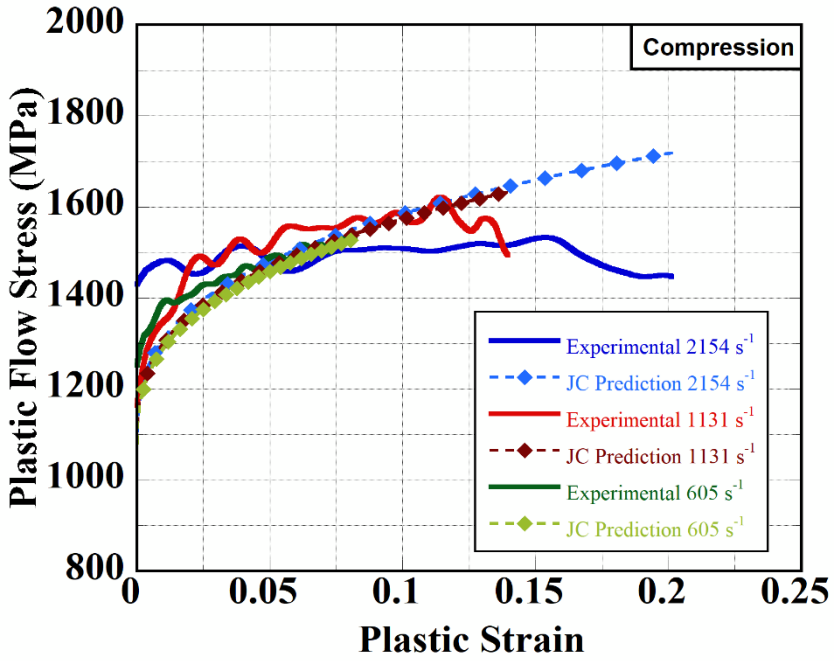

Figure 7.15. Comparative graphs of experimental results and JC predictions for the compression behavior of studied EBM-produced Ti64 for high-rate test regime.

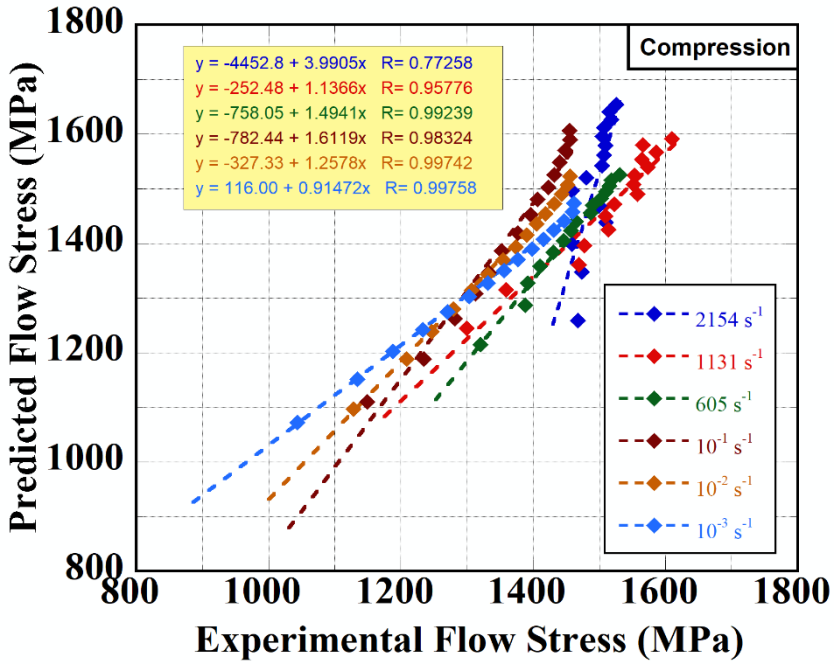

Figure 7.16. Predicted flow stress by using JC strength model and experimental flow stress curves of compression behavior EBM-produced Ti64 regarding all strain rates.

The compression stress-strain curves of the calibrated JC strength model and experiment at 10^{-3} s^{-1} are shown in Figure 7.17 together with those of a few JC models selected from Table 7.2. The selected JC models are the most convergent ones among the others listed in Table 7.2. The selected JC models underestimate the flow behavior as seen in Figure 7.17, except the JC parameters of Khan et al. It overestimates the flow stresses when the plastic strain excesses 10%. The related calculations of parameters offered by Austin et al. and Dabboussi et al. show relatively consistent results with the experimental results. It should be noted here that the calibrated JC strength model for compression behavior of studied EBM-produced Ti64 gives the only perfect matching flow with the experimental behavior comparing the JC models listed in Table 7.2. The predicted flow behavior curve slightly deviates from the experimental data curve due to thermal softening. In the flow-induced regions, adiabatic heating facilitates the dislocation motion by reducing the threshold stress level for the dislocation motion during plastic deformation. However, as previously stated, the JC strength model shows an almost linear increment with the flow stress even after the ultimate compressive stress.

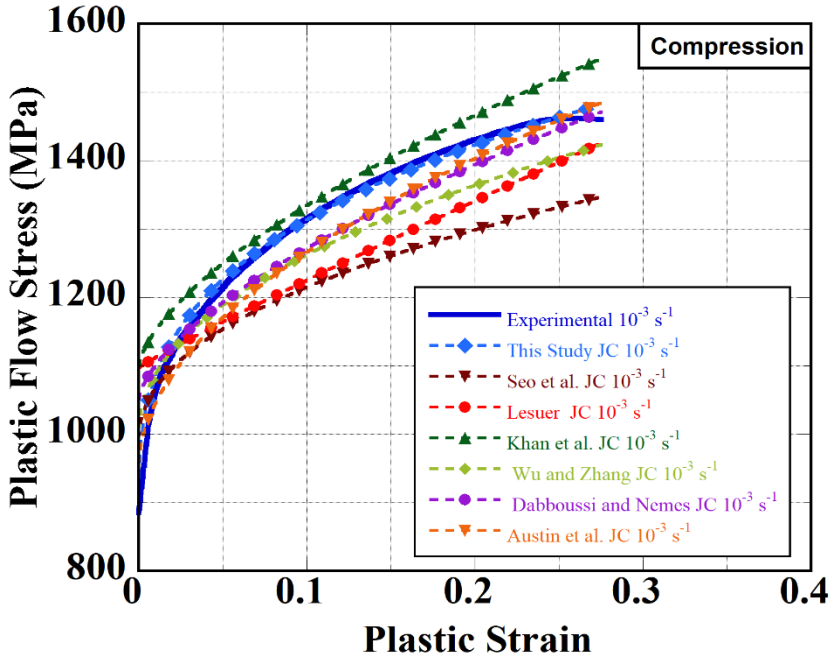

Figure 7.17. Comparison of prediction accuracy of compression JC strength parameters found in this study with the given parameters in the literature.

The calibrated JC failure model parameters of EBM-produced Ti64 are tabulated together with those published for Ti64 in Table 7.3. Most of the listed parameters belong to commercial Ti64 alloy. It is noticed that despite EBM-produced Ti64 being highly studied within broad scope, there are no experimentally calibrated JC failure model parameters for this material. In order to evaluate the convergence of the experimental failure strains and the predicted failure strains calculated by JC failure models calibrated in this study and previously published ones, comprehensive graphs of failure strains based on stress triaxiality, and strain rate are shown in Figure 7.18 and Figure 7.19, respectively. None of the considered JC models from the literature is able to predict the failure strains for EBM-produced Ti64. However, the calibrated JC failure model within this study exhibits perfect prediction ability considering both stress triaxiality and strain rate effects

Table 7.3. JC failure model parameters for Ti64 reported in the literature.

Process	D_1	D_2	D_3	D_4	D_5	Reference
Commercial	-0.8	1.18	-0.15	-0.012	2.1	Hammer [12]
Commercial	-0.09	0.27	0.48	0.014	3.87	Kay [196]
Commercial	-0.09	0.25	-0.5	0.014	3.87	Johnson [197]
Commercial	-0.09	0.25	-0.5	-0.023	3.214	Chen et al. [73]
Commercial	0.294	8.63	-8.4	-0.0213	4.22	Kıranlı [48]
Commercial	-0.09	29.997	-9.25	-0.2597	1.2681	Valoppi et al. [198]
Commercial	0.021	0.132	-1.1	0.0238	3.451	Wang et al. [187]
SLM / Vertical	0.005	0.43	-0.48	-	-	Wang and Li [195]
SLM / Vertical	0.105	16.7	-12.0	-	-	Wilson-Heid and Beese [199]
SLM / Horizontal	0.111	6.94	-10.8	-	-	
EBM / Vertical	0.0256	0.0438	-0.823	0.0522	3.87	**This Study**

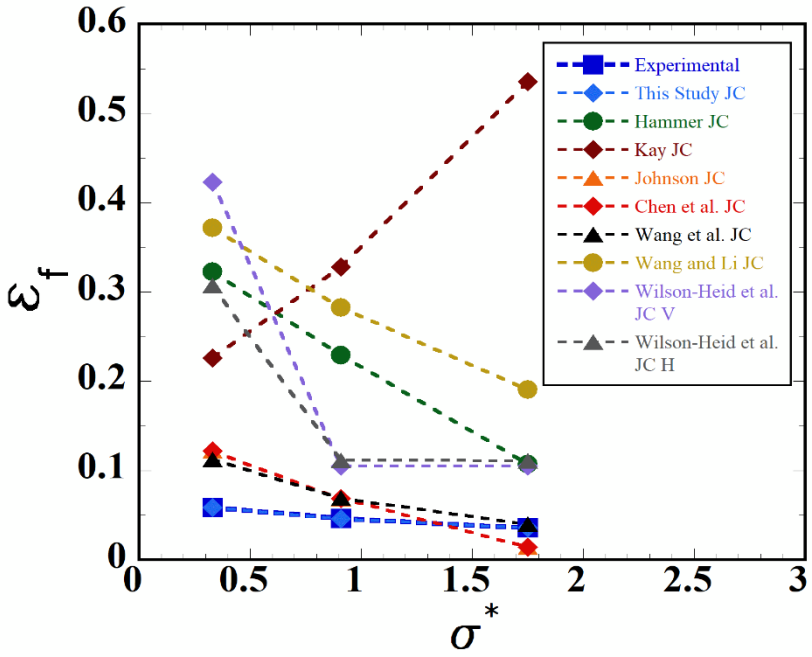

Figure 7.18. Experimental failure strains and predicted failure strains with JC failure models based on stress triaxiality.

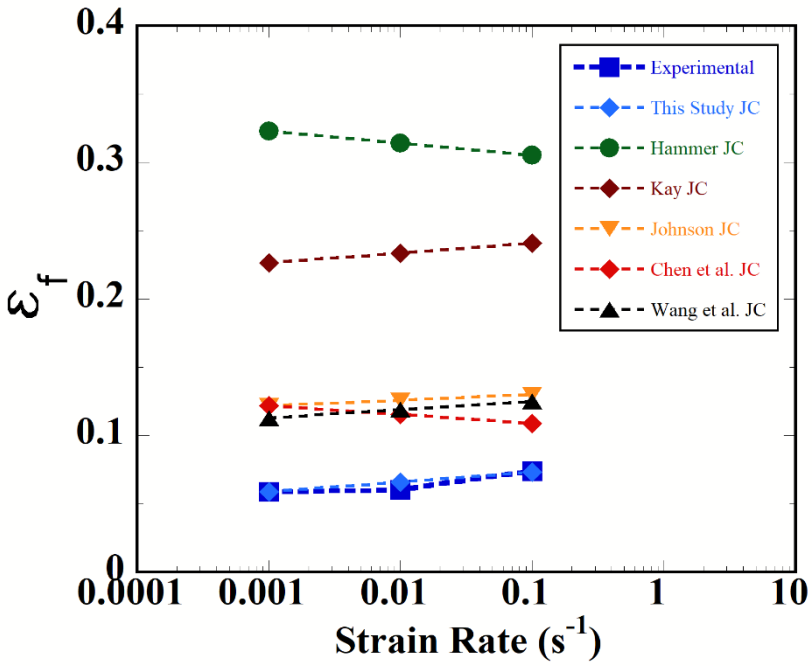

Figure 7.19. Experimental failure strains and predicted failure strains with JC failure models based on strain rate.

The calibrated JC strength and failure models are capable of perfectly predicting the material behaviors of EBM-produced Ti64 according to the experimental and predicted results evaluated above. These models can be utilized as material models in the numerical studies parts which attempt to predict the deformation behaviors of EBM-produced Ti64 under varying loading scenarios. However, the predicted flow behaviors slightly deviate when the material experiences adiabatic heating due to plastic strain saturation and exposes to excessive high-rate loadings (over 10^3 s^{-1}) which causes the alteration of the deformation mechanism of EBM-produced Ti64 during the plastic deformation. In order to increase the prediction accuracy of the JC strength model, it can be modified/developed by introducing new variables to involve adiabatic heating and strain rate effects in flow behavior predictions. As an alternative to this, different strength model relations which consider the physical state of the material during the plastic deformation and/or involve adiabatic heating conditions might be calibrated for numerical predictions of material behavior in EBM-produced Ti64 applications.

CHAPTER 8

CONCLUSIONS

In this study, the mechanical and microstructural properties of an EBM-produced Ti64 alloy were investigated experimentally. Microstructural properties were investigated for as-built parts by considering the build orientation, surface roughness, porosities, and phase constitutions. The deformation characteristics and mechanical properties were determined under varying loading regimes from quasi-static to high strain rates. Thereafter, the respective JC strength and failure model parameters were calibrated under tension and compression in order to numerically predict the material behavior by means of simulative approaches for the applications of this alloy.

Primary investigations of as-built parts showed that EBM-produced Ti64 possessed a high surface roughness that was noticeable even by bare eyes. The main factors resulting in a high rough surface were counted as the thermal radiation of melting energy to adjacent raked powders, build orientation, built part dimensions, and process parameters of EBM. The microstructural analysis of as-built parts showed that EBM-produced Ti64 consisted of α+β duplex phase with colony and basketweave morphologies in a mostly lamellar structure as a consequence of high thermal gradient dependent phase formation in Ti64. Additionally, the martensitic α' phase was inspected in some regions where high cooling rates occurred. Massive columnar β grains were found to stretch parallel to the build direction due to epitaxial growth rooted in heat flux from scanned layer to base plate of EBM system. Near equiaxed grain formations were detected in the direction perpendicular to the build direction. Microhardness tests revealed that directional microstructural alterations caused the directional anisotropy which was found ~79 MPa. Common porosities of AM methods such as gas pores and lack of fusion pores including keyhole pores were identified in all inspected regions irrespective of the build orientation and as-built part dimensions. In contrast to similar-sized gas pores, size variations of lack of fusion pores were big. The volume fraction of these porosities was found using the Archimedes method as 2.065% which was higher than the ones reported in the literature.

Mechanical properties of EBM-produced Ti64 alloy were studied under tension loadings at quasi-static rates (10^{-3}-10^{-1} s^{-1}) and compression loading at quasi-static and high strain rates (10^{-3}-2154 s^{-1}). The yield and tensile strength of EBM-produced Ti64 were found to comply with those listed in the standards and reported in the literature. EBM-produced Ti64 behaved nearly a perfectly plastic material under the tension with a relatively low strain hardening exponent, ~0.19. It suffered from extremely low ductility due to premature failure without necking. The high volume of porosity inside the bulk EBM-produced Ti64 parts stood as the most critical factor that was responsible for the premature failure of EBM-produced Ti64 under tension loading. The existence of the martensitic α' phase prompted the lower ductility and contributed to the failure of EBM-produced Ti64. The same material exhibited a ductile fracture mode under compression at all investigated strain rates. The fracture occurred through shear banding propagating 45° to the loading axis. The main reasons for the shear cracking were the adiabatic heating, followed by the shear band formation in the flow-induced region. High-rate loadings caused lower ductility as compared to quasi-static loadings. The plastic deformation of EBM-produced Ti64 under quasi-static strain rate was mainly controlled by dislocation slip while twinning appeared in addition to dislocation slip at high strain rates. This increased the strain hardening exponent of the compression over that of tension. Additionally, EBM-produced Ti64 showed a strain rate sensitivity both in tension and compression. The strength increased with increasing strain rate. The SRS parameter however decreased as the plastic strain increased.

Classical cup-and-cone type fracture under tension was identified in the tensile fracture surfaces. Tensile tested specimens revealed fracture evolution complying with the following steps: (1) fracture initiation on the sharp edges of lack of fusion defects (brittle zone), (2) equiaxed dimpled trans-granular fracture inside the grains (ductile zone), and (3) tearing of the scanned layers. In both quasi-static and high-rate compression, the fracture occurred via shear band formation. The shear band width increased with increasing strain rate. In the shear crack zone, shear dimples and smeared regions were observed.

The JC strength model and the JC damage model were calibrated using the experimental tension and compression stress-strain curves and the experimental tensile fracture strains, respectively. The JC strength and damage models were able to numerically predict the flow stresses and fracture strains. However, at excessively high strain rates (2154 s^{-1}), the JC strength model could not predict the flow stress due to the

complex deformation mechanisms including adiabatic heating. The calibrated JC strength model and the JC damage model were applicable numerical tools within the strain rate range between 10^{-3} and 10^{3} s^{-1}. In the light of the stated conclusions above, the following suggestions could be made in terms of the mechanical properties of EBM-produced Ti64 and the fidelity of the calibrated JC models:

- Post-HIP application to as-built parts with efficient heating and pressuring combination in order to improve the ductility of the produced parts.
- The optimization of EBM process parameters of the manufacturing to obtain less porous bulk product and to improve the mechanical properties, especially for higher ductility.
- The modification of classical parameters of JC models or introduction of new variables to define complex deformation mechanisms (hardening and softening mechanisms) at excessively high strain rates for convergently predicting the flow behavior of EBM-produced Ti64.

REFERENCES

1. Lütjering, G.; Williams, J. C., *Titanium*. Springer: Berlin; New York, **2003**; p 449.

2. Boyer, R.; Welsch, G.; Collings, E. W., *Materials Properties Handbook : Titanium Alloys*. ASM International: Materials Park, OH 44073-0002, **1994**; p 788.

3. Matthew J. Donachie, J., *Titanium: A Technical Guide*. Second Edition ed.; ASM International: Materials Park, OH 44073-0002, **2000**; p 216.

4. Murgau, C. C. Microstructure Model for Ti-6Al-4V used in Simulation of Additive Manufacturing. Doctoral Thesis, Luleå University Of Technology, Luleå, Sweden, **2016**.

5. Leyens, C.; Peters, M., *Titanium and Titanium Alloys: Fundamentals and Aplications*. Wiley-VCH Verlag GmbH & Co. KGaA: Weinheim, **2003**; p 523.

6. Åkerfeldt, P. Additive Manufacturing of Ti-6Al-4V: Relationship between Microstructure, Defects and Mechanical Properties. Doctoral Thesis, Luleå University Of Technology, Luleå, Sweden, **2016**.

7. Mohammadhosseini, A. Properties and Performance of Titanium alloy Processed by Electron Beam Melting Additive Manufacturing. Doctoral Thesis, Swinburne University of Technology, Hawthorn, Melbourne, Australia, **2015**.

8. Safdar, A. A study on Electron Beam Melted Ti-6Al-4V. Dissertation, Lund University, Lund, Sweden, **2012**.

9. Liu, S.; Shin, Y. C., Additive manufacturing of Ti6Al4V alloy: A review. *Materials & Design* **2019,** *164*, 107552.

10. Ahmed, T.; Rack, H. J., Phase transformations during cooling in α+β titanium alloys. *Materials Science and Engineering: A* **1998,** *243* (1), 206-211.

11. Pinke, P.; Réger, M., Heat Treatment of the Casted Ti6Al4V Titanium Alloy. *Materials Science and Technology, Special Issue - Constructional Materials 2005* **2005,** *5*, 6.

12. Hammer, J. T. Plastic Deformation and Ductile Fracture of Ti-6Al-4V under Various Loading Conditions. Master's Thesis, The Ohio State University, Federal Aviation Administration (FAA) William J. Hughes Technical Center, **2014**.

13. Herzog, D.; Seyda, V.; Wycisk, E.; Emmelmann, C., Additive manufacturing of metals. *Acta Materialia* **2016,** *117*, 371-392.

14. Calignano, F.; Manfredi, D.; Ambrosio, E.; Biamino, S.; Lombardi, M.; Atzeni, E.; Salmi, A.; Minetola, P.; Iuliano, L.; Fino, P., Overview on Additive Manufacturing Technologies. *Proceedings of the IEEE* **2017,** *PP*, 1-20.

15. Dzogbewu, T. C.; du Preez, W. B., Additive Manufacturing of Ti-Based Intermetallic Alloys: A Review and Conceptualization of a Next-Generation Machine. *Materials* **2021,** *14* (15), 4317.

16. Kardys, G. Factors to Consider When 3D Printing or Additive Manufacturing Metal Parts. https://insights.globalspec.com/article/7447/factors-to-consider-when-3d-printing-or-additive-manufacturing-metal-parts (accessed June 2021).

17. Lewandowski, J. J.; Seifi, M., Metal Additive Manufacturing: A Review of Mechanical Properties. *Annual Review of Materials Research* **2016,** *46* (1), 151-186.

18. Ladani, L.; Sadeghilaridjani, M., Review of Powder Bed Fusion Additive Manufacturing for Metals. *Metals* **2021,** *11* (9), 1391.

19. Herderick, E. D. Additive Manufacturing of Metals: A Review, *Materials Science and Technology (MS&T)*, October 16-20, 2011; Columbus, Ohio, USA, **2011**; p 13.

20. Mohd Yusuf, S.; Cutler, S.; Gao, N., Review: The Impact of Metal Additive Manufacturing on the Aerospace Industry. *Metals* **2019,** *9* (12), 1286.

21. Kim, T. Effects of Heat Treatment on the Microstructure and Mechanical Properties of Electron Beam Additively Manufactured Ti6Al4V with Powder Reuse. Master's Thesis, University of Washington, **2020**.

22. Dev Singh, D.; Mahender, T.; Raji Reddy, A., Powder bed fusion process: A brief review. *Materials Today: Proceedings* **2021,** *46*, 350-355.

23. Feenstra, D. R.; Banerjee, R.; Fraser, H. L.; Huang, A.; Molotnikov, A.; Birbilis, N., Critical review of the state of the art in multi-material fabrication via directed energy deposition. *Current Opinion in Solid State and Materials Science* **2021,** *25* (4), 100924.

24. Dass, A.; Moridi, A., State of the Art in Directed Energy Deposition: From Additive Manufacturing to Materials Design. *Coatings* **2019,** *9* (7), 418.

25. Chen, Y.; Zhang, X.; Parvez, M. M.; Liou, F., A Review on Metallic Alloys Fabrication Using Elemental Powder Blends by Laser Powder Directed Energy Deposition Process. *Materials* **2020,** *13* (16), 3562.

26. Wilson, J. M.; Piya, C.; Shin, Y. C.; Zhao, F.; Ramani, K., Remanufacturing of turbine blades by laser direct deposition with its energy and environmental impact analysis. *Journal of Cleaner Production* **2014,** *80*, 170-178.

27. Saboori, A.; Aversa, A.; Marchese, G.; Biamino, S.; Lombardi, M.; Fino, P., Application of Directed Energy Deposition-Based Additive Manufacturing in Repair. *Applied Sciences* **2019,** *9* (16), 3316.

28. Liu, M.; Kumar, A.; Bukkapatnam, S.; Kuttolamadom, M., A Review of the Anomalies in Directed Energy Deposition (DED) Processes & Potential Solutions - Part Quality & Defects. *Procedia Manufacturing* **2021,** *53*, 507-518.

29. Gong, H.; Rafi, K.; Gu, H.; Starr, T.; Stucker, B., Analysis of defect generation in Ti–6Al–4V parts made using powder bed fusion additive manufacturing processes. *Additive Manufacturing* **2014,** *1-4*, 87-98.

30. Kahlin, M. Fatigue Performance of Additive Manufactured Ti6Al4V in Aerospace Applications. Licentiate Thesis, Linköping University, Linköping, Sweden, **2017**.

31. GE Additive, GE Additive Production Playbook. GE Additive, West Chester, USA.

32. Airbus, Printing the future: Airbus expands its applications of the revolutionary additive layer manufacturing process. https://www.airbus.com/newsroom/news/en/2014/03/printing-the-future-airbus-expands-its-applications-of-the-revolutionary-additive-layer-manufacturing-process.html (accessed May 2020).

33. Parthasarathy, J.; Starly, B.; Raman, S., A design for the additive manufacture of functionally graded porous structures with tailored mechanical properties for biomedical applications. *Journal of Manufacturing Processes* **2011,** *13* (2), 160-170.

34. GE Additive, Additive Applications. https://www.ge.com/additive/additive-parts (accessed June 2020).

35. Gaytan, S. M.; Murr, L. E.; Medina, F.; Martinez, E.; Lopez, M. I.; Wicker, R. B., Advanced metal powder based manufacturing of complex components by electron beam melting. *Materials Technology* **2009,** *24* (3), 180-190.

36. Arcam EBM Systems, Arcam EBM Q20plus Datasheet. Arcam EBM - GE Additive, Sweden.

37. Arcam EBM Systems, Welcome to Manufacturing Unbound. Arcam EBM - GE Additive, Sweden.

38. Arcam EBM Systems, Inside Electron Beam Melting. Arcam EBM - GE Additive, Sweden.

39. Körner, C., Additive manufacturing of metallic components by selective electron beam melting — a review. *International Materials Reviews* **2016,** *61* (5), 361-377.

40. Cordero, Z. C.; Meyer, H. M.; Nandwana, P.; Dehoff, R. R., Powder bed charging during electron-beam additive manufacturing. *Acta Materialia* **2017,** *124*, 437-445.

41. Yiğitbaşı, S. T. Mechanical Properties of Ti6Al4V Parts Produced by Electron Beam Melting and Topology Optimization in Different Building Directions. Master's Thesis, Middle East Technical University, **2018**.

42. Ashtiani, H. R. R.; Shahsavari, P., Strain-dependent constitutive equations to predict high temperature flow behavior of AA2030 aluminum alloy. *Mechanics of Materials* **2016,** *100*, 209-218.

43. Zhao, J.; Quan, G.-Z.; Pan, J.; Wang, X.; Wu, D.-S.; Xia, Y.-F., A Modified Constitutive Model for Tensile Flow Behaviors of BR1500HS Ultra-High-Strength Steel at Medium and Low Temperature Regions. *High Temperature Materials and Processes* **2017,** *37* (1), 39-57.

44. Cai, J.; Wang, K.; Zhai, P.; Li, F.; Yang, J., A Modified Johnson-Cook Constitutive Equation to Predict Hot Deformation Behavior of Ti-6Al-4V Alloy. *Journal of Materials Engineering and Performance* **2015,** *24*, 32-44.

45. Zhao, H., A constitutive model for metals over a large range of strain rates Identification for mild-steel and aluminium sheets. *Materials Science and Engineering: A* **1997,** *230* (1), 95-99.

46. Cheng, W.; Outeiro, J.; Costes, J.-P.; M'Saoubi, R.; Karaouni, H.; Astakhov, V., A constitutive model for Ti6Al4V considering the state of stress and strain rate effects. *Mechanics of Materials* **2019,** *137*, 103103.

47. Xiao, M.; Li, F.; Zhao, W.; Yang, G., Constitutive equation for elevated temperature flow behavior of TiNiNb alloy based on orthogonal analysis. *Materials and Design* **2012,** *35*, 184-193.

48. Kıranlı, E. Determination of Constitutive Equation of A Biomedical Grade Ti6Al4V Alloy For Cross-Wedge Rolling. Master's Thesis, İzmir Institute of Technology, İzmir, Turkey, **2009**.

49. Gao, C. Y.; Zhang, L. C., A constitutive model for dynamic plasticity of FCC metals. *Materials Science and Engineering: A* **2010,** *527* (13), 3138-3143.

50. Hollomon, J. H., Tensile Deformation. *Transactions of the Metallurgical Society of AIME* **1945**, 268-290.

51. Ludwik, P., *Elemente der Technologischen Mechanik*. Springer, Berlin, Heidelberg: **1909**; p 59.

52. Johnson, G. R.; Cook, W. H. A constitutive model and data for metals subjected to large strains, high strain rates and high temperatures, *Proceedings 7th International Symposium on Ballistics*, The Hague, The Netherlands, **1983**; pp 541-547.

53. Johnson, G. R.; Cook, W. H., Fracture characteristics of three metals subjected to various strains, strain rates, temperatures and pressures. *Engineering Fracture Mechanics* **1985,** *21* (1), 31-48.

54. Lin, Y. C.; Chen, X.-M.; Liu, G., A modified Johnson–Cook model for tensile behaviors of typical high-strength alloy steel. *Materials Science and Engineering: A* **2010,** *527* (26), 6980-6986.

55. Zerilli, F. J.; Armstrong, R. W., Dislocation-mechanics-based constitutive relations for material dynamics calculations. *Journal of Applied Physics* **1987,** *61* (5), 1816-1825.

56. Samantaray, D.; Mandal, S.; Bhaduri, A. K.; Sivaprasad, P. V., An overview on constitutive modelling to predict elevated temperature flow behaviour of fast reactor structural materials. *Transactions of the Indian Institute of Metals* **2010,** *63* (6), 823-831.

57. Lin, Y. C.; Chen, X.-M., A combined Johnson–Cook and Zerilli–Armstrong model for hot compressed typical high-strength alloy steel. *Computational Materials Science* **2010,** *49* (3), 628-633.

58. Khan, A. S.; Liang, R., Behaviors of three BCC metal over a wide range of strain rates and temperatures: experiments and modeling. *International Journal of Plasticity* **1999,** *15* (10), 1089-1109.

59. Khan, A. S.; Suh, Y. S.; Chen, X.; Takacs, L.; Zhang, H., Nanocrystalline aluminum and iron: Mechanical behavior at quasi-static and high strain rates, and constitutive modeling. *International Journal of Plasticity* **2006,** *22* (2), 195-209.

60. Farrokh, B.; Khan, A. S., Grain size, strain rate, and temperature dependence of flow stress in ultra-fine grained and nanocrystalline Cu and Al: Synthesis, experiment, and constitutive modeling. *International Journal of Plasticity* **2009,** *25* (5), 715-732.

61. Sellars, C. M.; McTegart, W. J., On the mechanism of hot deformation. *Acta Metallurgica* **1966,** *14* (9), 1136-1138.

62. Fields, D. S.; Backofen, W. A., Determination of Strain Hardening Characteristics by Torsion Testing. *Proceeding of American Society for Testing and Materials* **1957,** *57*, 1259-1272.

63. Molinari, A.; Ravichandran, G., Constitutive modeling of high-strain-rate deformation in metals based on the evolution of an effective microstructural length. *Mechanics of Materials* **2005,** *37* (7), 737-752.

64. Voce, E., The relationship between stress and strain for homogeneous deformations. *Journal of the Institute of Metals* **1948,** *74*, 537-562.

65. Kocks, U. F., Laws for Work-Hardening and Low-Temperature Creep. *Journal of Engineering Materials and Technology* **1976,** *98* (1), 76-85.

66. Follansbee, P. S.; Kocks, U. F., A constitutive description of the deformation of copper based on the use of the mechanical threshold stress as an internal state variable. *Acta Metallurgica* **1988,** *36* (1), 81-93.

67. Lin, Y. C.; Chen, X.-M., A critical review of experimental results and constitutive descriptions for metals and alloys in hot working. *Materials and Design* **2011,** *32* (4), 1733-1759.

68. Gurusamy, M. M.; Rao, B. C., On the performance of modified Zerilli-Armstrong constitutive model in simulating the metal-cutting process. *Journal of Manufacturing Processes* **2017,** *28*, 253-265.

69. Yuan, Z.; Li, F.; Ji, G.; Qiao, H.; Li, J., Flow Stress Prediction of SiCp/Al Composites at Varying Strain Rates and Elevated Temperatures. *Journal of Materials Engineering and Performance* **2014,** *23* (3), 1016-1027.

70. Wu, S.-W.; Zhou, X.-G.; Cao, G.-M.; Liu, Z.-Y.; Wang, G.-D., The improvement on constitutive modeling of Nb-Ti micro alloyed steel by using intelligent algorithms. *Materials & Design* **2017,** *116*, 676-685.

71. Lin, Y. C.; Zhang, J.; Zhong, J., Application of neural networks to predict the elevated temperature flow behavior of a low alloy steel. *Computational Materials Science* **2008,** *43* (4), 752-758.

72. Mandal, S.; Sivaprasad, P. V.; Venugopal, S.; Murthy, K. P. N., Artificial neural network modeling to evaluate and predict the deformation behavior of stainless steel type AISI 304L during hot torsion. *Applied Soft Computing* **2009,** *9* (1), 237-244.

73. Chen, G.; Ren, C.; Lu, L.; Ke, Z.; Qin, X.; Ge, X., Determination of ductile damage behaviors of high strain rate compression deformation for Ti-6Al-4V alloy using experimental-numerical combined approach. *Engineering Fracture Mechanics* **2018,** *200*, 499-520.

74. Zerilli, F. J., Dislocation mechanics-based constitutive equations. *Metallurgical and Materials Transactions A* **2004,** *35* (9), 2547-2555.

75. Vural, M.; Caro, J., Experimental analysis and constitutive modeling for the newly developed 2139-T8 alloy. *Materials Science and Engineering: A* **2009,** *520* (1), 56-65.

76. Wang, Y.; Zeng, X.; Chen, H.; Yang, X.; Wang, F.; Zeng, L., Modified Johnson-Cook constitutive model of metallic materials under a wide range of temperatures and strain rates. *Results in Physics* **2021,** *27*, 104498.

77. Zhang, H.; Wen, W.; Cui, H., Behaviors of IC10 alloy over a wide range of strain rates and temperatures: Experiments and modeling. *Materials Science and Engineering A* **2009,** *504*, 99-103.

78. Li, H. Y.; Wang, X. F.; Duan, J. Y.; Liu, J. J., A modified Johnson Cook model for elevated temperature flow behavior of T24 steel. *Materials Science and Engineering: A* **2013,** *577*, 138-146.

79. Lai, X.; Li, H.; Li, C.; Lin, Z.; Ni, J., Modelling and analysis of micro scale milling considering size effect, micro cutter edge radius and minimum chip thickness. *International Journal of Machine Tools and Manufacture* **2008,** *48* (1), 1-14.

80. Choudhary, S.; Singh, P. K.; Khare, S.; Kumar, K.; Mahajan, P.; Verma, R. K., Ballistic impact behaviour of newly developed armour grade steel: An experimental and numerical study. *International Journal of Impact Engineering* **2020,** *140*, 103557.

81. Rotella, G.; Umbrello, D., Finite element modeling of microstructural changes in dry and cryogenic cutting of Ti6Al4V alloy. *CIRP Annals* **2014,** *63* (1), 69-72.

82. Meyer, H. W.; Kleponis, D. S., Modeling the high strain rate behavior of titanium undergoing ballistic impact and penetration. *International Journal of Impact Engineering* **2001,** *26* (1), 509-521.

83. Li, D.; Zhu, Z.; Xiao, S.; Zhang, G.; Lu, Y., Plastic flow behavior based on thermal activation and dynamic constitutive equation of 25CrMo4 steel during impact compression. *Materials Science and Engineering: A* **2017,** *707*, 459-465.

84. Hu, Q.; Zhao, F.; Fu, H.; Li, K.; Liu, F., Dislocation density and mechanical threshold stress in OFHC copper subjected to SHPB loading and plate impact. *Materials Science and Engineering: A* **2017,** *695*, 230-238.

85. Banerjee, B., The Mechanical Threshold Stress model for various tempers of AISI 4340 steel. *International Journal of Solids and Structures* **2007,** *44* (3), 834-859.

86. Zhang, F.; Shen, J.; Yan, X.-d.; Sun, J.-l.; Sun, X.-l.; Yang, Y.; Liu, Y., High-temperature flow behavior modeling of 2099 alloy considering strain effects. *Transactions of Nonferrous Metals Society of China* **2014,** *24* (3), 798-805.

87. Banerjee, A.; Dhar, S.; Acharyya, S.; Datta, D.; Nayak, N., Determination of Johnson cook material and failure model constants and numerical modelling of Charpy impact test of armour steel. *Materials Science and Engineering: A* **2015,** *640*, 200-209.

88. Wang, X.; Shi, J., Validation of Johnson-Cook plasticity and damage model using impact experiment. *International Journal of Impact Engineering* **2013,** *60*, 67-75.

89. Murugesan, M.; Jung, D. W., Johnson Cook Material and Failure Model Parameters Estimation of AISI-1045 Medium Carbon Steel for Metal Forming Applications. *Materials* **2019,** *12* (4), 609.

90. Çakırcalı, M.; Kılıçaslan, C.; Güden, M.; Kıranlı, E.; Shchukin, V. Y.; Petronko, V. V., Cross wedge rolling of a Ti6Al4V (ELI) alloy: the experimental studies and the finite element simulation of the deformation and failure. *The International Journal of Advanced Manufacturing Technology* **2013,** *65* (9), 1273-1287.

91. Wang, B.; Liu, Z., Shear localization sensitivity analysis for Johnson–Cook constitutive parameters on serrated chips in high speed machining of Ti6Al4V. *Simulation Modelling Practice and Theory* **2015,** *55*, 63-76.

92. Bai, Y.; Teng, X.; Wierzbicki, T., On the Application of Stress Triaxiality Formula for Plane Strain Fracture Testing. *Journal of Engineering Materials and Technology* **2009,** *131* (2), 021002.

93. Bridgman, P. W., *Studies in Large Plastic Flow and Fracture : With Special Emphasis on the Effects of Hydrostatic Pressure*. Harvard University Press: Cambridge, MA, USA, **1964**.

94. Cao, Y.; Zhen, Y.; Song, M.; Yi, H.; Li, F.; Li, X., Determination of Johnson–Cook parameters and evaluation of Charpy impact test performance for X80 pipeline steel. *International Journal of Mechanical Sciences* **2020,** *179*, 105627.

95. Gerstgrasser, M.; Smolenicki, D.; Akbari, M.; Klippel, H.; Roelofs, H.; Cadoni, E.; Wegener, K., Analysis of two parameter identification methods for original and modified Johnson-Cook fracture strains, including numerical comparison and validation of a new blue-brittle dependent fracture model for free-cutting steel 50SiB8. *Theoretical and Applied Fracture Mechanics* **2021,** *112*, 102905.

96. Arcam EBM Systems, Ti6Al4V ELI Titanium Alloy. Arcam EBM - GE Additive, Sweden.

97. ASTM E8 / E8M-16a, Standard Test Methods for Tension Testing of Metallic Materials. ASTM International: West Conshohocken, PA, **2016**.

98. ASTM E9-19, Standard Test Methods of Compression Testing of Metallic Materials at Room Temperature. ASTM International: West Conshohocken, PA, **2019**.

99. Spierings, A. B.; Schneider, M.; Eggenberger, R., Comparison of density measurement techniques for additive manufactured metallic parts. *Rapid Prototyping Journal* **2011,** *17* (5), 380-386.

100. ASTM E384-16, Standard Test Method for Microindentation Hardness of Materials. ASTM International: West Conshohocken, PA, **2016**.

101. Kuhn, H. A.; Medlin, D., *ASM Handbook, Volume 8: Mechanical Testing and Evaluation*. ASM International: Materials Park, OH 44073-0002, **2000**; p 2235.

102. Rodriguez, O. L.; Allison, P. G.; Whittington, W. R.; El Kadiri, H.; Rivera, O. G.; Barkey, M. E., Strain rate effect on the tension and compression stress-state

asymmetry for electron beam additive manufactured Ti6Al4V. *Materials Science and Engineering: A* **2018,** *713*, 125-133.

103. Luo, J.; Li, M.; Yu, W.; Li, H., The variation of strain rate sensitivity exponent and strain hardening exponent in isothermal compression of Ti–6Al–4V alloy. *Materials & Design* **2010,** *31* (2), 741-748.

104. Sangid, M. D.; Nicolas, A.; Kapoor, K.; Fodran, E.; Madsen, J., Modeling the Role of Epitaxial Grain Structure of the Prior β Phase and Associated Fiber Texture on the Strength Characteristics of Ti-6Al-4V Produced via Additive Manufacturing. *Materials (Basel)* **2020,** *13* (10).

105. Lesuer, D. R., *Experimental Investigations of Material Models for Ti-6Al-4V Titanium and 2024-T3 Aluminum*; DOT/FAA/AR-00/25; Lawrence Livermore National Laboratory, USA, **2000**; p 41.

106. Rafi, H. K.; Karthik, N. V.; Gong, H.; Starr, T. L.; Stucker, B. E., Microstructures and Mechanical Properties of Ti6Al4V Parts Fabricated by Selective Laser Melting and Electron Beam Melting. *Journal of Materials Engineering and Performance* **2013,** *22* (12), 3872-3883.

107. Chern, A. H.; Nandwana, P.; Yuan, T.; Kirka, M. M.; Dehoff, R. R.; Liaw, P. K.; Duty, C. E., A review on the fatigue behavior of Ti-6Al-4V fabricated by electron beam melting additive manufacturing. *International Journal of Fatigue* **2019,** *119*, 173-184.

108. Li, P.; Warner, D. H.; Fatemi, A.; Phan, N., Critical assessment of the fatigue performance of additively manufactured Ti–6Al–4V and perspective for future research. *International Journal of Fatigue* **2016,** *85*, 130-143.

109. Wang, P.; Sin, W. J.; Nai, M. L. S.; Wei, J., Effects of Processing Parameters on Surface Roughness of Additive Manufactured Ti-6Al-4V via Electron Beam Melting. *Materials* **2017,** *10* (10), 1121.

110. de Formanoir, C.; Michotte, S.; Rigo, O.; Germain, L.; Godet, S., Electron beam melted Ti–6Al–4V: Microstructure, texture and mechanical behavior of the as-built and heat-treated material. *Materials Science and Engineering: A* **2016,** *652*, 105-119.

111. Masuo, H.; Tanaka, Y.; Morokoshi, S.; Yagura, H.; Uchida, T.; Yamamoto, Y.; Murakami, Y., Influence of defects, surface roughness and HIP on the fatigue strength of Ti-6Al-4V manufactured by additive manufacturing. *International Journal of Fatigue* **2018,** *117*, 163-179.

112. Safdar, A.; Wei, L. Y.; Snis, A.; Lai, Z., Evaluation of microstructural development in electron beam melted Ti-6Al-4V. *Materials Characterization* **2012,** *65*, 8-15.

113. Sharma, H.; Parfitt, D.; Syed, A. K.; Wimpenny, D.; Muzangaza, E.; Baxter, G.; Chen, B., A critical evaluation of the microstructural gradient along the build

direction in electron beam melted Ti-6Al-4V alloy. *Materials Science and Engineering: A* **2019,** *744*, 182-194.

114. Gong, X.; Lydon, J.; Cooper, K.; Chou, K., Beam speed effects on Ti–6Al–4V microstructures in electron beam additive manufacturing. *Journal of Materials Research* **2014,** *29* (17), 1951-1959.

115. Antonysamy, A.; Prangnell, P.; Meyer, J., Effect of Wall Thickness Transitions on Texture and Grain Structure in Additive Layer Manufacture (ALM) Ti-6Al-4V. *Materials Science Forum* **2012,** *706-709*, 205-210.

116. Xu, J.; Zhu, J.; Fan, J.; Zhou, Q.; Peng, Y.; Guo, S., Microstructure and mechanical properties of Ti–6Al–4V alloy fabricated using electron beam freeform fabrication. *Vacuum* **2019,** *167*, 364-373.

117. Murr, L. E.; Esquivel, E. V.; Quinones, S. A.; Gaytan, S. M.; Lopez, M. I.; Martinez, E. Y.; Medina, F.; Hernandez, D. H.; Martinez, E.; Martinez, J. L.; Stafford, S. W.; Brown, D. K.; Hoppe, T.; Meyers, W.; Lindhe, U.; Wicker, R. B., Microstructures and mechanical properties of electron beam-rapid manufactured Ti–6Al–4V biomedical prototypes compared to wrought Ti–6Al–4V. *Materials Characterization* **2009,** *60* (2), 96-105.

118. Hao, Y.-L.; Li, S.-J.; Yang, R., Biomedical titanium alloys and their additive manufacturing. *Rare Metals* **2016,** *35* (9), 661-671.

119. Wang, P.; Tan, X.; Nai, M. L. S.; Tor, S. B.; Wei, J., Spatial and geometrical-based characterization of microstructure and microhardness for an electron beam melted Ti–6Al–4V component. *Materials & Design* **2016,** *95*, 287-295.

120. Galarraga, H.; Warren, R. J.; Lados, D. A.; Dehoff, R. R.; Kirka, M. M.; Nandwana, P., Effects of heat treatments on microstructure and properties of Ti-6Al-4V ELI alloy fabricated by electron beam melting (EBM). *Materials Science and Engineering: A* **2017,** *685*, 417-428.

121. Rodriguez, O. L.; Allison, P. G.; Whittington, W. R.; Francis, D. K.; Rivera, O. G.; Chou, K.; Gong, X.; Butler, T. M.; Burroughs, J. F., Dynamic tensile behavior of electron beam additive manufactured Ti6Al4V. *Materials Science and Engineering: A* **2015,** *641*, 323-327.

122. Antonysamy, A. A.; Meyer, J.; Prangnell, P. B., Effect of build geometry on the β-grain structure and texture in additive manufacture of Ti6Al4V by selective electron beam melting. *Materials Characterization* **2013,** *84*, 153-168.

123. Tan, X.; Kok, Y.; Tan, Y. J.; Descoins, M.; Mangelinck, D.; Tor, S. B.; Leong, K. F.; Chua, C. K., Graded microstructure and mechanical properties of additive manufactured Ti–6Al–4V via electron beam melting. *Acta Materialia* **2015,** *97*, 1-16.

124. Al-Bermani, S. S.; Blackmore, M. L.; Zhang, W.; Todd, I., The Origin of Microstructural Diversity, Texture, and Mechanical Properties in Electron Beam

Melted Ti-6Al-4V. *Metallurgical and Materials Transactions A* **2010,** *41* (13), 3422-3434.

125. Tang, M.; Pistorius, P. C.; Beuth, J. L., Prediction of lack-of-fusion porosity for powder bed fusion. *Additive Manufacturing* **2017,** *14*, 39-48.

126. Wang, P.; Tan, X.; He, C.; Nai, M. L. S.; Huang, R.; Tor, S. B.; Wei, J., Scanning optical microscopy for porosity quantification of additively manufactured components. *Additive Manufacturing* **2018,** *21*, 350-358.

127. Hrabe, N.; White, R.; Lucon, E., Effects of internal porosity and crystallographic texture on Charpy absorbed energy of electron beam melting titanium alloy (Ti-6Al-4V). *Materials Science and Engineering: A* **2019,** *742*, 269-277.

128. Galarraga, H.; Lados, D. A.; Dehoff, R. R.; Kirka, M. M.; Nandwana, P., Effects of the microstructure and porosity on properties of Ti-6Al-4V ELI alloy fabricated by electron beam melting (EBM). *Additive Manufacturing* **2016,** *10*, 47-57.

129. Gong, H.; Rafi, K.; Gu, H.; Janaki Ram, G. D.; Starr, T.; Stucker, B., Influence of defects on mechanical properties of Ti–6Al–4V components produced by selective laser melting and electron beam melting. *Materials & Design* **2015,** *86*, 545-554.

130. Maizza, G.; Caporale, A.; Polley, C.; Seitz, H., Micro-Macro Relationship between Microstructure, Porosity, Mechanical Properties, and Build Mode Parameters of a Selective-Electron-Beam-Melted Ti-6Al-4V Alloy. *Metals* **2019,** *9* (7), 786.

131. Ackelid, U.; Svensson, M. Additive Manufacturing of Dense Metal Parts by Electron Beam Melting, *International Powder Metallurgy Congress & Exhibition; Euro PM2009 proceedings*, European Powder Metallurgy Association: Shrewsbury, Copenhagen, Denmark, **2009**; pp 179-184.

132. Lu, S. L.; Tang, H. P.; Ning, Y. P.; Liu, N.; StJohn, D. H.; Qian, M., Microstructure and Mechanical Properties of Long Ti-6Al-4V Rods Additively Manufactured by Selective Electron Beam Melting Out of a Deep Powder Bed and the Effect of Subsequent Hot Isostatic Pressing. *Metallurgical and Materials Transactions A* **2015,** *46* (9), 3824-3834.

133. Bauereiß, A.; Scharowsky, T.; Körner, C., Defect generation and propagation mechanism during additive manufacturing by selective beam melting. *Journal of Materials Processing Technology* **2014,** *214* (11), 2522-2528.

134. Qian, M.; Xu, W.; Brandt, M.; Tang, H. P., Additive manufacturing and postprocessing of Ti-6Al-4V for superior mechanical properties. *MRS Bulletin* **2016,** *41* (10), 775-784.

135. Teixeira, Ó.; Silva, F. J. G.; Ferreira, L. P.; Atzeni, E., A Review of Heat Treatments on Improving the Quality and Residual Stresses of the Ti–6Al–4V Parts Produced by Additive Manufacturing. *Metals* **2020,** *10* (8), 1006.

136. Eklund, A.; Ahlfors, M.; Bahbou, F.; Wedenstrand, J., Optimizing HIP and Printing Parameters for EBM Ti-6Al-4V. *Key Engineering Materials* **2018,** *770*, 174-178.

137. Syed, A. K.; Awd, M.; Walther, F.; Zhang, X., Microstructure and mechanical properties of as-built and heat-treated electron beam melted Ti–6Al–4V. *Materials Science and Technology* **2019,** *35* (6), 653-660.

138. Bertolini, R.; Bruschi, S.; Ghiotti, A.; Pezzato, L.; Dabalà, M., Influence of the machining cooling strategies on the dental tribocorrosion behaviour of wrought and additive manufactured Ti6Al4V. *Biotribology* **2017,** *11*, 60-68.

139. Murr, L. E.; Gaytan, S. M.; Martinez, E.; Medina, F.; Wicker, R. B., Next Generation Orthopaedic Implants by Additive Manufacturing Using Electron Beam Melting. *International Journal of Biomaterials* **2012,** *2012*, 245727.

140. Thijs, L.; Verhaeghe, F.; Craeghs, T.; Humbeeck, J. V.; Kruth, J.-P., A study of the microstructural evolution during selective laser melting of Ti–6Al–4V. *Acta Materialia* **2010,** *58* (9), 3303-3312.

141. Pirozzi, C.; Franchitti, S.; Borrelli, R.; Caiazzo, F.; Alfieri, V.; Argenio, P., Study on the Factors Affecting the Mechanical Behavior of Electron Beam Melted Ti6Al4V. *Journal of Materials Engineering and Performance* **2017,** *26* (9), 4491-4499.

142. Popov, V.; Katz-Demyanetz, A.; Kovalevsky, A.; Biletskiy, R.; Strokin, E.; Garkun, A.; Bamberger, M., Effect of the hatching strategies on mechanical properties and microstructure of SEBM manufactured Ti-6Al-4V specimens. *Letters on Materials* **2018,** *8*, 468-472.

143. Wysocki, B.; Maj, P.; Sitek, R.; Buhagiar, J.; Kurzydłowski, K. J.; Święszkowski, W., Laser and Electron Beam Additive Manufacturing Methods of Fabricating Titanium Bone Implants. *Applied Sciences* **2017,** *7* (7), 657.

144. Davids, W. J.; Chen, H.; Nomoto, K.; Wang, H.; Babu, S.; Primig, S.; Liao, X.; Breen, A.; Ringer, S. P., Phase transformation pathways in Ti-6Al-4V manufactured via electron beam powder bed fusion. *Acta Materialia* **2021,** *215*, 117131.

145. Lu, W.; Shi, Y.; Li, X.; Lei, Y., Correlation Between Tensile Strength and Hardness of Electron Beam Welded TC4-DT Joints. *Journal of Materials Engineering and Performance* **2013,** *22* (6), 1694-1700.

146. Cahoon, J. R., An improved equation relating hardness to ultimate strength. *Metallurgical and Materials Transactions B* **1972,** *3* (11), 3040-3040.

147. Chan, K. S.; Koike, M.; Mason, R. L.; Okabe, T., Fatigue Life of Titanium Alloys Fabricated by Additive Layer Manufacturing Techniques for Dental Implants. *Metallurgical and Materials Transactions A* **2013,** *44* (2), 1010-1022.

148. Aliprandi, P.; Giudice, F.; Guglielmino, E.; Sili, A., Tensile and Creep Properties Improvement of Ti-6Al-4V Alloy Specimens Produced by Electron Beam Powder Bed Fusion Additive Manufacturing. *Metals* **2019,** *9* (11), 1207.

149. Leon, A.; Levy, G. K.; Ron, T.; Shirizly, A.; Aghion, E., The effect of hot isostatic pressure on the corrosion performance of Ti-6Al-4 V produced by an electron-beam melting additive manufacturing process. *Additive Manufacturing* **2020,** *33*, 101039.

150. Raghavan, S.; Nai, M. L. S.; Wang, P.; Sin, W. J.; Li, T.; Wei, J., Heat treatment of electron beam melted (EBM) Ti-6Al-4V: microstructure to mechanical property correlations. *Rapid Prototyping Journal* **2018,** *24* (4), 774-783.

151. Molaei, R.; Fatemi, A.; Phan, N., Significance of hot isostatic pressing (HIP) on multiaxial deformation and fatigue behaviors of additive manufactured Ti-6Al-4V including build orientation and surface roughness effects. *International Journal of Fatigue* **2018,** *117*, 352-370.

152. ASTM F136-13(2021)e1, Standard Specification for Wrought Titanium-6Aluminum-4Vanadium ELI (Extra Low Interstitial) Alloy for Surgical Implant Applications (UNS R56401). ASTM International: West Conshohocken, PA, **2013**.

153. Vilaro, T.; Colin, C.; Bartout, J. D., As-Fabricated and Heat-Treated Microstructures of the Ti-6Al-4V Alloy Processed by Selective Laser Melting. *Metallurgical and Materials Transactions A* **2011,** *42* (10), 3190-3199.

154. ASTM F1108-04, Standard Specification for Titanium-6Aluminum-4Vanadium Alloy Castings for Surgical Implants (UNS R56406). ASTM International: West Conshohocken, PA, **2004**.

155. Zhai, Y.; Galarraga, H.; Lados, D. A., Microstructure, static properties, and fatigue crack growth mechanisms in Ti-6Al-4V fabricated by additive manufacturing: LENS and EBM. *Engineering Failure Analysis* **2016,** *69*, 3-14.

156. Qiu, C.; Adkins, N. J. E.; Attallah, M. M., Microstructure and tensile properties of selectively laser-melted and of HIPed laser-melted Ti–6Al–4V. *Materials Science and Engineering: A* **2013,** *578*, 230-239.

157. Qiao, B.; Dong, C.; Tong, S.; Kong, D.; Ni, X.; Zhang, H.; Wang, L.; Li, X., Anisotropy in α′ martensite and compression behavior of Ti6Al4V prepared by selective laser melting. *Materials Research Express* **2019,** *6* (12), 126548.

158. Losertová, M.; Kubeš, V., Microstructure and mechanical properties of selective laser melted Ti6Al4V alloy. *IOP Conference Series: Materials Science and Engineering* **2017,** *266*, 012009.

159. Edwards, P.; O'Conner, A.; Ramulu, M., Electron Beam Additive Manufacturing of Titanium Components: Properties and Performance. *Journal of Manufacturing Science and Engineering* **2013,** *135* (6).

160. Austin, D. C.; Bevan, M. A.; East, D.; Brown, A. D.; Ameri, A. A. H.; Hazell, P. J.; Chen, A.; Chan, S. L. I.; Quadir, M. Z.; Escobedo, J. P. Microstructural Investigation and Impact Testing of Additive Manufactured TI-6AL-4V, *Characterization of Minerals, Metals, and Materials*, 2017; Springer International Publishing: Cham, **2017**; pp 191-199.

161. ASTM F3001-14, Standard Specification for Additive Manufacturing Titanium-6 Aluminum-4 Vanadium ELI (Extra Low Interstitial) with Powder Bed Fusion. ASTM International: West Conshohocken, PA, **2014**.

162. Peirs, J.; Tirry, W.; Amin-Ahmadi, B.; Coghe, F.; Verleysen, P.; Rabet, L.; Schryvers, D.; Degrieck, J., Microstructure of adiabatic shear bands in Ti6Al4V. *Materials Characterization* **2013,** *75*, 79-92.

163. Coghe, F.; Tirry, W.; Rabet, L.; Schryvers, D.; Van Houtte, P., Importance of twinning in static and dynamic compression of a Ti–6Al–4V titanium alloy with an equiaxed microstructure. *Materials Science and Engineering: A* **2012,** *537*, 1-10.

164. Roth, A.; Lebyodkin, M. A.; Lebedkina, T. A.; Lecomte, J. S.; Richeton, T.; Amouzou, K. E. K., Mechanisms of anisotropy of mechanical properties of α-titanium in tension conditions. *Materials Science and Engineering: A* **2014,** *596*, 236-243.

165. Becker, H.; Pantleon, W., Work-hardening stages and deformation mechanism maps during tensile deformation of commercially pure titanium. *Computational Materials Science* **2013,** *76*, 52-59.

166. Guden, M.; Celik, E.; Akar, E.; Cetiner, S., Compression testing of a sintered Ti6Al4V powder compact for biomedical applications. *Materials Characterization* **2005,** *54* (4), 399-408.

167. Tu, Z.; Lu, Y., Evaluation of typical concrete material models used in hydrocodes for high dynamic response simulations. *International Journal of Impact Engineering* **2009,** *36* (1), 132-146.

168. Zhou, X. Q.; Kuznetsov, V. A.; Hao, H.; Waschl, J., Numerical prediction of concrete slab response to blast loading. *International Journal of Impact Engineering* **2008,** *35* (10), 1186-1200.

169. Yang, H. S.; Gurewitz, G.; Mukherjee, A. K., Mechanical Behavior and Microstructural Evolution during Superplastic Deformation of Ti-6Al-4V. *Materials Transactions, JIM* **1991,** *32* (5), 465-472.

170. Ladani, L., Local and Global Mechanical Behavior and Microstructure of Ti6Al4V Parts Built Using Electron Beam Melting Technology. *Metallurgical and Materials Transactions A* **2015,** *46* (9), 3835-3841.

171. Donachie, M. J., *Titanium : A Technical Guide, 2nd Edition*. ASM International: Materials Park, Ohio 44073-0002, **2000**; p 216.

172. Ghosh, A. K.; Hamilton, C. H., Mechanical behavior and hardening characteristics of a superplastic Ti-6AI-4V alloy. *Metallurgical Transactions A* **1979,** *10* (6), 699-706.

173. Mirone, G.; Barbagallo, R.; Giudice, F.; Di Bella, S., Analysis and modelling of tensile and torsional behaviour at different strain rates of Ti6Al4V alloy additive manufactured by electron beam melting (EBM). *Materials Science and Engineering: A* **2020,** *793*, 139916.

174. Alaghmandfard, R.; Chalasani, D.; Odeshi, A.; Mohammadi, M. Microstructure and Mechanical Properties of Ti-6Al-4V Parts Fabricated by Electron Beam Melting under Dynamic Compression Tests, *Canadian Society for Mechanical Engineering International Congress 2020*, June 21-24, 2020; Charlottetown, PE, Canada, **2020**; p 5.

175. Nemat-Nasser, S.; Guo, W.-G.; Nesterenko, V. F.; Indrakanti, S. S.; Gu, Y.-B., Dynamic response of conventional and hot isostatically pressed Ti–6Al–4V alloys: experiments and modeling. *Mechanics of Materials* **2001,** *33* (8), 425-439.

176. Liu, Y.; Xu, H.; Zhu, L.; Wang, X.; Han, Q.; Li, S.; Wang, Y.; Setchi, R.; Wang, D., Investigation into the microstructure and dynamic compressive properties of selective laser melted Ti–6Al–4V alloy with different heating treatments. *Materials Science and Engineering: A* **2021,** *805*, 140561.

177. Lee, W.-S.; Lin, C.-F., High-temperature deformation behaviour of Ti6Al4V alloy evaluated by high strain-rate compression tests. *Journal of Materials Processing Technology* **1998,** *75* (1), 127-136.

178. Xiao, L.; Song, W.; Hu, M.; Li, P., Compressive properties and micro-structural characteristics of Ti–6Al–4V fabricated by electron beam melting and selective laser melting. *Materials Science and Engineering: A* **2019,** *764*, 138204.

179. Lee, W.-S.; Lin, C.-F., Plastic deformation and fracture behaviour of Ti–6Al–4V alloy loaded with high strain rate under various temperatures. *Materials Science and Engineering: A* **1998,** *241* (1), 48-59.

180. Seo, S.; Min, O.; Yang, H., Constitutive equation for Ti–6Al–4V at high temperatures measured using the SHPB technique. *International Journal of Impact Engineering* **2005,** *31* (6), 735-754.

181. Dumitrescu, M.; Elbestawi, M. A.; El-Wardany, T. I. Mist Coolant Applications in High Speed Machining of Advanced Materials, *3rd, International conference*

on metal cutting and high speed machining, Kluwer Academic: New York, Metz, France, **2002**; pp 329-340.

182. Calamaz, M.; Coupard, D.; Girot, F., A new material model for 2D numerical simulation of serrated chip formation when machining titanium alloy Ti–6Al–4V. *International Journal of Machine Tools and Manufacture* **2008,** *48* (3), 275-288.

183. Khan, A. S.; Sung Suh, Y.; Kazmi, R., Quasi-static and dynamic loading responses and constitutive modeling of titanium alloys. *International Journal of Plasticity* **2004,** *20* (12), 2233-2248.

184. Macdougall, D. A. S.; Harding, J., A constitutive relation and failure criterion for Ti6Al4V alloy at impact rates of strain. *Journal of the Mechanics and Physics of Solids* **1999,** *47* (5), 1157-1185.

185. Chen, G.; Ren, C.; Qin, X.; Li, J., Temperature dependent work hardening in Ti–6Al–4V alloy over large temperature and strain rate ranges: Experiments and constitutive modeling. *Materials & Design* **2015,** *83*, 598-610.

186. Yatnalkar, R. S. Experimental Investigation of Plastic Deformation of Ti-6Al-4V under Various Loading Conditions. Master's Thesis, The Ohio State University, **2010**.

187. Wang, C.; Suo, T.; Li, Y.; Xue, P.; Tang, Z., A New Experimental and Numerical Framework for Determining of Revised J-C Failure Parameters. *Metals* **2018,** *8* (6).

188. Wu, H. B.; Zhang, S. J., 3D FEM simulation of milling process for titanium alloy Ti6Al4V. *The International Journal of Advanced Manufacturing Technology* **2014,** *71* (5), 1319-1326.

189. Dabboussi, W.; Nemes, J. A., Modeling of ductile fracture using the dynamic punch test. *International Journal of Mechanical Sciences* **2005,** *47* (8), 1282-1299.

190. Raut, N.; Shinde, S.; Yakkundi, V., Determination of Johnson Cook parameters for Ti-6Al-4 V Grade 5 experimentally by using three different methods. *Materials Today: Proceedings* **2021,** *44*, 1653-1658.

191. Perez, J. A.; Eguía, V. M.; Sobrino, J. C.; Martínez, A. M., Experimental results and constitutive model of the mechanical behavior of Ti6Al4V alloy at high temperature. *Procedia Manufacturing* **2019,** *41*, 723-730.

192. Kotkunde, N.; Deole, A. D.; Gupta, A. K.; Singh, S. K., Comparative study of constitutive modeling for Ti–6Al–4V alloy at low strain rates and elevated temperatures. *Materials & Design* **2014,** *55*, 999-1005.

193. Hu, H.; Xu, Z.; Dou, W.; Huang, F., Effects of strain rate and stress state on mechanical properties of Ti-6Al-4V alloy. *International Journal of Impact Engineering* **2020,** *145*, 103689.

194. Hou, X.; Liu, Z.; Wang, B.; Lv, W.; Liang, X.; Hua, Y., Stress-Strain Curves and Modified Material Constitutive Model for Ti-6Al-4V over the Wide Ranges of Strain Rate and Temperature. *Materials* **2018,** *11* (6).

195. Wang, Z.; Li, P., Characterisation and constitutive model of tensile properties of selective laser melted Ti-6Al-4V struts for microlattice structures. *Materials Science and Engineering: A* **2018,** *725*, 350-358.

196. Kay, G., *Failure Modeling of Titanium 6Al-4V and Aluminum 2024-T3 With the Johnson-Cook Material Model*; DOT/FAA/AR-03/57; Lawrence Livermore National Laboratory, United States, **2003**; p 24.

197. Johnson, G. R., *Strength and Fracture Characteristics of a Titanium Alloy (.06Al, .04V) Subjected to Various Strains, Strain Rates, Temperatures and Pressures*; Naval Surface Weapons Center NSWC, United States, **1985**; pp 86-144.

198. Valoppi, B.; Bruschi, S.; Ghiotti, A., Modelling of Fracture Onset in Ti6Al4V Sheets Deformed at Elevated Temperature. *Procedia Manufacturing* **2016,** *5*, 248-258.

199. Wilson-Heid, A. E.; Beese, A. M., Fracture of laser powder bed fusion additively manufactured Ti–6Al–4V under multiaxial loading: Calibration and comparison of fracture models. *Materials Science and Engineering: A* **2019,** *761*, 137967.